Synthesis of cobalt-based nanohybrids and study of their magnetic and optical properties. Carbon coating and functionalization with luminescent dyes

Der Fakultät für Physik der Universität Duisburg-Essen
zur Erlangung des akademischen Grades eines
Doktors der Naturwissenschaften
genehmigte Dissertation

von

Miguel Comesaña-Hermo

aus

Vigo-Spanien

Referent Deutschland: Prof. Dr. Michael Farle
Korreferent Deutschland: Prof. Dr. Uwe Bovensiepen
Referent Frankreich: Prof. Dr. Catherine Amiens
Korreferent Frankreich: Prof. Dr. Jean-Yves Piquemal
Tag der mündlichen Prüfung: 13.01.2011

Université de Toulouse

THÈSE

En vue de l'obtention du

DOCTORAT DE L'UNIVERSITÉ DE TOULOUSE

Délivré par *l'Université Toulouse III - Paul Sabatier*
Discipline ou spécialité : *Chimie Organométallique et de Coordination*

Présentée et soutenue par *Miguel COMESAÑA-HERMO*
Le *13 janvier 2011*

Titre : *Synthesis of cobalt-based nanohybrids and study of their magnetic and optical properties. Carbon coating and functionalization with luminescent dyes.*

JURY

Marie-Joelle MENU, Einsegnant-chercheur, CNRS, Toulouse (France)	*Présidente*
Jean-Yves PIQUEMAL, Professeur à l'Université Paris VII (France)	*Rapporteur*
Uwe BOVENSIEPEN, Professeur à l'Université de Duisburg-Essen (Allemagne)	*Rapporteur*
Michael FARLE, Professeur à l'Université de Duisburg-Essen (Allemagne)	*Examinateur*
Bruno CHAUDRET, Directeur de recherches, CNRS, Toulouse (France)	*Invité*
Catherine AMIENS, Professeur à l'Université de Toulouse (France)	*Invité*

Ecole doctorale : *Sciences de la Matière*
Unité de recherche : *Laboratoire de Chimie de Coordination*
Directeur(s) de Thèse : *Catherine AMIENS et Michael FARLE*
Rapporteurs : *Jean-Yves PIQUEMAL et Uwe BOVENSIEPEN*

Acknowledgments

This thesis is the result of a collaborative project between the University Paul Sabatier settled in Toulouse (France) and the University of Duisburg-Essen (Germany). During my stay in Toulouse I have been under the direct supervision of Professor Catherine Amiens, whose pedagogical rigor, enthusiasm, scientific curiosity and kindness have been a continuous source of motivation for me. For the period of time that I have spent in Duisburg I have had the great pleasure of working with Professor Michael Farle. His vision of science and guidance have been extremely important for me. I would like to express my sincere gratitude to both of them.

I am truly thankful to Jean-Yves Piquemal, Professor at the University of Paris VII and Uwe Bovensiepen, Professor at the University of Duisburg for examining my work. Moreover my thanks go to Marie-Joëlle Menu and Bruno Chaudret from the University of Toulouse, whom accepted to participate in the jury of this thesis.

The work presented here would not be possible without the invaluable help provided by Diana Ciuculescu, whose hard work and perseverance have been a real example for me.

I would like to thank Marina Spasova for her indispensable help in the characterization of the TEM data, useful suggestions and for her comments on the manuscript. Similarly, Zi-An Li is acknowledged for his assistance with HRTEM and useful help with the analysis of the data. I also want to thank the technical assistance provided by Vincent Collière for HRTEM and SEM measurements.

Robert Estivill is acknowledged for the assistance with the experiments during his Erasmus stay in the University of Toulouse.

Bruno Chaudret is also acknowledged for his contribution to this work since most of the synthetic procedures that I have used during my thesis have been developed and improved by his group during the last 15 years.

I would also like to thank Karine Philippot as head of the group “Nanostructures and Organometallic Chemistry” in the Laboratoire de Chimie de Coordination (Toulouse).

Part of the work presented here has been done in collaboration with other research groups. In this context I would like to thank Nathan D. McClenaghan, Pinar Batat and Gediminas Jonusauskas from the University of Bordeaux for their assistance with time-resolved optical spectroscopy techniques, the analysis of data and the nice welcome at Bordeaux. Similarly I am indebted to Serge Mazères and Catherine Tardin for let me use their equipment and for the great number of meetings we had to discuss the optical spectroscopy data.

Pierre Lecante and Laure Vendier are acknowledged for the analysis and interpretation of WAXS and XRD data, respectively. Etienne Snoeck and Aurélien Masseboeuf are acknowledged for the magnetic holography measurements.

I thank Alain Mari and Lionel Rechignat for the assistance with the magnetic measurements and the enormous patience they showed building the set-up for the numerous magnetic measurements performed under irradiation.

I am acknowledged to Dmitry Tyutyunnikov and Sven Stienen for HRTEM and micromagnetic simulations as well as for the nice discussions on the results. I thank as well Horst Zähres for technical assistance.

My most sincere thanks go to Sabina Grubba and Helga Mundt for their invaluable help with all the paperwork and general issues during my stage in Duisburg.

I am indebted to Tom Kammermeier, David Serantes, Andreas Ney, Jürgen Lindner, Mehmet Acet and Detlef Spoddig for nice discussions on magnetism.

My stays in these two universities during the last three years have given me the opportunity to meet an important amount of people with whom it has been a real pleasure to work. Therefore, I cannot forget to thank Mar, Sar, Nabil, Patricia, Gorka, Fernando, Nina, Mirza, Pierre-Jean, Seda, Kilian, Vadim, Christian, Katharina, Yuri, Karine, Igor (to whom I am

deeply indebted for the translation of the abstract in german), Alfonso, Fred, Nerio, Virginie, Yan, Pierre, Clément, André, Gilles and many others.

I cannot forget to thank Professor Luis M. Liz-Marzán from the University of Vigo, for introducing me into the world of colloidal chemistry.

At last and certainly not least, I would like to thank my friends and family for their unconditional support. Among them I am especially thankful to my parents Miguel and Josefa, to whom I dedicate this thesis.

This work has been supported by the European Nanotool Project and the University of Duisburg-Essen.

Abstract

Cobalt nanoparticles (NPs) are important materials for applications in very different fields like magnetic storage technology, catalysis or medicine. These applications require different properties that are related with the surface state of the original particles. In this thesis we have functionalized the surface of isotropic and anisotropic Co NPs in order to fulfill this demand. Pre-synthesized Co nanowires have been submitted to a thermal treatment that permits the formation of carbon coated anisotropic objects, overcoming therefore one of the main limitations of this kind of materials: their instability towards oxidation. In other order of things, we have synthesized small Co NPs with a fluorophore (Rhodamine B) as unique stabilizer. Such system presents a very interesting opportunity to study the effect of the magnetic core over the optical properties of the dye and, at the same time, to observe how an excited organic molecule directly attached to the Co surface can have an effect over the magnetic properties of the particle. The same dye has been used under other synthetic conditions to promote the anisotropic growth of Co NPs, leading to the formation of monodisperse Co nanodisks. These particles are single domain and present blocked behavior at room temperature, being therefore interesting materials for magnetic data storage devices or permanent magnets.

Resumé

Les nanoparticules (NPs) magnétiques sont envisagées pour plusieurs applications très différentes comme le stockage magnétique d'information, la catalyse ou la médecine. Certaines propriétés indispensables pour ces applications sont liées à l'état de surface des NPs et à leur anisotropie. Pour répondre à cette demande, nous avons fonctionnalisé la surface de particules de Co de façon à les stabiliser vis-à-vis de l'oxydation et proposé une synthèse de NPs de morphologie optimisée. Plus précisément, des nanofilaments de Co ont été recuits post-synthèse selon un procédé préservant leur morphologie. Nous avons montré que la couche de carbone formée protège efficacement les NPs de l'oxydation. D'autre part, nous avons synthétisé des NPs de Co en utilisant un fluorophore organique (Rhodamine B) comme unique agent stabilisant. Ce système nous a permis d'étudier l'effet du cœur magnétique sur les propriétés optiques du fluorophore et, au même temps, d'observer comment l'excitation de la molécule liée à la surface peut induire une modulation de l'aimantation de la particule. Le même fluorophore a été utilisé pour la synthèse des NPs, conduisant à la formation de nanodisques. Ces particules sont monodomaines, bloquées à la température ambiante, paramètres fondamentaux pour leur possible implémentation dans le domaine du stockage magnétique.

Kurzfassung

Kobalt-Nanopartikel (NPs) sind wichtige Materialien für unterschiedliche Anwendungen auf den Gebieten der magnetischen Speichermedien, der Katalyse und der Medizin. Diese Anwendungen bedürfen verschiedener Eigenschaften der Nanopartikel, insbesondere derer im Zusammenhang mit der Oberfläche der NPs. Im Rahmen dieser Arbeit wurde die NP-Oberfläche funktionalisiert, um diesen Anforderungen zu genügen. Vorgefertigte Kobalt-Nanodrähte wurden einer thermischen Behandlung ausgesetzt, was zur Formation von anisotropen Objekten führte, die mit Kohlenstoff bedeckt waren. Diese Tatsache ermöglichte es, den Hauptnachteil des Materials zu umgehen – die Tendenz zur Oxidation. Auch wurden kleine Kobalt-Nanopartikel mit Hilfe von Fluorophor (Rhodamine B) als einen einzigartigen Stabilisator hergestellt. Solche Systeme bieten die Gelegenheit, die Effekte des magnetischen Kerns über die optischen Eigenschaften der Farbmittel zu untersuchen und zugleich zu beobachten, wie ein direkt an der Kobalt-Oberfläche angebrachtes, angeregtes organisches Molekül die magnetischen Eigenschaften des Nanopartikels beeinflussen kann. Die verwendeten Farbmittel können auch benutzt werden, um unter anderen Synthese-Bedingungen das anisotrope Wachstum von Kobalt-Nanopartikeln hervorzurufen, was dann zu Formation von monodispersen Kobalt-Nanoscheiben führt. Diese Partikel sind bei Raumtemperatur magnetisch geblockt und daher interessante Kandidaten für magnetische Speichermedien und als Permanentmagnete.

General Introduction

Nanoparticles (NPs) are the building blocks of nanotechnology, a multidisciplinary branch of science that has become in the last years a hot topic for scientists worldwide and will have a huge impact on our society in the decades to come. The possibility to finely control the synthesis of particles of a few nanometers gives rise to a variety of new features related with size and surface effects like, for example, superparamagnetism in magnetic materials, localized surface plasmon resonances in noble metals or quantum confinement in semiconductors, features that can be integrated into real devices and thus, be useful for a broad range of applications. In the particular case of magnetism the appearance of these phenomena is a feature of great importance due to the continuous demand of miniaturization in *e.g.* magnetic data storage devices (the aim is now to reach storage capacities over 1Tbits/inch^2) and the possibility of using magnetic NPs for the diagnosis and treatment of cancer (allowing a better localization of the tumor, better targeting of the medicine and reduction of the doses associated with localized thermal treatment). These are just two examples of ongoing research topics that have pushed magnetic NPs into the forefront of materials science research (see **Figure 1**).

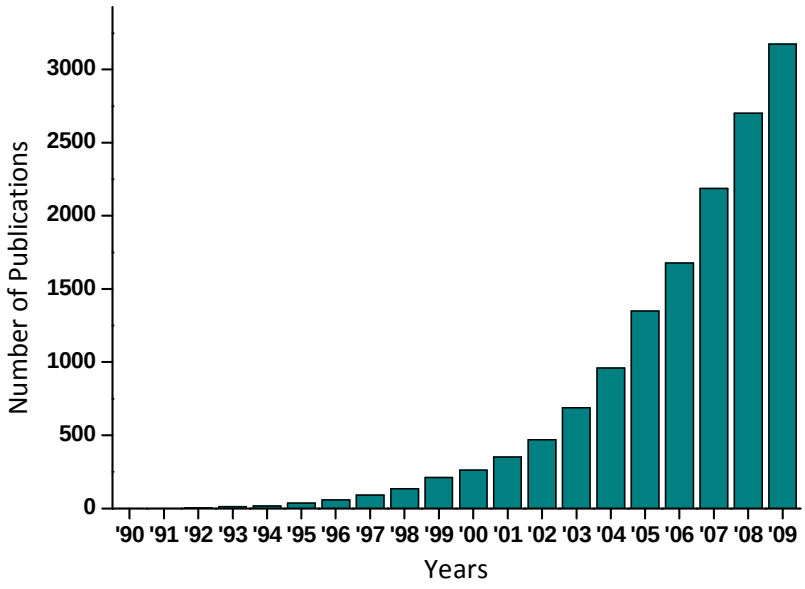

Figure 1. *Number of published items per year with "magnetic nanoparticles" as topic. Source: ISI Web of Knowledge®.*

Metallic magnetic NPs have a higher magnetization compared with their oxidized counterparts, making them very interesting substrates for magnetic storage (the higher the magnetization, the easier reading the information will be) or biological applications (the higher the magnetization, the easier it will be *e.g.* to magnetically guide the NPs in the body). For such applications they need to be stable for very long periods of time. However, it is well known that the ferromagnetic transition metals (iron, cobalt and nickel) oxidize easily under ambient conditions, a characteristic that is extremely intensified when the size of the matter decreases to a few nanometers. It is thus mandatory to coat or embed them in an inert matrix to stabilize their properties. Different coatings such as silica, noble metals or carbon, depending on the application envisaged, have been explored for their encapsulation with different degrees of success.

To reach ultra high density of data storage, the size of the magnetic NP which bears the bit of information has to be reduced down to a few nanometers. However, in this size range the energy barrier for the reversal of the magnetization becomes lower than thermal energy. Hence, thermal fluctuations make the spins fluctuate randomly, vanishing the net magnetization of the particles at room temperature, and in the absence of an applied magnetic field the magnetic information is lost. To overcome this physical limitation, the intrinsic anisotropy of the system must be increased, leading to particles with a “blocked” behavior and therefore remanent magnetization and coercivity. From the chemical point of view two sources for the control of magnetic anisotropy can be envisaged: first, tuning the chemical composition of the NP can afford NPs of very high anisotropy (*e.g.* FePt alloy has been intensively studied for this purpose) but it is difficult to control the exact composition, hence exact anisotropy, from one dot to the other which is a strong limitation for this approach; the alternative is to induce anisotropy via the control of the shape of the NP. In the last years robust chemical procedures have been developed for the synthesis of anisotropic oxide free cobalt NPs, overcoming therefore the thermal fluctuations and affording particles ferromagnetic at room temperature. Nevertheless, a compromise between effective anisotropy and energy costs has to be found, since very anisotropic objects or NPs with very high blocking temperatures require very high magnetic fields (or temperatures) to reverse their magnetic moments (writing the information can be too difficult). Consequently efforts to better optimize the shape of the NPs are still needed.

On the other hand, optically switchable magnetic materials have been attracting great interest since the discovery of photocontrollable magnetic compounds in 1996 [1] because of the continued demand driving the development of optical-memory and -switching devices. Until

now, although many interesting examples of photomagnetic phenomena have been reported, observations of photoswitching have been limited to low temperature operation, and mostly dedicated to molecular systems. Very recently, pioneering work by Einaga et al.[2] has aimed at developing new devices for the photomodulation of the magnetization of NPs, with the ultimate objective of developing faster writing means of magnetic data. One possibility can be the use of a photoswitchable matrix,[2] or to use dye molecules as antennae, hence motivating the development of new synthetic routes for multifunctional NPs.

This thesis is focused on the three major points presented above: protection against oxidation, shape control and design of multifunctional nanosystems. In the first chapter a short introduction concerning the synthesis and properties of magnetic NPs is presented. Chapters 2 and 3 report the synthesis of anisotropic cobalt nano-objects and their stabilization against oxidation by means of the formation of an amorphous carbon shell. In chapter 4 we present a new method for the synthesis of Co NPs stabilized with luminescent organic ligands together with their optical and magnetic characterization and preliminary results on the photomodulation of their magnetization.

---

[1] O. Sato, T. Iyoda, A. Fujishima, K. Hashimoto, Science, 272 (1996), 704.
[2] M. Suda, Y. Einaga, Angew. Chem. Int. Ed., 48 (2009), 1754.

Chapter I: Theoretical background

In this first chapter, we will give a brief introduction into the magnetism of ferromagnetic particles, emphasizing on the special features of single domain NPs. After this, an explanation for the mechanisms controlling the nucleation and growth of NPs in colloidal solutions will be presented in which the importance of a single nucleation event and its separation with respect to the growth process will be highlighted.

Finally, we will give a general overview to the most important synthetic protocols for the colloidal production of iron, cobalt and nickel NPs, stressing on the particular cases in which shape control is achieved.

1 Ferromagnetism

1.1 Atomic and bulk magnetism

1.1.1 Stoner criterion and magnetic moment

Within this paragraph we introduce and explain the main features of ferromagnetism in transition metals (TMs), together with a description of TM ferromagnetic NPs and their intrinsic phenomena.[1,2]

Ferromagnetism arises as a consequence of the exchange energy (quantum mechanical effect that occurs as a consequence of the indistinguishable character of the electrons) between neighbor electrons with overlapping wavefunctions situated at the d orbitals of different TMs. This effect can be described with an integral J for the interaction between two electrons (named i and j) each with a well defined wavelength:

$$J_{ij} = \int \phi_i^*(1)\phi_j^*(2) \left|\frac{e^2}{4\pi\epsilon_0 r_{12}}\right| \phi_i(2)\phi_j(1)d\vartheta \qquad \textbf{(1.1)}$$

where e represents the charge of the electron, r_{12} the distance between the two different coordinates and ϵ_0 the permeability of the vacuum.

The disposition of those electrons is due to the Hund's rules whereby the configuration with the highest multiplicity (respecting the Pauli Exclusion Principle) is the one with the lowest

energy. It means that the degenerated orbitals have to be filled with the maximum number of electrons in different orbitals (with paired spins), being the minimization of Coulomb interactions a commonly given reason for that behavior. In this configuration, the exchange interaction ensures a reduction of the total energy of the system. This exchange interaction is called intra-atomic exchange and is enough to explain the existence of atomic magnetic moments due to the discrete localization of electrons in atomic orbitals. Even if this explanation is of general use, it is important to remark that it is not sufficient to clarify the origin of ferromagnetism. Actually, it has been shown that the main reason behind the increased stability is a decrease in the screening of the electron-nuclear attractions when the electrons are far from each other, being these electron-nuclear interactions a source of stability for the atom.[3] Nevertheless, when we talk about metallic solids this model does not hold any more and the situation becomes more complex due to the delocalized character of valence electrons. In this case, the difference in energy between electronic orbitals becomes so small that they form continuous energy bands. Particularly, metals present a conduction band that is partly empty and partly filled with electrons. For the first period of TMs, this band is composed by the hybridization of 3d and 4s orbitals, being the later ones completely delocalized and thus, only of limited importance for the magnetic properties of the material.[i]

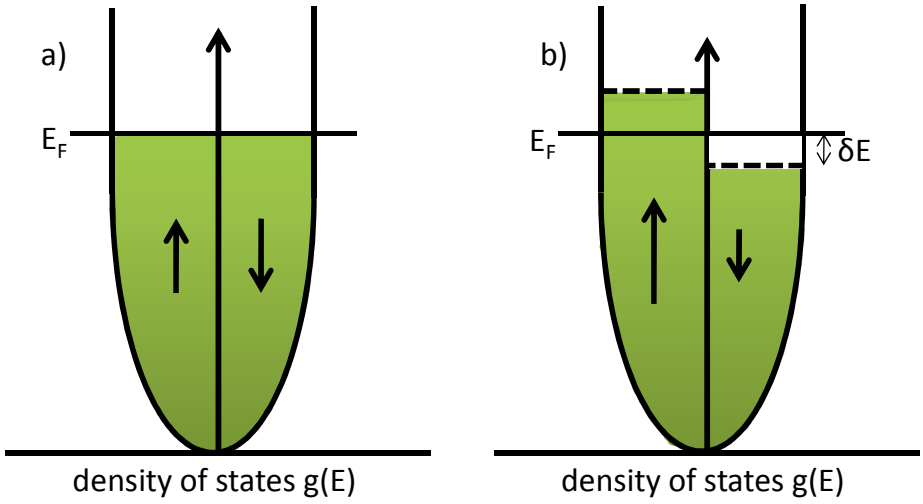

Figure 1-1. *Schematic representation for the density of states at the conduction band for a paramagnet (a) and a ferromagnet (b).*

[i] Due to the polarization by d orbitals a small s-polarization may arise.

Following the Stoner criterion, a metal is spontaneously ferromagnetic if it fulfills the condition:

$$J(E_F)g(E_F) > 1 \quad \textbf{(1.2)}$$

where $J(E_F)$ and $g(E_F)$ represent the exchange correlation energy and the density of states at the Fermi energy, respectively. It means that ferromagnetism will be spontaneously favored for strong exchange integrals and high density of states at the Fermi level. This quantitative condition is the result of the competition between two energy contributions: the exchange energy that favors the parallel alignment of spins through the shifting of the conduction bands and the corresponding rise in kinetic energy that is inversely proportional to the density of states at the Fermi level **(Figure 1-1)**.

This itinerant model for the appearance of ferromagnetism based on the splitting of spin-up and spin-down bands can be regarded also by assigning a local magnetic moment per atom (μ) which has two contributions:

- The spin magnetic moment (μ_{spin}).
- The orbital angular moment ($\mu_{orbital}$).

In this simplified model, the total magnetic moment of one atom is the sum of the spin and orbital magnetic moments, while correctly the total angular moment $\sqrt{J\,(J+1)}$ defines the magnetic moment per atom and orbital and spin quantum numbers lose their validity due to spin-orbital coupling. For a crystalline material with cubic symmetry the situation gets more complicated since the orbital magnetic moment is quenched by the crystal field energy, having almost no contribution to the total magnetic moment of the system. For instance, an example for the spin and orbital moments of Fe as an atom or in the bulk (with bcc structure) is given in **Table 1-1**.

Table 1-1. *Values for μ_S and μ_L in atomic and bulk Fe.*[4]

	Fe (atom)	***Fe (bulk)***
μ_S (μ_B)	4	2.2
μ_L (μ_B)	2	0.086

The interaction between the spin and the orbital magnetic moments is called spin-orbit (S-O) coupling and has a tremendous effect over different properties of magnetic materials like, for example, the magnetic anisotropy energy (MAE). S-O interaction can be described as the effect of the orbital motion of the electron on the orientation of its spin: the magnetic field B created as a consequence of the orbital motion of the electron around the nucleus directs the spin through a preferential direction of the space. Moreover, the situation is completely different for the arrangement of atoms inside a material. In this case, S-O interaction is affected by the coupling between the spins of the electrons and their respective environments (the crystalline lattice), that causes a splitting on the electronic levels of the atoms.

1.1.2 Magnetic Anisotropy Energy (MAE)

The magnetic anisotropy describes the preferential magnetization orientation of a material in one particular direction of space leading to easy, intermediate and hard directions of magnetization. It is composed of different contributions:

$$K_{total} = K_{magnetocrystalline} + K_{shape} + K_{strain} + K_{surface} \quad \textbf{(1.3)}$$

- Magnetocrystalline anisotropy energy: is the energy that preferentially directs the magnetization along certain crystallographic directions of the material and finds its origin in the S-O coupling described previously. The energetically favorable direction of magnetization is called easy axis of magnetization. For example, hexagonal cobalt **(Figure 1-2)** exhibits uniaxial anisotropy with the easy axis of magnetization along its [0001] direction.

  For a uniaxial anisotropy the energy is given by:

$$E_a^{uni} = K_{u2} V sin^2\theta + K_{u4} V sin^4\theta \quad \textbf{(1.4)}$$

  being K_{u2} and K_{u4} the anisotropy constants, V the volume of the material and θ the angle between the magnetization and the easy axis.

  When the system has a cubic symmetry **(Figure 1-2)** one obtains:

$$E_a^{cubic} = K_4 V(\alpha_1^2\alpha_2^2 + \alpha_2^2\alpha_3^2 + \alpha_1^2\alpha_3^2) + K_6 V\alpha_1^2\alpha_2^2\alpha_3^2 \quad \textbf{(1.5)}$$

K_4 and K_6 are again the anisotropy constants and α_1, α_2 and α_3 the cosines between the magnetization direction and the axes x, y, z.

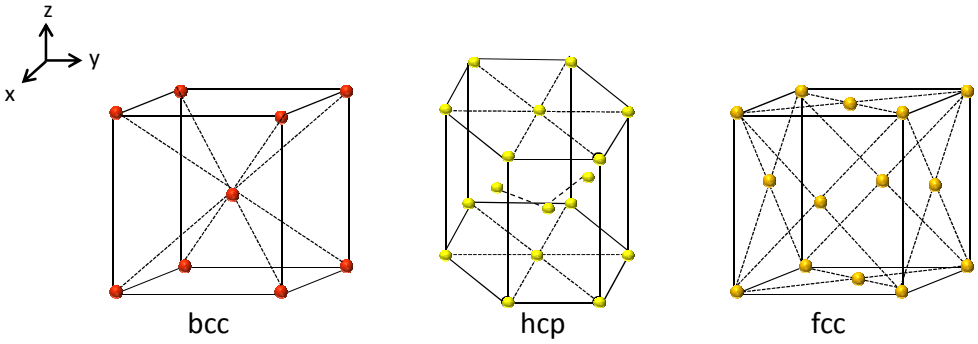

Figure 1-2. *Body-centred cubic, hexagonal close-packed and face-centred cubic crystal structures.*

- Shape anisotropy energy: is the component of the anisotropy that arises directly from the shape of the material. Therefore materials with a high aspect ratio will present an important shape anisotropy, which results in the so-called demagnetizing fields, which arise due to the appearance of surface charges (poles). These poles produce a magnetic field that acts in opposition to the magnetic induction formed within the material when an external field is applied. The internal field of a material (H_i) can be expressed as:

$$H_i = H_{appl} - NM \quad \textbf{(1.6)}$$

where H_{appl} is the applied field, M the magnetization of the sample and N the demagnetizing factor, a tensor normal to the surface whose magnitude depends on the shape of the magnetic material. The sum of the demagnetizing factors in three orthogonal directions of the material has to be 1 (in SI units):

$$N_X + N_Y + N_Z = 1 \quad \textbf{(1.7)}$$

In the case of a system with uniaxial shape anisotropy, for example a prolate ellipsoid, the magnitude of the demagnetizing field will be lower if the magnetization lies along the long axis. The demagnetizing factors in this case are:

$$N_Z(long\ axis) = \frac{1}{m^2-1}\left[\frac{m}{(m^2-1)^{1/2}} Ln\left(\frac{m+(m^2-1)^{1/2}}{m-(m^2-1)^{1/2}}\right) - 1\right] \quad \textbf{(1.8)}$$

$$m \gg 1,\ N_X = N_Y = \frac{1}{2}\left[1 - \frac{(Ln(2m-1))}{m^3}\right] \quad \textbf{(1.9)}$$

where m represents the aspect ratio between the long and short axes of the ellipsoid. In the particular case of a cylinder with infinitive length we obtain $N_Z = 0$ if the sample is

magnetized across the long axis and $N_X = N_Y = 1/2$ if magnetized in the perpendicular directions.

- Strain anisotropy energy: local change in atomic position results in altering the shape of the orbitals, affecting the S-O interaction and thus, contributing to magnetic anisotropy.

- Surface anisotropy energy: is related to the breaking of symmetry and the loss of coordination of the surface atoms. It can be enhanced due to the expansion of the lattice spacing of atomic planes close to the surface.[5] The contribution of the surface anisotropy energy to the total anisotropy of the system is size dependent and increases in importance when the size of the matter is reduced. In the limit of a small NP of a few nanometers in diameter it becomes the main contribution since surface effects overcome bulk contributions. Therefore, surface atoms give an important contribution to the effective anisotropy (K_{eff}). Assuming that the NP has spherical shape K_{eff} can be expressed as:

$$K_{eff} = K_V + \frac{6}{d} K_S \quad \textbf{(1.10)}$$

where K_V and K_S are volume and surface anisotropy constants, respectively and d is the diameter of the particle.

1.1.3 Domain walls

At the macroscopic scale, magnetic materials are composed by sub-regions called domains in which ferro- or antiferromagnetic ordering remains constant while between domains the orientations of magnetic moments are not the same, leading to the absence of net magnetization in zero magnetic field. Magnetic domains are separated by domain walls,[ii] which correspond to a gradual reorientation of magnetic moments between two regions oriented in different directions. The formation of domain walls (and therefore magnetic domains) is due to the possibility of lowering the high magnetostatic energy of a saturated configuration, and its width is given by the competition of MAE, exchange and magnetostatic energy. This effect is clearly seen in **Figure 1-3**.

[ii] There exist domain walls of Bloch and Neel type, depending on the orientation of the magnetic moment within the wall.

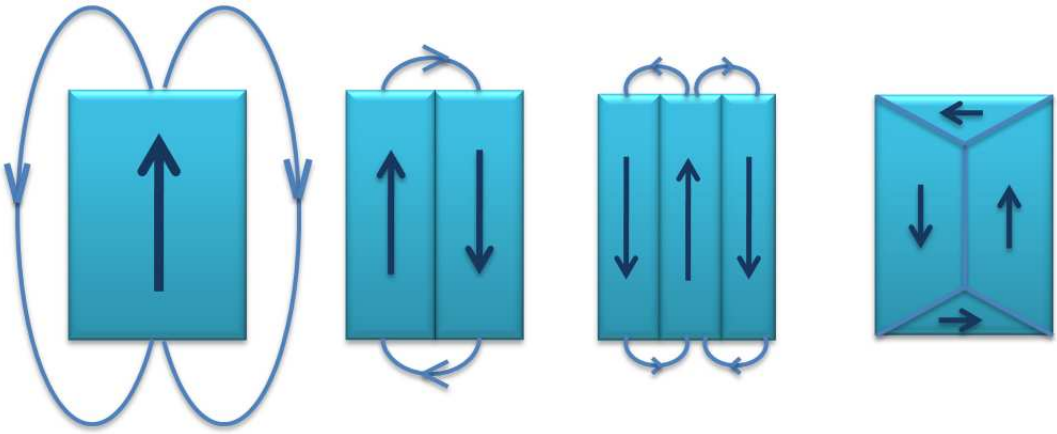

Figure 1-3. *Schematic view for the formation of domain walls with minimization of magnetostatic energy.*

When a magnetic field is applied to a ferromagnetic material, the domains which have their orientation lying along the direction of the magnetic field start to grow through domain wall motion, as represented in **Figure 1-4**. Furthermore, if the intensity of the field is high enough, the rotation of magnetic moments also facilitates the alignment of the magnetization of the material within the direction of the field, leading to a limit situation in which the material is in a saturated state reaching its highest value of magnetization (saturation magnetization or M_s).

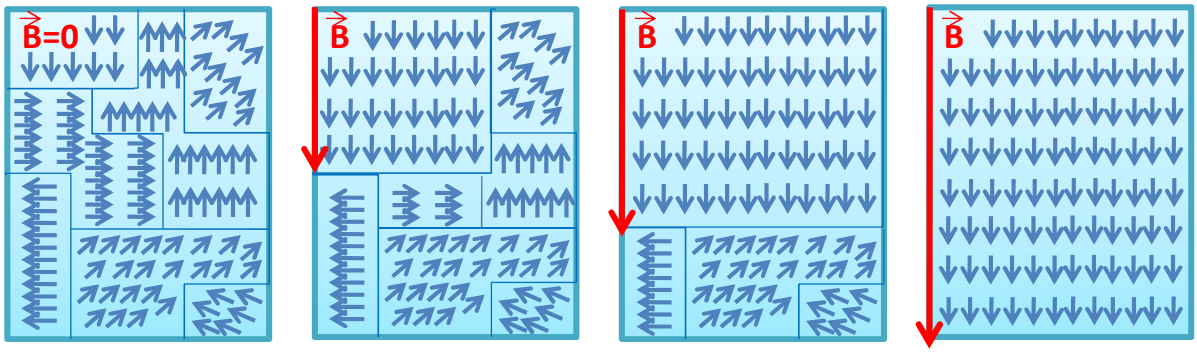

Figure 1-4. *Representation of domain wall motion in presence of an applied magnetic field.*

1.2 Magnetism in NPs

1.2.1 Surface effects

NPs open an interesting field of study since they form a bridge between the different magnetic properties presented by atoms and bulk materials. It is well known that size effects have a tremendous importance over the properties of materials at the nanoscale; and magnetism is not an exception: the size dependent change of the electronic properties has a strong impact in both spin and orbital magnetic moments. For instance, the changes in symmetry at the surface of the NPs lead to a narrowed d-band and localized surface states, thus affecting strongly the magnetic properties of the NPs.

Other consequence of the symmetry breaking at the surface of the NPs is the lower symmetry of the crystal field, leading to a higher spin polarization and higher values for the orbital magnetic moment. Nevertheless $\mu_{orbital}$ should never reach the higher atomic value due to the crystalline ordering of the NP and the partial loss in rotational symmetry.

Surface effects in magnetic colloidal NPs are a complicated subject since the presence of adsorbed molecules is expected to affect magnetism. In fact, quenching of ferromagnetism is found in some TM NPs when they are exposed to certain molecules.[6,7] S. Pick and H. Dreyssé have done an extensive study of the variations in surface magnetization for small cobalt clusters of high symmetry (concretely Co_{13} and Co_{55}) using a theoretical approach. They found that common adsorbates like carbon monoxide, oxygen or ammonia have different effects over the magnetization of these small clusters.[8,9] Chemisorption of a CO molecule at the surface of Co_{13} leads to the almost complete quenching of the magnetic moment of the atom where the molecule is adsorbed, while the remaining magnetic moment couples in an antiferromagnetic manner with respect to the cluster, with the subsequent reduction in magnetization. Besides this, the rest of the atoms are not substantially affected by the adsorption of the molecule and their corresponding magnetic moments remain constant. A similar effect is calculated when 12 CO molecules are attached to 12 surface atoms of a Co_{55} cluster since only the atoms in direct contact with the molecules show an almost complete loss of magnetic moment, coupling again antiferromagnetically with the rest of the cluster. Contrarily to this, when the same experiment was done in a Co_{13} cluster, in which 12 atoms are at the surface and just 1 stays at the core, the

magnetization collapses and the system becomes paramagnetic. In a similar calculation for the adsorption of oxygen on Co_{13} just a slight decrease of the magnetic moment of the surface atom is observed in agreement with previous results obtained for Co thin films.[10] Consequently, oxygen seems to affect the magnetism of Co structures only at high concentrations, most probably due to the formation of oxides. In the case of ammonia adsorption, 12 molecules were adsorbed to the 12 surface atoms of the Co_{13} cluster by its N atom in an atop configuration. Here no significant depletion of the magnetic moments was found, with a maximum decrease of 0.1 μ_B. On the other hand, NH_3 has a strong effect over the magnetic properties of small Ni clusters,[11] decreasing their spin multiplicity and therefore, quenching their magnetization. The different behavior is explained as a consequence of the "weaker" ferromagnetism of Ni if compared with Fe or Co, making it more sensitive to chemisorption processes. These simulations agree qualitatively with results obtained in colloidal systems. Osuna et al.[12] and Margeat et al.[6] found a big dependence of the magnetic properties of Co NPs on the presence of different adsorbates. Adsorption of electron withdrawing molecules such as CO or aluminum or boron based Lewis acids on preformed Co NPs lead to a drastic decrease of their magnetization per volume. On the reverse, if the corresponding adsorbates were electron donating ligands such as amines or amido-aluminium species (bound to the surface by the nitrogen) the magnetization of the system was not affected substantially.

1.2.2 Single domain NPs

The break-up of a ferromagnet in domains is no longer valid when its size is reduced below a critical value. Every magnetic material has a critical size at which the energy needed to create a domain wall is comparable with the magnetostatic energy that the material has to hold. The critical diameter for a monodomain, spherical particle is given by:

$$D_c = \frac{18\sqrt{AK_{eff}}}{\mu_0 M_S^2} \quad \textbf{(1.11)}$$

where A is the exchange constant (J/m), K_{eff} is the uniaxial anisotropy constant (J/m^3), μ_0 is the vacuum permeability ($4\pi \cdot 10^{-7} N/A^2$) and M_s is the saturation magnetization (Am^2/kg). This critical diameter changes depending on the material but normally lies between 10-100 nm.

A single domain particle holds a permanent moment called “supermoment”, which can be considered the sum of all individual atomic magnetic moments within the particle:

$$\mu = \mu_{at} N \quad \textbf{(1.12)}$$

being μ_{at} the atomic moment and N the number of magnetic atoms within the particle.

1.2.3 Superparamagnetism

In this section we will simplify and define the term superparamagnetism for an ensemble of single-domain, non interacting NPs with uniaxial anisotropy only.[13]

A single domain particle presents a permanent moment resulting from the strong coupling of the individual magnetic moments within the particle. In the easiest case of a particle with uniaxial anisotropy two possible opposite orientations of this “supermoment” along the easy axis are preferred, having both the same probability. In this ideal case the second term of **(1.4)** can be neglected and the energy of such a system follows the equation:

$$E_a = K_{eff} V sin^2\theta \quad \textbf{(1.13)}$$

where K_{eff} is the effective anisotropy and θ the angle between the magnetization direction and the easy axis of the particle **(Figure 1-5a)**. This expression describes two energy minima at θ= 0 and θ= π, corresponding with spin up and spin down configurations. Both minima are separated by an activation energy barrier (E_a) that corresponds to the highest anisotropy energy of the system ($K_{eff}V$) **(Figure 1-5b)**. At this size (< 10 nm) the energy barrier between the two possible orientations is very small, comparable with the thermal energy k_bT (where k_b is the Boltzmann’s constant and T the temperature). According to this, and in the absence of an applied magnetic field, if $k_bT > K_{eff}V$ energy fluctuations can overcome the energy barrier and reverse the magnetization of the particle leading to a zero net magnetization. Under these conditions the particle is in the superparamagnetic state.

The mean time of flipping between the two minima (relaxation time) is given by the Néel-Brown equation:

$$\tau = \tau_0 exp \frac{K_{eff} V}{k_b T} \quad \textbf{(1.14)}$$

where $\tau_0 \approx 10^{-12}$-10^{-9} seconds is the characteristic relaxation time of the material.

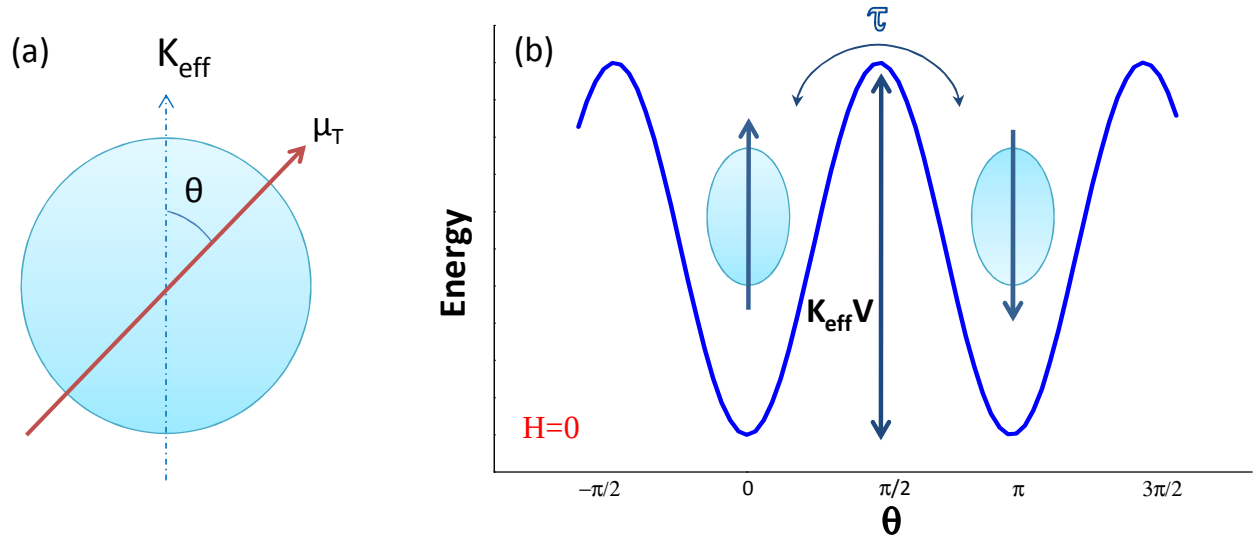

Figure 1-5. *(a) Representation of a single domain particle with uniaxial anisotropy K; μ_T represents the magnetic moment and θ the angle between it and the easy axis of magnetization. (b) Two possible spin configurations for a single domain particle with uniaxial anisotropy and in the absence of a magnetic field.*

The system is called blocked or static when the relaxation time τ is longer than the experimental measuring time τ_m. In this case the supermoment of the NP is "frozen" following the easy axis of magnetization. The transition temperature between blocked and superparamagnetic states is the so-called blocking temperature (T_B), being the temperature at which $\tau_m \approx \tau$. From the previous equation we obtain:

$$T_B = \frac{K_{eff}V}{k_b Ln\left(\frac{\tau_m}{\tau_0}\right)} \quad \textbf{(1.15)}$$

This expression is only valid if the inter-particle interactions are negligible.

At this point it is important to remark that the blocking temperature of a given system obtained experimentally depends on the technique used to study its magnetic properties. In fact, τ_m varies from several nanoseconds to hundreds of seconds, as presented in **Table 1-2**.

Table 1-2. *Values of time windows for different experimental techniques.*

Technique	***Experimental time window τ_m (seconds)***
Inelastic neutron scattering	10^{-12}-10^{-10}
Mössbauer spectroscopy	10^{-10}-10^{-7}
AC susceptibility	10^{-5}-10^{-1}
SQuID	100

For single domain particles three limiting behaviors can be discussed and explained with the help of theoretical models in the presence of external magnetic fields:

1. $k_bT >> K_{eff}V$. Isotropic superparamagnetism.

A system composed by non-interacting superparamagnetic NPs at a temperature well above T_B (without net magnetization) and thus in thermal equilibrium can be compared with Langevin's model for atomic paramagnetism since the behavior of these particles in the presence of an applied field is identical to that of an atomic paramagnet **(Figure 1-6a)**, where the magnitude of the magnetic moments (10^3-$10^5\mu_{at}$) is the only difference. Therefore their magnetization can be expressed as:

$$L\left(\frac{\upsilon\mu_p B}{k_B T}\right) M = \frac{1}{th\left(\frac{\upsilon\mu_p B}{k_B T}\right)} - \frac{k_B T}{\upsilon\mu_p B} \quad \textbf{(1.16)}$$

where ν represents the normalized particle volumes and $\mu_P(T)$ is the particle magnetic moment.

A superparamagnet shows no hysteresis (complete reversibility) when the magnetic field is removed due to thermal fluctuations of the magnetic moments, which are completely free to rotate and do not "feel" the easy axis of magnetization dictated by the magnetocrystalline and shape anisotropies.

2. $k_bT \geq K_{eff}V$. Anisotropic superparamagnetism.

When the energy barrier approaches the value of thermal energy but still lies below it, the magnetic moments start to "feel" the anisotropy energy and, on average, stay longer times parallel to the easy axes of magnetization than in any other direction.

3. $k_bT << K_{eff}V$. Blocked superparamagnetism. The system behaves like an assembly of ferromagnets.

The change in magnetization of a macroscopic ferromagnetic material does not depend only on the strength of the applied magnetic field but also on the previous state of the system (its magnetic history). As a result of this, ferromagnetic materials present two important features in their magnetization loops (M vs B): remanent magnetization M_R (magnetization when the magnetic field is removed) and coercive field H_C (field of opposite sign applied to return the system to a state of null magnetization). As explained before, domain wall motion and rotation of magnetic moments are the two mechanisms used to explain magnetization changes upon variation of the applied magnetic field. The magnetization reversal of blocked single domain particles is explained in most of the cases by coherent rotation of the magnetic moments since the formation of domain walls is energetically unfavored. This process follows the model postulated by Stoner and Wohlfarth,[14] in which the moments rotate coherently, remaining parallel to each other and without taking into account the temperature, being therefore only strictly correct for systems in the absolute zero. Nevertheless, other magnetization reversal processes can occur via other mechanisms like fanning or curling of the magnetic moments within the single domain particle.[15]

In the Stoner-Wohlfarth model the presence or absence of remanence and coercivity in non-interacting single domain particles with uniaxial anisotropy depends on the angle θ between the applied field and the easy axis of the particles:

- θ = 0 or 180°: rectangular hysteresis cycle with $M_R = M_S$ and $H_C = \frac{2K}{M_S}$ **(Figure 1-6b)**.
- θ = 90°: M_R and $H_C = 0$ **(Figure 1-6b)**.

In a real system formed by an assembly of these particles we have an average of all the possible angles between 0 and 180° and thus the actual hysteresis loop is a linear combination of all the possible orientations **(Figure 1-6c)**.

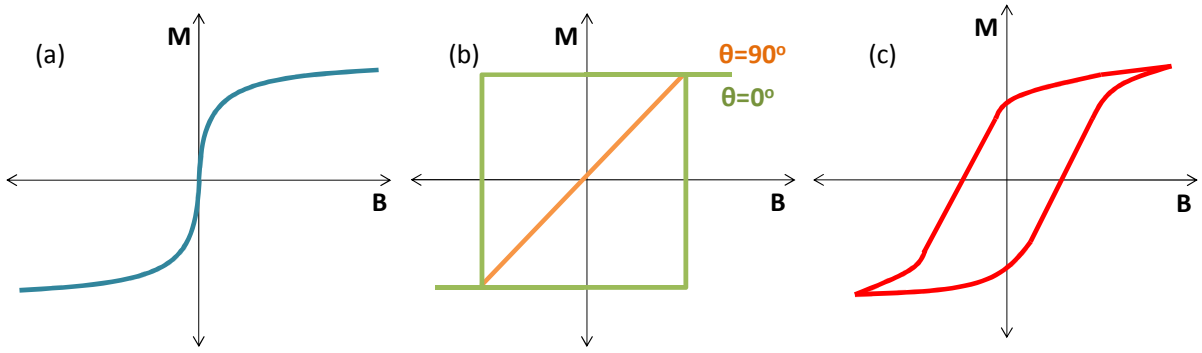

Figure 1-6. *(a) Hysteresis cycle for a single domain NP (or an assembly of such NPs with negligible interactions) in the superparamagnetic regime. (b) Hysteresis cycles for a spherical single domain NP in the "blocked" regime for two different angles (θ) with respect to the applied magnetic field, following the Stoner-Wohlfarth model. (c) Hysteresis cycles for an assembly of spherical single domain NPs in the "blocked" regime following the Stoner-Wohlfarth model.*

2 Mechanisms governing colloidal synthesis of NPs

It is well known that the control over the morphology of nanocrystals is a key parameter to finely tune their properties and thus, a major aspect to take into account for their implementation into real devices. Colloidal chemistry has risen as the most reliable method to fulfill this demand, leading to an enormous variety of sizes and shapes of NPs for almost any kind of material.[16] Nevertheless, the mechanisms governing colloidal chemistry (nucleation and growth) are far from being completely understood.

2.1 Nucleation

Nucleation, the process governing the formation of crystals, is a central area of research in nanotechnology due to its capital importance to control the morphology of NPs. However, its characterization is particularly challenging due to the very small length and time scales of the process, remaining therefore the center of continuous debates.

According to the classical nucleation theory (CNT), homogeneous nucleation of small crystallites takes place in supersaturated solutions. The growth of these nuclei to form larger clusters is controlled by the competition between bulk and surface energy. This competition is reflected in the expression for the free energy of a spherical crystallite with radius R:

$$\Delta G_{CNT} = \frac{4}{3}\pi R^3 n\Delta\mu + 4\pi R^2\gamma \quad \textbf{(1.17)}$$

where n represents the density of particles, Δμ (<0) the difference between the liquid and solid chemical potentials and γ the solid-liquid interfacial free energy density. The first term of the equation favors growth of the small nuclei since a bulk material is more stable than a supersaturated solution while the latter favors their dissolution due to the energy cost to create a solid-liquid interface. In fact, growth becomes favorable only when the nuclei reach a critical size (R_{crit}) at which the gain in bulk energy is dominating.

Following the classical nucleation theory, LaMer and Dinegar presented in 1950 the first complete mechanism for the formation of colloidal NPs in solution.[17] Even if this model was postulated for the formation and subsequent growth of sulfur colloids in organic solvents, nowadays it is accepted as a good approximation for the growth of metal nanocrystals upon decomposition of the corresponding precursor. Within this model the concentration of free atoms in solution grows as the precursor decomposes, reaching a critical concentration called concentration of supersaturation (C_{ss}), at which the single atoms start to aggregate homogeneously in small clusters **(Figure 1-7)**. Once these nuclei start to grow, the concentration of atoms decreases drastically below the supersaturation limit and thus, no more nucleation processes will take place leading to a solution of clusters with homogeneous size. Subsequently, the preformed clusters will grow atom-by-atom using the decomposed precursor as source. At the same time, two nuclei can coalesce (aggregation), leading to a loss in monodispersity.

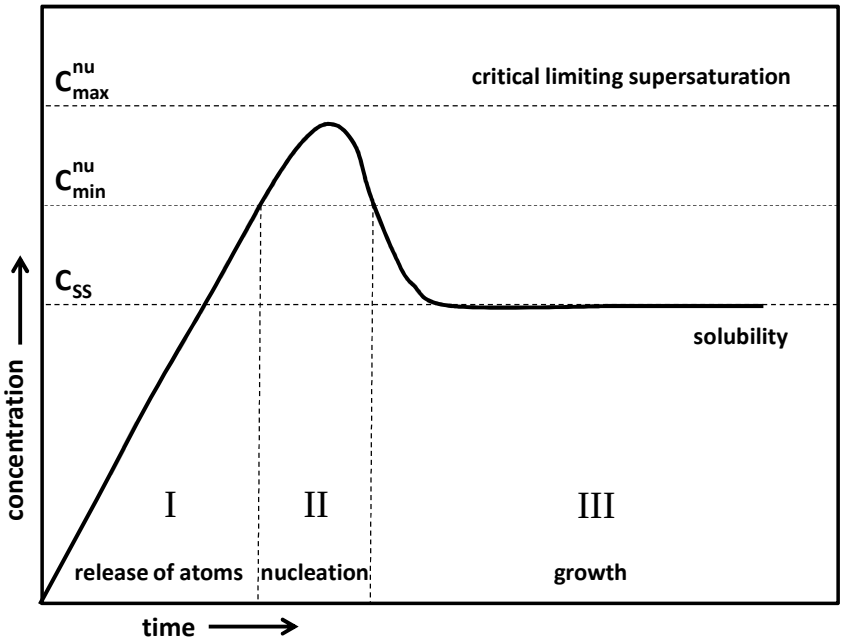

Figure 1-7. *Schematic representation of the nucleation and growth of atoms in solution (Adapted from Ref. 17).*

The structural elucidation of subnanometric nuclei is of fundamental importance to understand the driving forces beyond the nucleation of metallic NPs. In that direction, S. Auer and D. Frenkel postulated in 2001 that the structure of nuclei in the primitive stages of the growth present a metastable random hexagonal close-packed configuration (rhcp).[18] This arrangement corresponds to random stacking of fcc and hcp structures (possible due of the small free energy difference between them). Such structure has been also found in crystallization processes of polymeric colloidal particles at the microscopic scale[19] but the experimental observation of the crystal structure of atomic nuclei before NP formation remains a big challenge to overcome.

2.2 Growth

Once the small clusters overcome the critical radius R_{crit} they keep a well-defined morphology. These well defined clusters, which are commonly called seeds, play a major role over the final shape of the NPs, as they represent the first stage for the subsequent growth. When their synthesis is under thermodynamic control, the preferred structure of the seeds will be the one with the lowest interfacial free energy (γ), parameter that is given by:

$$\gamma = \frac{1}{2} N_b \varepsilon \rho_a \quad \textbf{(1.18)}$$

where N_b is the number of broken bonds, ε the bond strength and ρ_a the density of surface atoms. For an fcc metallic NP {110}, {111} and {100} are the low-index crystallographic facets which are normally exposed at the surface, being $\gamma_{\{111\}} < \gamma_{\{100\}} < \gamma_{\{110\}}$ their corresponding energetic sequence.[16,20] Therefore, for a growth process produced under thermodynamic conditions, these facets will grow very fast by preferential adsorption of atoms on the facets with higher interfacial energy. This sequence is responsible for the predilection of truncated octahedrons as the most stable structures for small single crystalline seeds, presenting a shape close to that of a sphere and {111} and {100} as exposed facets. On the other hand, if the synthetic process is under kinetic control rather than thermodynamic, the presence of seeds with a high surface tension becomes feasible and multiply twinned clusters can be produced in solution.[21] Nevertheless, they are confined to small sizes due to the strain energy caused by the twin planes, an energy contribution that grows with the size of the crystal. Both kinds of structures (single crystalline and twinned seeds) have been observed experimentally.

Other important factor that can determine the morphology of a NP is the relative growth rate of the different facets. These rates are related to the presence of capping agents in solution. Indeed, the selective chemisorption of a molecule on a particular crystallographic facet can diminish substantially the addition of adatoms in that surface, directing the growth to other facets of the crystal. It can also induce an oriented attachment of the seeds into anisotropic objects.[21,22] Alternatively, some molecules can also form micelles in solution which act as templates for the directed growth of anisotropic structures.[23] Heterogeneous nucleation can also serve as a versatile method to tune the morphology of nanocrystals. It consists on the use of well-defined pre-synthesized NPs as nucleation centers. In this case, if the composition of the original NP and the added metal atoms is the same, the growth is epitaxial, hence isotropic and the features of the seed (exposed facets or defects) are transferred to the final structure. This method is useful for the synthesis of bimetallic core-shell nanostructures, but in this case the growth of the deposited metal is not necessarily isotropic as epitaxy may not be achieved on each facet of the seeds, depending in the lattice mismatch between both species. Therefore, if the difference is big enough, the morphology of the final NPs can be completely different from that of the original seed.

3 Synthesis of metallic magnetic NPs

Ferromagnetic metals are important materials in our daily life and are expected to play a major role in nanotechnology research during the next years. Unfortunately, their reactivity towards water and oxygen (especially in the case of Fe and Co) makes magnetic transition metals (MTMs) NPs readily oxidized when exposed to any of these two agents. Therefore, the synthesis of nanostructured MTM has been historically devoted to their oxides which are less sensitive to ambient conditions but have a weaker magnetic response.

The increasing development in the colloidal synthetic methods devoted to the synthesis of metallic and semiconductor NPs during the last two decades has had a big impact in magnetism. When this *savoir-faire* was applied to the synthesis of magnetic NPs the quality of the synthesized materials improved substantially, leading to homogeneous and well-defined systems, which are ideal models for the study of magnetism at the nanoscale and of special interest in a broad range of applications like catalysis, medicine or computing science. Within the next pages we will try to give representative examples of the different colloidal methods leading to the synthesis of magnetic NPs, differencing between isotropic and anisotropic nanostructures. For the sake of simplicity we will only refer to pure iron, cobalt and nickel NPs, together with the alloys that they form with each other.

3.1 Isotropic growth of NPs

3.1.1 Thermal decomposition

Thermal decomposition of organometallic precursors in hot surfactant solutions at relatively high temperatures is the most widely used technique for the synthesis of monodisperse MTM NPs. In this case two different approaches have to be differenciated: in one case the mixture is prepared at room temperature and then submitted to reflux. In the other case, the surfactant is solubilized in the selected solvent, and the high temperature is reached just before the organometallic precursor is added. The second method is known as the fast-injection technique and normally gives the best results concerning size control and monodispersity because fast injection induces a very short and unique nucleation event, from which the

preformed nuclei rapidly grow leading to the formation of NPs. Different parameters like the surfactant to metal ratio, nucleation temperature or time can be adjusted to finely tune the size of the crystals. Consequently, size distributions as low as 5 % can be achieved with this method.

One of the first papers dealing with the synthesis of MTM NPs was reported in 1966.[24] In this work, the authors described the decomposition of $Co_2(CO)_8$ at high temperatures using different polymers as stabilizing agents. The resulting NPs were relatively homogeneous in size. By varying the polymer composition, the average molecular weight or the solvent used, NPs between 10 and 100 nm in diameter could by synthesized. Those particles formed chains on the TEM grids through dipolar interactions, in order to minimize their magnetostatic energy. Several years later and with a similar approach Griffiths, O'Horo and Smith[25] reported one of the first papers dealing with the decomposition of an organometallic precursor using the fast-injection method to synthesize MTM NPs. More precisely, they injected $Fe(CO)_5$ in a hot solution (150 ^oC) of polymers in a high boiling point solvent, following the results previously obtained by Thomas. Fe NPs ranging in size between 10 and 20 nm were synthesized and their results showed that the polymers used to stabilize the particles also acted as catalysts for the CO evolution in solution, increasing the decomposition rate of the organometallic precursor.[26] Nevertheless, modern synthetic methods rely on small organic molecules like carboxylic acids or amines as stabilizing agents for the synthesis of NPs. Those kinds of molecules are extremely good capping agents for MTM NPs, and have almost no effect over the magnetic properties of the system,[7] affording individual NPs (as opposed to embedded NPs) and colloidal solutions with long-term stability. For instance, Farrell et al.[27] used oleic acid and oleylamine to synthesize monodisperse Fe NPs from $Fe(CO)_5$. In this case, two different methods to grow the particles were presented:

1. Heterogeneous nucleation: introduction of pre-synthesized Pt seeds as nucleation sites for the decomposition of the precursors at 287 ^oC in the presence of the mentioned surfactants in octyl ether, leading to Fe NPs with a diameter ranging between 6 and 8 nm, depending on the concentration of the precursor.
2. Homogeneous nucleation: fast-injection of $Fe(CO)_5$ in the surfactants mixture at 100 ^oC leading to 9 nm Fe NPs. The solution was then submitted to reflux, turning black after 70 minutes, a clear indication of the formation of NPs **(Figure 1-8d-f)**.

Both approaches lead to final products with a high monodispersity in size but with an important difference in the crystallinity of the particles. The NPs obtained via homogeneous nucleation are more crystalline than those obtained from the Pt seeds. The authors explained this difference as a consequence of the long period of time (70 minutes) at which the solution was submitted to reflux in the case of homogeneous nucleation, allowing the NPs to recrystallize at higher temperature. Nevertheless, a shell of iron oxide was found at the surface of the particles independently of the method used. This superficial oxidation was attributed to the reaction of the carboxylic acid with the amine, forming an ammonium carboxylate that at high temperatures evolves, leading to the formation of an amide and releasing water, finally responsible for the oxidation.

Alternatively, the fast-injection method has been used for the synthesis of Co NPs holding a crystalline structure different than those previously known for metallic cobalt.[28] This new structure known as ε-Co (not to be confused with the ε-Co reported in the bulk phase diagram) is a complex cubic primitive structure, similar to the crystalline structure of β-Manganese. The synthetic protocol by Dinega and Bawendi consists in the fast injection of a solution of $Co_2(CO)_8$ in dried toluene over trioctylphosphine oxide (TOPO) at 50 ^oC, with subsequent aging at 110 ^oC. This method leads to NPs with irregular shape and a polydispersity in size of 15 %. Some years later, Puntes et al.[29] synthesized well crystalline and monodisperse ε-Co NPs with spherical morphology and sizes ranging from 3 to 17 nm using o-dichlorobenzene as solvent and a mixture of oleic acid and TOPO as surfactants. In this case the cobalt precursor is added at higher temperature (181 ^oC) and the reaction is stopped just after several minutes. In fact, this fast pyrolysis leads to the synthesis of NPs with a highly monodisperse character **(Figure 1-8a-c)**. Recently, Yang and coworkers[30] synthesized monodisperse 9 nm metallic Fe NPs through the fast injection of iron carbonyl in a hot solution of oleylamine in kerosene. Those NPs presented a T_B of 48 K and a relatively high saturation magnetization. The size of such particles could be varied playing with the reaction time, the molar ratio between the surfactant and the precursor or varying the concentration of the precursor in kerosene.

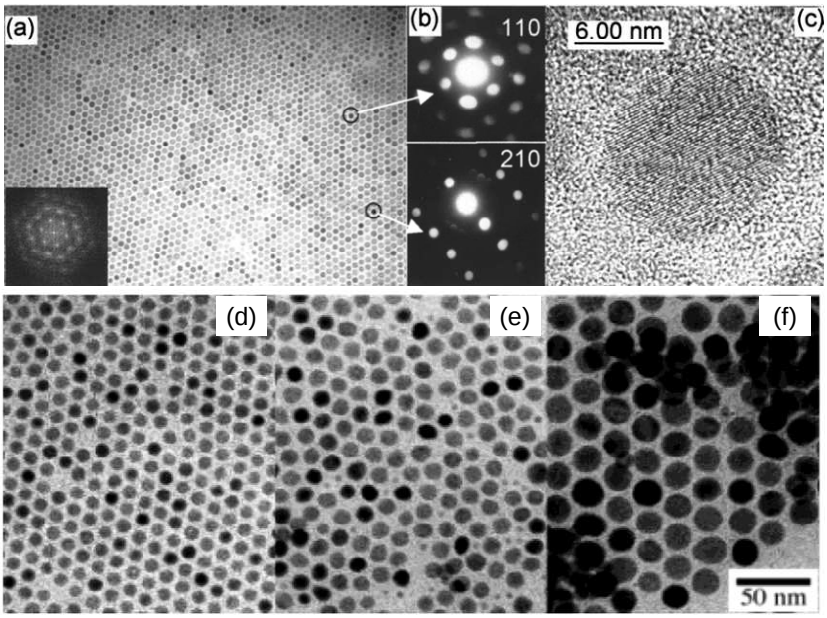

Figure 1-8. *(a-c) TEM, electron diffraction and HRTEM images, respectively of ε-Co NPs from Ref. 29. (d-f) TEM images from Fe NPs synthesized without Pt seeds according to Ref. 27.*

The size of the ligands can be used as a parameter to control the size of the final NPs. Actually, the bulkiness of phosphines has been used to direct particle growth in the synthesis of monodisperse Ni NPs,[31] controlling the size between 2 and 7 nm. In this particular case, the synthesis is obtained through the decomposition of a Ni-oleylamine complex that is prepared *in-situ* from the reaction of Ni(acetylacetonate)$_2$ with oleylamine. This intermediate is thermally decomposed at 200 ^{o}C, leading to fcc-Ni particles presenting very broad peaks on the XRD spectra, indicating that they are nearly amorphous.

3.1.2 Sonochemical decomposition

A sonochemical method has been developed for the synthesis of MTM NPs. Sonochemistry consists in submitting a reacting medium to a high intensity ultrasound. When cavitation takes place, the collapse of bubbles produces an enormous amount of energy, creating extreme conditions of pressure and temperature in localized volumes. Under these conditions precursors can be decomposed leading to free atoms in solution which can be stabilized with organic molecules to avoid aggregation. Following this idea K. S. Suslick et al.[32] obtained Fe NPs with diameters between 3 and 8 nm after decomposition of Fe(CO)$_5$ in the presence of polyvinylpyrrolidone (PVP) at 20 ^{o}C, using octanol as solvent and in the absence of oxygen

during the sonochemical decomposition. When oleic acid was used instead of PVP, an improvement in size control was achieved, leading to a more homogeneous size distribution centered at 8 nm. Nevertheless, in both cases, the particles presented amorphous structures and a saturation magnetization that did not exceed 50 % of the bulk value. With a similar system, de Caro and coworkers sonochemically decomposed the same organometallic precursor in the presence of the polymer poly(dimethylphenylene oxide) (PPO) in anisole.[33] They obtained metallic Fe NPs which had a big polydispersity in size and two different crystal structures: the smaller particles adopted the α-Fe (bcc) structure whereas the larger ones presented the γ-Fe ordering. The magnetic measurements of the final product showed a broad curve for the blocking temperature centered at 75 K with a very high irreversibility field, both features characteristic of a sample of NPs with a large size distribution.

Nickel NPs have been also obtained with a sonochemical method. More precisely, Koltypin et al.[34] decomposed the olefinic compound Ni(cyclooctadiene)$_2$ (Ni(COD)$_2$) in toluene at 0 ^{o}C and in the absence of oxygen. The as-synthesized amorphous product was converted into crystalline fcc Ni upon annealing at 500 ^{o}C. The annealed sample was composed of agglomerated polydisperse particles with superparamagnetic behavior and saturation magnetization lower than that of bulk fcc Ni.

The major drawback of this method is the possible decomposition of the stabilizing agent due to the extreme conditions leading to by-products difficult to eliminate and even carbide inclusion.

3.1.3 Chemical reduction

3.1.3.1 Polyols

Another method for the synthesis of MTM NPs is the use of hot liquid polyols. Such molecules can be used as both solvent and reducing agent for NPs synthesis (thanks to their high ε and μ). Polyols present a general molecular formula of the form: $HOCH_2[CH(OH)]_nCH_2OH$ and their reducing character comes from their multiple hydroxyl functional groups, which at high enough temperatures and under basic conditions can reduce metals with a weak electropositive character. In the late eighties, the first results showed the capability of polyols to reduce Co, Ni

or Cu hydroxides to produce micrometric metallic NPs with isotropic shape.[35] The method consists in a three step process:

1. The chosen hydroxide is partially dissolved in the polyol, generally ethylene glycol (EG), and the precipitation of an intermediate product is observed.
2. The intermediate phase is dissolved in the solvent and reduced at the same time.
3. The nucleation and growth of the particles is produced and the final product precipitates in the form of a nanostructured solid.

These three steps can be summarized in the next mechanism:

$$\text{Metal precursor} \xrightarrow{\text{solubilization}} [M]^{2+} \xrightarrow{\text{reduction}} M^0 \xrightarrow{\text{nucleation/growth}} M^0_n$$
$$[OH]^- \quad \text{polyol} \qquad \textbf{(1.19)}$$
$$\text{Intermediate (solid phase)}$$

Submicrometer sized particles can be obtained increasing the temperature or introducing a heterogeneous nucleation agent but still far above the critical radius for single-domain particles. The same group has synthesized iron or iron-based particles (Fe, Fe-Ni, Fe-Co and Fe-Ni-Co) with a simultaneous disproportionation reaction of Fe^{2+} accompanied by the reduction of Co and/or Ni hydroxides.[36] The disproportionation reaction[iii] of Fe^{2+} consists in the formation of metallic iron and magnetite with the subsequent release of water. Using a polyol as solvent and removing the water from the solution by distillation can lead to an increased rate in the formation of metallic Fe. For that purpose, a big excess of sodium hydroxide is also needed to prevent the formation of magnetite and keep the Fe^{2+} species in solution, in order to be homogeneously reduced by the polyol. Under such conditions the authors obtained submicrometric α-Fe particles with an oxygen content of only 2 %. The disproportionation reaction of Fe^{2+} in presence of the Co and Ni hydroxides showed a different degree of success: FeNi particles showed homogeneous composition and shape, where spherical particles with a narrow size distribution and a diameter around 100 nm were observed. Similar results were obtained for the FeNiCo

[iii] A disproportionation reaction consists in the simultaneous oxidation and reduction of a chemical species, leading to the formation of two different products.

composites. For both systems the particles consisted in a polycrystalline agglomerate of smaller nanometric particles with homogeneous composition. On the other hand, FeCo particles resulted in the agglomeration of individual Co and Fe NPs with irregular morphology and a segregated composition.

Joseyphus and coworkers used a similar approach for the synthesis of submicrometric Fe NPs,[37] using $FeCl_2$ as source of Fe. The submicrometric particles were composed by nanometric grains, and showed a high saturation magnetization close to that of bulk.

C. B. Murray et al. used 1,2-dodecanediol as reductant instead of EG or glycerol for the synthesis of homogeneous hcp-Co NPs ranging in size between 3 and 13 nm in diameter.[38] The synthesis consists in the reduction of cobalt acetate tetrahydrate in the presence of oleic acid (OA) and trioctylphospine (TOP) using diphenylether (DPE) as solvent. When the reaction is finished a size-selective precipitation process is of crucial importance to ensure the homogeneity of the sample. The as-synthesized hcp-Co NPs present superparamagnetic behavior, as expected from their small size and isotropic shape. Following the same procedure, fcc-Ni and CoNi NPs can be obtained again with a very narrow size distribution. Due to the uniformity of the size and shape of the NPs, they were perfect candidates for their organization in 2-D and 3-D superlattices. Actually, self-assembly was accomplished by slow evaporation of the solvent, allowing the NPs to diffuse to their most stable sites on the superlattices.

The polyol method has also been used for the synthesis of monodisperse FeCo NPs[39] using iron and cobalt acetylacetonates as metallic sources and oleic acid and oleylamine (or TOP) as surfactants. The size of the NPs ranged between 10 and 20 nm, depending on the initial molar ratio of the metal precursors. A post-synthetic annealing process was carried out in order to preserve particles from oxidation, leading to the formation of an outer carbon shell.

3.1.3.2 Borohydrides

C. B. Murray and S. Sun reported in 1999 the synthesis of spherical ε-Co NPs of different sizes (from 3 to 9 nm) by reduction of cobalt chloride with lithium triethyl borohydride.[40] In this case OA and phosphines with different alkyl chains were used to avoid the aggregation during the reduction at 200 ^{o}C. In fact, the size of the final particles is controlled by the aliphatic chain of the phosphines: bulkier phospines reduce the growth rate and thus, stabilize small particles,

while the smaller ones allow fast growth and thus, bigger NPs are obtained. Like in the previous example reported by C. B. Murray and coworkers, a tedious size-selective precipitation process is necessary to control the size of the NPs. The as-synthesized particles could be transformed into hcp or fcc-Co after annealing under controlled atmosphere at 300 and 500 ^{o}C, respectively; with the correspondent change of the magnetic properties of the crystals.

Reduction of $FeCl_2$ at room temperature with lithium triethylborohydride can also lead to the formation of bcc-Fe NPs when PMMA (poly(methyl methacrylate)) is used as stabilizer.[41] For small polymer concentrations the particles have a diameter of 23.5 nm with a standard deviation of the 31 % but, on the other hand, they are blocked at room temperature and their saturation magnetization represents the 85 % of the bulk value.

Borohydrides are compatible with the use of microemulsions as reactors for the synthesis of different kinds of NPs. This method has been extensively studied by the group of M.-P. Pileni during the last 20 years,[42,43] emerging as a good approach for the synthesis of NPs with a narrow size distribution and particularly suited for their self-assembly in superlattices. The authors have used this method for the synthesis of fcc-Co NPs in inverse micelles (water in oil microemulsions). Especially, they used the system water/isooctane with $NaBH_4$ as reducing agent and sodium(2-ethylhexyl)sulfosuccinate as surfactant. After extraction from the inverse micelles, the poorly crystalline particles were annealed under nitrogen atmosphere at 500 ^{o}C to obtain fcc-Co NPs with an average size of 5 nm. Nevertheless, small angle X-ray scattering showed that the particles were covered by a shell composed by Co metal together with Co_2B. Taking into account the crucial importance of surface effects at the nanoscale, the presence of these contaminants is expected to have an important effect over the magnetic properties of the system. In fact, the saturation magnetization of the particles was 2 times lower than that of bulk cobalt.

Inverse micelles have been also used for the synthesis of 4 nm Fe NPs whose crystal structure could be tuned depending on the surfactant used to form the emulsion.[44] Unfortunately, the magnetic properties of this system were not investigated.

3.1.4 Hydrothermal synthesis

This method consists in the formation of NPs in water solutions submitted to high temperatures and pressures inside an autoclave. Several papers describe the synthesis of magnetic NPs under these extreme conditions. Nevertheless, those examples are usually restricted to the formation of oxidized particles[45,46] and only a few examples dealing with the formation of MTM NPs through a hydrothermal approach have been reported so far. Two of these articles dealing with the formation of anisotropic Co particles are presented in the section devoted to the formation of anisotropic MTM NPs.

3.1.5 Hydrogenation of metal-organic complexes

Even though the examples presented above cover a broad spectrum of methods for the synthesis of MTM NPs **(Table 1-3)**, all of them present limitations concerning the properties of the final particles. Polydispersity, low crystallinity or contamination at the surfaces together with mandatory post-synthetic treatments are some of the undesirable features presented by those objects. Contrarily to this, an ideal system for the study of magnetism at the nanoscale should present uniform systems with control over composition, morphology and clean surfaces or presence of adsorbates with negligible effect over surface magnetism. In order to reduce economical costs for a hypothetical scale-up of the synthesis in industrial applications, high yields and minimization of post-synthetic treatments are also desirable.

In the group of Bruno Chaudret, a new method for the synthesis of MTM NPs has been developed during the last 15 years. It consists in the hydrogenation of amido or olefinic precursors under mild conditions, using polymers or organic molecules (usually carboxylic acids or amines) as stabilizers. One of the biggest advantages of this method consists in the nature of the organometallic compounds which, contrarily to other precursors used previously, lead to the formation of by-products with low affinities for the metallic surfaces and thus, do not alter the magnetic properties of the NPs. Osuna et al. used in 1996 the olefinic precursor $Co(\eta^3\text{-}C_8H_{13})(\eta^4\text{-}C_8H_{12})$ to synthesize small Co NPs in the range of 1-1.5 nm using PVP as stabilizer.[47] The particles showed an unexpected polytetrahedral atomic packing[48] and outstanding magnetic properties, presenting an enhanced magnetic moment per Co atom and a uniaxial anisotropy almost one order of magnitude higher if compared with bulk hcp-Co. On the other hand, when

the particles were exposed to CO a sudden collapse of magnetization appeared, most probably due to the quenching of surface magnetism, proving again the importance of surface chemistry on the magnetic properties of small NPs. Co NPs with the bulk hcp structure have been also synthesized under dihydrogen atmosphere.[49] In that case, OA was used as stabilizer and 2.5 nm particles were obtained.

Due to the good results obtained for the stabilization of cobalt colloids with PVP, a similar approach was developed for nickel, for which a similar olefinic precursor ($Ni(COD)_2$) was decomposed under dihydrogen using the same polymer as stabilizer.[50] In this case, two different samples were obtained, for which the molecular weight of PVP played an important role on the final morphology of the product, stabilizing well dispersed particles of 4 nm when a high molecular weight was used and agglomerates of 20-30 nm for low molecular weight ones. In both cases the structure of the resulting NPs was face-centered cubic, but the magnetic behaviors were clearly different: while both samples presented a saturation magnetization close to that of bulk Ni, their ZFC/FC curves differed drastically. Well isolated 4 nm NPs presented a clear superparamagnetic behavior with a blocking temperature of 30 K. At the same time, the sample of agglomerated particles showed hysteretic behavior even at room temperature most probably due to dipolar interactions between them.

However, no polyolefinic Fe derivative exists with such easy synthesis and fast reactivity towards dihydrogen. Amido complexes were demonstrated to be interesting alternatives in this case. Margeat et al.[51] and Lacroix et al.[52] obtained 1.5 nm Fe NPs by decomposition of $\{Fe(N[Si(CH_3)_3]_2)_2\}_2$ in mesytilene at 150 ^oC. The particles were stabilized either by a polymer (polydimethylphenyleneoxide) or only by the by-product of the precursor's decomposition (most likely $HN[Si(CH_3)_3]_2$). Similarly to the results obtained by Osuna et al. for Co, these Fe NPs present an anisotropy one order of magnitude higher than that of bulk Fe.

The decomposition of organometallic or metal–organic precursors under H_2 has been also used for the synthesis of bimetallic systems. In the particular case of MTM NPs, FeNi[53] and FeCo[54] NPs have been obtained with a narrow size distribution and exceptional magnetic properties. Both systems present low magnetocrystalline anisotropy and thus, their nanostructured counterparts could find interesting applications in telecommunications industry.

Table 1-3. *Comparison of the different methods leading to isotropic MTM NPs.*

Method	*Size control*	*Crystallinity*	*Max. value M_S (% bulk)*	*Surface*	*References*
Thermal decomposition	Very narrow size distribution	Good	95%	Oxidized	27
Sonochemical decomposition	Large size distribution	Poor	50%	Oxidized	32
Reduction with polyols	Narrow size distribution (after a size selection process)	Poor	80%	Oxidized	38
Reduction with borohydrides	Narrow size distribution (after a size selection process)	Good	85%	Oxidized	40
Reduction inside microemulsions	Regular size distribution	Poor	50%	Oxidized	42
Decomposition under H_2	Very narrow size distribution	Good	>100%	Clean	46

3.2 Anisotropic growth of NPs

The superparamagnetic limit is the main limitation for the use of single-domain particles in applications concerning the magnetic storage of information, limitation that consists in the thermal fluctuation of spins due to the minimization of their magnetic energy barrier at the nanoscale. Anisotropic NPs can overcome this restriction due to their higher anisotropy constants if compared with spherical particles, hence increasing the energy barrier.

In opposition to the extensive synthesis of anisotropic noble metal NPs, examples of solution-based anisotropic MTM NPs are scarce. While anisotropic noble metals can be obtained in countless sizes and shapes under mild reduction of metallic salts, most of the synthetic protocols to obtain MTM NPs require drastic conditions of temperature or pressure, under which the fine control of the morphology is a challenging task.

In this section we will report the anisotropic Fe, Co and Ni NPs referenced in the literature, with a special emphasis on the possible reason for their anisotropic growth.

3.2.1 Iron

Park et al. reported in 2000 the first paper dealing with the anisotropic colloidal synthesis of Fe NPs.[55] The protocol consists in a seed-mediated process in which preformed 2 nm spherical Fe NPs are used as nucleation sites for the growth of Fe nanorods (NRs). The reason for the anisotropic growth is the strong affinity of the surfactant (didodecyldimethylammonium bromide (DDAB)) to specific facets of the crystals, facilitating the coalescence of the individual spherical particles in one preferential direction **(Figure 1-9)**.

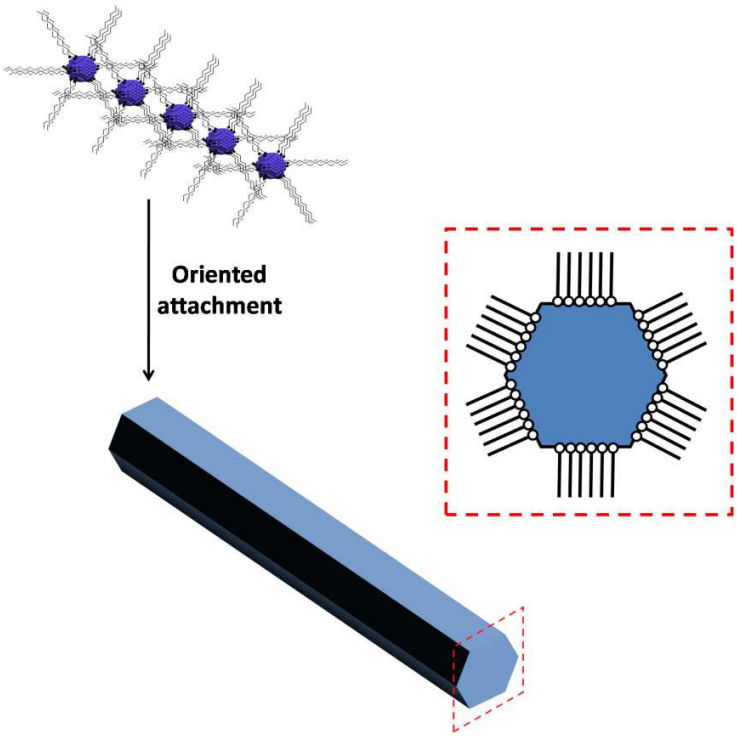

Figure 1-9. *Schematic representation for the growth of anisotropic objects in one preferential direction favored by the specific adsorption of ligands (inset).*

The length of the NRs can be varied between 11 and 27 nm while the diameter of 2 nm remains constant. Besides the increase in shape anisotropy, the MAE is not high enough to keep the magnetic moments of the rods blocked at room temperature and T_B (110 K) is still too low for potential applications.

The same research group reported 4 years later a general method for the large-scale production of NPs for several transition metal oxides.[56] Their method is based in one important principle already mentioned in this section: the separation of nucleation and growth processes.

This was experimentally controlled during the decomposition of the complex $Fe(oleate)_3$, that starts at 200 ^oC, while the fast growth of the NPs is not observed below 300 ^oC. Actually, when the precursor was aged at temperatures close to that of the nucleation process, long periods of time where necessary for the formation of NPs (whose morphology could not be finely controlled). What is more interesting for us is that, when the growth process took place at 380 ^oC **(Figure 1-10a)**, Fe nanocubes were produced instead of iron oxide NPs. These anisotropic objects present a mean edge length of 20 nm and a thin layer of oxide at their surface. In a subsequent work,[57] the authors obtained Fe nanocubes from the decomposition of Fe(II) stearate in presence of sodium oleate and OA. Thermal decomposition of the carboxylate complex is suggested to yield reducing agents like C, CO or H_2, responsible for the formation of Fe^0. However, no clear explanation for the anisotropic growth of the NPs is given. Furthermore, it was found that those nanocubes were not stable: after prolonged times of the reaction, their {110} facets were selectively etched by NaOH or Na_2O, both species coming from the decomposition of the sodium oleate at high temperatures, leading to the formation of Fe nanoframes. Both objects (cubes and frames) presented blocked behavior at room temperature.

Shavel and coworkers reported a similar procedure for the formation of Fe/Fe_3O_4 core/shell nanocubes.[58] The main differences between both methods are the introduction of a small amount of sodium oleate and the use of a different solvent (squalene), which is believed to play the role of reducing agent. Actually, the use of sodium oleate seems to be of critical importance due to its major role on the shape control of iron oxide nanocrystals.[59]

The method developed by Chaudret and coworkers to synthesize MTM NPs with clean surfaces and outstanding magnetic properties has been also applied to the synthesis of shape-controlled NPs under relatively mild conditions. In the particular case of iron, nanocubes with bcc structure have been produced from the decomposition of $Fe[N(SiMe_3)_2]_2$[60] in the presence of a long-chain carboxylic acid and a long-chain amine as stabilizers. The anisotropic growth was suggested to result from the directed coalescence of spherical NPs obtained on the first stages of the reaction or from their directed growth, both processes due to a preferential attachment of the ligands. The final particles had edges of 7 nm in length and self-assemble in micrometric 3D superstructures **(Figure 1-10b-f)**. The magnetic properties of the particles showed saturation

magnetization very close to that of bulk Fe and very low coercivity and remanent magnetization at room temperature.

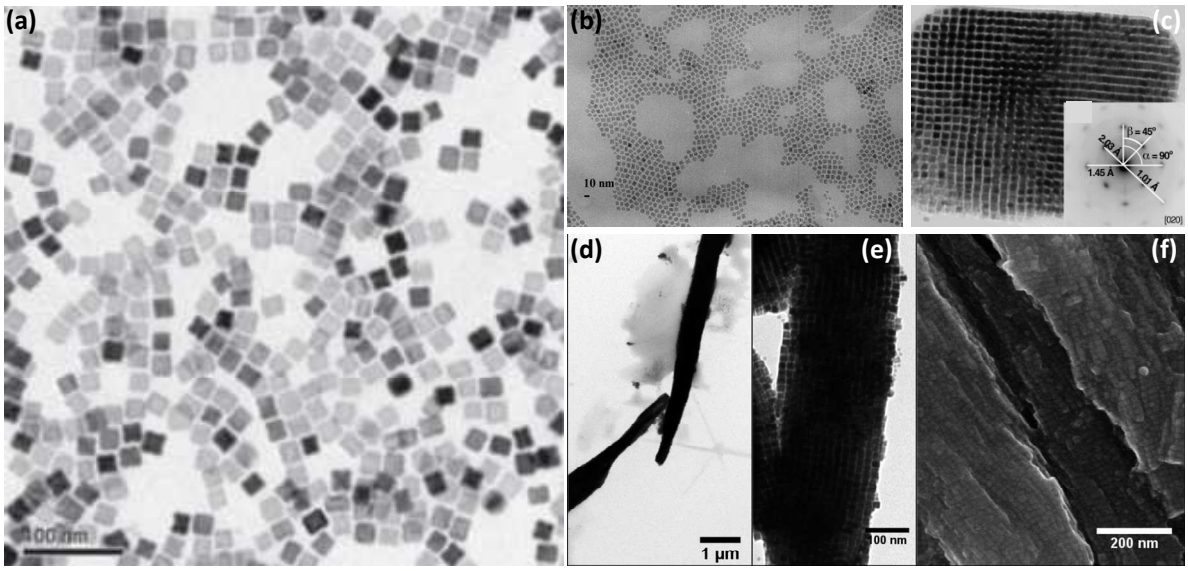

Figure 1-10. *(a) Fe nanocubes synthesized from an iron-oleate complex (Ref. 56). (b-f) Fe nanocubes obtained by hydrogenation of $Fe[N(SiMe_3)_2]_2$ (Refs. 60-61).*

Several years later, Lacroix et al.[61] published an extension of this work in which the main mechanisms beyond the shape controlled synthesis of the nanocubes were explained. In this study the authors observed that $Fe[N(SiMe_3)_2]_2$ transforms in the presence of the ligands (in this case HDA and palmitic acid) into new amido-Fe^{2+} and carboxylate-Fe^{2+} complexes respectively, being the latter more stable and thus, present in the medium for a longer period of time. This difference implies that the two intermediates have different contributions to the synthetic mechanism: while the amido complex is used as a source of iron atoms during the nucleation, the carboxylate intermediate is gradually decomposed during the growth step. The acid/amine mixture is also responsible for the formation of organic superstructures in which the anisotropic growth takes place. This lamellar phase is loaded with the carboxylate-Fe^{2+} intermediate. Together they are responsible for the anisotropic growth of the final NPs, which preferentially expose their {100} surfaces due to specific binding of the carboxylic acid. When the acid content is reduced, the organic superstructures are not produced any longer and only isotropic growth of polycrystalline spheres is produced. Finally, variation of synthetic parameters like time or temperature can induce a change on the morphology of the final particles (star-like, octapods) or

finely tune their size (big cubes with edges of 27 nm have been obtained). A general scheme of this mechanism can be found in **Figure 1-11**.

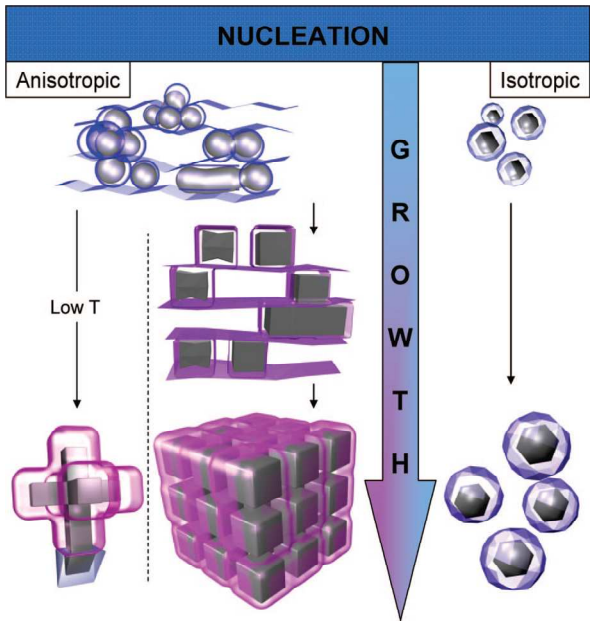

Figure 1-11. *Schematic representation of the mechanism controlling the formation of Fe nanocubes presented by Lacroix and coworkers in Ref. 61.*

3.2.2 Cobalt

Magnetic data recording devices require NPs with high magnetocrystalline and shape anisotropy constants. According to this, metallic cobalt NPs with anisotropic shapes would be the perfect candidates for this application, because, unlike iron and nickel, cobalt presents a uniaxial hexagonal primitive structure, property that gives hcp-Co the highest magnetocrystalline anisotropy of all the MTMs. In order to obtain anisotropic Co nano-objects, the use of surfactants with preferential affinity for the facets perpendicular to the axis of easy magnetization would be the best option to maximize the total magnetic anisotropy of the system, leading to a morphology in which the intrinsic magnetocrystalline anisotropy lies along the same direction than the anisotropic growth of the crystal.

The first paper dealing with the shape control of Co NPs in solution was published in 1995,[62] where the authors presented the formation of Co nanodisks obtained from the decomposition of cobalt hydroxide in basic solutions through reduction with hydrazine. The particles were polydisperse and irregular in shape, with a length and thickness of 100 and 15 nm,

respectively and a distorted hexagonal structure. Lorentz force microscopy was used to elucidate the magnetic character of the particles, which consisted in single domains. Unfortunately, the lack of a complete study of the magnetic and structural properties of the sample and the fact that the reaction was done in water without the use of capping agents lead us to doubt about the usefulness of this method for the well-controlled synthesis of MTM NPs.

The group of A. P. Alivisatos in Berkeley is known worldwide for their extensive study of colloidal particles with special interest in semiconductor nanocrystals (quantum dots). In this particular field, they have developed the first example of shape-controlled synthesis of CdSe NPs[63] using a mixture of surfactants to control the growth rate of different crystal facets. In the same research group, this knowledge was transferred to the synthesis of Co NPs with controlled morphology.[64] Here the authors use the fast-injection technique for the fast nucleation of Co NPs in dichlorobenzene using the mixture of OA and TOPO as surfactants. After a few seconds of reaction at 181 ^{o}C, the authors found an anisotropic shape that in the first moment was attributed to Co nanorods. Later, they observed that the sample was composed of hcp-Co nanodisks[65] which tend to lie on their side when deposited on a TEM grid **(Figure 1-12a)**. Nevertheless, those particles are not stable in solution, leading to monodisperse spherical ε-Co NPs after several seconds[29] (or tens of minutes when replacing TOPO for a linear amine). Particles with the same morphology were obtained by Park et al.[66] using dodecylamine as unique stabilizer, while the other parameters were the same to those reported by Puntes.

The polyol process previously presented for the synthesis of MTM nanocomposites has been slightly varied by G. Viau and coworkers, leading to the synthesis of Co nanorods with a fantastic control over the morphology of the particles[67] **(Figure 1-12b)**. One of the main variations regarding the first papers dealing with the polyol method is the inclusion of a different source of metallic atoms: instead of a Co hydroxide here the precursors are cobalt carboxylates obtained by the reaction between cobalt chloride and the selected sodium carboxylate. Like in the previous papers, the composition and morphology of the final particles depends on the equilibrium between the solid intermediate and the metal atoms in solution **(1.19)**. Furthermore, their length and diameter could be tuned depending on experimental parameters like length of the aliphatic chain of the cobalt carboxylate, temperature ramp and NaOH concentration. If Co acetate is used instead of Co complexes with long aliphatic chains, sea urchin-like morphologies

are obtained in which the anisotropic particles grow from an isotropic Co core. On the other hand, hexagonal platelets instead of rods can be obtained for slow enough temperature ramps. In order to improve the magnetic properties of the nanorods assemblies, the authors aligned their long axis in frozen toluene at 140 K, using a magnetic field applied inside the SQuID magnetometer. Under these conditions, a remanent magnetization as high as 0.95 M_s was obtained, indicating the very good orientation of the rods. The same polyol process was used for the synthesis of bimetallic CoNi nanowires[68] and nanodumbbells[69] whose shapes depended on the ratio of the metals, in addition to the other experimental parameters mentioned before.

As it was presented before for the synthesis of Fe nanocubes, the combination of acids and amines as stabilizers can induce an anisotropic growth during the hydrogenation of organometallic precursors at relatively mild temperatures. In the case of Co, nanorods with a hcp structure and single crystalline character have been obtained through the decomposition of $Co(\eta^3\text{-}C_8H_{13})(\eta^4\text{-}C_8H_{12})$[70] **(Figure 1-12c)**. The explanation for such anisotropic growth is very similar to that reported in the case of Fe nanocubes:

1. Supramolecular ordering of an intermediate Co complex that directs the growth of the nuclei formed upon hydrogenation.
2. Preferential attachment of the carboxylic acid onto the {10-10} facets of cobalt.[71]

These rods present a very thin diameter (4 nm) and a length that can be varied between 20 and 150 nm, depending on the size of the aliphatic chain of the ligand. This high shape anisotropy keeps the particles blocked at room temperature with a higher coercive field if compared with the Fe nanocubes obtained with the same method, as a consequence of the higher anisotropy energy of the cobalt nanorods. The nature of the ligands has an important effect over the self-assembly of the rods as well, leading to super-lattices when stearic acid and hexadecylamine are used.[72] This feature is of crucial importance for the implementation of these particles into magnetic data storage devices, as they already offer an ordered pattern of magnetic single domains. When an excess of acid is added with respect to the other reactants, the anisotropic growth is more developed and wires (particles with a higher aspect ratio) are obtained reaching lengths above the micrometer, while the diameter remains practically constant with respect to the original rods. Interestingly and despite the huge ratio between length and diameter of these original wires, each of them still consists in a single magnetic domain.[73] In

conclusion, this method leads to the formation of anisotropic Co structures whose length and magnetic properties can be tuned by the adjustment of the surfactant mixture. Such particles do not present oxidation at their surface contrarily to those produced by the polyol method and their capping ligands do not alter their magnetism in a substantial way. Similar results were obtained when $[Co\{N(SiMe_3)_2\}_2]$ was used as precursor, keeping the other parameters constant.[74]

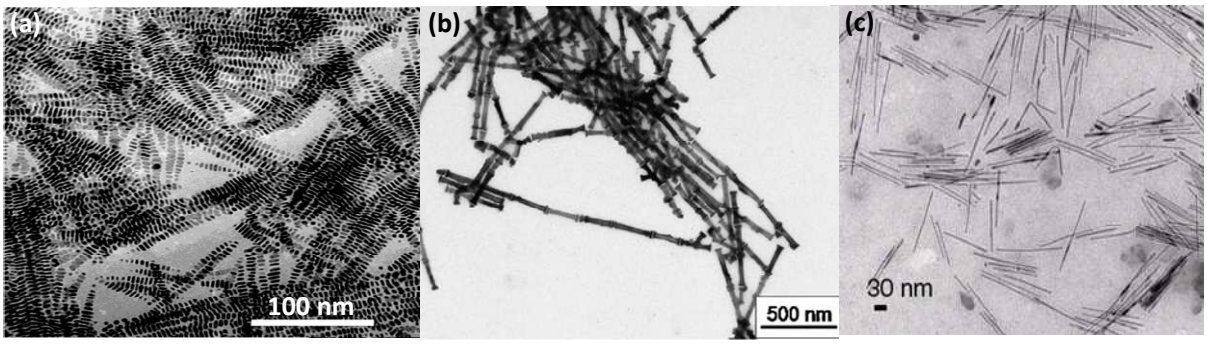

Figure 1-12. *Cobalt anisotropic NPs: (a) nanodisks (Ref. 64); (b,c) nanorods (Refs. 67 and 70, respectively).*

Less anisotropic shapes like nanocubes can be also obtained for ε-Co NPs.[75] In this case the direct decomposition of $Co_2(CO)_8$ in ionic liquids (ILs) holding N-alkyl imidazolium side chains at 150 ^oC leads to particles with different morphologies depending on the nature of the ILs, which are supposed to act as a template. Cubic NPs with an edge length of 50 nm were obtained after 5 minutes of reaction, but as previously observed for Co nanodisks, they tend to rearrange over long periods of time.

Xu and coworkers reported in 2007 the hydrothermal synthesis of hcp Co nanoplatelets.[76] Here the use of anionic surfactants like sodium dodecylsulfate (SDS) which could interact strongly with the Co cations in solution was a key factor in order to obtain regular particles with a length above 100 nm and a thickness of 8 nm. The mechanism for the formation of the platelets develops throw a two steps process: first the metallic salt reacts with NaOH forming a cobalt hydroxide which, under hydrothermal conditions, produces $Co(OH)_2$ nanoplatelets in the presence of SDS. Those objects are subsequently reduced with $H_2PO_2^-$, forming the metallic cobalt colloids. The structural characterization showed that the sample was composed by hcp-Co, with a thin layer of oxide at the surface. These results are surprising if we take into account that the reaction has been performed in distilled water and that no special precautions concerning

oxidation were taken. The hydrothermal approach was also extended to the synthesis of Ag, Ni and Cu anisotropic objects and could be generalized to many inorganic materials.

With a similar approach and using ethylene diamine as capping agent and ethylene glycol as solvent, highly monodisperse hcp-Co microcrystals with different morphologies have been obtained,[77] being the amount of Co salt, the nature of the amine and the temperature at which the solvothermal process takes place the parameters that lead to a sharp control over the shape of the microparticles. Actually, disk-like structures and micro-octadecahedra have been obtained when the reaction temperature was settled at 473 K and 513 K, respectively. If the temperature is increased more till 533 K prism-like structures composed by the stacking of hexagonal disks are formed.

3.2.3 Nickel

Ni is the magnetic transition metal with the lowest magnetic anisotropy and magnetic moment per atom. It is therefore less interesting than iron or cobalt for magnetic storage applications. Nevertheless, some examples of shape controlled synthesis of Ni NPs are present in the literature and some objects with T_B above room temperature have been successfully synthesized due to the important increase in shape anisotropy.

Decomposition of $Ni(COD)_2$ under a stream of dihydrogen at 60°C, leads to a mixture of spherical and trigonal particles when tetra-n-octylammonium glycolate is used as surfactant.[78] The partial control over the morphology most probably comes from the specific adsorption of the glycolate on some crystal facets of Ni, feature that seems to be related with the presence of a hydroxyl group in the α position with respect to the carboxylate group.

Continuing with the hydrogenation of organometallic precursors, the decomposition of the same complex under 3 bars of H_2 and in the presence of HDA leads to the synthesis of Ni nanorods,[79] with a better control over particle size if compared with the previous case. Here, the selective attachment of the aliphatic amine is responsible for the synthesis of fcc-Ni nanorods with 4 nm in diameter and 15 nm in length. Besides the increase in shape anisotropy the particles remain superparamagnetic at room temperature, with a T_B of 100 K. Even if the practical interest of these NPs is limited by their superparamagnetic behavior at room temperature, it is interesting to remark that the presence of HDA does not affect the magnetic properties of the surface atoms,

corroborating other experimental results obtained by the same group. On the other hand, when TOPO was used as stabilizer, an important depletion of magnetization was observed, a similar behavior than that observed with CO adsorption.[7]

Ni nanosheets with triangular and hexagonal shapes were obtained from the decomposition of a Ni^{2+} salt. The size and morphology control arises as a consequence of the variation of the reaction kinetics when small amounts of $Fe(CO)_5$ are added.[80] In fact $Fe(CO)_5$ is oxidized in solution due to the presence of oxygen traces, leading to Fe^{3+}. Subsequently these Fe^{3+} ions can oxidize Ni^0 back to Ni^{2+}, slowing down the reaction rates and facilitating the formation of bigger objects presenting a well-crystallized structure. The size of the nanosheets can be varied between 19 and more than 100 nm by the amount of $Fe(CO)_5$ added, leading (for the bigger sizes) to ferromagnetic objects with blocking temperatures as high as 400 K. The formation of the bigger particles is explained by two different mechanisms: atom-by-atom growth of the smaller nanoplatelets and direct connection between several of them.[81] Nevertheless, no clear explanation for the shape control obtained in the beginning of the reaction is given in these papers; however the results obtained may be tentatively linked to those reported for the synthesis of Ag[82] and Cu[83] nanoplatelets. For these cases the nuclei formed in the first stages of the reaction have random hexagonal close packed (rhcp) structure due to the presence of random stacking of fcc and hcp structures. If those original nuclei grow within an fcc ordering, their original morphology develops an hexagonal shape due to the six fold symmetry of their atoms. In this case, defects may appear along the [111] direction, due to the loss in symmetry of the normal ABCABC ordering. Within this scenario and in the presence of one single stacking fault, the seed presents alternating concave and convex orientations in the position where the twin plane terminates. In the convex facets, the addition of one atom is restricted due to the low number of neighbors present to stabilize it. On the other hand, the addition of an extra atom is favored in the concave side due to the higher number of neighbors. This difference favors the growth of the concave facets at the expenses of the convex ones, thus leading to a triangular platelet from an originally hexagonal seed **(Figure 1-13a)**.

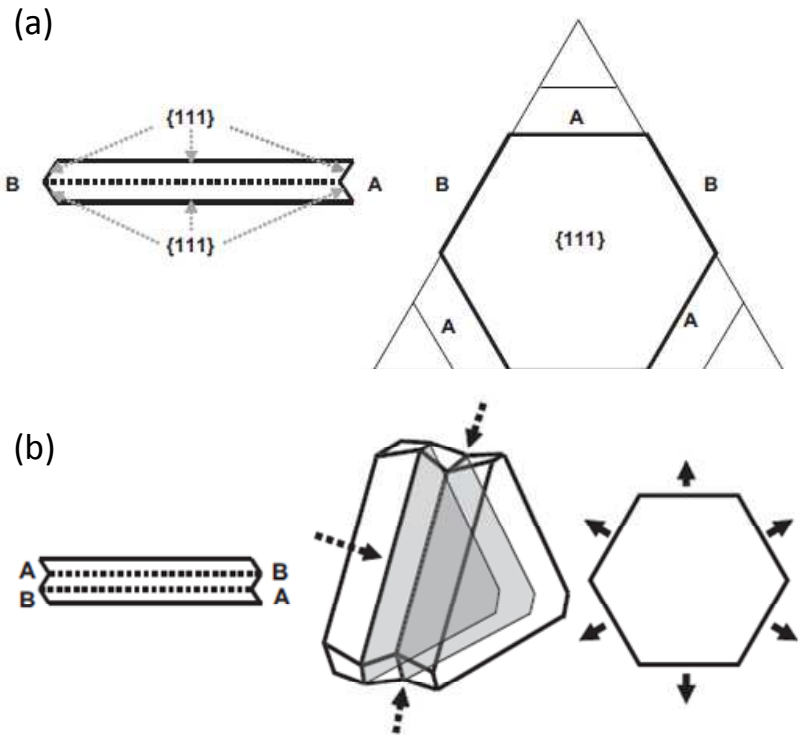

Figure 1-13. *Formation of anisotropic NPs as a consequence of the presence of staking faults (from Ref. 21).*

Independently, if two parallel stacking faults form instead of a single one, the concave and convex orientations will match with each other, due to the 60^{o} reorientation of the second twin plane with respect to the first one. In this case, the growth of the six external facets will be equal and thus, the hexagonal shape of the original seed will be kept all along the synthesis **(Figure 1-13b)**. A repair mechanism has been designed to further favor the growth of concave facets over that of convex ones. Triangular and hexagonal palladium nanodisks have been obtained by coupling the polyol reduction together with an oxidative etching process with Fe^{3+} ions and the pair Cl^{-}/O_2.[84] These oxidizing agents dissolve faster the convex facets than the concave ones back into palladium ions which will next deposit onto the more favorable concave facets, thus promoting shape control. Here, the relatively low temperature at which the reaction takes place is a key factor, because above 100 ^{o}C the etching process would attack the defects present on the original seeds and thus, the morphology of the final particles would be altered. A similar mechanism may be at stake in the case of the synthesis of the Ni nanotriangles reported above.

4 Conclusion

In this chapter we have given a brief introduction to ferromagnetism, highlighting the special features of ferromagnetic NPs. We have seen that at the nanometric scale surface effects become the main contribution to the anisotropy of the matter, being responsible for the unique magnetic properties found in NPs. Those surface effects arise as a consequence of the symmetry breaking experienced by superficial atoms, leading to a narrowing of the d bands and a higher spin polarization.

Even though the interest in NPs is out of question, we have observed that the mechanisms directing their formation in colloidal solutions are extremely difficult to control. In this case, several parameters have to be taken into account:

1. The competition between bulk and surface energies dictates the formation of nuclei in supersaturated solutions.
2. The formation of a unique nucleation event is very important for the homogeneous aggregation of the nuclei and the formation of a monodisperse product.
3. A random hexagonal close-packed configuration is predicted to form during the first stages of nucleation due to the low energy difference between fcc and hcp structures.
4. For a chemical reaction under thermodynamic control, the synthesized NPs will tend to expose at their surfaces the crystallographic facets with the lowest interfacial free energy ({111}, {100} and {110}). On the other hand, if the reaction is under kinetic control, multiple twinned clusters with a high surface tension can be formed.
5. The anisotropic growth of a NP is a complex process and is mainly controlled by three parameters: the nature of the original seed, the specific adsorption of organic ligands at some crystallographic facets and the use of mesoporous materials as templates for the directed growth.

In the last part of this chapter we have introduced the most important methods leading to the synthesis of isotropic and anisotropic MTM NPs. Within all these methods, the hydrogenation of metal-organic complexes presents the best results concerning size and shape

control and magnetic properties of the final NPs. This method has been selected for the synthesis of the nano-objects reported in this dissertation.

---

[1] R. C. O'Handley, Modern Magnetic Materials. Principles and Applications, John Wiley and Sons, Ed. 2000.
[2] C. Kittel, Introduction to Solid State Physics, John Wiley and Sons, Ed. 1996.
[3] I. N. Levine, Quantum Chemistry, Prentice-Hall, Ed. 1991.
[4] J. Bansmann, S. H. Baker, C. Binns, J. A. Blackman, J.-P. Bucher, J. Dorantes-Davila, V. Dupuis, L. Favre, D. Kechrakos, A. Kleibert, K.-H. Meiwes-Broer, G. M. Pastor, A. Perez, O. Toulemonde, K. N. Trohidou, J. Tuaillon, Y. Xie, Surf. Sci. Rep. 56 (2005), 189.
[5] R. M. Wang, O. Dmitrieva, M. Farle, G. Dumpich, H. Q. Ye, H. Poppa, R. Kilaas, C. Kisielowski, Phys. Rev. Lett., 100 (2008), 017205.
[6] O. Margeat, C. Amiens, B. Chaudret, P. Lecante, R. E. Benfield, Chem. Mater., 17 (2005), 107.
[7] N. Cordente, C. Amiens, B. Chaudret, M. Respaud, F. Senocq, M.-J. Casanove, J. Appl. Phys., 94 (2003), 6358.
[8] S. Pick, H. Dreyssé, Phys. Rev. B, 59 (1999), 4195.
[9] S. Pick, H. Dreyssé, Surf. Sci., 460 (2000), 153.
[10] J. Bansmann, L. Lu, M. Getzlaff, Surf. Sci., 371 (1998), 402.
[11] B. Chen, A. W. Castleman, S. N. Khanna, Chem. Phys. Lett., 304 (1999), 423.
[12] J. Osuna, D. de Caro, C. Amiens, B. Chaudret, E. Snoeck, M. Respaud, J.-M. Broto, A. Fert, J. Phys. Chem., 100 (1996), 14571.
[13] S. Bedanta, W. Kleeman, J. Phys. D: Appl. Phys., 42 (2009), 013001.
[14] E. C. Stoner, E. P. Wohlfarth, Phil. Trans. R. Soc. Lond. A, 240 (1948), 599.
[15] B. D. Cullity, C. D. Graham, Introduction to Magnetic Materials, John Wiley and Sons, Ed. 2009.
[16] Y. Xia, Y. Xiong, B. Lim, S. E. Skrabalak, Angew. Chem. Int. Ed., 48 (2009), 60.
[17] V. K. LaMer, R. H. Dinegar, J. Am. Chem. Soc., 72 (1950), 4847.
[18] S. Auer, D. Frenkel, Nature, 409 (2001), 1020.
[19] P. N. Pusey, W. van Megen, W. P. Bartlett, B. J. Ackerson, Phys. Rev. Lett., 63 (1989), 2753.
[20] J.-M. Zhang, F. Ma, K.-W. Xu, Appl. Surf. Sci., 229 (2004), 34.
[21] C. Lofton, W. Sigmund, Adv. Funct. Mater., 15 (2005), 1197.
[22] M. Niederberger, H. Cölfen, Phys. Chem. Chem. Phys., 8 (2006), 3271.
[23] J. Gao, C. M. Bender, C. J. Murphy, Langmuir, 19 (2003), 9065.
[24] P. H. Hess, P. H. Park, J. Appl. Polym. Sci., 10 (1966), 1915.
[25] C. H. Griffiths, M. P. O'Horo, and T. W. Smith, J. Appl. Phys., 50 (1979), 7108.
[26] T. W. Smith, D. Wychlck, J. Phys. Chem., 84 (1980), 1621.
[27] D. Farrell, S. A. Majetich, J. P. Wilcoxon, J. Phys. Chem. B, 107 (2003), 11022.
[28] D. P. Dinega, M. G. Bawendi, Angew. Chem. Int. Ed., 38 (1999), 1788.
[29] V. F. Puntes, K. M. Krishnan, P. Alivisatos, Appl. Phys. Lett., 78 (2001), 2187.
[30] H. Yang, F. Ito, D. Hasegawa, T. Ogawa, M. Takahashi, J. Appl Phys., 101 (2007), 09J112.
[31] J. Park, E. Kang, S. U. Son, H. M. Park, M. K. Lee, J. Kim, K. W. Kim, H.-J. Noh, J.-H. Park, C. J. Bae, J.-G. Park, T. Hyeon, Adv. Mater., 17 (2005), 429.
[32] K. S. Suslick, M. Fang, T. Hyeon, J. Am. Chem. Soc., 118 (1996), 11960.
[33] D. de Caro, T. Ould Ely, A. Mari, B. Chaudret, E. Snoeck, M. Respaud, J.-M. Broto, A. Fert, Chem. Mater., 8 (1996), 1987.
[34] Y. Koltypin, A. Fernandez, T. C. Rojas, J. Campora, P. Palma, R. Prozorov, A. Gedanken, Chem. Mater., 11 (1999), 1331.
[35] F. Fievert, J. P. Lagier, B. Blin, B. Beaudoin, M. Figlarz, Solid State Ionics, 32/33 (1989), 198.
[36] G. Viau, F. Fiévert-Vincent, F. Fiévert, J. Mat. Chem., 6 (1996), 1047.
[37] R. J. Joseyphus, D. Kodama, T. Matsumoto, Y. Sato, B. Jeyadevan, K. Tohji, J. Magn. Magn. Mater., 310 (2007), 2393.
[38] C. B. Murray, S. Sun, H. Doyle, T. Betley, MRS Bulletin, 26 (2001), 985.
[39] G. S. Chaubey, C. Barcena, N. Poudyal, C. Rong, J. Gao, S. Sun, J. Ping. Liu, J. Am. Chem. Soc., 129 (2007), 7214
[40] S. Sun, C. B. Murray, J. Appl. Phys., 85 (1999), 4325.
[41] Z. Guo, L. L. Henry, V. Palshinc, E. J. Podlaha, J. Mat. Chem., 16 (2006), 1772.

[42] A. Taleb, C. Petit, M. P. Pileni, Chem. Mater., 9 (1997), 950.
[43] L. Motte, F. Billoudet, E. Lacaze, J. Douin, M. P. Pileni, J. Phys. Chem. B, 101 (1997), 138.
[44] J. P. Wilcoxon, P. P. Provencio, J. Phys. Chem. B, 103 (1999), 9809.
[45] T. J. Daou, G. Pourroy, S. Bégin-Colin, J. M. Grenèche, C. Ulhaq-Bouillet, P. Legaré, P. Bernhardt, C. Leuvrey, G. Rogez, Chem. Mater., 18 (2006), 4399.
[46] X. Sun, C. Zheng, F. Zhang, Y. Yang, G. Wu, A. Yu, N. Guan, J. Phys. Chem. C, 113 (2009), 16002.
[47] J. Osuna, D. de Caro, C. Amiens, B. Chaudret, E. Snoeck, M. Respaud, J.-M. Broto, A. Fert, J. Phys. Chem., 100 (1996), 14571.
[48] F. Dassenoy, M.-J. Casanove, P. Lecante, M. Verelst, E. Snoeck, A. Mosset, T. Ould Ely, C. Amiens, B. Chaudret, J. Chem. Phys. 112 (2000), 8137-8145.
[49] F. Dumestre, S. Martinez, D. Zitoun, M.-C. Fromen, M.-J. Casanove, P. Lecante, M. Respaud, A. Serres, R. E. Benfield, C. Amiens, B. Chaudret, Faraday Discuss., 125 (2004), 265.
[50] T. O. Ely, C. Amiens, B. Chaudret, E. Snoeck, M. Verelst, M. Respaud, J.-M. Broto, Chem. Mater., 11 (1999), 526.
[51] O. Margeat, F. Dumestre, C. Amiens, B. Chaudret, P. Lecante, M. Respaud, Prog. Solid State Chem., 33 (2005), 71.
[52] L.-M. Lacroix, S. Lachaize, A. Falqui, T. Blon, J. Carrey, M. Respaud, F. Dumestre, C. Amiens, O. Margeat, B. Chaudret, P. Lecante, E. Snoeck, J. Appl. Phys, 103 (2008), 07D521.
[53] O. Margeat, D. Ciuculescu, P. Lecante, M. Respaud, C. Amiens, B. Chaudret, Small, 3 (2007), 451.
[54] C. Desvaux, C. Amiens, P. Fejes, P. Renaud, M. Respaud, P. Lecante, E. Snoeck, B. Chaudret, Nat. Mater. 4 (2005), 750.
[55] S.-J. Park, S. Kim, S. Lee, Z. G. Khim, K. Char, T. Hyeon, J. Am. Chem. Soc., 122 (2000), 8581.
[56] J. Park, K. An, Y. Hwang, J.-G. Park, H.-J. Noh, J.-Y. Kim, J.-H. Park, N.-M. Hwang, T. Hyeon, Nat. Mater., 3 (2004), 891.
[57] D. Kim, J. Park, K. An, N.-K. Yang, J.-G. Park, T. Hyeon, J. Am. Chem. Soc., 129 (2007), 5812.
[58] A. Shavel, B. Rodríguez-González, M. Spasova, M. Farle, L.M Liz-Marzán, Adv. Funct. Mater., 17 (2007), 3870.
[59] M. V. Kovalenko, M. I. Bodnarchuk, R. T. Lechner, G. Hesser, F. Schäffler, W. Heiss, J. Am. Chem. Soc., 129 (2007), 6352.
[60] F. Dumestre, B. Chaudret, C. Amiens, P. Renaud, P. Fejes, Science, 303 (2004), 821.
[61] L.-M. Lacroix, S. Lachaize, A. Falqui, M. Respaud, B. Chaudret, J. Am. Chem. Soc., 1313 (2009), 549.
[62] C. P. Gibson, K. J. Putzer, Science, 267 (1995), 1338.
[63] X.P. Peng, L. Manna, W.D. Yang, J. Wickham , E. Scher, A. Kadavanich , A.P. Alivisatos, Nature, 404 (2000), 59.
[64] V. F. Puntes, K. M. Krishnan, A. P. Alivisatos, Science, 291 (2001), 2115.
[65] V. F. Puntes, D. Zanchet, C. K. Erdonmez, A. P. Alivisatos, J. Am. Chem. Soc., 124 (2002), 12874.
[66] J.-I. Park, N.-J. Kang, Y.-W. Jun, S. J. Oh, H.-C. Ri, J. Cheon, ChemPhysChem, 3 (2002), 543.
[67] Y. Soumare, C. Garcia, T. Maurer, G. Chaboussant, F. Ott, F. Fiévet, J.-Y. Piquemal, G. Viau, Adv. Funct. Mater., 19 (2009), 1971.
[68] D. Ung, G. Viau, C. Ricolleau, F. Warmont, P. Gredin, F. Fiévet, Adv. Mater., 17 (2005), 338.
[69] D. Ung, Y. Soumare, N. Chakroune, G. Viau, M.-J. Vaulay, V. Richard, F. Fiévet, Chem. Mater., 19 (2007), 2084.
[70] F. Dumestre, B. Chaudret, C. Amiens, M.-C. Fromen, M.-J. Casanove, P. Renaud, P. Zurcher, Angew. Chem. Int. Ed., 41 (2002), 4286.
[71] D. Ciuculescu, F. Dumestre, M. Comesaña-Hermo, B. Chaudret, M. Spasova, M. Farle, C. Amiens, Chem. Mater., 21 (2009), 3987.
[72] F. Dumestre, B. Chaudret, C. Amiens, M. Respaud, P. Fejes, P. Renaud, P. Zurcher, Angew. Chem. Int. Ed., 42 (2003), 5213.
[73] E. Snoeck, R. E. Dunin Borkowski, F. Dumestre, P. Renaud, C. Amiens and B. Chaudret, P. Zurcher, Appl. Phys. Lett., 82(1) (2003), 89.
[74] F. Wetz, K. Soulantica, M. Respaud, A. Falqui, B. Chaudret, Mater. Sci. Eng. C, 27 (2007), 1162.
[75] M. Scariot, D. O. Silva, J. D. Scholten, G. Machado, S. R. Teixeira, M. A. Novak, G. Ebeling, J. Dupont, Angew. Chem. Int. Ed., 47 (2008), 9075.
[76] R. Xu, T. Xie, Y. Zhao, Y. Li, Cryst. Growth Des., 7 (2007), 1904.
[77] L. J. Zhao, L. F. Duan, Y. Q. Wang, Q. Jiang, J. Phys. Chem. C, 114 (2010), 10691.
[78] J. S. Bradley, B. Tesche, W. Busser, M. Maase, M. T. Reetz, J. Am. Chem. Soc., 122 (2000), 4631.
[79] N. Cordente, M. Respaud, F. Senocq, M.-J. Casanove, C. Amiens, B. Chaudret, Nano Lett., 1 (2001), 565.

[80] Y. Leng, Y.Wang, X. Li, T. Liu, S. Takahashhi, Nanotechnology, 17 (2006), 4834.
[81] Y. Leng, Y. Li, X. Li, S. Takahashi, J. Phys. Chem. C, 111 (2007), 6630.
[82] (a) I. Pastoriza-Santos, L. M. Liz-Marzán, Nano Lett., 2 (2002), 903. (b) V. Germain, J. Li, D. Ingert, Z. L. Wang, M. P. Pileni, J. Phys. Chem. B, 107 (2003), 8717.
[83] C. Salzemann, J. Urban, I. Lisiecki, M.-P. Pileni, Adv. Funct. Mater., 15 (2005), 1277.
[84] Y. Xiong, J. M. McLellan, J. Chen, Y. Yin, Z.-Y. Li, J. Am. Chem. Soc., 127 (2005), 17118.

Chapter II: Synthesis of Co nanodisks

1 Introduction

Miniaturization of magnetic materials has emerged as the best option to improve the recording densities in magnetic data storage technology. Within the different techniques that lead to the formation of smaller and smaller magnetic grains, colloidal synthesis of MTM NPs should play an important role in the near future. In this context, anisotropic NPs (small enough to be single domain yet with large shape anisotropy to overcome the superparamagnetic limit) are the most interesting candidates for this kind of application. The Co nanorods obtained by hydrogenation of an olefinic precursor presented in Chapter I fulfill all these requirements. Nevertheless, two main difficulties have to be faced when working with these NPs: their oxidation under ambient conditions (subject that is studied in the third chapter of this manuscript) and their successful arrangement on a substrate in such a manner that their magnetic moments remain perpendicular to it. Taking into account their highly anisotropic shape, this task is not straightforward. Also, their very high anisotropy may be a disadvantage when reversal of their magnetization is required (encoding of magnetic data). Therefore, a compromise has to be found. Co NPs with a smaller shape anisotropy like, for example, nanodisks could partially solve this problem since their arrangement on a flat substrate and reversal of their magnetization should be easier, while the energy for magnetization reversal could still allow long term data storage. Therefore, the synthesis of hcp-Co nanodisks with their c axis perpendicular to the plane of the disk could be one step forward towards the implementation of MTM NPs into real devices (if their easy axis of magnetization coincides with the c axis, which imposes geometrical constraints).

As presented in the previous chapter, most of the processes designed for the colloidal synthesis of NPs lead to the production of isotropic materials with spherical morphology. Nevertheless, one and two-dimensional structures like nanorods, nanowires and nanoplates of various shapes (disks, triangles, etc) have also been obtained for different materials. These are mostly observed when the synthesis is under kinetic rather than thermodynamic control. Indeed, under true thermodynamic control spheres would be the only objects present at the end of the reaction. However, the presence of strongly adsorbed ligands may alter the thermodynamics of the nano-objects and stabilize unusual shapes. The anisotropic growth of NPs is, in most cases,

controlled by three main experimental factors: the use of mesoporous materials as templates for the directed growth, the selective chemisorption of organic molecules onto some crystallographic facets of the crystals and the morphology of the original seed from which the growth takes place. This last mechanism becomes extremely important in the synthesis of 2D NPs, due to the presence of twin planes in the first stages of the synthesis. Those twin planes create favorable and unfavorable sites for the addition of atoms and thus direct the 2D growth of the final particles.[1]

The only work presenting the synthesis of disk-shaped MTM NPs attributes shape control to the specific adsorption of chemical species on some of their crystallographic facets. More precisely, Puntes et al.[2] obtained Co nanodisks from the fast decomposition of $Co_2(CO)_8$ at high temperature due to preferential adsorption of oleic acid and linear amines at the {0001} facets. However, these ligands promote Ostwald ripening of the nanodisks upon time. Hence, the objects cannot be isolated in high yield. Other systems like Ag,[3] Cu_2S[4], some rare-earth oxides[5] (La_2O_3, Eu_2O_3 and Sm_2O_3) and micrometric Co crystals[6] are also examples of disk-shaped materials in which the anisotropic growth is directed by preferential adsorption of organic molecules.

In this chapter we introduce a protocol for the synthesis of stable disk-shaped Co NPs. The importance of the different stabilizing agents used and the structural properties of the final particles are investigated. Several techniques such as transmission electron microscopy, magnetic measurements, UV-visible spectroscopy or X-ray diffraction are used in order to elucidate the mechanisms of the formation of these new NPs. Comparisons with simulations and previous results are also discussed.

2 Results and discussion

2.1 Selection of the experimental conditions

Chaudret and coworkers developed several years ago a simple and reproducible strategy for the synthesis of Co and Fe anisotropic NPs[7] consisting in the decomposition of an organometallic precursor under dihydrogen in the presence of a mixture of acids and amines with

long chains at 150 °C. It was suggested that formation of intermediate carboxylate complexes and their supramolecular organization, associated with preferential coordination of the carboxylic acid onto certain faces of the nanocrystals were key factors governing the anisotropic growth. The excellent results concerning morphology control and magnetic performance obtained with the synthesis of Co nanorods,[7a,b] made us believe that this approach could be adapted to the synthesis of Co NPs with other sizes and shapes and therefore, with new magnetic properties. In our experiments we decided to use the same olefinic precursor of Co ($Co(\eta^3\text{-}C_8H_{13})(\eta^4\text{-}C_8H_{12})$) due to its importance in the final magnetic properties of the particles.[8] In fact, the main variation introduced in our synthesis is the use of a new kind of ligand (Rhodamine B) instead of a carboxylic acid with a long aliphatic chain **(Figure 2-1)**. Rhodamine B (RhB) possesses a carboxylic acid function that could coordinate at the surface of the NPs. Contrarily to the ligands used for the synthesis of rods or wires, RhB has a rigid flat polyaromatic side, which could change its adsorption selectivity onto Co surfaces and its supramolecular organization.

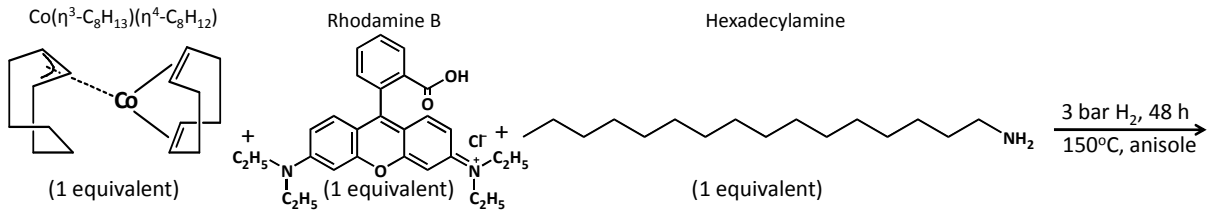

Figure 2-1. *General scheme for the synthesis of Co nanodisks.*

2.2 Synthesis

While we have introduced this variation, other parameters of the reaction (use of an aliphatic amine, molar ratios between the reactants, temperature, solvent and time) have been kept constant with respect to the synthesis of the original rods. Therefore, the reaction was performed with an equimolar amount of each reactant, at 150 °C, in anisole and for a reaction time of 48 hours. After this period of time the reacting medium was allowed to cool down to room temperature and the excess of dihydrogen was removed. At this point we found that the solution had a red color and two different solids were observed: a blue precipitate that remained in the bottom of the Fischer-Porter bottle and a black solid stuck to the stirring bar (Sample 2-1). The red solution and the blue solid have been isolated and stored under argon to avoid any oxidation prior to further characterization. The black precipitate has been washed with anisole

and collected from the magnetic stirring bar. TEM images from this black solid show the presence of Co anisotropic, rod-like objects with a length of 21.5 nm, a thickness of 12.5 nm and size distributions below 20 % **(Figure 2-2b,c)**. These objects tend to stack together forming long chains of particles **(Figure 2-2a and 2-3a)** when deposited on the carbon-copper grid. 3D electron tomography has also been performed on the particles.

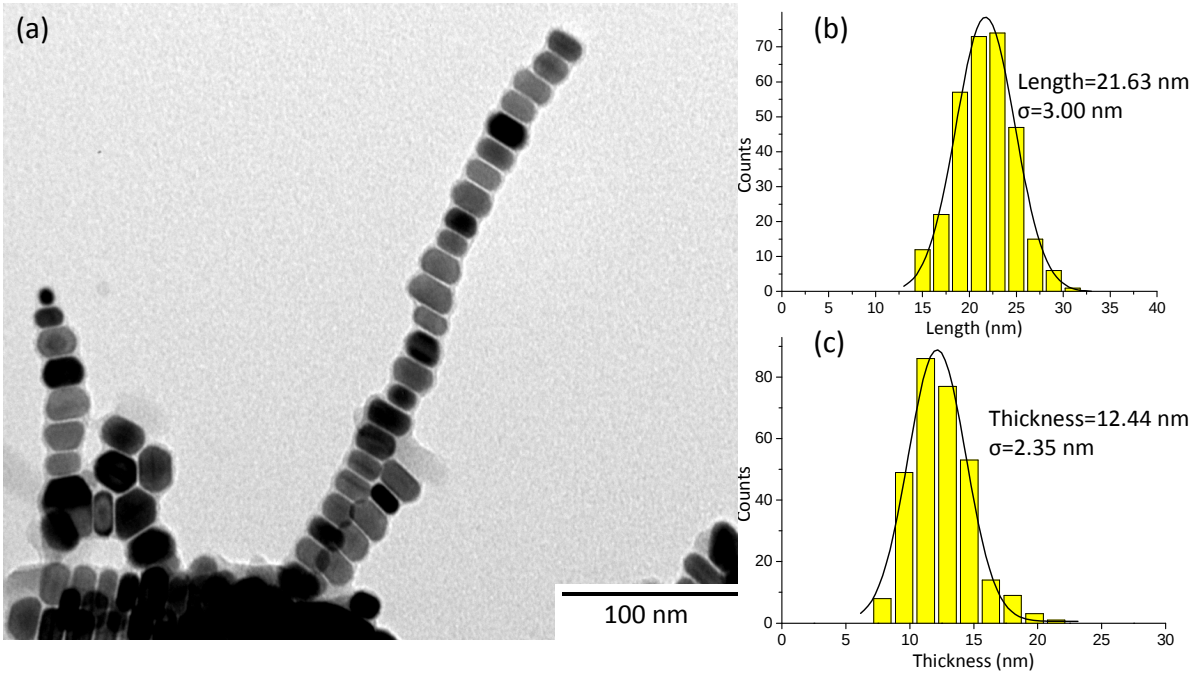

Figure 2-2. *(a) TEM image of the as-synthesized Co anisotropic objects from sample 2-1, (b,c) size histograms of their length and thickness, respectively.*

Despite the rod-like morphology, 3D electron tomography and tilting experiments show that the NPs are actually disks rather than rods **(Figure 2-3)**. These particles are thus similar to those obtained by Puntes and coworkers,[2] even though in their work the nanodisks (with a thickness of 4 nm and a diameter of 90 nm in the case of the larger ones) are unstable structures which evolve after several minutes into spherical ε-Co NPs with sizes between 3 and 17 nm depending on the reaction conditions. Here the particles have been obtained after 48 hours of reaction and moreover, longer periods of time (1 week) do not have any effect on the final shape of the NPs, proving that the growth mechanism is irreversible.

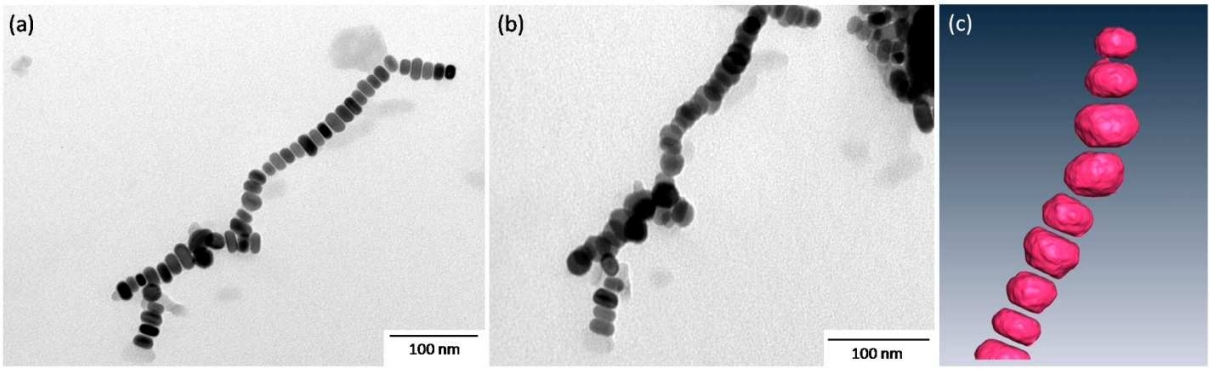

Figure 2-3. *TEM images of the Co nanodisks before (a) and after (b) tilting the sample holder 45°. In (c) frame of a video obtained from 3D electron tomography on Sample 2-1.*

2.3 Structural characterization of the NPs

2.3.1 High resolution electron microscopy (HRTEM) studies

The anisotropic objects obtained in Sample 2-1 have been studied with high resolution electron microscopy (HRTEM) in order to elucidate their crystalline structure. To do this, two different samples were prepared:

1. A drop of a solution of the particles in THF was directly cast on a carbon coated Cu TEM grid.
2. A small amount of the powder was mixed with a polymeric resin. The mixture was subsequently cut into very thin stripes (50 nm) which were deposited on Cu grids prior to their carbonization. This technique is known as ultramicrotomy.

The samples prepared following the first method are arranged on the TEM grid forming chains that can reach several hundreds of nm in length. In this case, the disk-shaped particles remain perpendicular to the substrate **(Figure 2-4a,b)**. Even though the NPs are single crystals, they present stacking faults with a density that changes from one particle to the other **(Figure 2-4d,e)**. The diffraction pattern obtained from one of the particles shows a hexagonal close packed structure (hcp), with its c axis perpendicular to the direction of preferential growth of the particle, in opposition to previous results observed for Co nanorods and nanowires synthesized in a similar way. The Fast Fourier Transformation (FFT) shows two singularities: the presence of splitted reflections and the appearance of two new spots corresponding to (0001) and (000-1)

atomic planes (red squares in **Figure 2-4f**), forbidden reflections for this crystallographic structure.

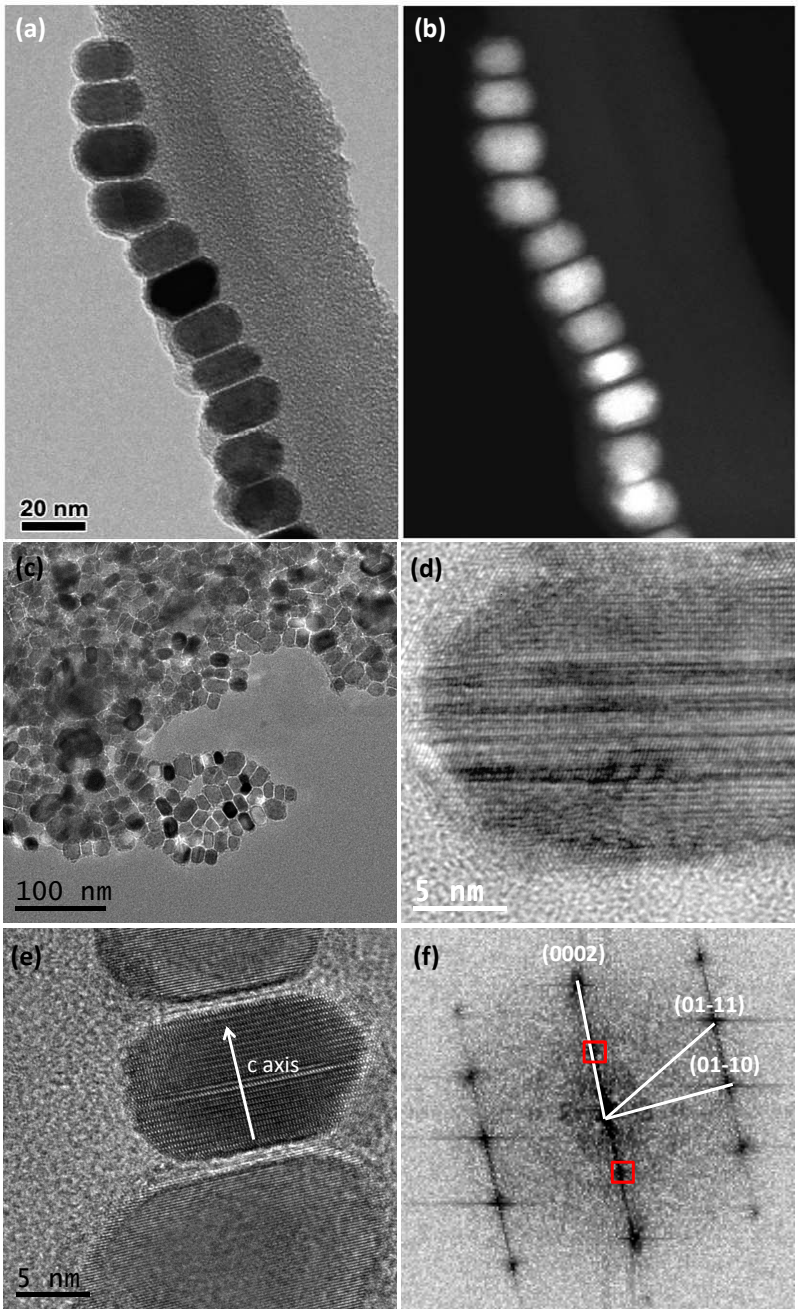

Figure 2-4. *Images (a) and (b) show TEM pictures of the nanodisks obtained in Sample 2-1 with conventional bright field HRTEM and High-Angle Annular Dark-Field (HAAD) STEM, respectively. A view of the sample obtained after deposition of one drop of the solution is found in (c). Stacking faults in the structure of a representative nanodisk can be seen in (d) and (e). The fast Fourier transform (FFT) represented in (f) corresponds to the central particle observed in image (e) with a zone axis [2-1-10]. The forbidden reflections are marked with red squares.*

The TEM samples prepared by ultramicrotomy have the advantage of presenting particles in both orientations, perpendicular and parallel to the grid **(Figure 2-5a)**. The later cannot be obtained from a sample prepared by deposition of one drop of the solution, due to the chain formation. Therefore, ultramicrotomy allows the study of the Co nanodisks from a different zone axis, in this case [1-21-3] for most of the particles, this means a 60 degrees tilting with respect to the previous study and 30 degrees with respect to the substrate. Again, an hcp structure is elucidated from the diffraction pattern **(Figure 2-5c)** but no extra reflections or splitting of the original ones are observed in this case.

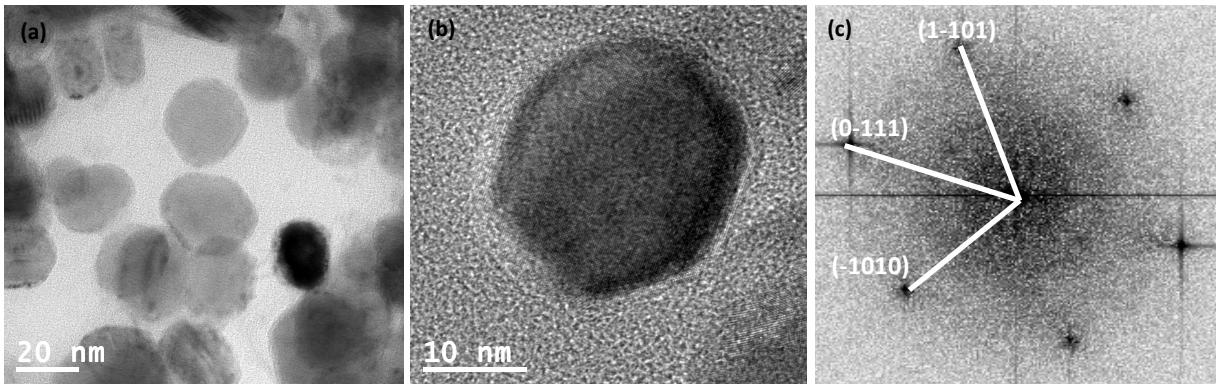

Figure 2-5. *(a-b) HRTEM images of a sample obtained by ultramicrotomy composed by Co nanodisks. The zone axis of the disk observed in (b) is [1-21-3], while (c) represents its corresponding FFT.*

2.3.2 HRTEM simulations

A model has been constructed in order to create a simulated FFT that can be compared with the experimental data. To do this, a hexagonal close packed structure was modeled with MATLAB® using the parameters for hcp cobalt. Once the model was constructed, it was introduced in Quantitative Scanning Transmission Electron Microscopy (QSTEM), a special software that creates a simulated two dimensional image from which a FFT can be obtained.

Simulated images of hcp structures (ABABAB…) under the two different zone axes [2-1-10] and [1-21-3] and their corresponding FFT are represented in **Figure 2-6**. As expected, the angles and interatomic distances are those obtained experimentally for the Co nanodisks (within the experimental error). The original model can be disturbed by the random addition of twin

planes in the hcp structure.[i] When this is done, splitting of the reflections is observed **(Figure 2-6d,h)**, effect that is proportional to the number of twin planes added to the original structure.

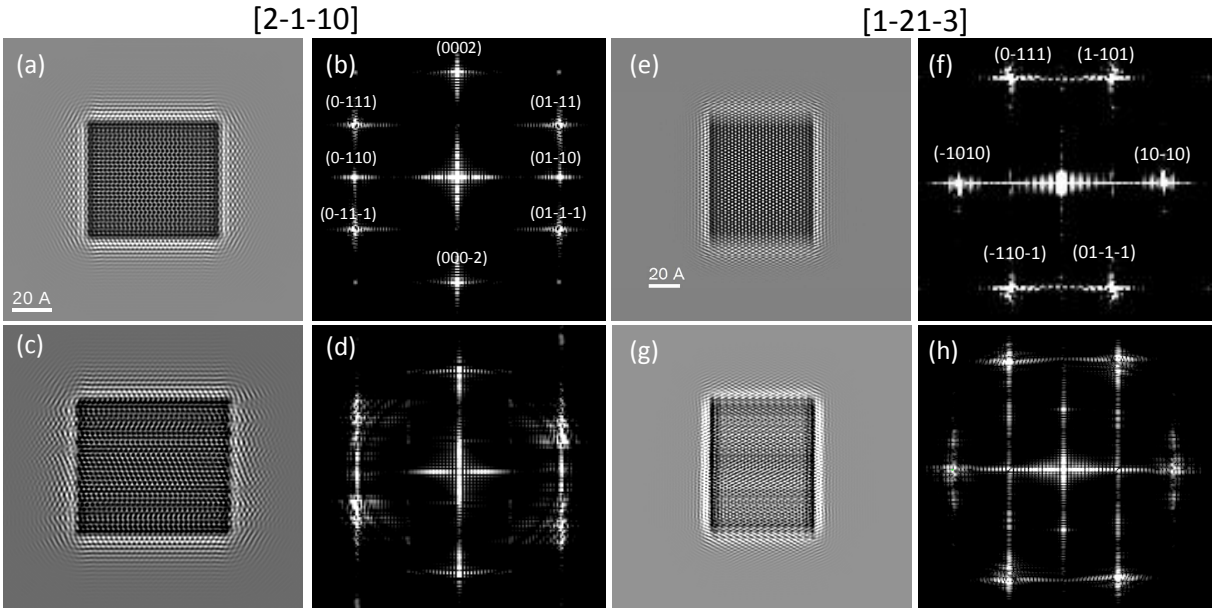

Figure 2-6. *Simulated images (a,c,e,g) and their corresponding FFT (b,d,f,h) for a hcp Co structure without defects (a,e) and with a random distribution of them (c,g).The images in the left side correspond to the zone axis [2-1-10] while the ones in the right have been obtained for the direction [1-21-3].*

2.3.3 Discussion

The HRTEM study of the Co nanodisks shows unambiguously that these particles have a hexagonal close packed structure, with their c axis perpendicular to the growth direction, one of the prerequisites for the target material of this study. Nevertheless, we found defects in the particles that we ascribe to the formation of stacking faults in the early stages of the reaction. Those defects are perpendicular to the c direction of the crystal and become easily observable when the particles are organized on the TEM grid, in a perpendicular disposition with respect to the substrate. The presence of stacking faults in the hcp structure has a clear effect on the FFT of the particles taken with [2-1-10] as zone axis since splitting of the reflections and appearance of new ones corresponding to the (0001) and (000-1) atomic planes are found in the diffraction pattern. While the presence of splitted reflections is an unambiguous consequence of the defects observed in the structure,[3] the origin of the extra reflections is still unclear. Indeed, forbidden

[i] The superposition of planes used for the simulation of an hcp structure with random defects is: ABABABCABACABCABCABCABACABACAB.

reflections are only found experimentally when the nano-objects are observed under the [2-1-10] zone axis while under the [1-21-3] zone axis neither splitting of the original FFT points nor extra reflections are found **(Figure 2-5c)**. Actually, the simulations show that a high density of defects is needed to observe a clear change in the FFT, where splitting of the reflections is observed **(Figure 2-6d,h)**. The lack of variations in the experimental FFT for [1-21-3] is not surprising since the defects are not directly viewed under this zone axis (there is an angle of 60 degrees with respect to the twin planes).

2.4 Structural characterization of the by-products

As mentioned before, the synthesis of the Co nanodisks leads to the formation of two by-products at the end of the reaction: a blue precipitate (Sample 2-Blue) and a red solution (Sample 2-Red).

Sample 2-Blue has been crystallized: the solid was solubilized in a mixture of anisole and methanol (1:1) inside a thin glass tube and placed into the fridge of the glovebox. After one month small blue crystallites were observed, isolated and studied by X-ray diffraction. The diffraction data show that the actual molecule consists in a Co^{2+} center within a tetrahedral environment of four chloride anions. Two hexadecylammonium cations complete the structure **(Figure 2-7a)**. The Co-Cl distances range between 2.25 and 2.28 Å, normal values for a tetrahedral cobalt chloride complex (XRD data can be found in the Experimental Section). It is noteworthy that the long range order evidences a lamellar supramolecular organization of the complex **(Figure 2-7b)**, fact that could be related with the anisotropic growth of the particles. Control experiments show that this complex, $CoCl_4(HDAH)_2$, forms from the reaction between the Co precursor and HDA-HCl. This ammonium salt could itself originate from the reaction between HDA and RhB (see scheme in **Figure 2-9**).

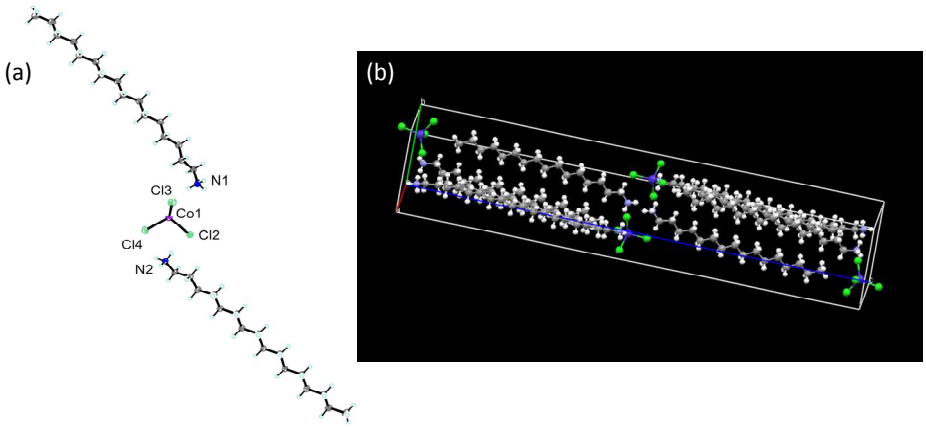

Figure 2-7. *(a) Crystal structure of the blue solid after recrystallization. (b) Spatial arrangement of the complexes forming a lamellar superstructure.*

The second by-product of the reaction (Sample 2-Red) has been characterized by means of UV-visible absorption spectroscopy using anisole as solvent **(Figure 2-8)**. At first sight, the shape of the spectrum resembles that of RhB with a 30 nm blue shift. However, the relative intensities of the two characteristic absorptions are different from those observed in the spectrum of RhB. Furthermore, after comparison to literature data, the blue shift of the spectrum is too large to be explained by coordination to a metal center.[9] In fact, the shape and position of the absorption bands are indicative of the presence of a Co^{2+} complex in octahedral environment. Given the structure of Sample 2-blue, it is highly probable that the red complex corresponds to its soluble form in anisole, with coordination of two supplementary HDA ligands.

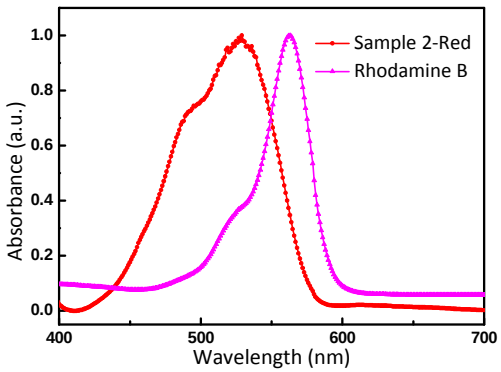

Figure 2-8*. Absorption spectra of the red solution (Sample 2-Red), by-product formed in Sample 2-1. The absorption spectrum of RhB in anisole is plotted as a reference.*

In conclusion, no signal for RhB could be evidenced in solution at the end of the reaction. Dispersion of the NPs in methanol leads to a pink fluorescent solution supporting the presence of RhB at the surface of the Co NPs. However, this represents only a minor fraction of the RhB introduced initially, as the organic content in the powder represents no more than 3 % of the total (according to microanalysis results). Taking into account that the Co atoms at the surface are estimated to be a 6.6 % of the total, we can roughly estimate the presence of 1 RhB molecule per 18 superficial Co atoms. Excess RhB is suggested to be present in solution in its closed basic form, which is colorless, as a result of its reaction with HDA **(Figure 2-9)**.

2.5 Investigation of the origin of the anisotropic growth

2.5.1 Hypotheses

The important difference in morphology and structure between the new particles presented here and the nanorods obtained previously with a similar procedure lead us to think that RhB plays a major role over the control of the morphology of the particles. At this stage three main hypotheses can be made:

- The anisotropic growth is governed by the structure of the seeds: Lofton and Sigmund showed that the formation of nuclei presenting several stacking faults directs the preferential formation of disk-shaped NPs.[1] Confirmation of this mechanism is a difficult task to accomplish since it involves the characterization of intermediates that are formed in the very first stages of the reaction and are very difficult (if not impossible) to isolate.

- Template-assisted formation of anisotropic NPs: the use of templates or micelles in solution to direct the growth of colloidal particles has been already reported.[10] Here the lamellar long range organization of the $Co(Cl)_4(HDAH)_2$ complex presented above could act as a template for the anisotropic growth of the NPs *i.e.* selectively direct the growth of the preformed seeds towards a preferential configuration (if this long range order exists in solution and at the temperature range at which the reaction takes place).

- Selective adsorption of ligands: the preferential adsorption of ligands at some crystallographic facets is the most-widely used explanation for the formation of

anisotropic nano-objects (see Chapter I). Therefore, the coordination of RhB or the pair RhB/HDA could explain the shape of the particles presented here.

Each of these three models or a combination of them could account for the formation of the Co nanodisks. Since the characterization of the seeds formed in the very first stages of the colloidal reaction was not experimentally possible, we have decided to focus our efforts on the role played by the by-products of the synthesis and the importance of HDA and most importantly RhB, molecule that presents different functional groups that could participate in the synthesis of the particles.

2.5.2 Role of $Co(Cl)_4(HDAH)_2$

This complex does not decompose under dihydrogen in the conditions required for the synthesis of the Co nanodisks. Therefore, it is issued from a competing reaction and cannot be regarded as a Co reservoir in solution. However, due to its supramolecular arrangement, it could template the anisotropic growth of the nanoparticles.

In order to elucidate if $Co(Cl)_4(HDAH)_2$ has an important role on the formation of the Co disks we have decomposed $Co(\eta^3\text{-}C_8H_{13})(\eta^4\text{-}C_8H_{12})$ under dihydrogen in the presence of this complex, following the same conditions of time and temperature previously described for the synthesis of the cobalt nanodisks (Scheme in **Figure 2-9**). At the end of the reaction, a blue precipitate that is only soluble at high temperatures (unreacted $Co(Cl)_4(HDAH)_2$ complex) and a black precipitate on the magnetic stirring bar coming from the decomposition of $Co(\eta^3\text{-}C_8H_{13})(\eta^4\text{-}C_8H_{12})$ are observed (Sample 2-2). When the black solid is studied with transmission electron microscopy, polydisperse particles with sizes above 100 nm **(Figure 2-9a)** and cubic NPs with edges of 80 nm **(Figure 2-9b,c)** are found. These cubic objects do not show a clear crystalline structure and seem to be formed by a metal-organic complex. Actually, they experience morphological changes under the electron beam. Unfortunately, and due to the instability of the nanocubes presented here, further characterization of their structure and chemical composition could not be achieved. Nevertheless, it is clear that $Co(Cl)_4(HDAH)_2$ is not the key parameter for the anisotropic growth of the NPs.

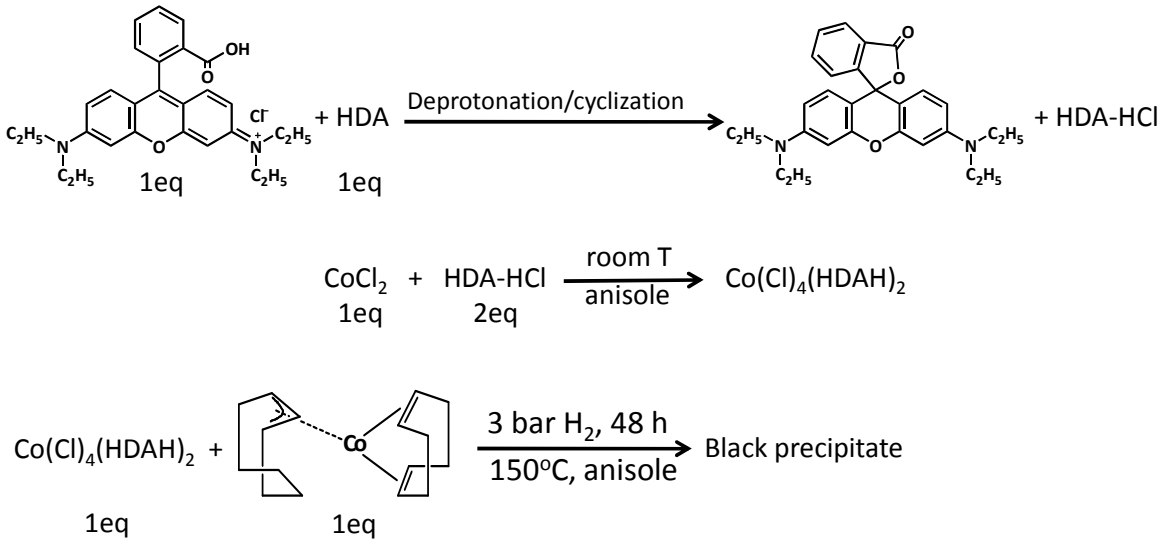

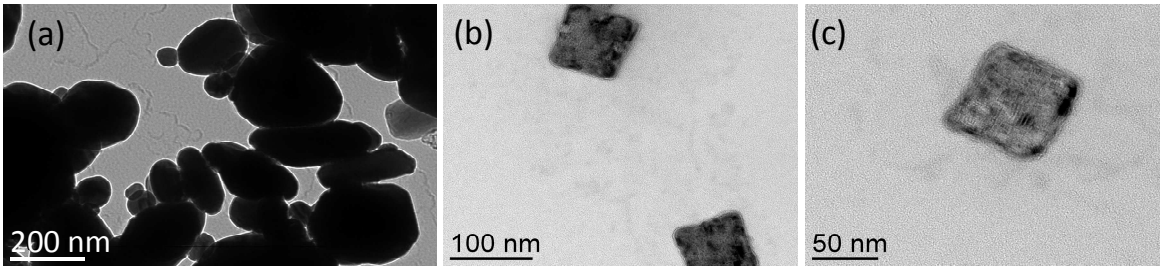

Figure 2-9. *Top: reaction scheme for the synthesis of Sample 2-Blue and Sample 2-2. Bottom: TEM images of Sample 2-2: (a) polydisperse particles and (b,c) nanocubes formed by a metal-organic complex that decomposes under the electron beam.*

2.5.3 Role of HDA

Shape control is achieved in several metals when amines are present as capping agents alone or in the presence of other molecules like carboxylic acids or phosphines (see Chapter I). In this case, their special affinity for some crystallographic facets of the NPs seems to be the major reason to explain this phenomenon. However, previous experiments[11] have shown that HDA is too labile to stabilize NPs in the conditions used here for the synthesis of the Co nanodisks. At the same time its presence was mandatory for the synthesis of rods or wires of Co, most probably because it facilitates the formation of intermediate carboxylate complexes and/or their supramolecular organization.[12]

Here the importance of HDA was also proved by performing a control reaction in which RhB was used as unique stabilizer while the rest of the parameters were kept constant. In this

case when the reaction is finished, a black precipitate is again recovered on the magnetic stirring bar (Sample 2-3). However, the TEM images of this sample show the presence of agglomerated particles without any control over their size and shape **(Figure 2-10)**, indicating therefore the importance of HDA on the formation of Co nanodisks.

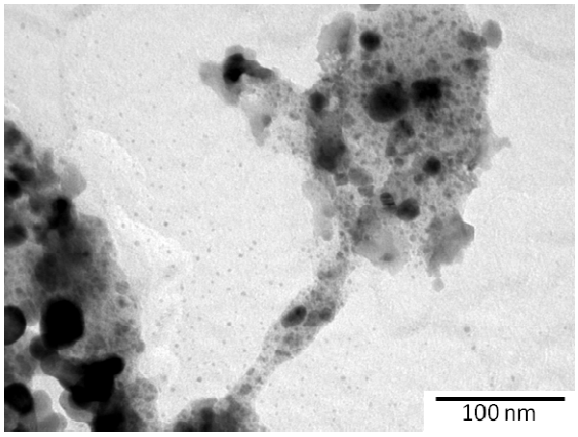

Figure 2-10. *TEM image of the Sample 2-3.*

2.5.4 Role of Rhodamine B

RhB presents different possible anchoring sites. First its carboxylic acid function can participate in the formation of intermediate or side complexes, or coordinate at Co surfaces. It presents also fused aromatic rings with a large density of π electrons which could interact in a flat configuration with the surface of the NPs. Indeed it was recently observed by NMR that a phenyl group from a chiral diphosphite ligand used for the stabilization of Pd NPs interacted strongly with the Pd surface.[13] Moreover this molecule also possesses amine functions that can interact with metallic surfaces. In order to understand the importance of each function, we carried out control experiments with molecules bearing common points with the chemical structure of RhB **(Figure 2-11)**. Six different molecules (control ligands) have thus been tested under the same experimental conditions than those presented for Sample 2-1:

- Samples 2-4, 2-5, and 2-6 were chosen to test the behavior of a deactivated carboxylic acid function in the synthesis of Co NPs, in comparison with the carboxylic acids with linear alkyl chains used for the synthesis of Co nanorods and wires (such as stearic acid for example, $C_{18}H_{36}O_2$). Sample 2-6 introduces a steric hindrance around the carboxylic acid function closer to that of RhB.

– Samples 2-7 and 2-9 were chosen to test the role of the aromatic part of RhB. Also RhB base has been tested (Sample 2-8) due to the fact that it could be formed in the reacting medium as a consequence of the reaction between RhB and HDA. In this particular case, no HDA was added in the reacting medium.

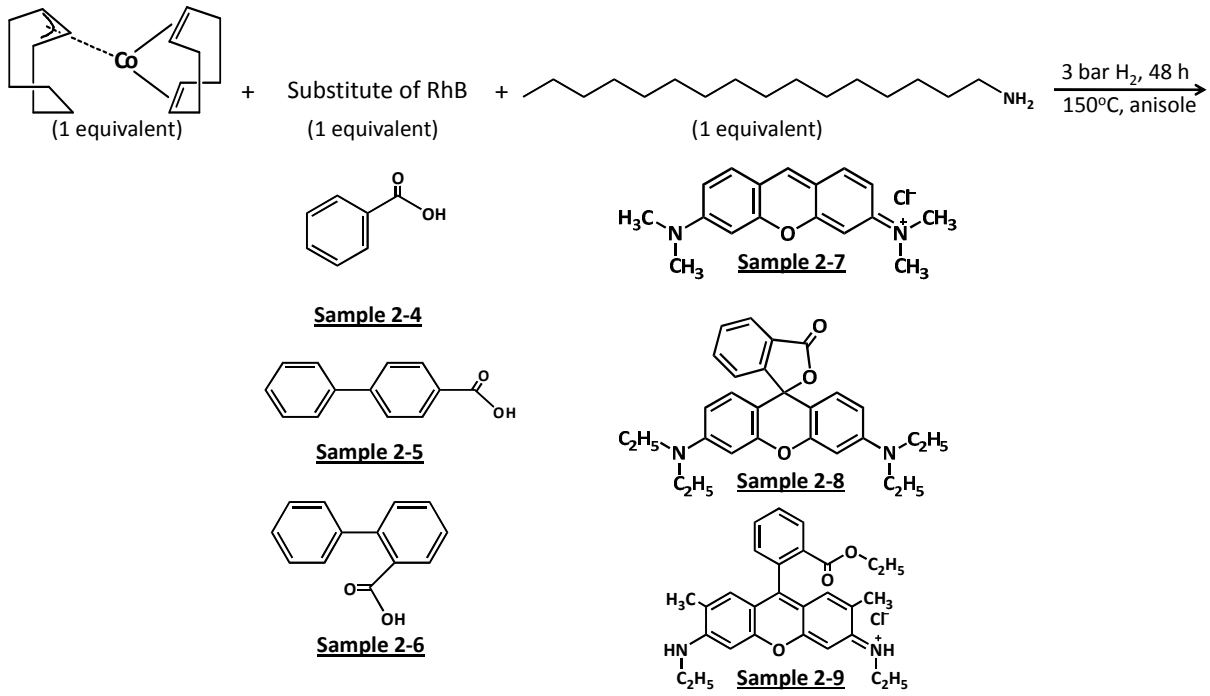

Figure 2-11. *General scheme for the control experiments performed with different molecules in replacement of RhB.*

2.5.4.1 Benzoic acid and Biphenyl-4-carboxylic acid

In comparison with stearic acid, used in combination with HDA for the synthesis of nanorods or wires of Co, these acids should interact more weakly with Co while, at the same time, being more prone to staking, as π interactions are somewhat stronger than Van der Waals interactions between linear alkyl chains. After 48 hours of reaction, we obtain a dark brownish solution without evidence of precipitation, a clear proof for the presence of small superparamagnetic Co NPs (Samples 2-4 and 2-5). In fact, when a drop of the solution is cast on a TEM grid and studied with the microscope, spherical NPs with a mean diameter of 2.2 nm ± 0.5, or 2.9 nm ± 0.4, for benzoic and biphenyl-4-carboxylic acid respectively, are found **(Figure 2-12)** without any trace of nanodisks or nanorods.

Interestingly, for Sample 2-5 the NPs are mostly confined into urchin-like superstructures, as observed on the TEM grid. The formation of such superstructures arises most probably from the self-assembly of excess biphenyl-4-carboxylic acid, which act as template for the assembly of the Co NPs.

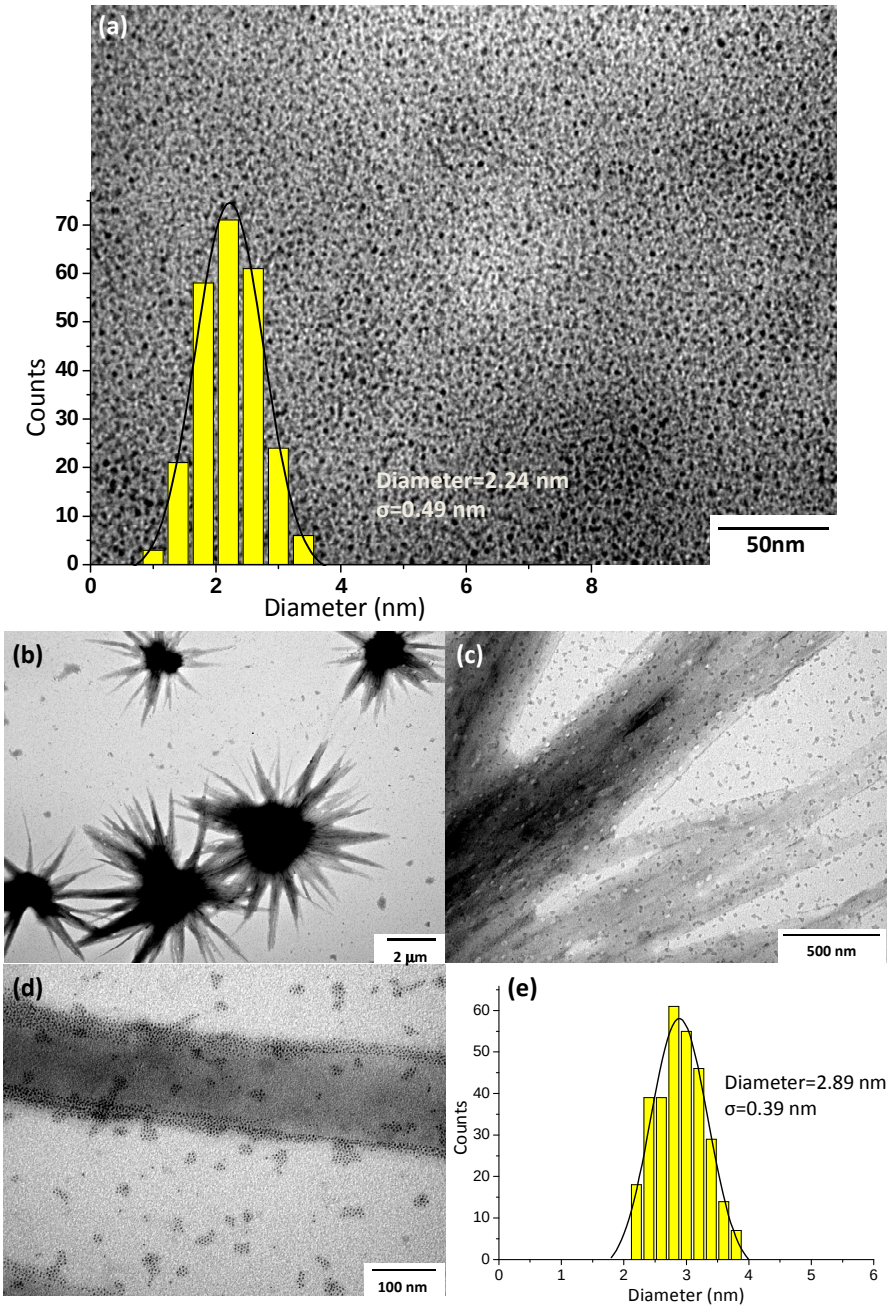

Figure 2-12. *(a) TEM image and size histogram for Sample 2-4. (b- d) TEM images with different magnification from the star-like superstructures obtained in Sample 2-5, while in (e) we can observe the size histogram of the small particles.*

We explain the formation of isotropic small Co NPs as the result of the formation of an unstable Co carboxylate intermediate in the first stages of the reaction. Such unstable species will lead to the fast formation of nuclei on a single event and therefore to the formation of small and uniform NPs.

2.5.4.2 Biphenyl-2-carboxylic acid

In opposition to the results obtained with benzoic acid or biphenyl-4-carboxylic acid, a black solid is obtained when biphenyl-2-carboxylic acid is used (Sample 2-6). Such solid is composed by a mixture of spherical and rod-like NPs **(Figure 2-13a,b)**. The population of spherical particles has a mean diameter of 5.5 nm (σ = 0.6 nm) and the rod-shaped ones have an aspect ratio of 3.45, while both present an hcp structure. In the case of the rods, the c axis of the crystal corresponds to the direction of preferential growth. The larger volume of the NPs obtained here is coherent with the increased steric hindrance of the ligand and explains why they precipitate and stick strongly to the magnetic stirring bar.

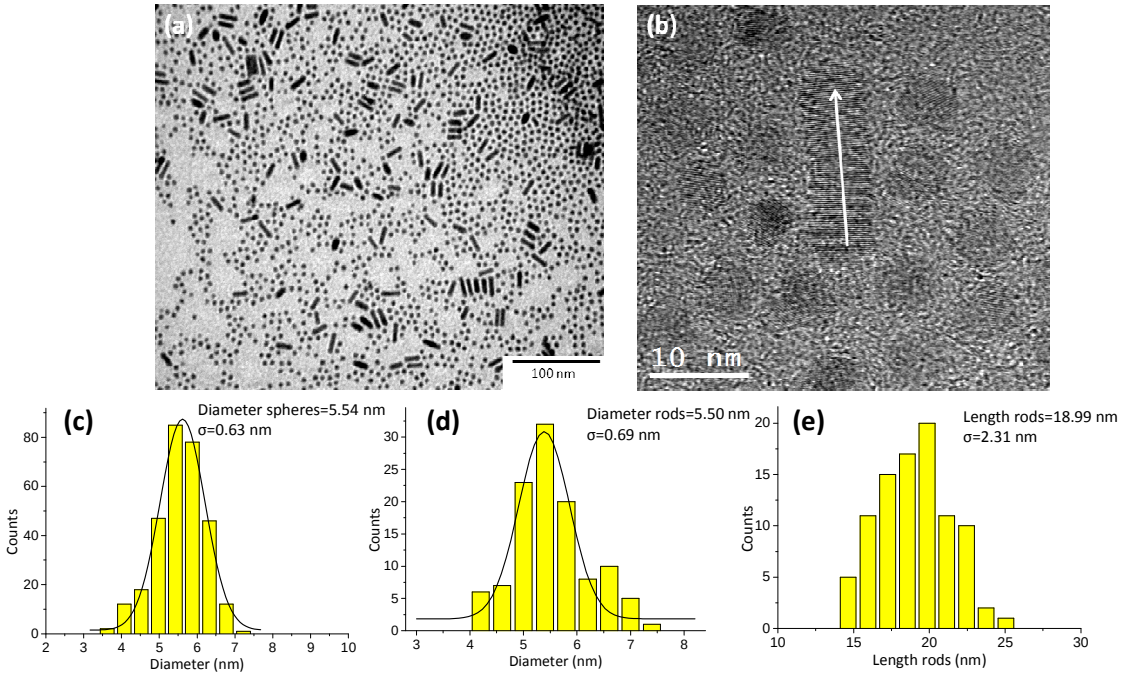

Figure 2-13. *(a) TEM and (b) HRTEM images of the mixture of spheres and rods present in Sample 2-6, the arrow indicates the direction of the c axis. (c-e) Size histograms for the diameter of the spheres and the length and diameter of the rods.*

Tilting experiments have been performed in order to clarify the real morphology of the anisotropic particles. The observations exclude the presence of disk-shaped Co particles and emphasize the importance of the structure of the carboxylic acid on the final shape of the nanomaterial. It is noteworthy that the diameter of the rods perfectly matches the diameter of the isolated NPs, in opposition to what is observed during the formation of rods in long chain carboxylic acid/HDA mixtures, where the diameter of the isolated NPs found in the medium is often smaller than that of the rods. Here the observations (identical diameter and large distribution of the length of the rods) are in agreement with an anisotropic growth via an oriented attachment process.

2.5.4.3 Pyronin Y

In all the variants to the original synthesis presented in the previous paragraphs we have used carboxylic acids to replace RhB as one of the capping agents (together with HDA) during the synthesis but in none of them nanodisks have been observed. It points out the importance of the aromatic moiety of RhB for the perpendicular growth of the NPs with respect to the c axis of the Co structure. We have thus decided to use Pyronin Y since it is a good model for the aromatic part of RhB **(Figure 2-11)**. Therefore, the influence of the aromatic rings together with the two tertiary amines can be studied as an alternative to the stabilization of NPs by adsorption of a carboxylic acid.

At the end of the reaction a green solution is obtained together with a black precipitate deposited on the stirring bar (Sample 2-7). The green coloration of the solution is tentatively attributed to the formation of a Co^{3+} complex, like for example the well-known trans-$[CoCl_2(NH_3)_4]Cl$ Werner complex (in this case HDA would replace NH_3, by analogy with the Sample 2-Blue evidenced before). The transmission electron microscopy images of the solid show the presence of 8 nm spherical NPs with a narrow size distribution and big micrometer sized particles **(Figure 2-14)**. Actually, when the NPs are observed with a higher magnification, we observe that even if the majority of them are perfect single crystals, a small population presents twin planes like those observed in Sample 2-1. We tilted the sample holder in order to elucidate the actual morphology of the objects, recording images at different degrees of tilt. This study showed that only the NPs with stacking faults present an anisotropic morphology. In comparison with the nanodisks obtained in Sample 2-1, here the anisotropic particles present a

smaller size and aspect ratio between length (12 nm) and thickness (8.5 nm), unfortunately and due to the small population of them, we could not obtain a size histogram.

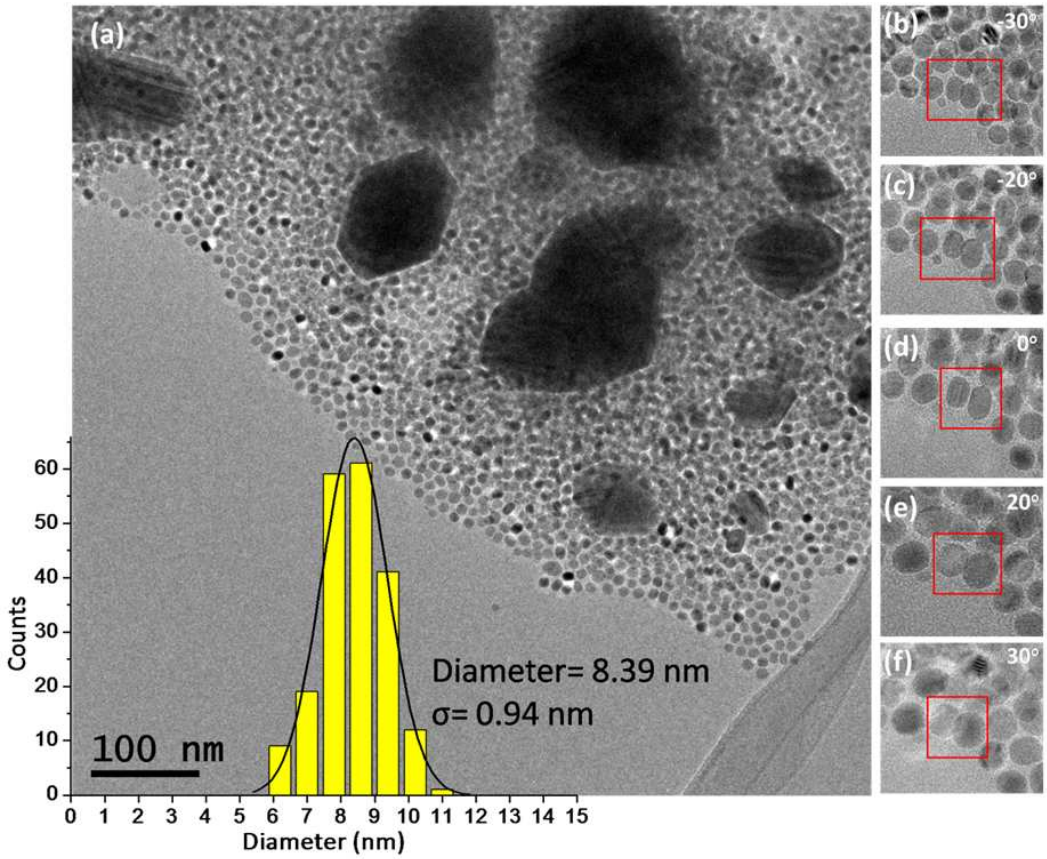

Figure 2-14. *TEM images of the particles obtained in Sample 2-7 together with their size histogram. The red quares represent the same two particles at different tilting angles between -30º (b) and +30º (f).*

HRTEM studies of both kinds of objects (anisotropic objects with twin planes and spheres) show that both have hcp structure. As we have seen before in the case of the nanodisks synthesized in Sample 2-1, the presence of the defects produces a splitting of the reflections present in the FFT. Furthermore, another parallelism between both samples arises from their crystallographic structure, since both present their c axes perpendicular to the direction of anisotropic growth **(Figure 2-15)**.

We attempt to explain the presence of two different populations as a different growth process dependent on the morphology of the original seed: if the seed presents morphological defects like twin planes, the 2D growth will be favored over the isotropic one.[1] On the other hand, in the absence of defects the isotropic growth governs the reaction.

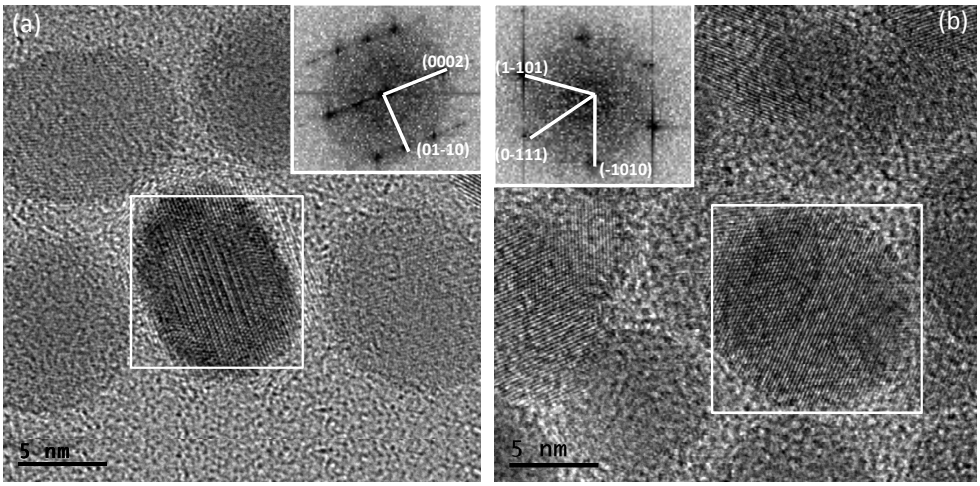

Figure 2-15. *HRTEM images of the anisotropic objects (a) and spheres (b) obtained in Sample 2-7.*

Actually when the same reaction is performed in the absence of HDA (Sample 2-7bis) the control over the morphology of the product is lost and only big aggregates composed by irregular particles are obtained **(Figure 2-16)**, evidencing the importance of the amine in the stabilization of the NPs obtained in Sample 2-7.

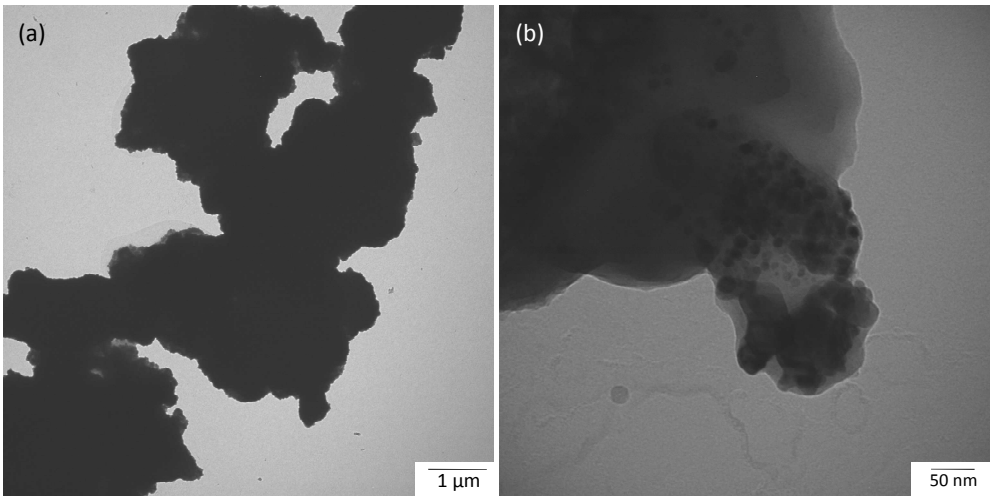

Figure 2-16. *TEM images of Sample 2-7bis with different magnification. In (b) we can see that the aggregates are composed by irregular NPs.*

2.5.4.4 Rhodamine B base

As discussed above, proton transfer between RhB and HDA in apolar solvents, evidenced by the formation of the $[(CoCl_4)(HDAH)_2]$ complex, can generate the closed form of RhB: RhB base. This molecule presents 2 amine functions which could interact with the Co surface in

addition to the aromatic moiety. A reaction was thus carried out decomposing the Co precursor in the presence of RhB base (Sample 2-8), all conditions of solvent, concentration, H_2 pressure and temperature remaining unchanged (no HDA was added). In this case, large agglomerates of Co NPs with a large size distribution (size of the particles ranging between 12 and 50 nm) were observed **(Figure 2-17)**.

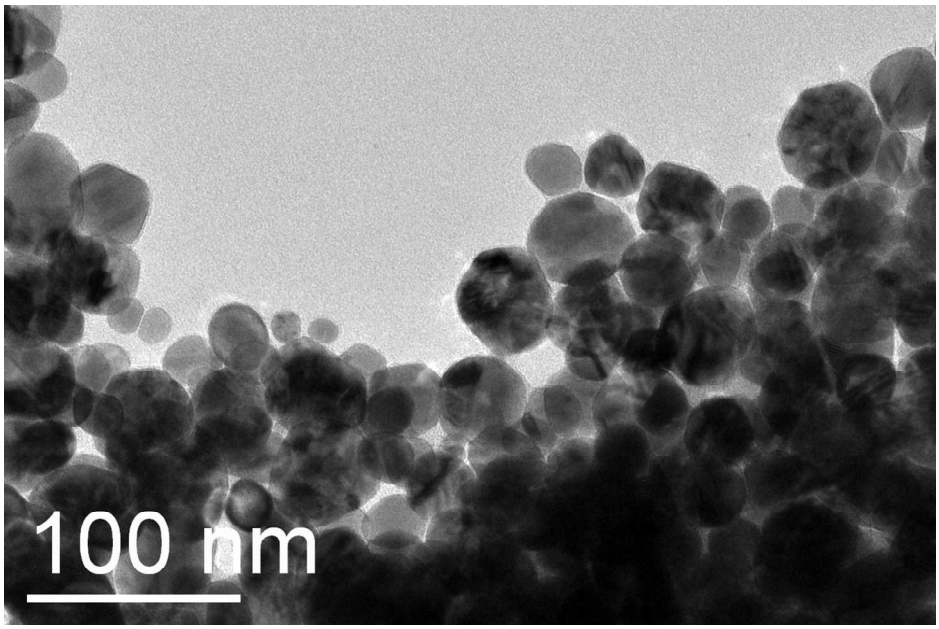

Figure 2-17. *Representative TEM image of Sample 2-8.*

2.5.4.5 Rhodamine 6G

Resembling RhB, Rhodamine 6G belongs to the same family of fluorophores **(Figure 2-11)**. Within all the molecules used as alternatives to RhB, Rhodamine 6G is structurally the closest one. The main difference in this case is the presence of the ester function instead of the free carboxylic acid. Like in Sample 2-1, 2-6 (biphenyl-2-carboxylic acid) and 2-7 (Pyronin Y) a black solid is recovered and characterized by transmission electron microscopy (Sample 2-9). Disk-shaped Co NPs are again observed but their morphology is different from that of the particles obtained when RhB is used as ligand **(Figure 2-18)**. The length of these disk-shaped NPs lies between 10 and 15 nm, while they seem to be thinner than those obtained previously. Unfortunately, their agglomerated character has made impossible the realization of a size histogram. Other parallelism between the two samples is the fact that both present stacking faults when they lay perpendicular to the substrate (see Structural Characterization) suggesting a

similar mechanism of formation. Besides this, the arrangement of the particles forming chains is lost while the control of the morphology of the particles is reduced. Irregular NPs with sizes between 100 and 500 nm are observed all over the TEM grid (dark areas pointed by green arrows in **Figure 2-18**), together with some bigger agglomerates with sizes above the micrometer. Still, the strong similarities between samples 2-1 and 2-9 suggest that the carboxylic acid moiety does not play a major role in shape control.

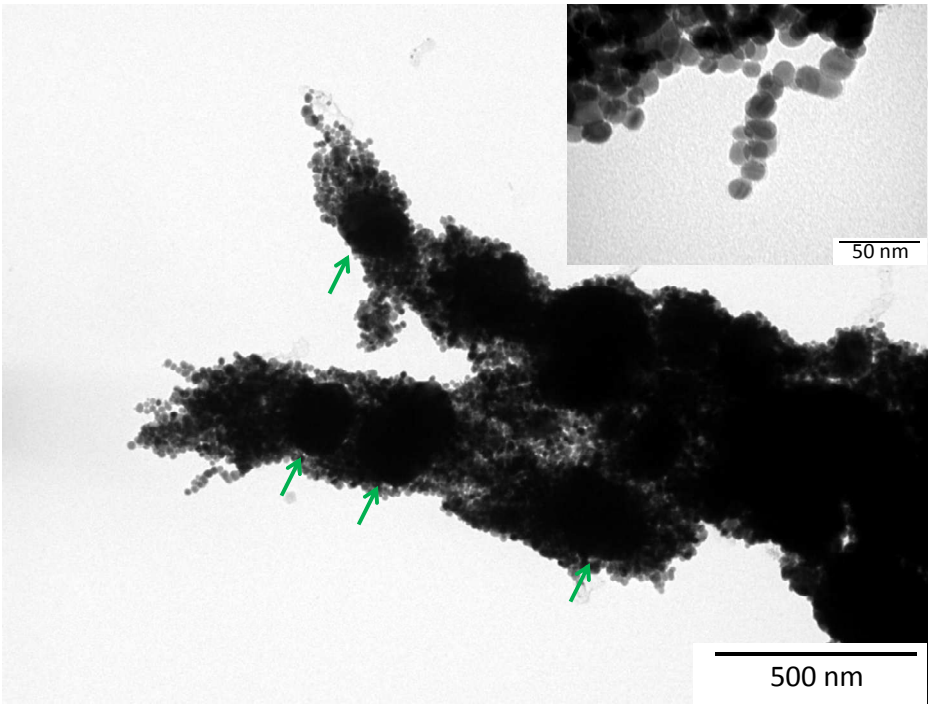

Figure 2-18. *TEM images of Sample 2-9. The green arrows indicate the presence of submicrometer particles. In the inset we can observe the presence of disk-shaped NPs.*

2.5.5 Discussion

Table 2-1 summarizes the main results obtained from the control experiments. They lead to the conclusion that:

a) The complexes still present at the end of the synthesis do not act as Co reservoir, and do not participate in the anisotropic growth of the Co NPs. Nevertheless, the formation of $Co(Cl)_4(HDAH)_2$ evidences the cyclization of an important amount of RhB molecules and thus only a small quantity of regular RhB would be able to interact with the Co

surface. Actually, microanalysis shows that only a very small amount of organic molecules are present at the surface of the nanodisks.

b) The carboxylic acid function of RhB plays a limited role on the formation of cobalt nanodisks since disk shaped NPs can be also obtained when using Rhodamine 6G or Pyronin Y as ligands.

c) The formation of Co nanorods is not only restricted to the use of aliphatic carboxylic acids. In fact, aromatic ones with a high steric hindrance like biphenyl-2-carboxylic acid (used in Sample 2-6) are able to direct the growth of the NP in one preferential direction, probably via an oriented attachment process.

Finally, if the mechanism of the growth of the nanodisks is still unclear, we have made progress in the understanding of the key parameters. A cooperative effect of the various anchoring sites of the dye, which would favor its adsorption on extended surfaces of the Co nanocrystals, may be a first reason. Calculations to better understand the interaction between this molecule and the surface would be interesting to carry out. Presently, the results obtained from the control experiments and structural studies suggest that due to its bulkiness RhB does not interact with the forming NPs until they reach a large enough size. The first stages of the reaction would thus be under kinetic control, favoring the formation of NPs with stacking faults which may be at the origin of the anisotropic growth. Furthermore, a comparison of the surface energy of the different crystallographic facets of Co shows that the {10-10} facets have a higher energy than the {0001} ones,[14] preferential growth of the latter is thus expected if ligands do not coordinate strongly on the surface. In comparison, it is supposed that Co nanorods are stabilized when carboxylic acids strongly coordinate at the {10-10} facets, thus lowering their surface energy. Due to this preferential attachment, the {0001} facets of these particles show a lower density of ligands, statement supported by the fast oxidation of these facets when the particles are exposed to air if compared with the rest of the crystal **(Figure 2-19a)**. In opposition to this behavior, HRTEM images of partially oxidized Co nanodisks show that their oxidation starts in the facets perpendicular to the [0001] direction **(Figure 2-19b-d)**.

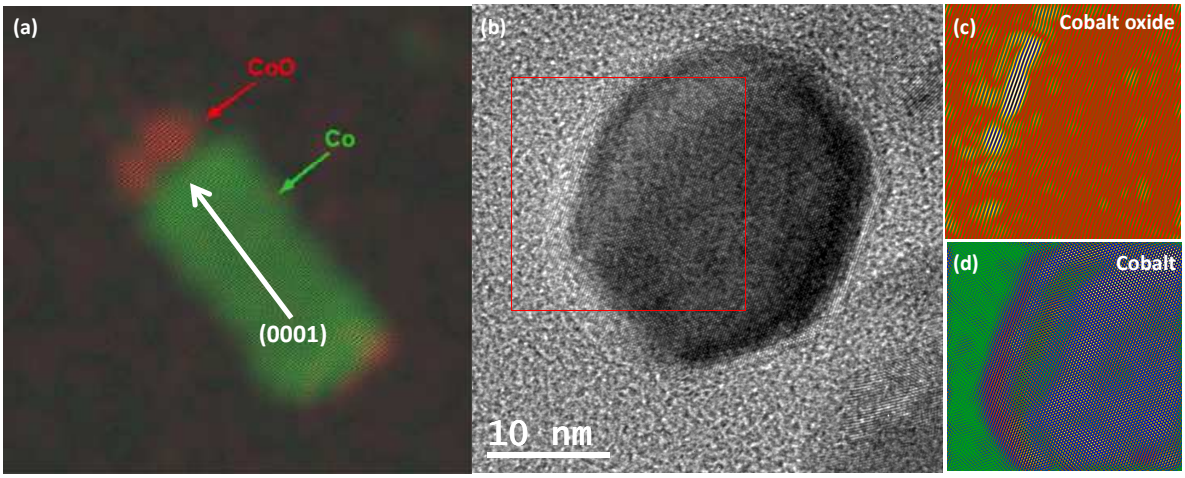

Figure 2-19. *(a) HRTEM image of a partially oxidized Co nanorod.[11] The green coloration corresponds to metallic Co while the red one is CoO. (b) HRTEM image for a Co nanodisk. The red square represents the area used to calculate the FFT for which the mask was applied in order to obtain the reconstructed images with the two contributions for Co oxide (c) and metallic Co (d).*

Another parameter that can help us to understand the anisotropic growth of the disks is the role played by HDA. As we have seen for Sample 2-3 this molecule is of capital importance. Actually, we believe that HDA is preferentially attached at the {0001} surface, as previously postulated by Puntes et al. to explain the formation of Co NPs with similar shape.[2] Such interaction leads to further minimization of the surface energy of this facet, accelerating its growth at the expenses of the others and thus, favoring the formation of the disks.

Table 2-1. *Comparison of the different morphologies of NPs obtained in the presence of control ligands together with HDA. (*Sample 2-8 was done without the presence of the amine)*

Control Ligand	*Single or bimodal population*	*Monodispersity*	*Anisotropic growth*	*Disk-shaped NPs*
Rhodamine B (S. 2-1)	Single	Good	Yes	Yes
Benzoic acid (S. 2-4)	Single	Good	No	No
Biphenyl-4-carboxylic acid (S. 2-5)	Single	Good	No	No
Biphenyl-2-carboxylic acid (S. 2-6)	Bimodal	Good	Yes	No
Pyronin Y (S. 2-7)	Single	Good	Yes	Yes
RhB base (S. 2-8)*	Single	Bad	No	No
Rhodamine 6G (S. 2-9)	Bimodal	Bad	Yes	Yes

2.6 Magnetic characterization

2.6.1 SQuID measurements

The magnetic properties of the Co nanodisks obtained with RhB and HDA as ligands (Sample 2-1) have been investigated in a Superconducting Quantum Interference Device (SQuID).[ii] For the preparation of the sample, a certain amount of product in powder form (normally between 15 and 20 mg) was introduced into a gelatin capsule. Moreover, silicon grease was used to avoid the mechanical movement of the particles during the measurements. All the preparations have been done inside an Ar-filled glovebox to avoid the contact of the sample with ambient conditions.

Two magnetization cycles have been recorded for Sample 2-1 between -5T and 5T at 2 and 300 K. As we can see in **Figure 2-20**, the magnetization cycles at both temperatures present hysteretic behavior. Actually, when the blocking temperature was calculated using **(1.15)**,[iii] a T_B of 2075 K was obtained. Even though this value is well above room temperature, it is still very low if compared with the temperature expected for objects of similar size but with a more anisotropic shape like, for example, nanorods or nanowires.[7] The same comparison holds for the important difference in coercive field of random assemblies of these objects (186 mT for the disks and 500-800 mT for the rods),[15] being both effects (reduced T_B and reduced H_C) a consequence of the smaller K_{eff} of the disk-shaped NPs.

[ii] For experimental details about the operation of this instrument the reader is referred to the Experimental Section.
[iii] This T_B has been calculated using the measuring time of the SQuID magnetometer.

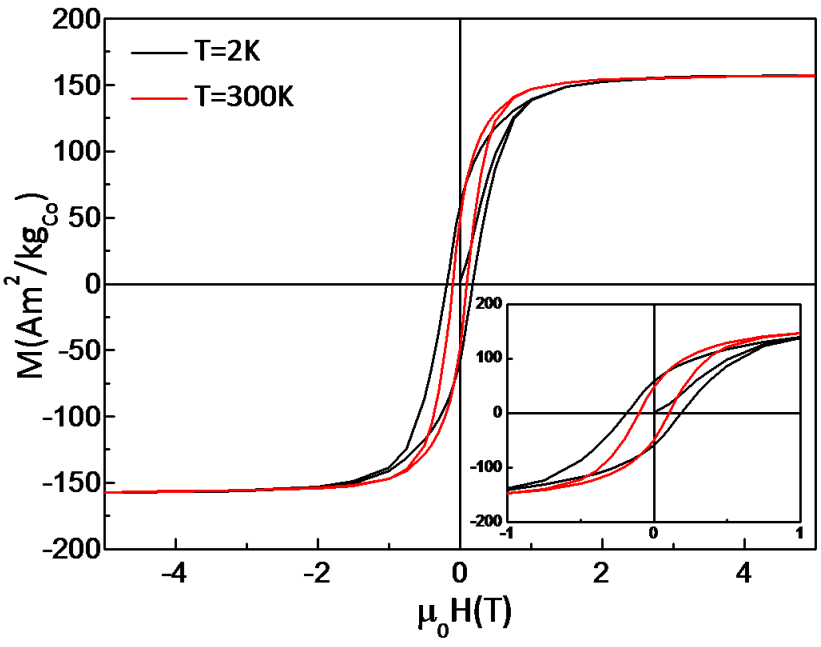

Figure 2-20. *Magnetization curves of Sample 2-1 at 2 and 300 K (black and red curves respectively), the inset shows an enlargement of the curve between ±1 T.*

Two factors reveal the high purity of the NPs surfaces:

a. Absence of exchange bias (as observed in **Figure 2-21a**, where ZFC/FC magnetization cycles measured at 2 K and between ±5 T are represented).
b. The magnetization values of the as-synthesized particles **(Table 2-2)**, very close to the bulk value (163 $A{\cdot}m^2kg^{-1}$).[iv]

Both factors confirm the absence of oxidation during the preparation of the sample.

The magnetic properties of the Co nanodisks obtained with RhB have been compared with those of the agglomerated disks obtained in the presence of Rhodamine 6G and with the spherical particles synthesized with benzoic acid **(Figure 2-21b)**. For such a comparison, the hysteresis loops have been recorded at 2 K, well below the blocking temperature of all the samples. The highest coercive field (186 mT) is that of Sample 2-1. No direct conclusion on the anisotropy of individual NPs can be made as strong dipolar interactions participate in each sample to the effective anisotropy.

[iv] The magnetization values reported here have been calculated taking into account the total Co content in the sample after determination by inductively coupled plasma mass spectrometry (ICP-MS).

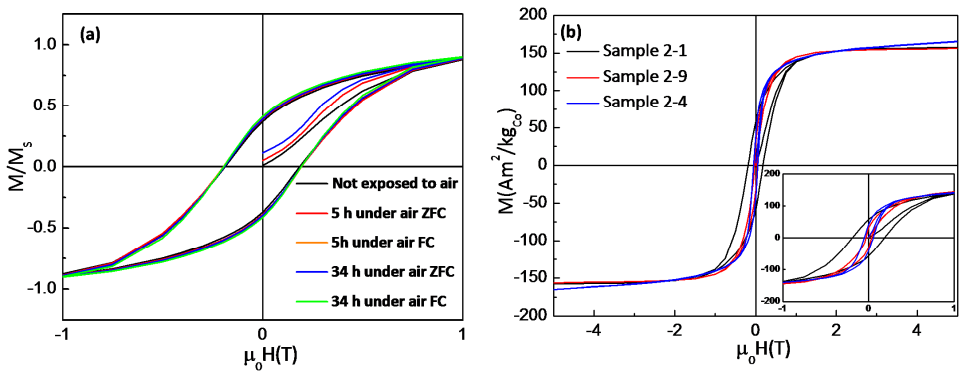

Figure 2-21. *(a) Magnetization curves recorded for Sample 2-1 cooling with (FC) and without (ZFC) an applied field after different times of exposition to air. (b) A comparison of the curves obtained for samples 2-1, 2-4 and 2-9 at 2 K. The inset represents the same curves restricted to ±1 T.*

In opposition to Samples 2-1 and 2-9 which present well-saturated magnetization curves with similar values of M_S, Sample 2-4 is not saturated at 2 K even under a magnetic field of 5 T. This phenomenon could arise as a consequence of a disordered spin structure at the surface of the NPs. Furthermore, it presents a saturation magnetization slightly higher than the bulk value **(Table 2-2)**. This could also mean that residual traces of a Co complex are present in the final material.

Table 2-2. *Values for the saturation magnetization, the coercive field and the ratio between remanent and saturation magnetizations for Samples 2-1, 2-4 and 2-9.* Sample 2-4 is not saturated at 5 T.*

Sample	*T (K)*	M_S (Am^2/kg_{Co})	$\mu_0 H_C$ (mT)	M_R (Am^2/kg_{Co})	M_R/M_S (%)
Sample 2-1	2	157.3	186	58.3	37
Sample 2-1	300	156.8	100	48.5	30.9
Sample 2-4	2	165.4*	52.9	41.8	25.2
Sample 2-9	2	156.5	32.8	32.2	20.6

2.6.2 Magnetic holography

Given the size of the objects in Sample 2-1, a intriguing question was whereas they were still single domain, and if the c axis still remained the easy axis of magnetization. Indeed, depending on the geometry of the disks (diameter over thickness) the magnetization can either be in- or out- of plane or even present a vortex-like behavior with a singularity in the center of the disk, pointing perpendicularly.[16] Recently, Co nanowires with 7 nm in diameter and up to several

micrometers in length demonstrated to present single magnetic domain by off-axis electron holography.[17] This technique allows measuring the remanent state of ferromagnetic NPs at room temperature, giving a direct imaging of the in-plane magnetic induction fields from the object under study.

Here, despite our best efforts it was not possible to find isolated Co nanodisks on the TEM grids to record a hologram of a single isolated one. Micromagnetic calculations have thus been carried out to answer this question (see below). Still, the formation of chains of the nanodisks synthesized in Sample 2-1 is an interesting finding that has been investigated. As shown in **Figure 2-22a**, the columns of Co nanodisks present a magnetic induction parallel to the direction of the column, and thus, parallel to the [0001] direction of the particles. Therefore, when they are stacked together forming long columns, strong dipolar interactions between adjacent Co disks make them behave cooperatively but not like a single particle, as demonstrated by micromagnetic simulations. In **Figure 2-22b** we can see how two columns of disks located parallel to each other, display a magnetic flux closure disposition. This behavior is similar to that observed in four Fe nanocubes arranged into a square.[18]

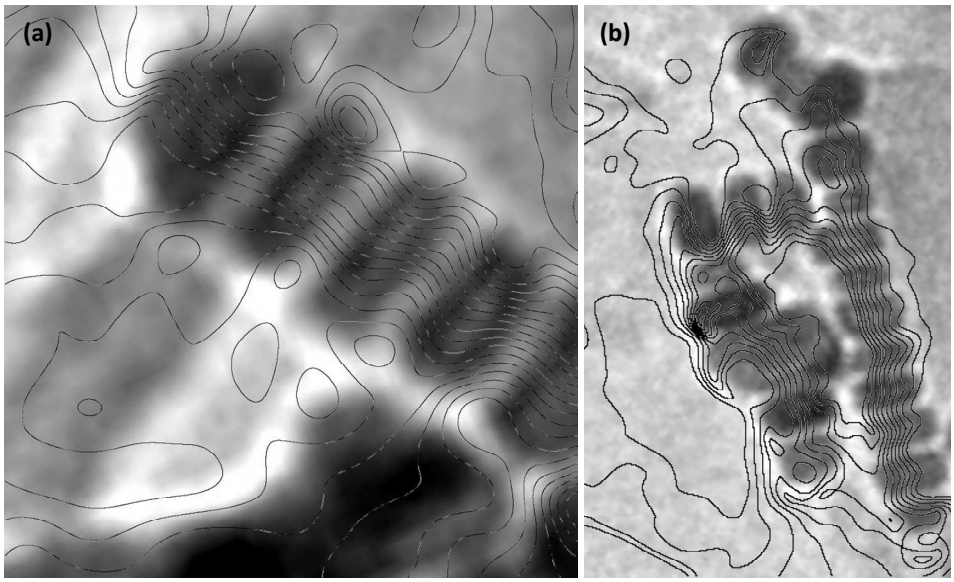

Figure 2-22. *Magnetic holography images of the cobalt nanodisks obtained in Sample 2-1, where the black curves represent the stray field distribution.*

2.6.3 Micromagnetic simulations

The magnetic behavior of the Co nanodisks has been simulated using OOMMF (Object Oriented MicroMagnetic Framework), a free software developed for the simulation of micromagnetic structures. In our case the interest of using OOMMF resides in the possibility to simulate the magnetic behavior of a single nanodisk and a chain of them, comparing the result with the magnetization measurements. Several parameters like shape, magnetization, exchange constant and magnetocrystalline anisotropy of the specimen have to be fixed in order to run the simulation. Actually, the dimensions of the NPs have been obtained from TEM images (21 nm of diameter and 12 nm of thickness) while the rest of the parameters correspond to the bulk values (M= $1500 \cdot 10^3$ A/m, $K_{magnetocrystalline} = 5 \cdot 10^5$ J/m^3 and A= $30 \cdot 10^{-12}$ J/m).[v] The simulations are calculated without taking thermal fluctuations into account (T= 0 K).

We have simulated the magnetic behavior of two different specimens: one disk and a chain of them (reproducing the arrangement observed experimentally).[vi] For each system its magnetic behavior was simulated with an applied external magnetic field (B_{ext}) in two different

[v] All the parameters included in the micromagnetic simulations together with a simple sketch of the nanodisks can be found in the Experimental Section.
[vi] Due to computer and time limitations, the chain of Co disks has been limited to 6 NPs.

directions: one parallel to the c axis of the particle (out of plane) and one perpendicular (in plane).

In the first simulation (single particle case) we first observe that the stable magnetic configuration (in zero field) is that of a single domain NP (without domain wall formation) and with the magnetization pointing perpendicular to the plane of the disk. We observe that if we apply the magnetic field out of plane (corresponding to the uniaxial magnetocrystalline anisotropy axis of the disk) we obtain a square loop with a coercive field of 747 mT **(Figure 2-23a)**, while if the magnetic field is applied in plane (perpendicular to the magnetocrystalline uniaxial anisotropy axis) a loop without coercivity but high anisotropy field is obtained as a consequence of the different paths followed by the magnetization of the NP depending if the magnetic field increases or decreases in magnitude **(Figure 2-23b)**. This phenomenon is a direct effect of the magnetocrystalline anisotropy of the system and can be easily explained following the simple scheme highlighted by characters and arrows in **Figure 2-23b**: We start with a high B_{ext} at which the magnetic moments of the sample are completely aligned along the field (i). Decreasing the magnitude of the field we arrive at one point (ii) at which B_{ext} is not strong enough to keep the magnetic moments perpendicular to the magnetocrystalline anisotropy axis and thus, they suddenly rearrange out of plane almost parallel to the magnetocrystalline anisotropy axis (iii). Nevertheless, the magnetic field has to be completely removed in order to find a 0 degrees tilt between magnetization and c axis. Then, when B_{ext} is increased in the other direction, a gradual variation of the magnetization is found (iv) instead of the sharp increase previously observed. Here the magnetocrystalline anisotropy acts in opposition to the increase of B_{ext}, trying to keep the magnetization out of plane.

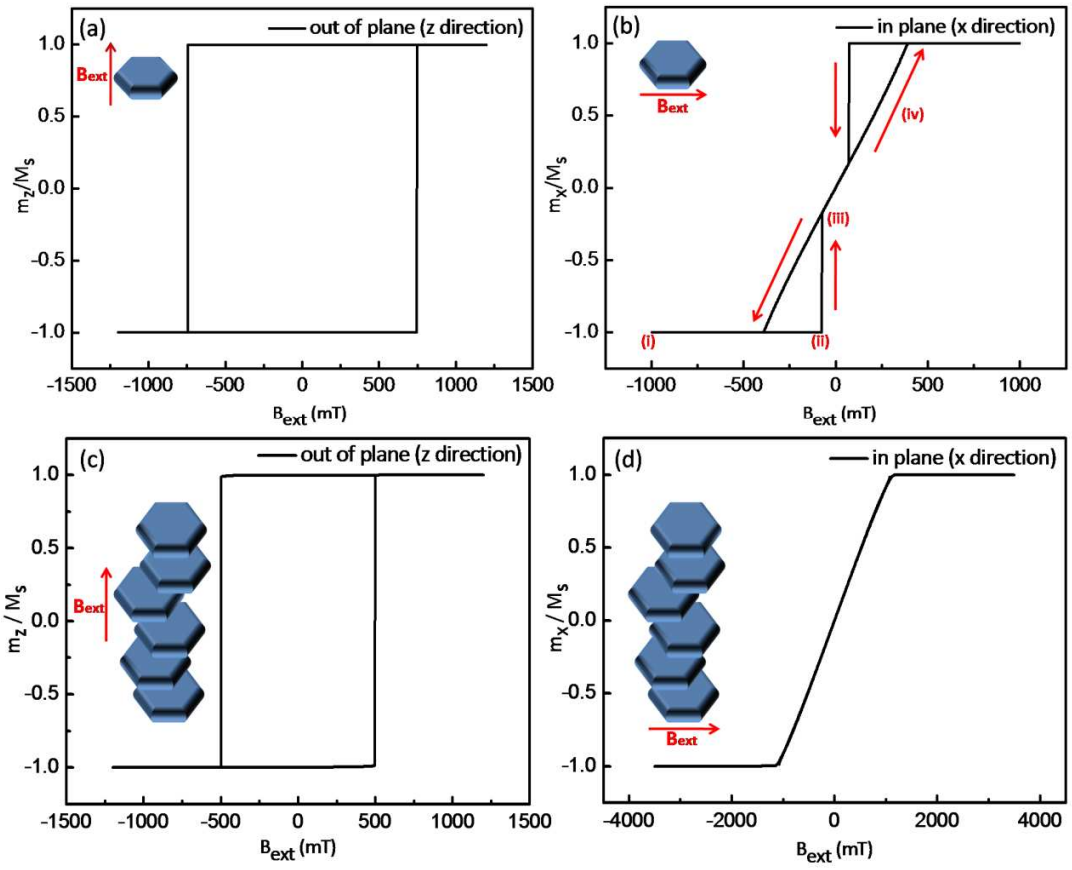

Figure 2-23. *Simulated magnetic loops for one disk (a,b) and a chain of them (c,d) under a magnetic field oriented in different directions.*

We performed similar simulations in one chain of 6 particles, each of them with the same morphology as that presented before. In order to reproduce the disposition of the NPs found on the TEM grids, we introduced small displacements in the coordinates of one nanodisk with respect to its neighbors instead of a perfect columnar alignment. On the other hand, a constant spacer of 1 nm was assumed between particles. Similarly to what was obtained for a single Co disk, a square-like loop with a coercive field of 500 mT is obtained when the magnetic field is applied parallel to the c axis of the NPs **(Figure 2-23c)**. Nevertheless, when B_{ext} was applied in plane (perpendicular to the axis of the chain) we observe a magnetization loop that does not present coercivity **(Figure 2-23d)**. In this case we can clearly see that the chain of disks do not behave like a single NP since the magnetization reversal of the simulated disks varies depending in their position within the chain: starting from a saturated system with all the magnetic moments

aligned in plane **(Figure 2-24a)**, the field is reduced and the first NPs that rearrange their magnetic moments out of plane are those situated in the middle of the chain **(Figure 24b)**, most probably because of the stronger interactions produced by the neighbor particles. On the other hand, when the field increases again the first particles that reorient their magnetic moments in plane are those situated at the extremities **(Figure 2-24d)**. Following the same reasoning, those two particles are more "free" to interact with the external magnetic field than those at the middle of the chain and thus, rearrange their magnetic moments more easily.

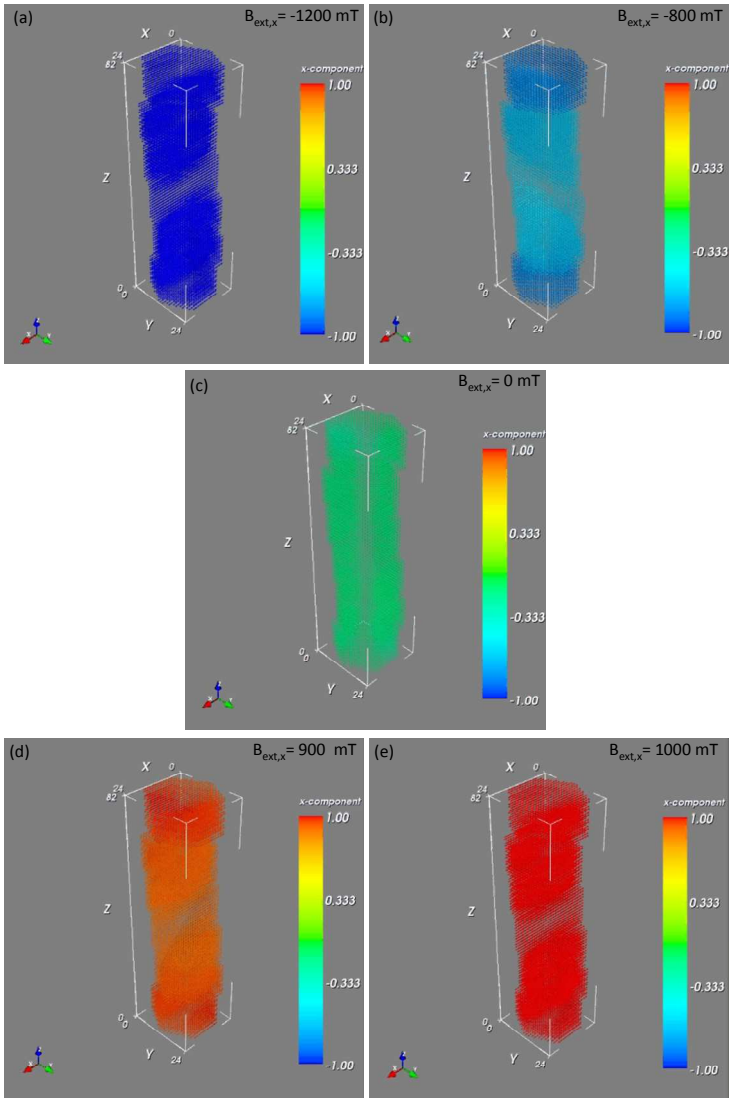

Figure 2-24. *Schematic view of the magnetization reversal of the chain of NPs at different field intensities when an external magnetic field is applied in the x direction (in plane).*

2.6.4 Discussion

Sample 2-1 presents clean surfaces with no trace of oxidation and the effect of the ligands over the magnetic properties of the NPs is negligible, since the former present a saturation magnetization comparable to that of bulk Co. Theoretical calculations show that these objects are single domain NPs with an easy axis perpendicular to the plane of the disk and a maximum coercive field of 746 mT for magnetization reversal. Previous micromagnetic simulations calculated for circular Co dots show that the spontaneous magnetization of disk-shaped Co NPs can have three different configurations: in plane, out of plane and vortex, depending on the aspect ratio of the material and thus, on its demagnetizing energy.[16] *E.g.* for a NP with the dimensions and aspect ratio of those presented here, out of plane magnetization is expected, in total agreement with our calculations. These objects are thus good candidates for magnetic data recording. Taking into account their size and the presence of ligands at their surface, an homogeneous 2D assembly of these objects is expected to hold magnetic densities of 0.7 Tb/in^2.

However, the images obtained in TEM show that the nanodisks tend to stack together forming long chains with lengths of several hundreds of nanometers, being therefore difficult to obtain a 2D flat arrangement of these objects.

3 Conclusion

The decomposition of $Co(\eta^3\text{-}C_8H_{13})(\eta^4\text{-}C_8H_{12})$ at 150 ^oC with dihydrogen as reducing agent and using an equimolar mixture of RhB and HDA as stabilizing agents, leads to the synthesis of monodisperse hcp Co nanodisks. The hcp structure of these particles present stacking faults in the plane perpendicular to the [0001] direction of the crystal. We believe that the defects observed by HRTEM, parallel to the direction of preferential growth of the particles play an important role on their morphological development as already reported by Lofton and Sigmund.[1]

Moreover, we think that the bulkiness of the RhB prevents its interaction with the NPs in the very first stages of the reaction, thus allowing the expansion of {0001} facets, contrarily to what is observed in the case of Co nanorods synthesis, where the strong coordination of

carboxylic acids lowers the energy of the {10-10} facets. This assumption could be also favored by the specific adsorption of HDA on the {0001} facets of the crystal, thus minimizing surface energy. It is noteworthy that these NPs are single domain and that their magnetic moments lay perpendicular to the direction of preferential growth, in opposition with previous results obtained for Co nanorods and nanowires.

The anisotropic growth of the particles is, at the same time, responsible for their blocked behavior at room temperature ($\mu_0 H_C$ = 746 mT from OOMMF calculations), feature of particular interest in nanotechnology research for the development of magnetic recording devices. Nevertheless, the lower anisotropic character of these nanodisks if compared with Co nanorods or nanowires (K_{eff} one order of magnitude smaller) has an important effect over their coercive field and blocking temperature, estimated to be around 2075 K, lower than that of Co nanorods. The next challenge now lies in their 2D organization on a substrate.

---

[1] C. Lofton, W. Sigmund, Adv. Funct. Mater., 15 (2005), 1197.
[2] V. F. Puntes, D. Zanchet, C. K. Erdonmez, A. P. Alivisatos, J. Am. Chem. Soc., 124 (2002), 12874.
[3] S. Chen, Z. Fan, D. L. Carroll, J. Phys. Chem. B, 106 (2002), 10777.
[4] Y. Wang, Y. Hu, Q. Zhang, J. Ge, Z. Lu, Y. Hou, Y. Yin, Inorg. Chem., 49 (2010), 6601.
[5] R. Si, Y.-W. Zhang, L.-P. You, C.-H. Yan, Angew. Chem. Int. Ed., 44 (2005), 3256.
[6] L. J. Zhao, L. F. Duan, Y. Q. Wang, Q. Jiang, J. Phys. Chem. C, 114 (2010), 10691.
[7] (a) F. Dumestre, B. Chaudret, C. Amiens, M.-C. Fromen, M.-J. Casanove, P. Renaud, P. Zurcher, Angew. Chem. Int. Ed., 2002, 41, 4286. (b) F. Dumestre, B. Chaudret, C. Amiens, M. Respaud, P. Fejes, P. Renaud, P. Zurcher, Angew. Chem. Int. Ed., 2003, 42, 5213. (c) F. Dumestre, B. Chaudret, C. Amiens, P. Renaud, P. Fejes, Science, 2004, 303, 821.
[8] M. Respaud, J. M. Broto, H. Rakoto, A. R. Fert, L. Thomas, B. Barbara, M. Verelst, E. Snoeck, P. Lecante, A. Mosset, J. Osuna, T. O. Ely, C. Amiens, B. Chaudret, Phys. Rev. B, 57 (1998), 2925.
[9] D. L. Thorn, W. C. Wultz, J. Phys. Chem., 93 (1989), 1234.
[10] J. Gao, C. M. Bender, C. J. Murphy, Langmuir, 19 (2003), 9065.
[11] F. Dumestre, PhD Thesis, Université de Toulouse, 2003.
[12] D. Ciuculescu, F. Dumestre, M. Comesaña-Hermo, B. Chaudret, M. Spasova, M. Farle, C. Amiens, Chem. Mater., 2009, 21, 3987.
[13] I. Favier, M. Gómez, G. Muller, M. R. Axet, S. Castillón, C. Claver, S. Jansat, B. Chaudret, K. Philippot, Adv. Synth. Catal., 349 (2007), 2459.
[14] Q. Jiang, H. M. Lu, Surf. Sci. Rep., 63 (2008), 427.
[15] (a) F. Wetz, K. Soulantica, M. Respaud, A. Falqui, B. Chaudret, Mater. Sci. Eng. C, 27 (2007), 1162. (b) K. Soulantica, F. Wetz, J. Maynadié, A. Falqui, R. P. Tan, T. Blon, B. Chaudret, Appl. Phys. Lett., 95, (2009), 152504.
[16] L. D. Buda, I. L. Prejbeanu, U. Ebels, K. Ounadjela, Comp. Mat. Sci., 24 (2002), 181.
[17] E. Snoeck, R. E. Dunin-Borkowski, F. Dumestre, P. Renaud, C. Amiens, B. Chaudret, P. Zurcher, Appl. Phys. Lett., 82 (2003), 88.
[18] E. Snoeck, C. Gatel, L. M. Lacroix, T. Blon, S. Lachaize, J. Carrey, M. Respaud, B. Chaudret, Nano Lett., 8 (2008), 4293.

Chapter III: Carbon coating of anisotropic magnetic objects

1 Introduction

1.1 Precedents in the literature

As presented in chapter I, a protocol for the direct synthesis of cobalt based anisotropic NPs (rods and wires) has been developed by Chaudret and coworkers. These objects display ferromagnetic behavior at room temperature and a magnetization close to that of bulk cobalt;[1] such properties make them interesting for their implementation in high density magnetic data storage devices or into permanent magnets. Nevertheless, their high air-reactivity remains a problem for those applications.

In the last years, the stabilization of magnetic NPs against oxidation has been the focus of many research efforts, and different approaches have being studied. For example, Yoshio Kobayashi and co-workers synthesized cobalt NPs surrounded with a SiO_2 shell,[2] transforming the as-synthesized amorphous cores into highly-crystalline metallic cobalt NPs upon annealing. Another approach is the encapsulation of air sensitive magnetic NPs within a noble metal shell that is not only responsible for the passivation against oxidation but may also make the system optically active in the UV-visible range due to the localized surface plasmon resonances (typical features of Au and Ag metals at the nanometric scale). The group of Prof. Cheon has successfully exploited this idea with the synthesis of NPs composed of a cobalt core and a shell of gold, palladium or platinum by a redox-transmetalation process in which metal ions from noble metal complexes are reduced at the surface of the cobalt NPs while neutral cobalt atoms are oxidized forming a new complex as by-product of the reaction[3] **(Figure 3-1)**. Following a completely different idea J. Zhang et al. reduced gold on the surface of chemically synthesized iron NPs with laser irradiation.[4] Such particles were stored under normal laboratory conditions for several months and no oxidation of the iron core was evidenced after that period of time. Even if those results document the interest for SiO_2 or noble metals, carbon is the most widely used protective layer due to the stability of carbon shells at high pressures and temperatures or under strong acidic and basic conditions. Two main strategies have been reported: the use of an extra source of carbon to encapsulate Co NPs and the annealing of Co NPs stabilized by an organic polymer matrix or surfactant. For example cobalt NPs with a 1 nm thick carbon shell have been synthesized from the gas phase using acetylene as carbon source.[5] Those particles

present the saturation magnetization of bulk cobalt and air stability up to 190 °C. Cobalt/graphite core/shell spherical NPs have been also successfully synthesized[6] by the arc-discharge method[i] along with anisotropic objects composed by metal-filled carbon nanotubes (CNTs). The most successful results were obtained by C. Guerret-Plécour and co-workers who synthesized CNTs filled with 15 different metals (including Fe, Co and Ni).[6a] The main drawback of this method is the low yield of the reaction and the presence of complex mixtures of products that require further purification. Another interesting approach was developed by S. Liu and co-workers[7] who placed magnesium powder and $Co(CO)_3NO$ inside a tightly-closed vessel subsequently submitted to 900 °C. In this case the cobalt complex is both source of Co atoms for the growth of the NPs and source of carbon for the growth of the shell. This experiment lead to CNTs filled with cobalt wires with 20 nm in diameter and a few micrometers in length.

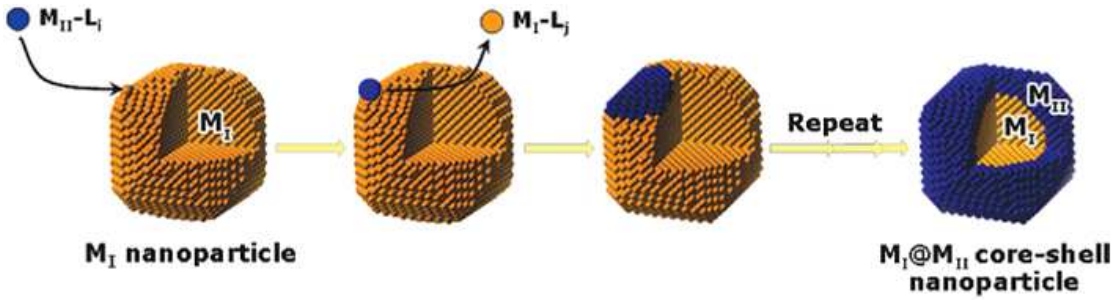

Figure 3-1. *Representation of the redox-transmetalation process reported in Ref. 3 in which noble metal ions (M_{II}) from the metal complexes (M_I-L_i) are decomposed at the surface of a cobalt (M_I) NP while neutral M_I atoms are oxidized, forming M_I-L_j complexes as by-product of the reaction.*

One-pot formation of Co NPs and carbon shell is also observed during the reduction of cobalt oxides with carbon monoxide or a mixture of CO + H_2. The deposition of the carbon shell appears as a consequence of a disproportionation reaction of CO into CO_2 and carbon, leading to the formation of carbon protected hcp Co nanocrystals stable till 700 °C.[8]

The use of block copolymers for the synthesis of cobalt NPs has been also reported in the literature: A.-H. Lu and co-workers[9] used chemically pre-synthesized partially oxidized spherical Co NPs with an excess of pluronic surfactant (a block copolymer based on ethylene oxide and propylene oxide) as templates for the formation of cobalt-graphite core/shell composites upon annealing. This composite remains stable even under strong acidic and basic conditions. With a

[i] This technique consists in the vaporization of two carbon electrodes driven by a potential energy under an inert gas flow at low pressures.

similar approach, air stability is achieved once the block copolymer is transformed into graphite after submitting the original particles to a thermal treatment at 700 °C for four hours under a continuous argon flow.[10] Those particles present a magnetization close to that of bulk cobalt and an improvement in crystallinity if compared with the as-synthesized ones, being both features a consequence of this high temperature thermal treatment.

Air-stable FeCo nanoalloys have been fabricated by Desvaux and coworkers due to the formation of a carbon shell after the annealing of poorly crystalline FeCo NPs.[11] In this case the authors found that the carbon source was interstitial material present in the original FeCo as a consequence of the decomposition of the $Fe(CO)_5$ precursor.[12] As the temperature increases during annealing the carbon diffuses out of the core of the particles while the crystallization takes place. Simultaneously, the organic ligands stabilizing the NPs contribute to the formation of the carbon matrix.

In the work presented here a similar approach (burning out the organic surfactants and using them as carbon source for the stabilization of cobalt nanowires and nanorods) was selected as the best solution to avoid the corrosion. Two important differences with respect to the previous system have to be mentioned:

1. Cobalt nanowires and nanorods are single crystals and have hexagonal close-packed structure (hcp). No interstitial carbon has been evidenced, contrary to the amorphous crystalline structure of the FeCo NPs.
2. The annealing of anisotropic objects could induce shape instabilities, therefore a complete study of their behavior during thermal treatment is mandatory.

1.2 Thermal instability of wires: Rayleigh-Plateau instability

Nanowires are also called quasi one-dimensional materials because of their huge aspect ratio (length-to-width ratio) and are expected to play a very important role in different technological applications as, for example, interconnections in electronic or optoelectronic devices.[13] It is also important to notice that a nanowire is a thermodynamically unstable shape because of its high surface to volume ratio and high interfacial tension. Studies on the thermal stability of uncoated nanowires made of copper and gold has been already reported.[14] In both cases the instability and subsequent decomposition of these wires into a chain of spherical particles was observed at a temperature much lower than the corresponding melting point of the

bulk material. These morphological instabilities have been explained by the Rayleigh-Plateau instability effect.

Joseph Plateau (1801-1883) was a Belgian physicist who studied the instability of cylindrical fluid jets as a consequence of an external perturbation whatever its origin (thermal, mechanical or electric). He understood that the instability of these fluid jets was driven by the liquid surface tension: when the free surface of a liquid cylinder undulates at a wavelength larger than the circumference of the cylinder the system collapses into a more stable conformation (a chain of spheres),[15] minimizing the surface tension, while the total volume remains unchanged.

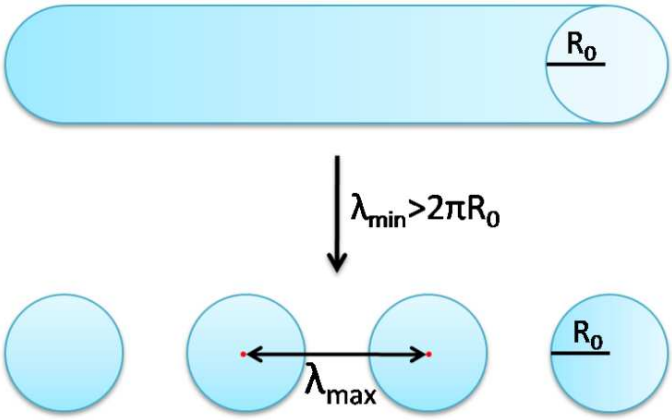

Figure 3-2. *Scheme representing the Rayleigh instability effect on a cylindrical wire of radius R_0 under an external perturbation.*

Some years later, Lord Rayleigh (1842-1919) revisited and extended the work of Plateau.[16] He established that the instability of cylindrical fluid jets relates to a well-defined wavelength, and thus explained the regularity in spacing of the drops that form upon thermal treatment of the jets.

In the year 1965 Nichols and Mullins extended this study to solid cylinders.[17] In their work they modeled the external perturbation as the sinusoidal function (r) reported in Equation 1:

$$r = R_0 + \delta \sin\left(\frac{2\pi}{\lambda} z\right) \quad \textbf{(3.1)}$$

where R_0 is the radius of the initial wire, δ and λ are the amplitude and wavelength of the perturbation and z is the coordinate along the axis of the cylinder. The main conclusion of their

study was that the initial morphology is not stable when the wavelength of the perturbation is larger than the cylinder's circumference ($\lambda_{min} = 2\pi R_0 \lambda$), similarly to fluid jets **(Figure 3-2)**.

We believe that this diffusion of atoms with a characteristic wavelength appears as a consequence of the thermal excitation of phonon[ii] modes, which present discrete states in nanostructures due to quantum effects. For this reason, only a determined number of phonon waves with characteristic frequencies are allowed to propagate through the crystal, being their sinusoidal nature responsible of the decomposition of the wire into a regular chain of spheres.

Another important conclusion obtained from the work by Nichols and Mullins is that the maximum growth of the perturbation matches with a specific wavelength (λ_{max}) that controls the final spacing between spheres. If the instability of such a cylinder appears as a consequence of the excited phonon modes and the subsequent diffusion of surface atoms, the value of the specific wavelength λ_{max} is derived as 8.89 R_0.

From a kinetics point of view, since the mobility of surface atoms is significantly lower for solids than for liquids, the kinetics governing the process modeled by Nichols and Mullins is reduced in comparison with that governing the Rayleigh-Plateau process, requiring thermal activation to be observed. When submitted to high temperatures, the particles suffer a melting transition due to the energy gain of their surface atoms.

The melting behavior of crystal structures (at the macroscopic or microscopic scale) is defined as a two-steps process:[18]

1. The atoms at the surface start to melt.
2. The perturbation gets propagated through the crystal into the core.

This effect appears as a consequence of the different environment experienced by the atoms since those at the surface have a lower symmetry (number of neighbors) than those at the core, leading to weaker bond strengths and therefore an easier melting.

Actually, the reason for the lower melting temperatures of metallic NPs compared with their correspondent bulk counterparts should be directly related with the proportion of surface atoms (the smaller the diameter of the wire, the higher the surface/core atoms ratio) since in this

[ii] Phonons represent the quantization of the modes of lattice vibrations in crystalline solids.

case surface melting processes are favored. A good experimental example of this idea is the study made by S. Karim and co-workers on gold nanowires[14b] with diameters between 87 and 132 nm which already present instabilities at 300 ^{o}C after an annealing time of 30 minutes, far below the melting point of the bulk metal (1064 ^{o}C).

It is inferred that the kinetics of the transformation from wires to droplets will be higher for smaller objects like those presented in this chapter.

2 Results

2.1 Synthesis and thermal properties of cobalt nanorods and nanowires

As described previously,[1] the decomposition of the organometallic complex Co(η^3-C_8H_{13})(η^4-C_8H_{12}) under 3 bars of H_2 and in the presence of 2 equivalents of oleic acid and 1 equivalent of oleylamine leads to the formation of cobalt nanowires with several microns in length and with a diameter of 7 nm. If instead of a 2/1 ratio for the acid/amine mixture one equivalent of each is used for the decomposition of the organometallic complex, it leads to the synthesis of cobalt nanorods with 4 nm in diameter and with a tunable length (between 40 and 120 nm) depending on the length of the aliphatic chain of the ligands. Both kinds of nano-objects (wires and rods) are single crystals and present the same hexagonal close-packed (hcp) structure **(Figure 3-3, right)**. For this study the length of the rods has been fixed at approximately 100 nm.

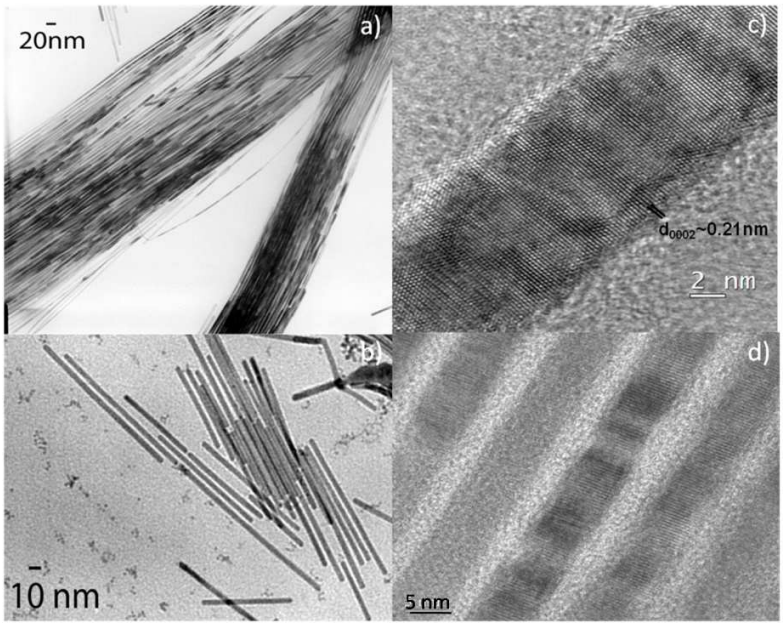

Figure 3-3. *Low (a-b) and high (c-d) resolution TEM images of cobalt nanowires (up) and nanorods (bottom).*

With respect to the model by Nichols and Mullins, the corresponding theoretical values for λ_{min} and λ_{max} of the as-synthesized cobalt nanorods and nanowires are specified in **Table 3-1**:

Table 3-1. *λ_{min} and λ_{max} theoretical values for cobalt nanowires and nanorods*

	Nanowire (radius ≈ 3.5 nm)	***Nanorod (radius ≈ 2 nm)***
λ_{min} ($2\pi R_0$)	21.99	12.57
λ_{max} ($8.89R_0$)	31.11	17.78

To perform the decomposition of the ligands present at the surface of those anisotropic objects an annealing temperature had to be chosen. With that purpose in mind thermogravimetric analysis of both rods and wires was performed under inert atmosphere (a constant He flow). In the case of the wires a sudden loss of mass was observed at 300 ^{o}C in a single step while in the case of the cobalt nanorods the loss was clearly achieved in two subsequent steps: the first one between 170 and 330 ^{o}C and the second between 550 and 600 ^{o}C **(Figure 3-4)**. As a compromise, the annealing temperature in the oven was settled at 350 ^{o}C with a plateau of 30 minutes before cooling down to room temperature for both rods and wires. Two different heating rates were selected: 5 and 10 ^{o}C/minute.

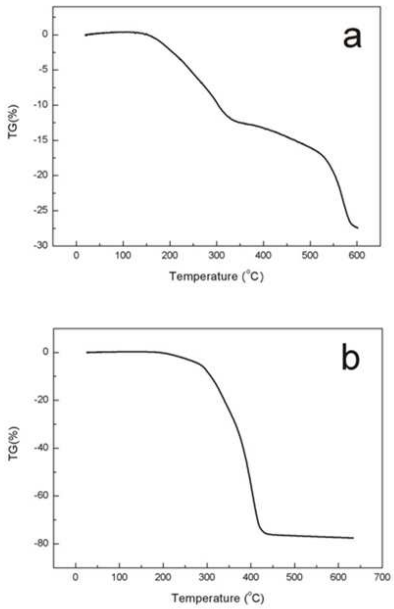

Figure 3-4. *TGA profiles of Co nanorods (a) and nanowires (b) recorded under a continuous He flow. The difference in the amount of material decomposed during the thermal treatment is due to the different excess of ligands present in each sample.*

2.2 In-situ annealing inside the TEM

The thermal annealing of cobalt nanowires was first studied in situ in a transmission electron microscope casting a drop of a solution of the nanowires (or nanorods) in toluene onto a nickel grid (this material allows the study at higher temperatures than those reached with copper grids). In this experiment the sample was heated in-situ in the microscope chamber under high vacuum conditions (approximately 10^{-6} mbar). In **Figure 3-5** we can observe already at 350 ^{o}C that the decomposition of the nanowires is not regular. Furthermore, the high resolution electron microscopy images do not show the formation of any carbon shell during the whole process and in fact, it seems that the metal simply vanishes from the support. This process takes place in a progressive manner starting with the formation of small pits in the surface of the particles that become bigger as the temperature increases till some point at which the defects are so big that each particle starts to decompose in several fragments of irregular shapes and lengths. We assume that if the nanowires are submitted to relatively high temperatures for enough time (always below 1495 ^{o}C, the melting temperature for bulk cobalt) all the metal will be sublimed from the surface of the grid. We attribute this phenomenon to the low pressure inside the

microscope chamber, because under such conditions desorption of the ligands and sublimation of cobalt atoms will occur.[19] Nevertheless, even if the carbon coating is not achieved under these conditions, it is interesting to remark that after their irregular fragmentation, the remaining particles are still monocrystalline, keeping their original hcp structure and orientation.

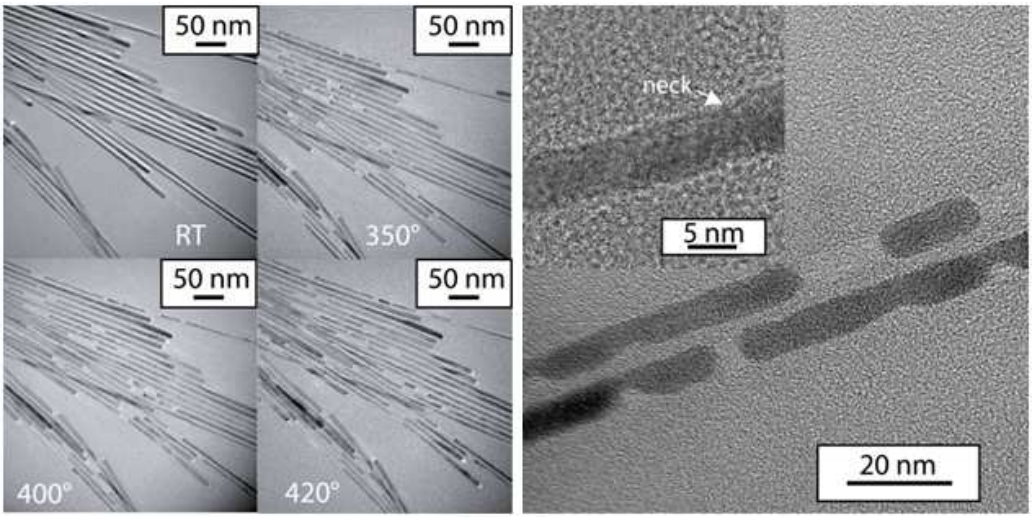

Figure 3-5. *In-situ thermal annealing of cobalt nanowires prepared from Co(η^3-C_8H_{13})(η^4-C_8H_{12}) (left) and HRTEM images in the region where they transform (right).*

As the melting point of nanostructured materials depends strongly on their size, different behaviors are expected upon annealing of cobalt nanorods from those obtained for the wires.

We annealed the rods following exactly the same procedure developed for the wires. In this case just after several minutes of electron illumination and even at room temperature the rods lost their monocrystalline structure, leading to the apparition of polycrystalline particles which in a further step underwent the evaporation process. Once again the decomposition was irregular showing that the evaporation most probably takes place where the contact with the carbon support is tighter, similarly to what was observed for the wires. We initially expected a higher stability (higher fragmentation temperature) for the rods due to their lower aspect ratio compared with the nanowires which present lengths up to several micrometers. However, low energy gain of the electron beam was sufficient to induce the fast decomposition of the rods **(Figure 3-6)**, even at temperatures lower than those recorded for the wires. As we decrease the diameter and length of the wires, the percentage of surface atoms is increased and therefore the melting and sublimation temperatures are lower for the cobalt nanorods than for the nanowires,

increasing the kinetics of the transformation and thus, decreasing the activation barrier for the fragmentation process. This suggests that despite the presence of surfactants, both wires and rods are metastable nano-objects.

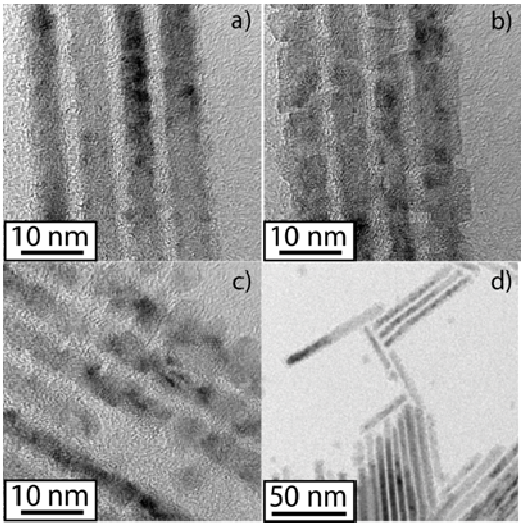

Figure 3-6. *Monocrystalline original nanorods (a); polycrystalline structure after several minutes (b-c) and general overview of the studied sample (d).*

2.3 Thermal annealing under argon atmosphere

2.3.1 Co nanowires

Annealing of the wires was performed in the powder form under static argon atmosphere in a conventional oven. In that case the selected heating rate was 10 ^{o}C/minute and the maximum temperature 350 ^{o}C with a plateau of 30 minutes. TEM analysis of the resulting sample showed that the powder is made of NPs embedded into an amorphous carbon shell **(Figure 3-7)**, demonstrating the thermal fragmentation of the initial Co nanowires.

Besides this instability, the high resolution electron microscopy (HRTEM) study of the sample showed that the Co NPs retain the original hcp structure **(Figure 3-7)**; it means that the fragmentation is not generated as a consequence of a phase transition process (the transition from hcp to fcc Co takes place at 417 ^{o}C for bulk material).

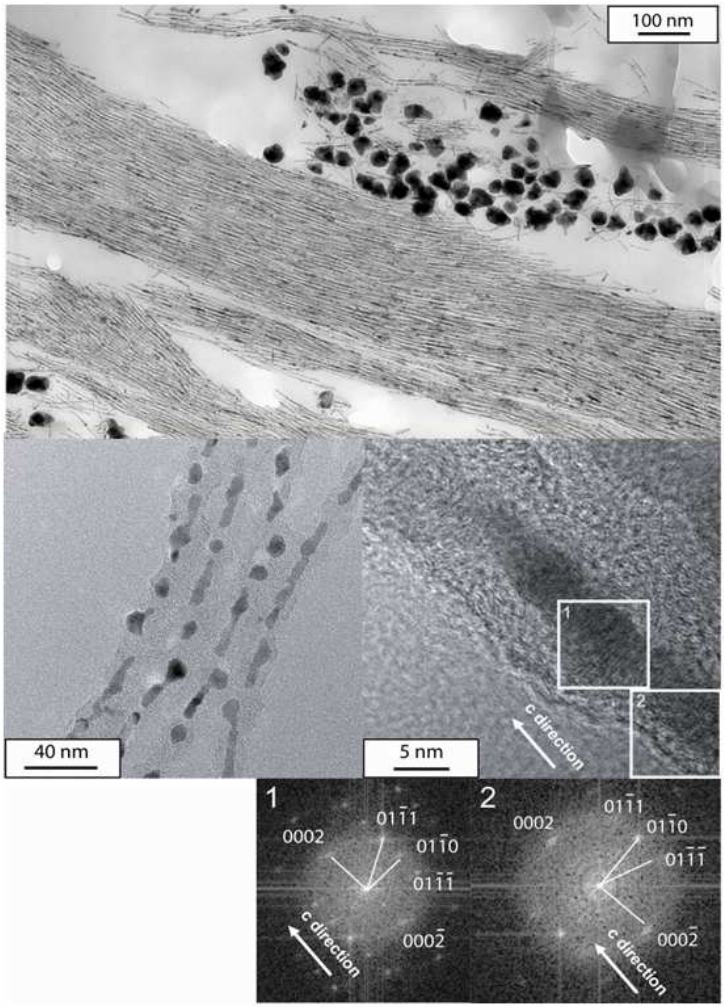

Figure 3-7. *TEM (top) and HRTEM (middle) images of annealed powder under Ar at 350 °C and FT from regions 1 and 2.*

Afterwards, Raman spectroscopy was used to characterize the nature of the carbon shell **(Figure 3-8)**. After annealing at 350 °C, the two characteristic peaks of amorphous carbon were visible: 1330 cm^{-1} for the D-band and 1697 cm^{-1} for the G-band. Nevertheless, the comparison of this spectrum with the sample before annealing showed that some undecomposed ligands are still present (peaks at 2848 and 2882 cm^{-1}), in agreement with the TGA analysis, in which the temperature for the total decomposition of the ligands is 400 °C.

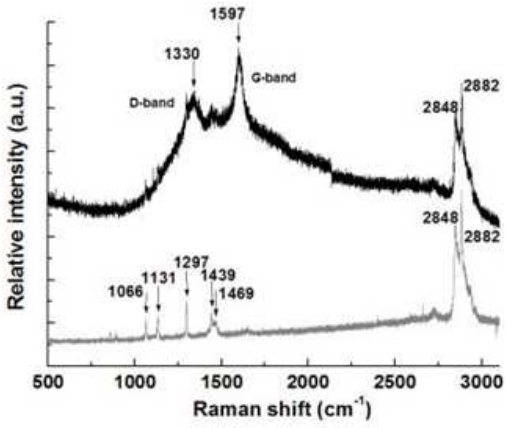

Figure 3-8. *Raman spectrum of Co nanowires before (grey line) and after (black line) annealing at 350 °C.*

If the same annealing procedure is performed at 500 °C (temperature at which all the ligands are decomposed) all Co nanowires dissociate into particles caged in tube-like structures **(Figure 3-9)**. Even taking into account the irregular size and shape of the NPs it is important to point out that the measured mean distance between consecutive particles within the carbon shell is 30 (± 7) nm, in agreement with the theoretical value from the model by Nichols and Mullins **(Table 3-1)**.

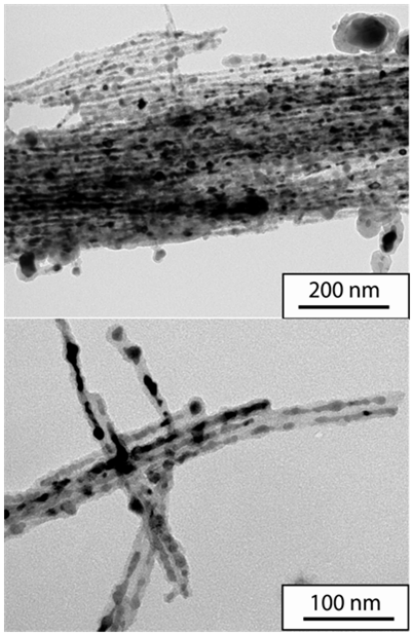

Figure 3-9. *Co nanowires annealed at 500 °C.*

Nevertheless, the loss in anisotropy and thus in coercivity due to the fragmentation of the wires remains a problem for their implementation in future devices: it was thus necessary to optimize the annealing process. As mentioned before, the propagation of the fluctuations from the surface to the core of the particles is a key parameter controlling their fragmentation since two processes are in competition: decomposition of the ligands and decomposition of the wires. As the first process starts at temperatures below 350 ^{o}C, we diminished the heating rate during annealing in order to favor carbon shell formation over fragmentation (in this case it was settled to 5 ^{o}C/min, keeping the other parameters constant). When the experiment was performed under these conditions the synthesis of unbroken cobalt nanowires within a continuous carbon shell was successfully achieved **(Figure 3-10)**. HRTEM studies were performed on those objects and the diffraction patterns showed that the initial hcp structure was maintained. Finally our primary goal (the formation of core/shell cobalt/carbon anisotropic objects) has been successfully achieved, opening a broad spectrum of possible applications for the near future.

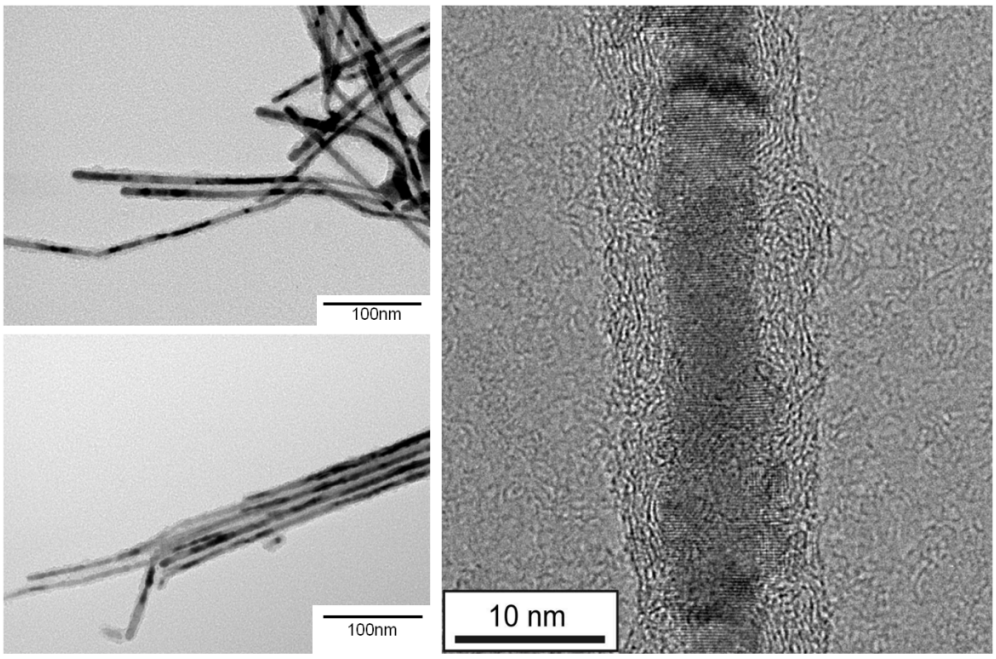

***Figure 3-10**. Low (left) and high (right) resolution images of carbon coated cobalt nanowires obtained after annealing at 350 °C (5 ^{o}C/min as temperature ramp).*

2.3.2 Cobalt nanorods

The rods were also annealed in the powder form under Ar atmosphere into a sealed quartz tube. In this case when the annealing was carried out at 350 ^{o}C with a plateau of 30

minutes, scanning electron microscopy (SEM) investigation showed rod-like objects even if they already present some defects in their surface **(Figure 3-11)**. Unfortunately, when the sample was studied in TEM the particles were found to be completely decomposed and embedded in an organic matrix which retained the shape of the initial rods.

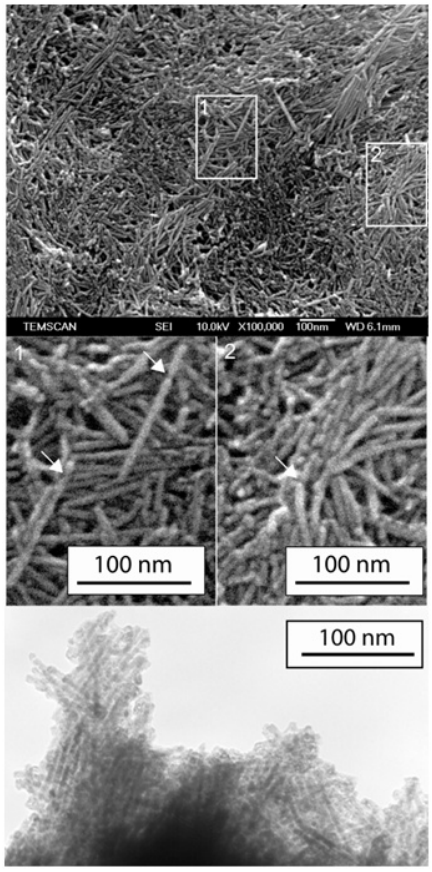

Figure 3-11. *(Top) SEM images of the powder annealed at 350 °C with closer view of the regions 1 and 2; (bottom) TEM image of the same sample.*

The annealing of Co nanorods under an inert argon atmosphere was also performed directly on a TEM grid in the oven under identical conditions than those previously described. In this case one drop from the solution of the rods was deposited on a carbon coated Ni grid that was subsequently submitted to the annealing conditions mentioned before. In this case the remaining nanorods were completely fragmented, similarly to what was observed when the rods were annealed in the powder form, but without formation of a carbon shell. Surprisingly, isolated irregular nanoparticles with a big polydispersity in size were present on the grid. These NPs were characterized by means of electron microscopy, more precisely with electron energy loss

spectroscopy (EELS), technique that allows us to determine the chemical composition of nanostructures. The spectrum shows that those particles consist in a Co/Ni alloy for which the exact structure was not successfully determined **(Figure 3-12)**.

The behavior of TEM grids made out of different transition metals like copper, nickel or gold has been already studied under in-situ heating experiments.[20] It was found that the vapor pressure of the metal and its interaction with the carbon foil were the two key points to take into account for the formation of NPs. In the case of nickel the formation of nickel carbide is favored at 275 ^{o}C. Afterwards this compound gets decomposed again in fcc-nickel and amorphous carbon at temperatures close to 325 ^{o}C.[21] Taking into account that our annealing process has a maximum temperature of 350 ^{o}C and a plateau at that temperature is maintained for 30 minutes, Ni_3C should not be expected to be the final structure after the whole heating process is finished. On the other hand, the high mobility of the surface Co atoms at the temperatures reached in our experiments makes them good candidates to interact with the nickel atoms desorbed from the metallic grid leading to the formation of Co/Ni nanostructures.

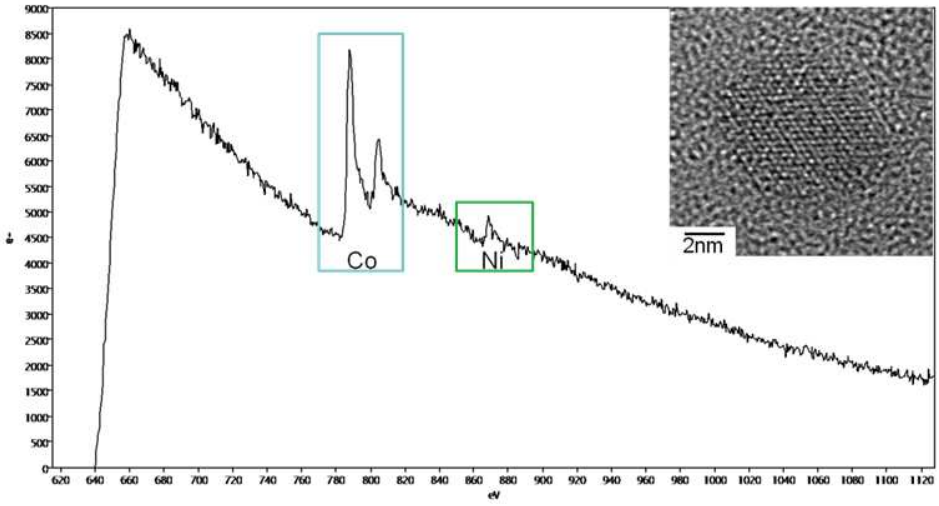

Figure 3-12. *EELS spectrum of the Co_xNi_y NPs. In the inset a HRTEM image of a typical NP.*

2.4 Magnetic characterization

The hysteresis cycle for the sample of Co nanowires before and after annealing at 350 ^{o}C is represented in **Figure 3-13**, presenting a saturation magnetization close to that of bulk Co, fact that rules out the formation of cobalt carbides during annealing, since in that case the saturation

magnetization would experience a drastic decrease in comparison with the magnetization of pure metallic Co. It is remarkable that the hysteresis curve before annealing has a particular shape: the coercive field is not regular and it gets narrower close to zero field (indicated by arrow (1) in **Figure 3-13**). This behavior is a consequence of the presence of spherical fcc Co particles as a by-product of the original reaction **(Figure 3-7, top)**. Indeed, these NPs have a lower magnetic anisotropy for two different reasons: reduced shape anisotropy (isotropic morphology) and reduced magnetocrystalline anisotropy since for fcc-Co its value is one order of magnitude lower than that of hcp-Co. In the case of the magnetization loop recorded after annealing, the lower coercivity is the expected consequence of the loss in shape anisotropy after the decomposition of the wires into chains of spheres. Besides that, some high coercive material is still present, evidencing the presence either of not decomposed wires after annealing at 350 ^{o}C or chains of interacting NPs.

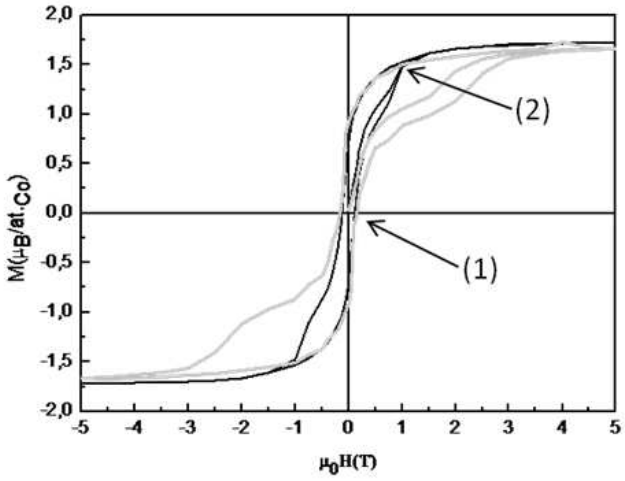

Figure 3-13. *Magnetization loops recorded at 2 K for Co nanowires before (grey line) and after annealing (black line). The arrows highlight the loss in coercivity due to the presence of big fcc Co particles (1) and the residual high coercivity of the annealed sample (2).*

Even if the carbon shell is amorphous, magnetic measurements after air exposure were performed to study its usefulness as passivating agent. SQuID measurements of the annealed sample were performed right after annealing and after one month of air exposure for comparison. No significant decrease in magnetization was observed demonstrating the air stability of these core-shell nanomaterials **(Figure 3-14)**. For comparison, a 12 % loss of magnetization is observed after 1 week of air exposure for a non-annealed sample.

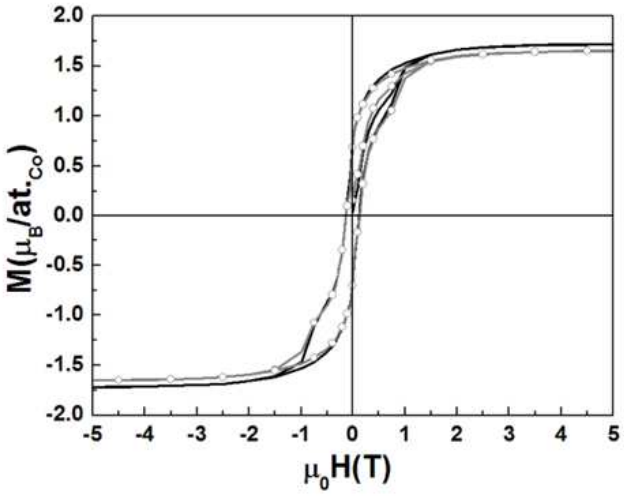

Figure 3-14. *Magnetization loops recorded at 2 K for Co nanowires after annealing at 350 °C (10 °C/min ramp): as annealed (black solid line) and after one month exposure to air (grey solid line).*

2.5 Discussion

The model reported by Nichols and Mullins[17] presented in the introduction has been used during the last 15 years to explain the thermal instability of metal nanostructures even at temperatures far below the melting points of their respective bulk metals. In 2004 M. E. Toimil-Molares and co-workers[14a] reported the decomposition of copper nanowires between 400 and 600 °C. In this case the authors observed the conservation of the volume and regularity in spacing between spheres after the annealing process, in total agreement with the model described by Nichols and Mullins; a fact that we have also found in our system. It is not surprising that the obtained value for λ_{max} fits better with the high temperature annealing rather than with the one obtained at 350 °C (for which λ_{max} is 21 (± 4) nm) because at 500 °C the fragmentation is complete and therefore the regularity in spacing is improved. Such result is a rough approximation since the particles observed are not perfectly spherical, but at least it supports the fact that Plateau-Rayleigh instability is responsible of the fragmentation observed in the nanowires. We believe that these irregularities in shape and spacing of the NPs are due to the simultaneous formation of the carbon shell during the heating process.

Taking into account the large aspect ratio and small diameter (7 nm) of the Co nanowires presented here and comparing the behavior with results reported in the literature, instability could be expected even at room temperature. Nevertheless, here the presence of ligands on the surfaces of the particles lowers their surface tension and prevents the diffusion of surface atoms at low temperatures. A supplementary contribution of energy (in this case thermal energy) is necessary to anneal the ligands and allow surface diffusion with the subsequent decomposition of the wires into a chain of spheres. This behavior was observed when the wires were annealed under static argon atmosphere with a heating ramp of 10 ^{o}C per minute till 350 ^{o}C. Besides this, it was possible to find the correct conditions to successfully obtain intact Co nanowires based on a kinetic differentiation of the two steps involved in the process: carbon shell formation and reconstruction of the nano-objects. For this purpose thermal annealing was performed under argon atmosphere but with a lower heating ramp (5 ^{o}C/min) ensuring decomposition of the ligands before decomposition of the wires.

On the other hand when the Co nanowires were annealed directly in the transmission electron microscope, *i.e.* under high vacuum conditions, no carbon shell was evidenced and the metal directly evaporated from the grid without following any periodicity. This difference is tentatively explained as a consequence of the irregular contact between the wires and the amorphous carbon film. In fact, there is another factor which must be taken into account: in the antechamber of the microscope the particles are under high vacuum conditions, and the stabilizing ligands may be desorbed from the surface upon heating, a fact that could have dramatic consequences for the stability of the anisotropic objects.

In the case of Co nanorods and because of their much smaller size, it was impossible to find parameters to successfully anneal them to obtain the cobalt-carbon core-shell structure, most probably because they melt more easily.

3 Conclusions

We have evidenced that it is possible to anneal single crystalline Co anisotropic NPs obtained by wet chemistry methods, leading to nano-objects with ferromagnetic behavior at

room temperature and long term stability against air oxidation. On the other hand the annealing process must be performed carefully to avoid the fragmentation of the wires into chains of Co spheres which still present the original hcp structure of the wires when they are annealed at too high temperatures or simply too fast. In that case, the excitation of phonon modes with the subsequent fast diffusion of the surface atoms[22] is responsible of the fragmentation. Such diffusion process has a random character and, due to energy minimization, leads to the formation of a chain of spheres, in agreement with the model established by Lord Rayleigh.[16] At the same time, the Co atoms participate in the formation of the carbon shell. Only when we selected 350 ^{o}C as maximum temperature with a heating rate of 5 ^{o}C/min undecomposed Co nanowires with a passivating carbon shell were observed without change of their original structure and thus without loss in magnetization and anisotropy.

[1] F. Dumestre, B. Chaudret, C. Amiens, M.-C. Fromen, M.-J. Casanove, P. Renaud, P. Zurcher, Angew. Chem. Int. Ed., 41 (2002), 4286.
[2] Y. Kobayashi, M. Horie, M. Konno, B. Rodríguez-González, L. M. Liz-Marzán, J. Phys. Chem B, 107 (2003), 7420.
[3] W. R. Lee, M. G. Kim, J. R. Choi, J.I. Park, S. J. Ko, S. J. Oh, J. Cheon, J. Am. Chem. Soc., 127 (2005), 16090.
[4] J. Zhang, M. Post, T. Veres, Z. J. Jakubek, J. Guan, D. Wang, F. Normandin, Y. Deslandes, B. Simard, J. Phys. Chem. B, 110 (2006), 7122.
[5] R. N. Grass, E. K. Athanassiou, W. J. Stark, Angew. Chem. Int. Ed., 46 (2007), 4909.
[6] (a) C. Guerret-Plécour, Y. Le Bouar, A. Loiseau, H. Pascard, Nature, 372 (1994), 22. (b) K. Lafdi, A. Chin, N. Ali, J. F. Despres; J. Appl. Phys. 1996, 6007. (c) J. Jiao, S. Seraphin, X. Wang J. C. Withers; J. Appl. Phys., 1996, 103.
[7] S. Liu, J. Zhu, Y. Mastai, I. Felner, A. Gedanken; Chem. Mater., 12 (2000), 2205.
[8] V. A. de la Peña O'Shea, P. Ramírez de la Piscina, N. Homs, G. Aromí, J. R. G. Fierro, Chem. Mater., 21 (2009), 5637.
[9] A.-H. Lu, W.-C. Li, N. Matoussevitch, B. Spliethoff, H. Bonnemann, F. Schuth, Chem. Commun., 1 (2005), 98.
[10] M. A. Zalich, V. V. Baranauskas, J. S. Riffle, M. Saunders, T. G. St. Pierre, Chem. Mater., 18 (2006), 2648.
[11] C. Desvaux, C. Amiens, P. Fejes, P. Renaud, M. Respaud, P. Lecante, E. Snoeck, B. Chaudret, Nat. Mater. 4 (2005), 750.
[12] C. Desvaux, P. Lecante, M. Respaud, B. Chaudret, J. Mat. Chem., 20 (2010), 103.
[13] Y. Xia, P. Yang, Y. Sun, Y. Wu, B. Mayers, B. Gates, Y. Yin, F. Kim, H. Yan, Adv. Mater., 15 (2003), 353.
[14] (a) M. E. Toimil-Molares, A. G. Balogh, T. W. Cornelius, R. Neumann, C. Trautmann, Appl. Phys. Lett., 85 (2004), 5337. (b) S. Karim, M. E. Toimil-Molares, W. Ensinger, A. G. Balogh, T. W. Cornelius, E. U. Khan, R. Neumann, J. Phys. D, 40 (2007), 3767.
[15] J. Plateau, Transl. Annual Reports of the Smithsonian Institution, 1873, p. 1863.
[16] Lord Rayleigh, Proc. London Math. Soc., 10 (1878), 4.
[17] F. A. Nichols and W. W. Mullins, Trans. Metall. Soc. AIME, 233 (1965), 1840.
[18] O. Gulseren, F. Ercolessi, E. Tossati, Phys. Rev. B, 1995, 51 (1995), 7377.
[19] B. C. Sales, J. E. Turner, M. B. Maple, Phys. Rev. Lett., 44 (1980), 586.
[20] Z. Zhang, D. Su, Ultramicroscopy, 109 (2009), 766.
[21] R. Sinclair, T. Itoh, R. Chin, Microsc. Microanal., 8 (2002), 288.
[22] J. Feng and H. C. Zeng, J. Phys. Chem. B, 109 (2005), 17113.

Chapter IV: Synthesis of cobalt NPs decorated with luminescent dyes: quenching of luminescence and photomodulation of magnetization

1 Introduction

1.1 Hybrid systems with optical and magnetic functionalities

Photoswitchable molecular species are the subject of a large research effort, as they would bring faster and remote control of devices, hence are the promise of new optimized technologies. However, despite their increasing implication in nanotechnology, very few reports tackle the photomodulation of the magnetic properties of nanocrystals. Investigating the possibility of controlling the magnetization of NPs by light requires the design of hybrid magnetic/light responsive nanocomposites, and the understanding of the mechanisms governing the interaction between the two functionalities. In the last years, the design of hybrid systems holding different functionalities has been one of the main objectives in nanotechnology research with interesting applications in medicine, catalysis, photovoltaic industry or biotechnology. In the particular case of medicine, nanosystems holding fluorescent and magnetic functionalities are very promising for the diagnosis and treatment of different diseases. For example, the use of magnetic NPs holding fluorescent molecules as MRI contrast agents and fluorescent markers (both, *in-vivo* and *in-vitro*) has experienced an enormous development due to their multi-mode imaging capabilities.

This increasing interest in the development of fluorescent-magnetic nanocomposites has led to a broad range of different materials, which has been roughly classified into eight sub-categories[1] **(Figure 4-1)**:

1. Magnetic cores coated with an inorganic polymer containing fluorescent components.
2. Organic polymer-coated magnetic NPs functionalised with a fluorescent moiety.
3. Ionic aggregates consisting of a magnetic core and fluorescent ionic compounds.
4. Fluorescently labelled bilipid-coated magnetic nanoparticles.
5. Magnetic cores covalently bound to fluorescent entities via molecular spacers.
6. Magnetic cores directly coated with semiconducting shells.
7. Magnetically doped QDs.
8. Nanocomposites, consisting in magnetic nanoparticles and QDs encapsulated within an organic polymer or silica matrix.

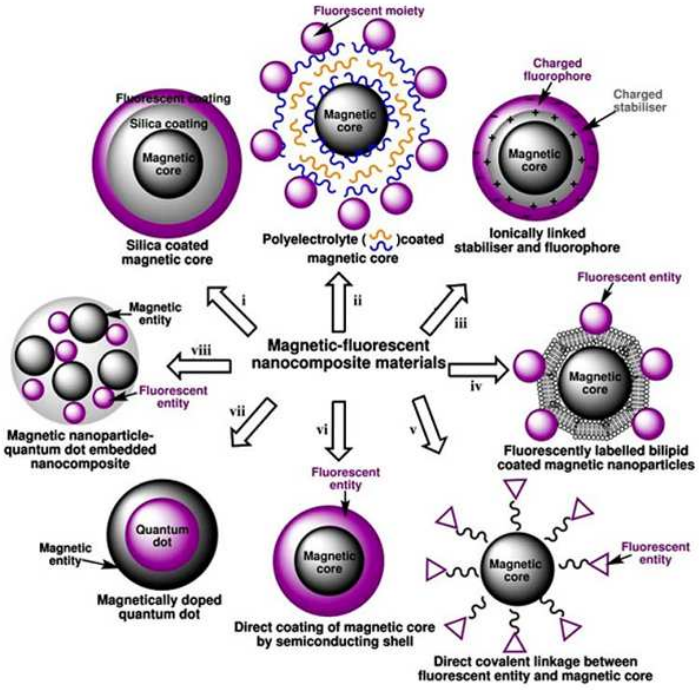

Figure 4-1. *Classification of the different magnetic-fluorescent composites presented in Ref. 1.*

Given the applications envisaged, most of the previously published papers dealing with fluorescent-magnetic composites are focused on the effect of the magnetic core over the optical properties of their fluorescent motifs. Furthermore, as a result of their air stability, most of the work published so far has been dedicated to the synthesis and study of fluorophores attached to magnetic oxide NPs, despite their lower magnetization.

However and as stated above, the opposite process (a light-promoted variation of the magnetization as a consequence of the fluorescent entity) could be a source of interesting phenomena where light-modulated magnetization at the nanoscale would be envisaged as the final goal. In this context, one possibility could be to use fluorophores as antennas to control energy or electron exchange with the magnetic core or change the dielectric environment of the core in the case of fluorophores with a highly polarized excited state.

It is thus important to emphasize the interest in systems composed by an organic fluorophore in close contact with the magnetic core, which represent an intermediate stage between cases 5 and 6 of the above classification. These hybrids present the optimal conditions

under which interactions between both entities are maximized, being therefore the perfect scenario for a study on the effect of the magnetic properties of the NP over the fluorescent dye and *vice-versa*. Such interactions will be discussed in detail within this section.

Consequently, from now on we will focus on the study of magnetic-fluorescent composites obtained by the direct attachment of the fluorophore to the surface of a magnetic core, more precisely an oxide-free magnetic core, in order to get a strong magnetic response. As far as we know, no work has been developed on such hybrids.

Prior to the presentation of the experimental results, we will give a brief introduction of the main characteristics of photoluminescence spectroscopy together with the principal mechanisms governing quenching and enhancement of fluorescence near a metal (Au and Ag) or magnetic NP.

1.2 Introduction to fluorescence spectroscopy

The term luminescence refers to the ability of some chemical species to emit light when exposed to certain stimuli like electrical currents, chemical reactions or light irradiation, among others. In this introduction we will focus on photoluminescence, a phenomenon produced after absorption of photons by some chemical species. For a deeper insight into this field the reader is referred to the excellent books by Lakowicz[2] and Lumb.[3]

The photoluminescent processes can be divided into two categories:

- Fluorescence: emission produced between two electronic levels[i] with the same multiplicity (singlet states: $S^* \rightarrow S_0$) (S_0 is the fundamental state and S* is the excited one) and thus, allowed by the laws of quantum mechanics. In this case, a rapid deactivation with fast photon emission takes place ($k_{fluo} = 10^8\ s^{-1}$).
- Phosphorescence: the excited state has triplet multiplicity and therefore, the decay of the electron back to the singlet fundamental state ($T^* \rightarrow S_0$) is forbidden. As a result of this,

[i] In the UV-visible range of the electromagnetic spectrum, absorption or emission of light implies changes in the occupation of the electronic levels of the chemical species. At the same time, those levels are divided in vibrational and rotational states. In absorption and fluorescence spectroscopy, the transitions between different vibrational levels are responsible for the fine structure of the spectra while rotational transitions are too weak and only participate in broadening slightly this fine structure.

the emission rates of phosphorescence are low ($k_{phos} = 10^3$-10^0 s^{-1}). That is the reason for the exceptional emission of some phosphorescent materials minutes or even hours after excitation.

1.2.1 Fluorescence: basic principles

The easiest way to understand the different processes involved in photoluminescence is the use of the Jablonski diagram **(Figure 4-2)**. In this model, the different electronic and vibrational energy levels involved are represented in a simplified way. Moreover, the transitions between the different energy levels are represented as vertical lines: as the time scales of the absorption processes are too fast for a significant displacement of the nuclear centers (10^{-15} s), the symmetry of the molecule involved does not change during photoexcitation or photoemission. Such behavior is dictated by the Franck-Condon principle.

For a typical photoexcitation process **(Figure 4-2)**, a photon of light is absorbed by the fluorophore and one electron is excited to a higher electronic state ($S_0 \rightarrow S^*$). Once the electron arrives at a higher vibrational level of S*, it rapidly relaxes to the lowest vibrational level (v = 0) by a fast process called internal conversion ($\tau_{IC} \cong 10^{-12}$ s). It is important to remark that the electronic transition occurring during the absorption of a photon, implies a variation of the electronic density of the molecule due to the transition of an electron from the HOMO (highest occupied molecular orbital) to the LUMO (lowest unoccupied molecular orbital), orbitals that present different spatial electronic localizations within the molecule. As a result, the dipolar moment of the molecule is modified.

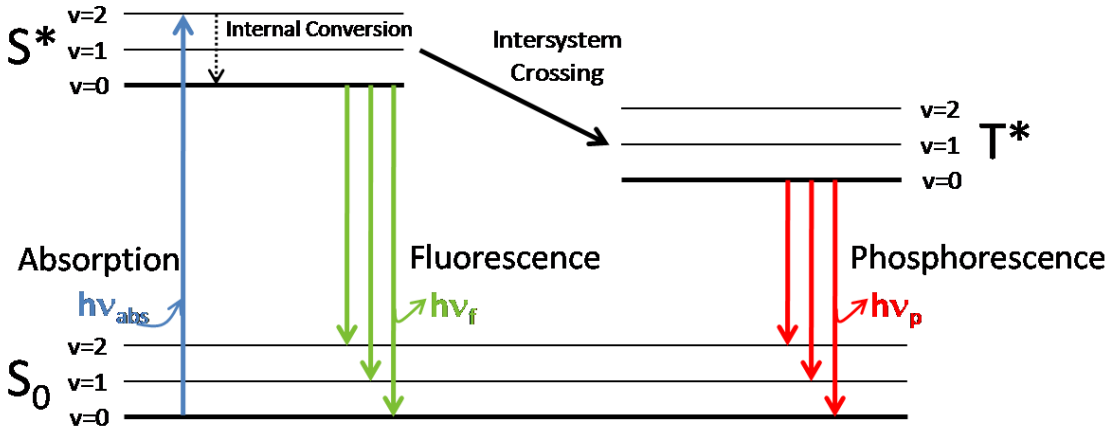

Figure 4-2. *Jablonski diagram representing the two possible emission processes produced after absorption of a photon of energy $E \cong S^*\text{-}S_0$. Modified from Ref. 2.*

Once the electron has reached thermal equilibrium, it decays again to any of the vibrational states of the ground electronic level. Because the same transitions are involved in both absorption and emission processes, most of the emission spectra between the first excited state and the bottom level ($S^1 \rightarrow S_0$) are mirror images of the absorption spectra associated to the reciprocal absorption process ($S_0 \rightarrow S^1$). Nevertheless this rule presents an important number of exceptions in real systems due to different chemical reactions, *i.e.* proton dissociation or formation of excited-state dimers.

The electron can also be transferred to an excited state of different multiplicity during its desexcitation pathway. This process is called intersystem crossing and leads to the appearance of phosphorescence. As explained before, phosphorescence is an emission process that has a low probability to occur if compared with fluorescence. This phenomenon is rarely observed in solutions measured at room temperature due to its competition with other deactivation processes.

Table 4-1. *Lifetimes of the different processes included in the Jablonski diagram.*

Process	***Lifetime (s)***
Absorption	10^{-15}
Internal Conversion	10^{-12}
Fluorescence	10^{-8}
Phosphorescence	10^{-3}-10^{0}

1.2.2 General characteristics of absorption and emission spectra

Ultraviolet-visible (UV-vis) absorption and fluorescence spectroscopies are complementary techniques since the first one deals with transitions from fundamental to excited states (absorption) and the second one with transition from excited states to fundamental ones (emission). The Lambert-Beer law is used to quantify the absorption in diluted solutions (usually between 0.01 and 1 $mol \cdot L^{-1}$):

$$A = log_{10}\left(\frac{I_0}{I}\right) = \varepsilon bc \quad \textbf{(4.1)}$$

where A represents the absorbance of the absorbing species, I_0 is the intensity of the incident light, I the transmitted intensity, b the mean free path through the sample (in cm), c the molar concentration of the absorbing species ($mol \cdot L^{-1}$) and ε is the molar extinction coefficient ($L \cdot mol^{-1} \cdot cm^{-1}$), parameter that describes how efficiently a chemical species absorbs light.[ii]

The main limitation of this method is that it is restricted to a certain range of concentrations, out of which the relation between absorption and concentration is not linear any more. The information obtained in absorption spectroscopy is of crucial importance in fluorescence, since the maximum of absorbance for a given fluorophore corresponds with the excitation wavelength at which the fluorescence intensity will reach its maximum value. Actually, if all the absorbed photons would be directly re-emitted the maximum of absorbance and the maximum of fluorescence would coincide at the same wavelength. Nevertheless and as we have seen before, part of the energy absorbed by the system is released in the form of heat due to internal conversion. As a consequence of this, the energy of the emitted photon differs from the energy of the absorbed one ($\lambda_{abs} < \lambda_{em}$) and the emission spectra are red-shifted. This difference is known as the Stokes shift **(Figure 4-3)**.

[ii] ε is also an important parameter in fluorescence spectroscopy since its value is directly related with the capability of a fluorophore to emit light.

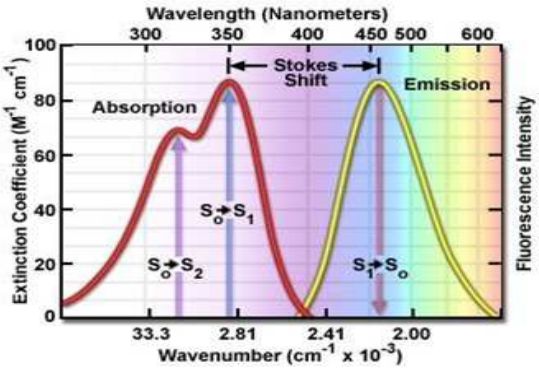

Figure 4-3. *Absorption and emission spectra of quinine, in which Stokes shift is clearly observed.*

Taken from: ***http://www.microscopyu.com/articles/fluorescence/fluorescenceintro.html***

1.2.3 Physical characteristics of fluorophores: quantum yield and fluorescence lifetime

Under the same experimental conditions, fluorescent species differ in their emission efficiency. The emission efficiency of a fluorophore is expressed as the quantum yield (Q_F), *i.e.* the ratio of number of emitted photons to the number of absorbed ones:

$$Q_F = \frac{number\ of\ photons\ emitted}{number\ of\ photons\ absorbed} \quad \textbf{(4.2)}$$

Following this relation, if Q_F is close to 1 it means that the fluorophore is highly fluorescent. On the other hand, if Q_F is close to 0, it is poorly fluorescent. As an example, we report in **Table 4-2** the quantum yields of some organic fluorophores extensively reported in the literature.

Table 4-2. *Quantum yields of some commonly used organic fluorophores.*[4,5]

Dye (solvent)	***Quantum Yield (Q_F)***
Cy3 (ethanol)	0.09
Cy5 (ethanol)	0.4
Rhodamine B (basic ethanol)	0.65
Rhodamine 6G (ethanol)	0.95
Texas Red (ethanol)	0.93
Nile Red (dioxane)	0.7
Fluorescein	0.97

Another crucial parameter of a fluorophore is the lifetime of its excited state or fluorescence lifetime (τ). This parameter describes how much time the electron spends in the excited state prior to its decay back to the fundamental level:

$$\tau = \frac{1}{\Gamma + k_{nr}} \quad \textbf{(4.3)}$$

where Γ and k_{nr} represent the radiative and non radiative decay rates (see Quenching of Fluorescence). In reality, the emission rate of a fluorophore is a statistic process and just a small number emits light within one precise time interval. Therefore τ represents an average for the decay time of a fluorophore.

1.2.4 Quenching of fluorescence

Different processes can decrease (or quench) the fluorescent properties of a fluorophore. Those quenching processes can be classified in two main groups: those intrinsic of any fluorophore and those which appear as a consequence of an intermolecular interaction.

1.2.4.1 Intrinsic non radiative processes

Part of the excited electrons relaxes without emission of photons via internal conversion and nonradiative decay **(Figure 4-4)**, leading to a decrease of the fluorescence intensity. This quenching mechanism is an intrinsic property of all the fluorophores, having an important effect on their quantum yields:

$$Q_F = \frac{\Gamma}{\Gamma + k_{nr}} \quad \textbf{(4.4)}$$

Due to this intrinsic property, the quantum yield of a fluorophore can never reach its maximum value (1).

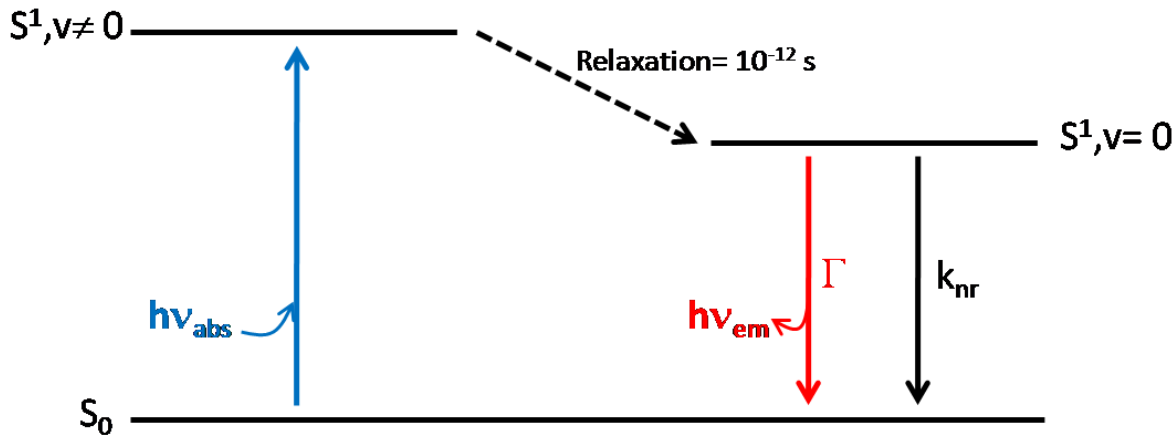

Figure 4-4. *Simplified Jablonski diagram representing the radiative and non radiative decay rates of an excited fluorophore.*

Actually, other factors like temperature, solvent effects, reorientation of the molecules, formation of aggregates, excited state reactions or energy and electron transfer processes can affect strongly the radiative and non radiative decay rates and thus, the emission spectra. Some of these factors will be explained in more detail within the next sections.

1.2.4.2 Intermolecular relaxation processes

In this case, the quenching process appears as a consequence of the interaction between the fluorophore and other species that can be the solvent, an organic molecule, metal ions or a NP. Such interaction can be static or dynamic in character, depending if both species react to form a stable complex or interact by simple collision:

– Dynamic quenching: occurs when an excited-state fluorophore (F*) experiences contact with another molecule in solution, called quencher (Q).

$$F^* + Q \rightarrow F + Q + heat \quad \textbf{(4.5)}$$

The Stern-Volmer equation describes this quenching process:

$$\frac{F_0}{F} = 1 + k_q \tau_0 [Q] = 1 + K[Q] \quad \textbf{(4.6)}$$

where F_0 and F are the fluorescence intensities in the absence and presence of quencher, respectively. K is the Stern-Volmer quenching constant that indicates the sensitivity of a fluorophore to a quencher, k_q the bimolecular quenching constant and τ_0 the lifetime of

the fluorophore in the absence of quencher. Examples of dynamic quenchers are dioxygen, halogens, some metal ions and electron-deficient molecules and sometimes the solvent itself.

Two examples of dynamic quenching processes are:

1. An excited fluorophore interacts with a dioxygen molecule that has a triplet configuration. Such quencher induces a transformation of the excited state of the fluorophore, which becomes a triplet excited state by intersystem crossing. Afterwards, the fluorophore can decay via a non-radiative process or be quenched again by the same molecule.
2. An excited fluorophore can exchange its excited electron with a fundamental electron from the quencher. This exchange leads to a fluorophore in its fundamental state and an excited quencher that decays back to its original condition by a nonradiative process.

– Static quenching: this process occurs when fluorophores form stable non fluorescent complexes with other molecules.

$$F + Q \rightarrow [F - Q] \quad \textbf{(4.7)}$$

The name static quenching is due to the fact that these complexes are formed at the fundamental state. Here the dependence of the fluorescence with the concentration of the quencher is given by:

$$\frac{F_0}{F} = 1 + K_a[Q] \quad \textbf{(4.8)}$$

where K_a represents the constant governing the association process between fluorophore and quencher leading to the formation of the complex.

In this case the lifetime of the sample is not altered by the quenching process, since those fluorophores that remain free will have unaltered excited states. Actually, the decrease in fluorescence intensity is a consequence of the lower number of fluorophores that can emit light.

For both dynamic and static quenching, molecular contact between the fluorophore and the quencher is mandatory and therefore, both processes are limited to very small distances. Furthermore, most of the quenching mechanisms in which a fluorophore and a quencher are involved include energy or electron transfer processes as the main

interaction between both species. Therefore, both quenching pathways should be described in more detail.

1.2.4.3 Förster Resonance Energy Transfer process (FRET): a particular case of intermolecular quenching

A phenomenon of crucial importance in fluorescence spectroscopy is the so-called Förster Resonance Energy Transfer process (FRET). This process consists in the nonradiative energy transfer from the excited state of a fluorophore (donor) to another molecule (acceptor) and occurs when the emission spectrum of the donor overlaps with the absorption spectrum of the acceptor **(Figure 4-5)**.

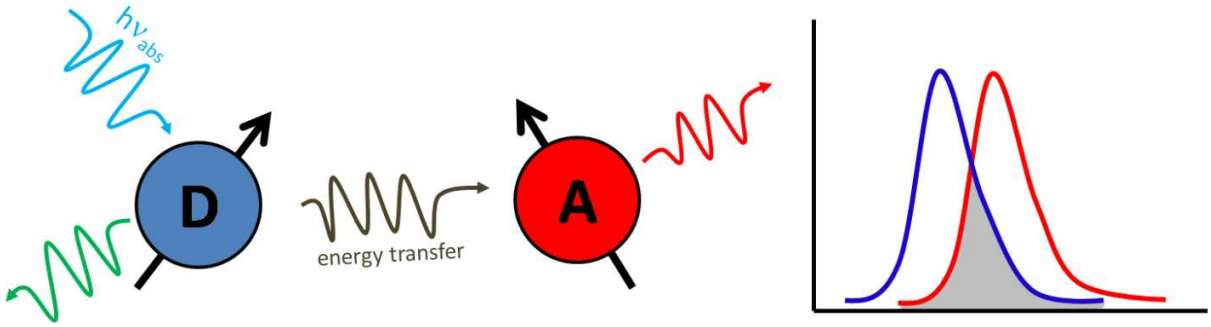

Figure 4-5. *Left: Schematic representation of the FRET mechanism between a donor (D) and an acceptor (A), with their respective dipolar moments. Right: overlap between the emission spectrum of the donor (blue) and the absorption spectrum of the acceptor (red).*

As a consequence of this interaction, the donor experiences a decrease of its intrinsic fluorescence intensity and lifetime. It is important to remark that FRET does not involve an intermediate photon between both species. In fact, the energy is transferred through a non-radiative dipole-dipole coupling and therefore, the relative orientation of the dipoles plays an important role. Nevertheless the limiting parameter controlling the efficiency of the FRET mechanism is the distance between donor and acceptor:

$$R_0 = \frac{900(ln10)\kappa^2 Q_d J}{128\pi^5 N n^4} \quad \textbf{(4.9)}$$

where R_0 is the Förster distance (in nm), that is defined as the critical distance at which 50 % of the excitation energy is transmitted to the acceptor. In the formula n is the refractive index of the medium, Q_d is the fluorescence quantum yield of the donor in the absence of the acceptor, κ^2 is

the orientation factor for the dipole-dipole interaction, N the Avogadro's number and J is the normalized spectra overlap integral.

Typically, FRET occurs for distances below 10 nm. This value is approximate and gives an idea of the distances at which the energy transfer is not sufficiently efficient to result in an important quenching of the donor. The rate of energy transfer is given by:

$$k_T(r) = \frac{1}{\tau_D}\left(\frac{R_0}{r}\right)^6 \quad \textbf{(4.10)}$$

where τ_D represents the fluorescence lifetime of the donor in the absence of the acceptor, r is the distance between donor and acceptor and R_0 is the Förster distance.

In general terms, FRET can be considered as a quenching process, since it causes a decrease of fluorescence intensity of the fluorophore (donor) involved. Nevertheless, a brief comparison can clarify the main differences between FRET and the *classic* quenching processes:

1. The mean distances involved in both processes differ substantially. While in a *classical* quenching process direct contact is needed between molecules, FRET can be efficient at distances up to 10 nm.
2. As FRET is not based on a direct contact between donor and acceptor, it is not affected by steric factors or electrostatic interactions.
3. In FRET, the energy absorbed by the acceptor can be re-emitted in the form of light (in the particular case in which the acceptor is a fluorophore), while in *classical* quenching processes, the excess of energy absorbed by the quencher is dissipated as heat.

FRET is a process of fundamental importance in biology and biochemistry, since it is used as "spectroscopic ruler" for the measurement of distances between sites of biomolecules with potential interest. In the last years, FRET has found another interesting application in nanoscience as a mechanism to understand the interaction between luminescent dyes and different kinds of NPs. This mechanism, together with electron transfer processes, has opened a new field of research in surface chemistry and physics. Actually, hybrid nanosystems formed by the adsorption of fluorophores at the surface of metal or semiconductor NPs is expected to play a major role in photovoltaic industry and medicine.

1.2.4.4 Electron transfer process

The quenching of fluorescence mediated by an electron transfer mechanism involves in most cases the transfer of one electron from the excited fluorophore (donor) to the fundamental state of another molecule (quencher or acceptor). This phenomenon can be static if the excited state comprises the formation of a donor-acceptor complex with the correspondent separation of charges (D^+-A^-) or dynamic if it is produced within the framework of molecular collisions (see **Figure 4-6**).

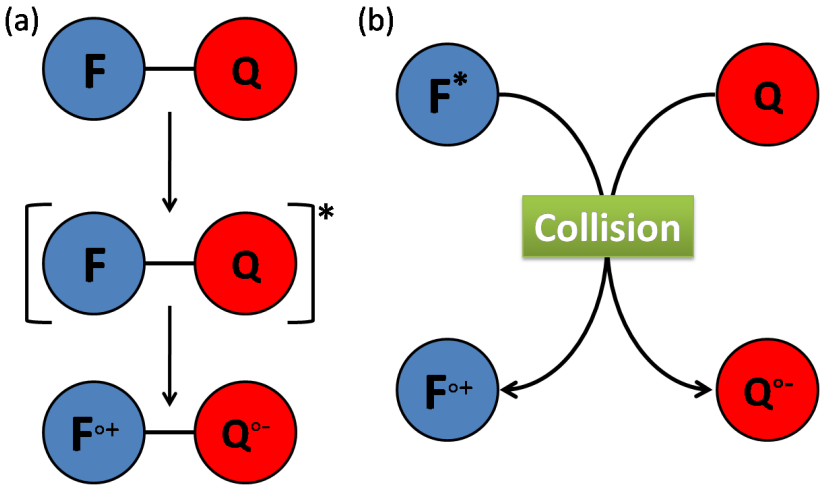

Figure 4-6. *Schematic diagrams representing static (a) and dynamic (b) electron transfer processes.*

As reported by Saik and coworkers,[6] the opposite process (electron transfer from the quencher to the fluorescent entity) is also possible. For example, N,N-dimethylaniline (DMA) forms a complex with different rhodamine derivatives and transfers one electron to the excited state of the molecule (such process can be understood as a hole transfer from the fluorophore to the DMA).

1.2.5 Organic fluorophores

Among the different chemical species presenting fluorescent properties, organic fluorophores are the most extensively used. Their optical properties are a consequence of the unsaturated character of their structure, presenting aromaticity in most cases.[iii]

[iii] An aromatic hydrocarbon presents a planar conjugated cyclic molecular structure with a delocalized cloud of (4n+2) π electrons (where n is an integer). Benzene is the simplest aromatic hydrocarbon (n=1).

The organic fluorophores can be intrinsic (those that occur naturally, like some aromatic aminoacids) and extrinsic (used to label the molecule of interest when this one is non-fluorescent). Within the group of extrinsic fluorophores, rhodamines occupy an important position due to their high quantum yields and molar extinction coefficients, high stability against photobleaching and their low sensitivity to the polarity of the solvent. A wide number of rhodamine derivatives is available from commercial sources **(Figure 4-7, top)** and are mostly used in biology for the labeling of proteins, DNA or lipids. Within this family of dyes, the fluorescent properties come from the resonant structure formed by the three conjugated rings and the two amines present in the lower part of the molecules, structure that is formally known as Pyronin **(Figure 4-7, bottom)**. Even if these molecules are normally represented as planar structures, their fourth aromatic ring is tilted by 90 degrees with respect to the rest of the structure in order to minimize steric repulsions, fact of crucial importance for the use of any of those molecules as stabilizer in the synthesis of NPs.

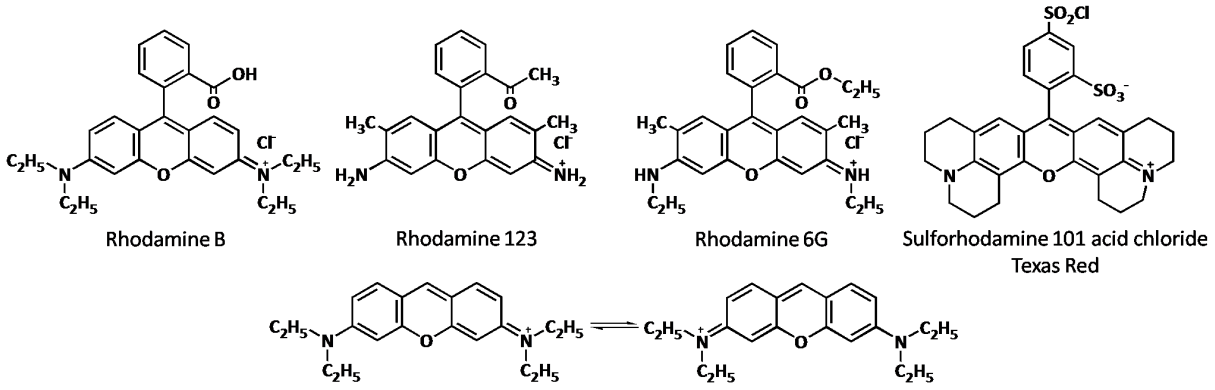

Figure 4-7. *Four examples of commonly used rhodamine derivatives (up). Two resonant contributions of the conjugated part of Rhodamine B responsible for the optical properties of the molecule (down).*

One parameter to take into account when working with organic luminescent dyes is their tendency to self-aggregate, phenomenon that leads, in most cases, to an important decrease of the fluorescence intensity. Such aggregation is the result of the strong electronic interactions between the aromatic rings of the molecules (π-stacking), resulting in the self-quenching of fluorescence and dramatically reduced quantum yields.

1.3 Interaction between NPs and fluorescent dyes

The optical properties of fluorescent entities are strongly modified in the presence of metal or magnetic NPs because both radiative and nonradiative decay rates can be altered in the vicinity of a surface. Therefore, quenching or enhancement of fluorescence can appear, depending on the experimental conditions.

The most representative examples are detailed below, classified with respect to the nature of the NP.

1.3.1 Noble metal NPs (Au, Ag)

Noble metals at the nanometric scale are known for their intense localized surface plasmon resonances (LSPR), result of the coherent oscillation of the surface conduction electrons excited by coherent electromagnetic radiation.[7] In the case of Au and Ag NPs, the wavelength of the radiation falls in the visible range of the spectrum. When fluorescent molecules are attached at the surface of those particles, the enhancement of the electromagnetic field near the surface has an important effect over the optical properties of the dye. In this case, two main processes have to be differentiated, both with opposite effects over the fluorescence intensity. First, the local field enhancement increases the excitation rate of the fluorophore with the subsequent enhancement of fluorescence. Second, electron or energy transfer between the molecule and the metal surface increases the nonradiative decay rate, inducing a quenching of fluorescence.

Dulkeith et al., reported fluorescence quenching for a fluorophore attached at the surface of a Au NP with a diameter of 12 nm[8] while the distance (d) between both entities was precisely controlled with a single stranded DNA molecule between 2 and 16 nm. Electron transfer has been neglected due to the weak conduction character of the DNA strand while energy transfer is presented as the main quenching mechanism. Here, both radiative and nonradiative decay rates vary as a function of d (radiative decay decreases with d while nonradiative decay experiences the opposite behavior). The change in nonradiative rate is explained as a consequence of energy transfer, while the decrease in the radiative one is due to a destructing interference effect (out-of-phase radiation of the molecular dipole and the dipole induced on the NP). Another important characteristic of this work is the fact that energy transfer is achieved even though the spectral

overlap between the absorption band of the particle (acceptor) and the emission band of the fluorophore (donor) is relatively weak. A similar experiment in which the distance between fluorophore and particle was constant (1 nm) was performed by the same research group.[9] In this case the diameter of the particle was varied between 1 and 30 nm. A clear quenching effect due to energy transfer was observed for all the diameters studied here, with decrease and increase of the radiative and nonradiative decay rates, respectively. The effect of the diameter of the Au core is only clear in the case of the nonradiative decay rate, where an important increase with the size of the particle is observed in the experimental data.

Although classical FRET mechanism is used as the reference model to explain the energy transfer mechanism between NP and fluorophore, a research group from Florida State University has shown that in the particular case of a molecular dipole interacting with the surface of a metal NP[10] the traditional Förster range doubles up to 22 nm and presents a different distance dependence ($1/R^4$ instead of $1/R^6$). Furthermore, a corroboration of the theoretical model with experimental results is included in their papers.

Electron transfer has been also studied as the deactivation pathway of an organic fluorophore attached to the surface of a Au NP.[11,12] Here the interaction of pre-synthesized Au NPs with pyrene thiol and chlorophyll a, respectively, leads to the formation of complexes in which the electron transfer takes place between the fluorophore and the metal NP. Under these conditions the metal surface holds a negative extra electric charge while the fluorophore remains in the form of a radical, prior to conversion to the fundamental state **(Figure 4-8)**.

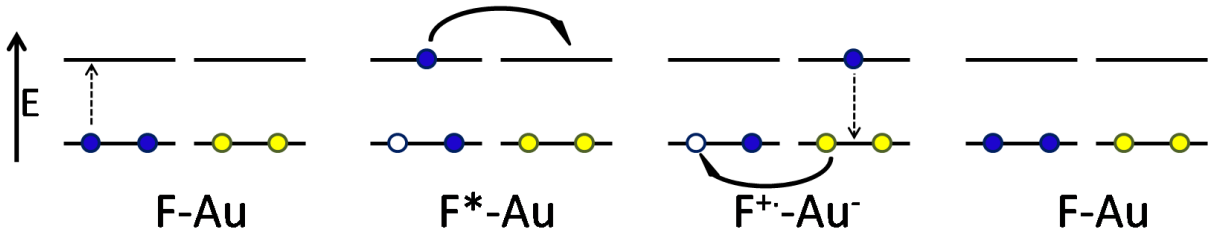

Figure 4-8. *Schematic representation of an electron transfer process between a fluorophore and a gold NP. Blue and yellow circles represent electrons from the fluorophore and the gold NP, respectively. The white circle represents an electronic hole. For the sake of simplicity the energetic states of the Au NP have been represented as discrete levels. (Note: Fluorophore and NP not to scale).*

Although less frequent, fluorescence enhancement has also been observed for fluorophores in the proximity of metal surfaces,[13] but at distances at which energy or electron

transfer could not play a major role (≅ 100 nm). Such effect is explained as a consequence of the enhancement of both dye excitation and radiative emission rates. Recently, fluorescence enhancement has been also reported for fluorophores directly attached at the surface of Ag NPs[14] using DNA layers of 5.5 nm as spacers between both entities. In this study the brightest fluorescence is obtained when the maximum of absorbance of the plasmon band from the Ag NP is blue-shifted from the emission maximum of the fluorophore. Gold nanoshells with diameters ranging between 24 and 120 nm have been used with similar results.[15] Here, a new parameter (the higher scattering efficiency of the bigger shells) is introduced in order to explain the important increase in fluorescence enhancement with the size of the particle.

Different results from those reported above have been obtained by Battistini and coworkers.[16] In their experiments a dye anchored to the surface of a Au NP by hydrocarbon chains of different lengths present fluorescence enhancement for the shorter distances and quenching for the longer ones. The geometrical disposition of the dye with respect to the metal surface seems to be the key parameter in this case (*i.e.* the dipole/dipole interaction).

The contradictory cases reported here exemplify the difficulty of obtaining conclusions that could be generalized. Actually, mechanisms of quenching and enhancement of fluorescence generally coexist in the same dye-NP system. Nevertheless, the relative simplicity of their synthesis and the competition between electron and energy transfer processes, make Au and Ag colloids perfect models to understand all the possible mechanisms governing the interaction between a fluorophore and a NP.

1.3.2 Magnetic NPs

Superparamagnetic NPs have been also functionalized with luminescent ligands in order to obtain hybrid systems with optical and magnetic functionalities. In the majority of cases iron oxide NPs are used as templates due to their biocompatibility and air-stability. Within those hybrids, fluorescence measurements have been used as a tool to understand the interaction between iron oxide NPs and biological molecules. Bertorelle et al.[17] have functionalized iron oxide NPs with rhodamine B and fluorescein to form magnetic-fluorescent composites that are subsequently used for the labeling of living cells. Here the authors found a fluorescence intensity 3.5 times lower than that of the free dyes, fact that was attributed to an energy transfer between

the dye and the molecule. In another example, the direct interaction between a magnetic oxide NP and the bovine serum albumin protein[iv] has been proved by the presence of static quenching together with some structural changes in the protein due to its interaction with the NP.[18] Such modifications on the structure of the protein highlight the strong effect of NPs on biological molecules and the risk that those systems could entail for living organisms. The same protein has been used by other groups to functionalize cobalt ferrite[19] and iron oxide[20] NPs, prior to the use of those hybrids as drug carriers in *in-vitro* studies. Another example of quenching of fluorescence in magnetic NPs is the work developed by Chandra and coworkers, where APTS-coated Fe_3O_4 NPs are functionalized with doxorubicin (DOX), an anticancer drug with fluorescent properties.[21] The release of the drugs from the surface of the NPs is monitored by fluorescence spectroscopy and a recovery of fluorescence is observed, proportional to the rate of release. In this case the fluorescence quenching is attributed to a partial overlapping of the emission band of the dye with the absorption band of the magnetic NP.

1.3.3 Conclusion

We can conclude that fluorescence quenching is reported in most of the systems in which an organic fluorophore is attached at the surface of a noble metal, or magnetic oxide NP. The decrease in fluorescence is generally related to the small distances between both species. However, the geometry of the system and more precisely, the relative configuration between the dipole of the fluorophore and the induced dipole of the particle, dictates the nature of the process (electron or energy-mediated). Yet nothing is known in the case of oxide free magnetic NPs.

2 Synthesis of oxide-free magnetic-fluorescent NPs.

2.1 Selection of the experimental conditions

Oxide-free magnetic NPs stabilized with organic fluorophores can be reached by two different synthetic approaches:

[iv] Bovine serum albumin (BSA) presents intrinsic fluorescence from its tryptophan residue.

- Functionalization of the already-prepared NPs by replacing the preexisting ligands with a fluorescent moiety (exchange-ligand strategy).
- Single step process consisting in the direct synthesis of the NPs using a dye as unique stabilizer. This approach is straightforward and avoids tedious purification steps. It was thus selected for this work.

The synthesis of Co NPs stabilized with a fluorophore has been performed through the decomposition of an organometallic complex under dihydrogen and in the presence of fluorescent molecules as unique stabilizing agents. For this purpose, $Co(\eta^3\text{-}C_8H_{13})(\eta^4\text{-}C_8H_{12})$[22] has been chosen as the source of Co atoms. This organometallic complex is highly reactive and can be decomposed at room temperature, leading to the synthesis of well crystallized Co NPs with outstanding magnetic properties and clean surfaces.[23] The fast kinetics of the reaction regularly allows the formation of very small NPs of a few nm, which is important when phenomena taking place at the surface have to be investigated. In addition, the only by-product obtained after hydrogenation of $Co(\eta^3\text{-}C_8H_{13})(\eta^4\text{-}C_8H_{12})$ is cyclooctane, a volatile molecule with negligible affinity with the metal surface of the NPs and therefore with no effect over the magnetic properties of the product. Furthermore it will not compete with the dye for coordination to the metal surface.

Concerning the fluorophore, we decided to work with Rhodamine B (RhB) due to its high quantum yield and the presence in its structure of different functional groups (carboxylic acid, amine and ammonium functions) that have been largely used to stabilize MTM NPs (see Chapter I). Even though RhB is a well-known dye in fluorescence spectroscopy due to its application as biological marker, little is known about its behavior in weakly polar solvents like those used for the synthesis of MTM NPs.

The two species used here ($Co(\eta^3\text{-}C_8H_{13})(\eta^4\text{-}C_8H_{12})$ and RhB) present very different structures and therefore their respective behaviors in solution differ substantially, especially at room temperature: while RhB is very soluble in polar solvents like water or alcohols with a short aliphatic chain, the Co complex is normally used in distilled aromatic solvents like anisole, mesitylene or toluene. Tetrahydrofuran (THF) was found as the best compromise in terms of solubility between both reactants but unfortunately this solvent is gradually photodecomposed, leading to the formation of peroxides, molecules that could damage the aromatic ring of RhB and

therefore affect its optical properties. Subsequently, anisole has been selected as solvent for all the synthesis presented in this chapter, since acceptable solubilities are obtained for the organometallic precursor and the dye. In comparison with the synthesis reported in Chapter II, working at room temperature has the added advantage of favoring the interaction between RhB and Co, which was evidenced to stabilize only relatively large Co NPs at elevated temperatures. Working at room temperature, one could expect the stabilization of smaller particles.

2.2 Synthesis of Co/RhB NPs

To prepare the hybrid composite of Co NPs and RhB, we introduced inside a Fischer-Porter bottle 1 equivalent of $Co(\eta^3\text{-}C_8H_{13})(\eta^4\text{-}C_8H_{12})$ and 0.2 equivalents of RhB in 20 mL of distilled anisole **(Figure 4-9)**. The mixture was pressurized with 3 bars of H_2 and reacted at room temperature for 14 hours, after which a dark pink solution was observed. Subsequently, the remaining H_2 was removed, the solvent evaporated and a black-pink powder was recovered (Co/RhB: Sample 4-1). When this powder was studied by TEM, NPs with a mean diameter of 3.8 nm and a standard deviation of 0.6 nm were observed **(Figure 4-9, bottom)**.

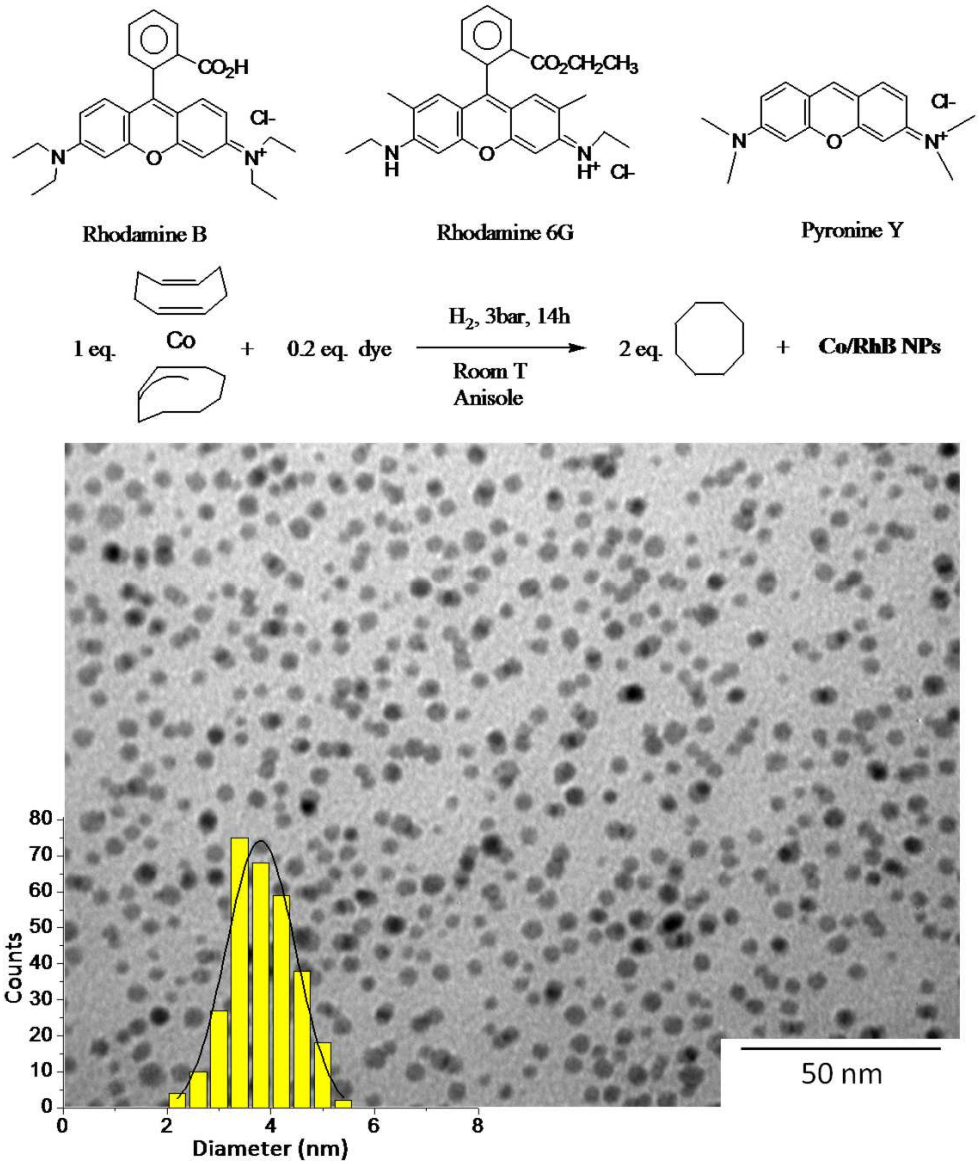

Figure 4-9. *(top) Structures of the dyes used as stabilizers and general scheme of the reaction. (bottom) Typical TEM image of sample 4-1 together with a size histogram of the particles.*

Inductively coupled plasma mass spectrometry (ICP-MS) was performed to know the exact composition of the powder **(Table 4-3)**. Both experimental and theoretical percentages were very similar and the small differences between them appear most probably due to the presence of some residual anisole. Finally, the sample was stocked in the glovebox in the powder form in order to preserve it from oxidation and pollutants.

Table 4-3. *Experimental (ICP-MS) and theoretical values for the chemical composition of Sample 4-1.*

Element	*Experimental %*	*Theoretical %*
Co	33.9	38.0
C	47.1	43.5
H	4.76	4.0
N	3.2	3.6

2.3 Decomposition of $Co(\eta^3\text{-}C_8H_{13})(\eta^4\text{-}C_8H_{12})$ without stabilizers

The effectiveness of the interaction between RhB and the Co nuclei formed in solution was tested performing a new synthesis in which all the parameters were kept constant with respect to the previous one unless the use of RhB. In this case the decomposition of $Co(\eta^3\text{-}C_8H_{13})(\eta^4\text{-}C_8H_{12})$ in anisole was done without any stabilizer (Sample 4-2). The product observed in TEM presents particles with a different morphology than those obtained in Sample 4-1: a mixture of big agglomerates and polydisperse NPs was observed **(Figure 4-10)**. This result shows that anisole only weakly coordinates at the surface of the NP, even at room temperature, and so will not compete with RhB.

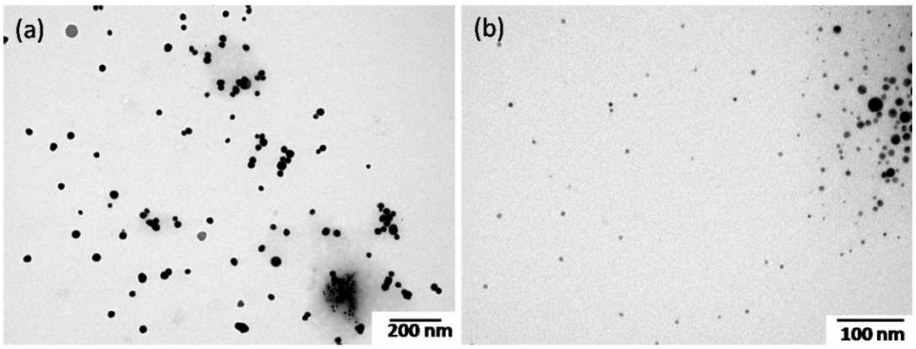

Figure 4-10. *Images representing the NPs obtained in Sample 4-2.*

2.4 Synthesis of Co NPs with different organic fluorophores

Due to the presence of different functional groups in the chemical structure of RhB that could work as linkers between the molecule and the particles, we performed control experiments using organic molecules with structural similarities with RhB **(Figure 4-9, top)**. Therefore, indirect conclusions from the role of the different functional groups present in the dye could be

obtained. With the exception of the different molecules used here as stabilizers (Rhodamine 6G (Sample 4-3) and Pyronin Y (Sample 4-4)) the rest of the parameters were those used in the synthesis of Sample 4-1. The results are completely different from those obtained when RhB was used as ligand. Actually, Sample 4-3 is composed by polydisperse NPs with a bigger diameter than those obtained previously **(Figure 4-11a)**, some of them displaying a worm-like morphology. In comparison, the TEM images from Sample 4-4 show the presence of micrometer sized aggregates **(Figure 4-11b)**.

The worst control over the size distribution and morphology of the particles obtained in both cases suggests that the RhB molecules are attached at the surface of the Co NPs by their carboxylic acid groups. Identification of the coordination mode of RhB on the Co surface was investigated by IR spectroscopy. However results were not conclusive due to the presence of a too large excess of non-coordinated RhB.

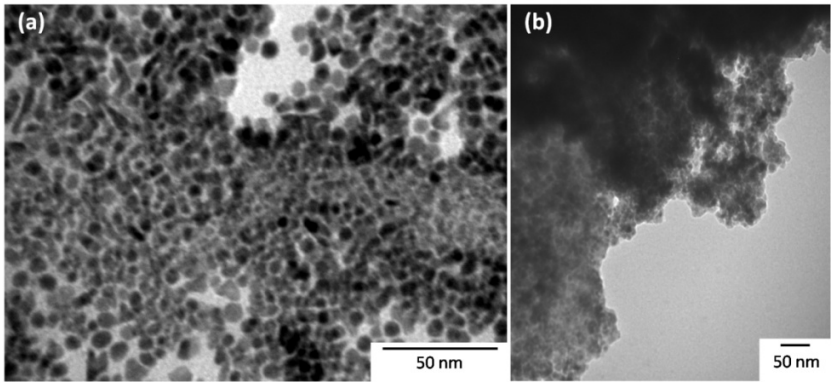

Figure 4-11. *TEM images of Sample 4-3 (a) and Sample 4-4 (b).*

3 Structural characterization

To elucidate the crystal structure of the Co/RhB hybrid, we performed wide angle X-ray scattering measurements on the product (Sample 4-1) (for details on the technique see Experimental Section). Preparation of the sample (introduction of a small amount of powder into a Lindemann glass capillary[v]) was done inside the glovebox prior to the sealing of the capillary,

[v] Lindemann glass presents a very weak absorption of X-rays due to its special composition by light atoms (a lithium borate-beryllium oxide).

in order to avoid oxidation of the sample during the measurement. The radial distribution function (RDF) obtained for those particles gives a very good agreement when compared with a model RDF from a cluster of 457 atoms arranged in a ε-Co structure **(Figure 4-12)** that consists in a complex cubic primitive structure (that of β-Mn). The first peak of the spectrum corresponds to the mean value of the first interatomic distance within the particle, in this case 0.2499 nm. In opposition to the hcp or fcc structures for Co, the experimental FDR does not show a peak centered at 0.37 nm typical of the octahedral sites present in compact structures. Another important feature of the RDF is its coherent length, parameter that relates with the size of the crystalline domains within the particle. Here, a coherent length of around 3 nm is observed. Comparison with the mean particle diameter obtained from TEM images (3.8 nm) suggests a crystallographic disorder of the outside Co layer.

Even though hcp and fcc are by far the most commonly observed crystalline structures for Co NPs, ε-Co has been found before in Co NPs obtained by the fast-injection method.[24,25]

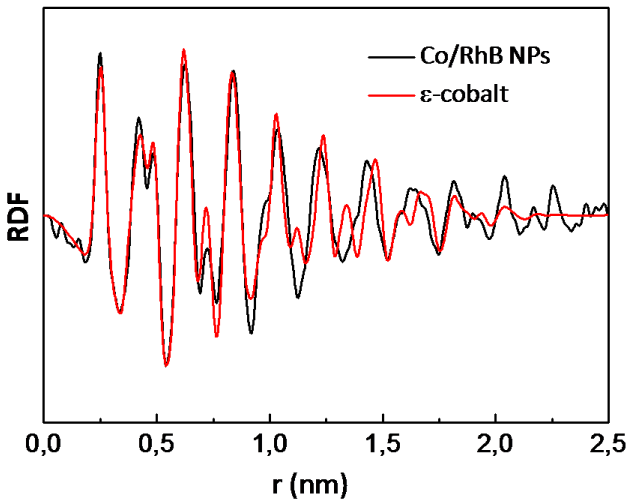

Figure 4-12. *WAXS spectra for Sample 4-1 (black) and a calculated model with ε structure (red).*

4 Purification of the system

Given the size of the NPs (3.8 nm), the percentage of surface cobalt atoms is about 30%. The Co/RhB ratio used during the synthesis (20 %) thus corresponds to an average of 2 RhB for

3 surface Co atoms. Given the bulkiness of this ligand it is however improbable that all RhB coordinates at the NPs surface. Size exclusion chromatography[vi] (SEC) has been used to elucidate this question. During this purification treatment, two different fractions were easily observed in the column **(Figure 4-13a)**, the first one corresponding to the Co NPs and the second to the excess of RhB. Absorption spectra of both fractions **(Figure 4-13b)** corroborates our assumption: fraction 1 shows a high diffusion signal due to the presence of NPs and the typical signature of RhB while fraction 2 only presents the typical absorption signature of the free dye. Furthermore, upon addition of $(NH_4)SCN$ to the later, no trace of the characteristic blue complex $(NH_4)_2[Co(SCN)_4]$ (ε=19500 at λ=620nm)[3] could be evidenced ruling out the presence of Co^{II} ions, excluding therefore the presence of a molecular complex formed between a cobalt center and RhB.

The colloidal solution corresponding to fraction 1 is only stable for a very short time, indicating that excess RhB most probably participates in the stabilization of the NPs, maybe via the establishment of Van der Waals interactions with coordinated RhB. All the spectroscopic and magnetic studies have thus been performed on unpurified samples.

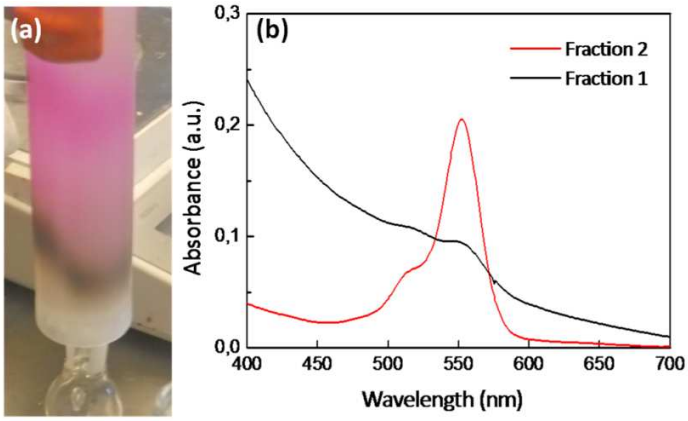

Figure 4-13. *(a) SEC of Sample 4-1 where the two fractions are clearly observed: the brown one corresponds to the Co/RhB NPs and the pink one is the excess of RhB. (b) Absorption spectra of both fractions.*

[vi] SEC is a chemical method in which molecules are separated as a function of their hydrodynamic volume. Therefore, in a chromatographic column in which the components of a mixture are eluted (transported), those with the bigger sizes will be eluted faster than the smaller ones.

5 Optical properties

The optical properties of Sample 4-1 have been studied by absorption and fluorescence spectroscopy in both steady-state and time resolved modes (see the Experimental Section for more details). Nevertheless, prior to the characterization of the hybrid Co/RhB and under the same conditions, we studied the absorption and fluorescence properties of the free organic dye. Such measurements provide us with useful information about the stability of the dye in solution and its natural emission properties in the absence of any quencher. For that purpose diluted solutions of free RhB were prepared in distilled anisole inside the glovebox. In order to avoid exposure to ambient conditions during the measurements, air-tight quartz cells were used and the samples were measured just after preparation. All the fluorescence experiments were performed with an excitation wavelength of 550 nm.

5.1 Static optical spectroscopy

Absorption and fluorescence spectra of RhB in anisole are presented in **Figure 4-14**. In the absorption spectra we can observe the characteristic signal of RhB with the maximum centered at 559 nm. On the other hand the fluorescence spectra show the emission band of that molecule with the maximum intensity located at 579 nm. In both cases we observe an increase in the intensity of the signals during the first 60 minutes after the preparation of the solution. After this period of time, only slight variations are observed in both absorption and emission spectra. We attribute the increase during the first 60 minutes after the preparation of the sample to the presence of RhB aggregates that are progressively dissolved. The presence of those aggregates has been confirmed with Dynamic Light Scattering (DLS) measurements,[vii] where hydrodynamic diameters above 100 nm were obtained **(Figure 4-14d)**. The small variation in fluorescence intensity once the RhB is solubilized may come from the tendency of RhB to form stacks in solution, increasing the nonradiative emission rate by intermolecular quenching. These results indicate the difficulty of obtaining quantitative data from the absorption and fluorescence spectra; this will also be the case with the solutions of Co/RhB nanohybrids.

[vii] DLS measurements have been carried out with a Zetasizer from Malvern Instruments. The source of light is a He-Ne laser with a wavelength of 633 nm.

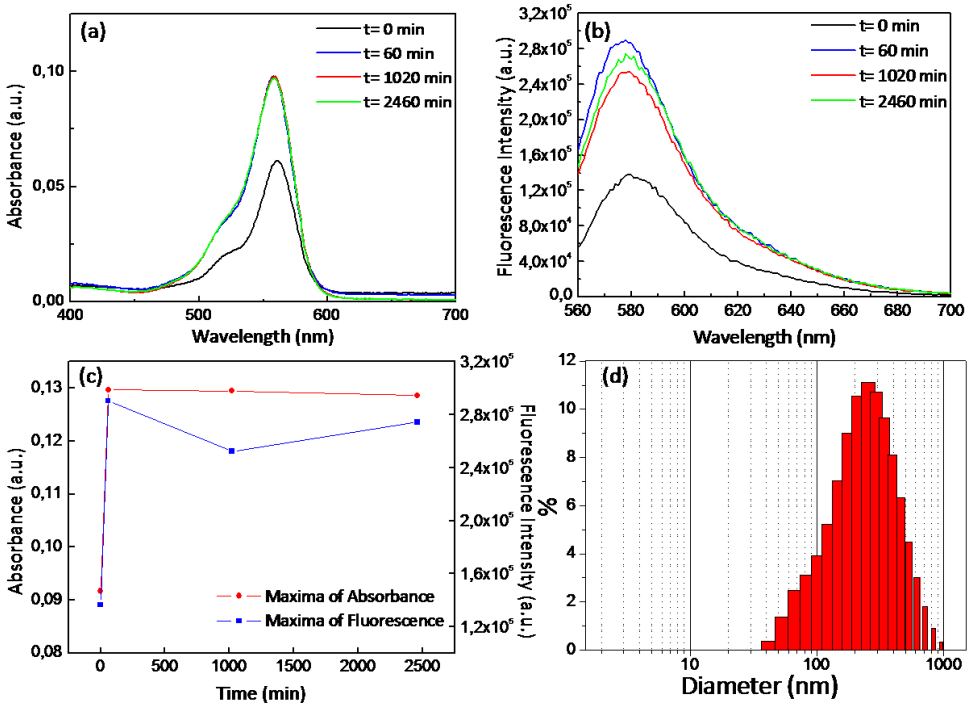

Figure 4-14. *Images (a) and (b) show the absorption and emission spectra of RhB in anisole at different times after preparation of the solution, respectively. (c)Represents the variation of the absorption and emission maxima as a function of time and (d) shows the hydrodynamic diameters obtained by DLS from a solution of RhB in anisole.*

We have recorded absorption and fluorescence spectra of Co/RhB NPs following the conditions explained above in order to observe the possible effect of the Co NP over the optical properties of RhB. In this case, the characteristic absorption spectrum of RhB is found with a maximum of absorbance centered at 560 nm, while at the same time a very weak fluorescence signal if compared with the emission spectrum of the free dye is observed. The emission signal is quenched by more than 99 % **(Figure 4-17)**.

The oxidation of the Co/RhB NPs leads to an interesting finding that confirms the direct attachment of the dye to the surface of the NPs. Actually, when the fluorescence of the sample is measured at different oxidation times, an increase of the fluorescence proportional to the oxidation time is observed **(Figure 4-15d)**. Such process has been followed by TEM, casting drops of the solution on carbon coated Cu grids. In those samples, a clear evolution of their morphology from the original 3-4 nm particles to the only presence of big aggregates with oxidation time was observed **(Figure 4-15a-c)**. We explain both effects as a consequence of the

lower affinity of RhB for oxidized surfaces, with the subsequent release of free dyes into the solution as the oxidation at the surface of the particles increases. Subsequently and due to the lack of stabilizers around the particles, they tend to aggregate and coalesce. Similarly, RhB-transition metal complexes become unstable when exposed to air, tending to release rhodamine.[26]

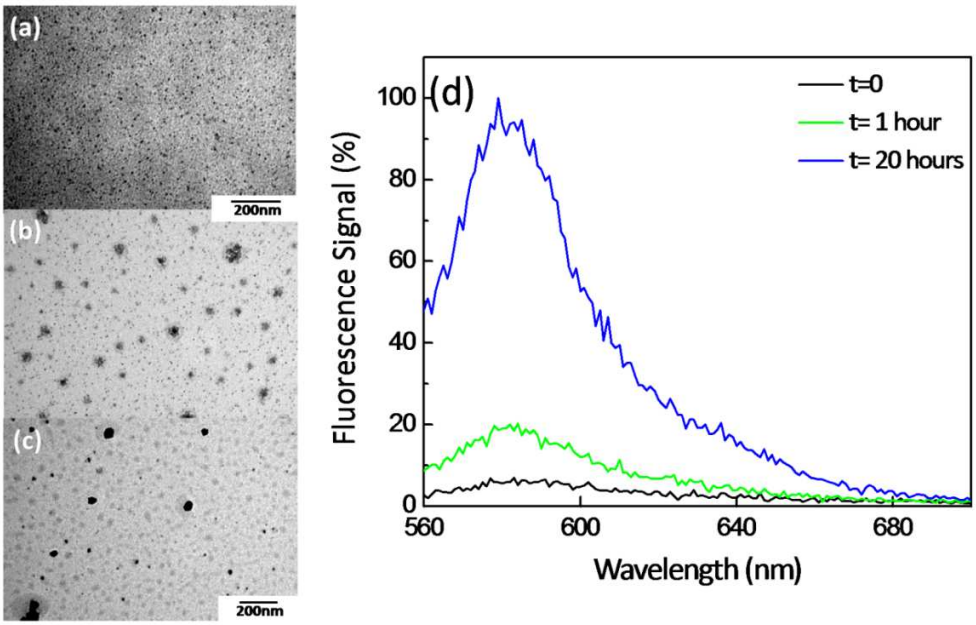

Figure 4-15. *(a-c) TEM images of Co/RhB NPs before exposure to air (a), and after 2 days (b) and one week (c) of air exposure. (d) Fluorescence spectra of Co/RhB as a function of oxidation time.*

Another experiment was performed to investigate the interaction between the Co NPs and RhB. In this case we added another molecule that could replace RhB at the surface of the NP. We used oleic acid (OA) for that purpose, due of its high affinity for metal surfaces and prior use for the stabilization of Co NPs. To carry this experiment we simply added an excess of OA and measured the resulting fluorescence spectra, comparing the intensity with that of the solution before addition of the surfactant **(Figure 4-16)**. As observed previously with the partial oxidation of the sample, an increase in the fluorescence intensity after addition of OA is clear, effect attributed to the release of RhB from the surface. This dynamic equilibrium confirms the weak affinity of the deactivated and sterically hindered carboxylic acid of the RhB if compared with that of oleic acid.

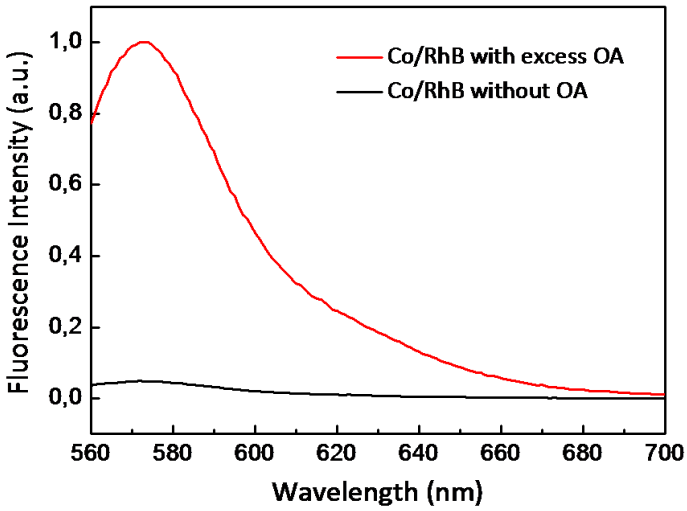

Figure 4-16. *Fluorescence intensity before (black) and after (red) an excess of oleic acid was added to the solution of Co/RhB NPs.*

To clarify if a direct interaction between RhB and the Co NP is mandatory for an effective quenching we performed another experiment in which RhB was mixed with different amounts of Co NPs with similar size stabilized with oleic acid **(Figure 4-17)**. In this case, the fluorescence decrease was less dramatic (50 % of the total intensity). We interpret the difference between both quenching efficiencies as a result of different quenching mechanisms. Therefore, we can attribute the almost complete quenching of fluorescence in the Co/RhB hybrids as a consequence of a chemical interaction between the adsorbed molecules and the magnetic NPs.

Quenching of the excess of unbound RhB can be explained taking into account its tendency to form stacks, situation that favors intermolecular quenching of their respective excited states.

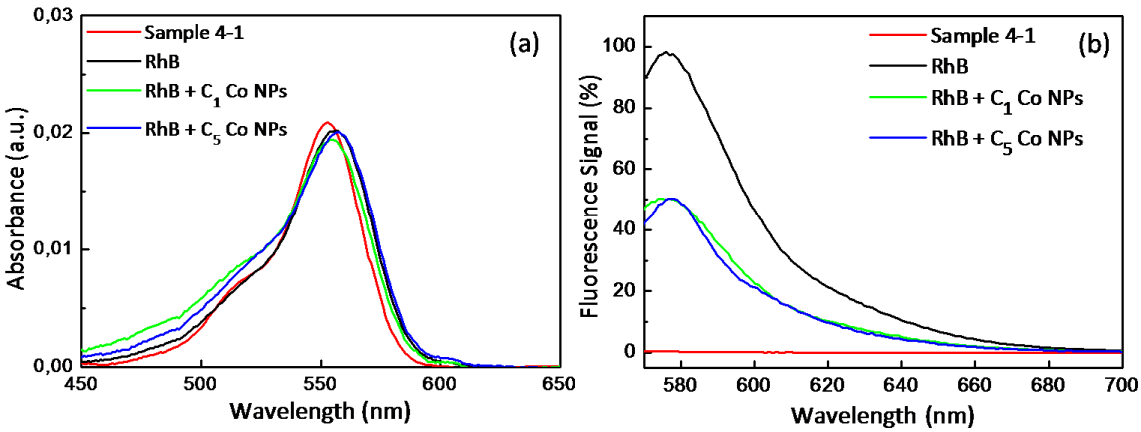

Figure 4-17. *Absorption (a) and fluorescence (b) spectra of Co/RhB NPs and comparison with free RhB, and free RhB with two different concentrations of Co NPs stabilized with oleic acid (C_5 represents 5 times the concentration of C_1).*

5.2 Time resolved optical spectroscopy

Time-resolved fluorescence and transient absorption spectroscopies have been used to investigate the nature and rates of the quenching process observed. While the first is used to measure the decay times of a given excited state, the second gives direct information about its nature.

Time-resolved fluorescence performed in anisole solutions of the Co/RhB hybrids shows two components:

1. Extremely weak fluorescence decay with a very short lifetime (< 20 ps: below the instrumental response).
2. Longer fluorescence lifetime (2.8 ns).

The faster component is attributed to the RhB directly linked to the Co NP while the slower refers to unbound molecules, which present unquenched decay rates. Such statement has been done after comparison with free RhB solubilized in anisole, solution that presents two decay times of 215 ps and 3.2 ns respectively **(Figure 4-18)**. The value of 3.2 ns corresponds to the free RhB in solution while the faster component suggests the presence of aggregates in the solution (as previously observed in static measurements).

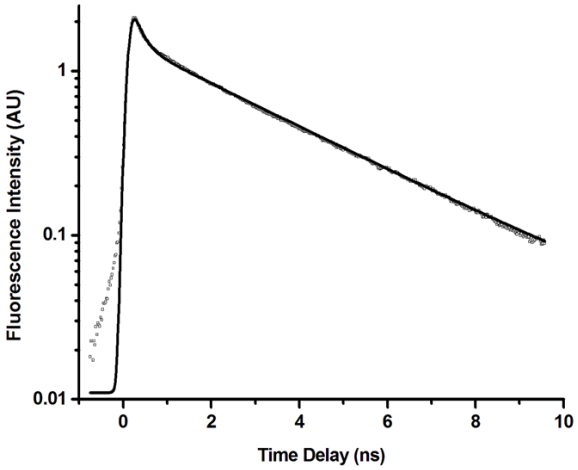

Figure 4-18. *Fluorescence decay of RhB in anisole showing two components of 215 ps and 3.2 ns (λexc: 532 nm and measured at 580 nm).*

From both quenched and unquenched lifetimes we can obtain the quenching rate (k_{PET}). Developing **(4.3)** for a fluorophore with and without quencher:

$$k_{PET} = \frac{1}{\tau} - \frac{1}{\tau_0} \cong 5 \cdot 10^{10} s^{-1} \quad \textbf{(4.11)}$$

where τ_0 and τ represent the unquenched and quenched lifetimes, respectively. Such quenching rate is two orders of magnitude higher than those observed for CdSe/Co hybrids[27,28] ($2.5 \cdot 10^8$ s^{-1} for Co/CdSe core/shell NPs and $6.9 \cdot 10^8$ s^{-1} for Co NPs grown on the tips of CdSe nanorods) and comparable to the value obtained in CdS/RhB.[29] This proves that the excited state of RhB interacts more efficiently with Co NPs than semiconductor moieties, representing the best conditions to observe the possible modification of the properties of the magnetic NP.

Once the quenching decay rate was quantified, we studied the nature of the process by transient absorption spectroscopy (TRABS). In this technique a first laser pulse of high intensity (pump) is used to populate the excited state of the dye. Before it (and at a controlled delay of time) a white light pulse of lower intensity (probe) is used to study the absorption spectrum of the final solution **(Figure 4-19, left)**, which at this point contains dye molecules in the excited and fundamental states (the latter being a residual contribution that appears due to incomplete photoexcitation during the first laser pulse or due to fast desexcitation). Then a differential absorption spectrum is calculated (absorption of the final spectrum minus absorption of initial

spectrum) and plotted as a function of the wavelength. The processes observed in TRABS spectra can be divided into four main categories:[30]

1. Ground state bleach (dashed line in **Figure 4-19, right**): after excitation the number of molecules in the ground state has been diminished and therefore the ground state absorption in the excited sample has a lower intensity than that of the non-excited one. Thus, a negative contribution will be observed on the TRABS spectrum.
2. Stimulated emission (dotted line in **Figure 4-19, right**): due to the population of the excited state, the photons from the probe pulse induce the emission of other photons from the excited molecules, which therefore decay to their respective ground states. The correspondent signal of this process normally overlaps with the ground state bleach, merging into one band.
3. Excited state absorption (solid line in **Figure 4-19, right**): once a molecule is promoted to its lower excited state, some transitions can occur from this state to higher excited ones. Here, a positive contribution to the TRABS spectrum is obtained.
4. Product absorption: once the molecule is excited some reaction that was forbidden at the fundamental state can occur and some transient molecular states can be stabilized. Triplet states or charge separated states are examples of this kind of transient products. In any of those cases a positive contribution is obtained.

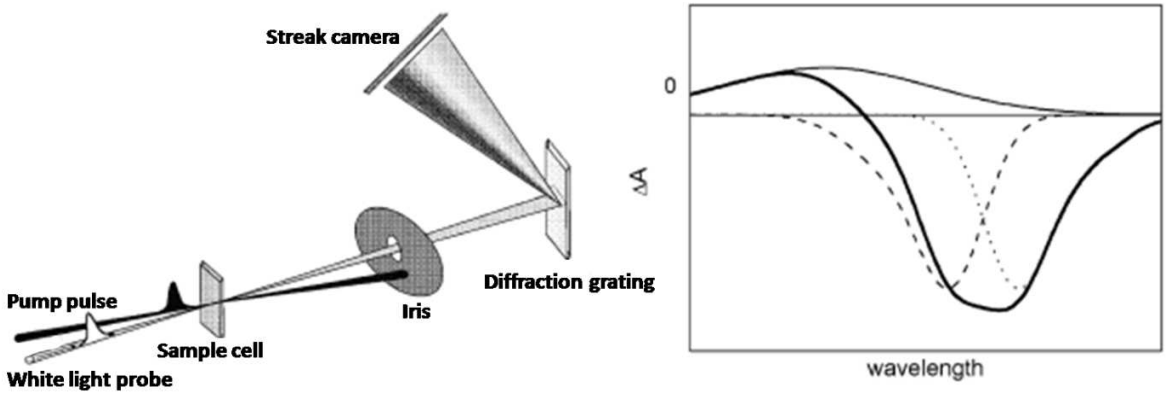

Figure 4-19. *Left side: schematic representation of the experimental set-up used in transition absorption spectroscopy. Right side: Contributions to ΔA spectrum: ground state bleach (dashed line), stimulated emission (dotted line), excited-state absorption (solid line) and sum of these contributions (gray line). Modified from Ref. 30.*

TRABS measurements on a solution of RhB in anisole after excitation at 532 nm shows two signals **(Figure 4-20)**: the negative signal represents the overlap of ground state bleach and stimulated absorption while the positive one represents the excited state absorption of RhB at 450 nm.

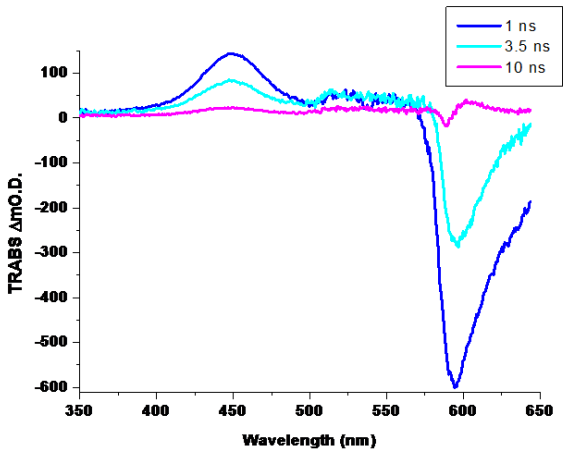

Figure 4-20. *TRABS spectrum of RhB in anisole at different time delays after excitation at 532 nm.*

For the sample of Co/RhB NPs we performed similar experiments. We found a positive absorption signature (typical from the absorption of the excited state) centered at 430 nm, signal ascribed to an anion radical of RhB after comparison with published data[31] **(Figure 4-21)**.

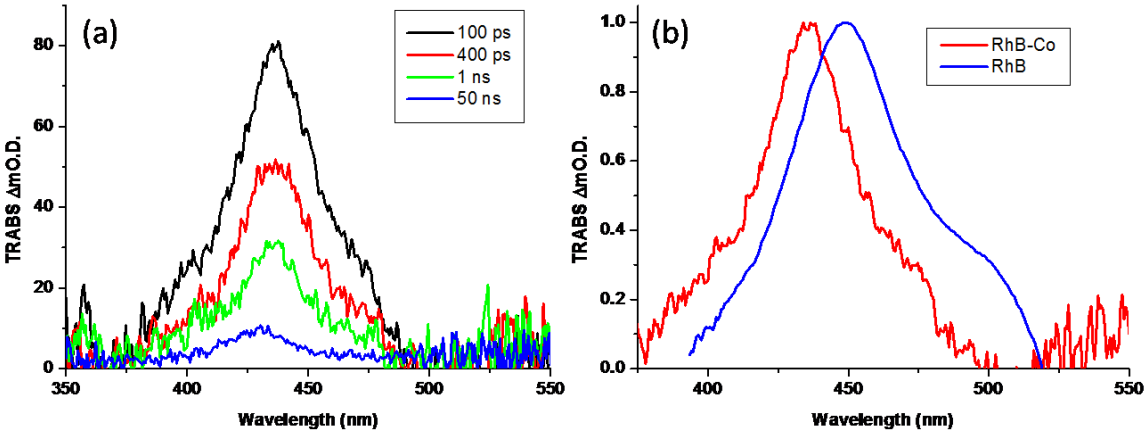

Figure 4-21. *(a) Enlarged TRABS spectrum of Co/RhB hybrids solubilized in anisole and comparison with a solution of the free dye in the same solvent (b).*

This result indicates an electron transfer process from the metal surface to the HOMO of the excited RhB, with the following charge separation. Subsequently, the excited state decays by charge recombination, but in this case the electron involved is the one present in the LUMO of the excited RhB **(4.12)**.

$$Co - RhB \xrightarrow{h\vartheta} (Co - RhB)^* \xrightarrow{e^- \, transfer} (Co^{h+} - RhB^{e-})^{*} \xrightarrow{recombination} Co - RhB \quad \textbf{(4.12)}$$

The decay profile as a function of time of this absorption band can be deconvoluted into two contributions **(Figure 4-22)** that differ substantially on their time scales: 220 ps and 61 ns respectively.

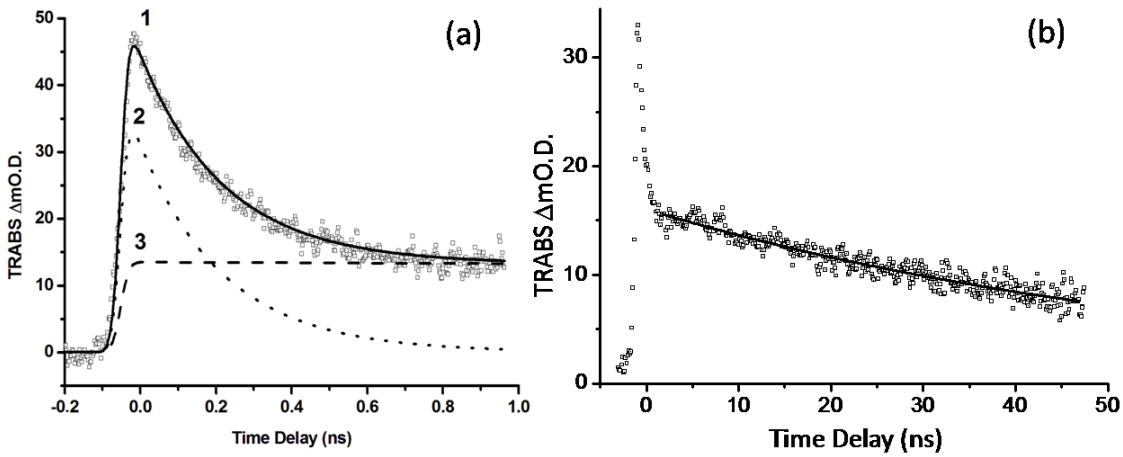

Figure 4-22. *Disappearance of the charge separated state of Co/RhB NPs in anisole on two different timescales measured at 430 nm, showing individual components: a) short timescale, trace 1 represents experimental data while 2 and 3 are two constituent components related to the recovery of the RhB S_0 state with the lifetime of 220 ps associated with 2. b) Longer timescale showing persistence of one component (lifetime 61 ns).*

On the other hand, the partial oxidation of the sample under ambient conditions decreases the capacity of the Co surface to act as an electron donor. In fact, a residual emission is observed in the oxidized sample, fact that can be related with the decomplexation of the RhB molecules from the oxidized Co surface. This finding is in agreement with the steady-state fluorescence spectra and the TEM images recorded on the particles as a function of oxidation time.

On longer time scales the recombination process from the excited state of the molecule to the oxidized surface is observed but with longer time constants than those observed for non-

oxidized NPs: 900 ps and 212 ps with respect to the original 220 ps and 61 ns, respectively **(Figure 4-23)**.

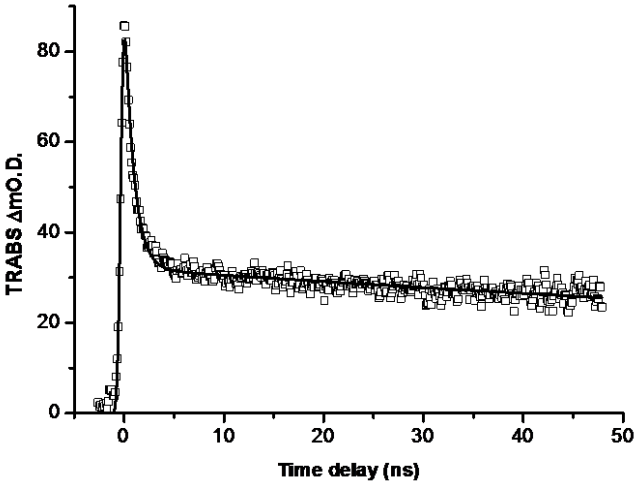

Figure 4-23. *Relaxation of the charge separated state of oxidized Co/RhB hybrids in anisole measured at 430 nm.*

5.3 Discussion

The data presented here show explicitly the physical interaction between RhB and the Co core when both entities are chemically connected. A strong static quenching is observed, leading to the disappearance of more than 99 % of the original fluorescence intensity. No such pronounced quenching is observed when RhB is mixed in solution with Co NPs stabilized with oleic acid, further confirming the importance of the direct interaction between dye and NP as main contribution for the drastic quenching of fluorescence.

Within this process, an electron transfer from the metal surface to the excited state of the molecule is observed, producing an excited intermediate with a net charge separation. Moreover, the energy difference between the Fermi level of Co (-5.2 eV)[32] and that of leuco dyes (-6.0 eV)[33] is in agreement with the electron transfer mechanism reported here **(Figure 4-24)**. The origin of the two contributions observed in this electron transfer process is difficult to assert but may be related with recombination of the electron with two different kinds of Co atoms since the electron can migrate back to a superficial Co atom or to the bulk of the NP. The difference in

nature comes from the different environment of surface Co atoms with respect to those present at the core.

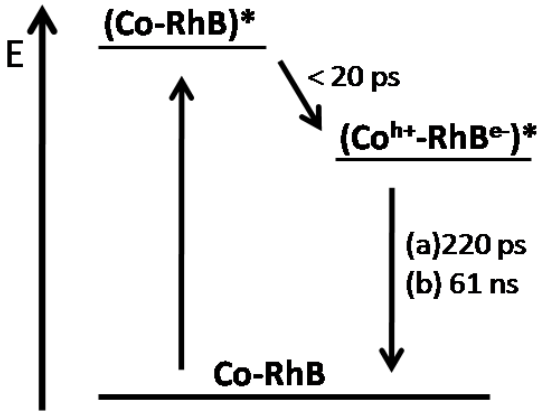

Figure 4-24. *Schematic representation of the excitation, charge transfer and desexcitation processes occurring on the Co/RhB hybrid upon light excitation (the time scales are also represented). Note: energy levels not at scale.*

Another mechanism that could explain this dual recombination arises from the excess of RhB present in the sample, most probably stacked forming multilayers around the particle. Such aggregation could lead to a second desexcitation pathway: in addition to the direct transfer of the electron back to the NP, it could be transferred from the excited radical RhB to a neighbor RhB molecule that is not attached to the metal surface. This process could be extended to several other molecules (since they are stacked together) until the electron finally returns to the Co NP **(Figure 4-25)**.

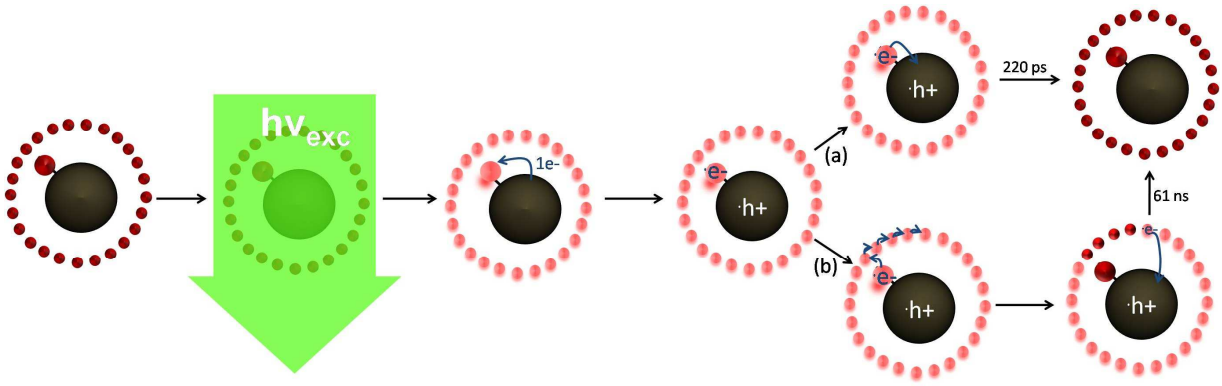

Figure 4-25. *Schematic representation of the excitation and recombination of the Co/RhB system where the big grey sphere represents the Co NPs and the small red ones are RhB molecules. (a) Represents the electron transfer through different RhB molecules prior to recombination with the Co NP and (b) represents the direct path between the attached RhB molecule and the particle.*

Other studies show electron transfer between a semiconductor NP and RhB.[29] More precisely, hybrids composed by CdS NPs with adsorbed RhB lead to the formation of a charge separated complex with a long lifetime (above the nanosecond regime) when the QD is excited by light irradiation. In this case, electron transfer from the QD to the LUMO of the dye has been elucidated by transient absorption spectroscopy. When CdSe NPs are used instead of CdS, a competition between electron and energy transfer is established due to the higher overlap of the absorption band of CdSe with the emission band of the dye.[34] Nevertheless, electron transfer remains the most important quenching process of the QD in this system, while energy transfer has only a secondary role (16 %).

In the case of Co/RhB hybrids, energy transfer can be ruled out as a reason for the important decrease in fluorescence. Indeed, in opposition to noble metals, cobalt NPs do not present localized surface plasmon resonances in the visible range of the spectrum nor do they present strong absorptions like quantum dots. Therefore, quenching is expected to be governed by a photoinduced electron transfer process.

In a similar way, fluorescence quenching has been also found in hybrid systems composed by magnetic and semiconductor NPs. Zanella and coworkers used FePt NPs as templates for the growth of semiconductor shells (PbS, ZnS, CdS, CdSe).[35] The final core-shell material present very weak fluorescence signals, fact that the authors explain as a consequence of electron transfer to the magnetic core. The growth of Co NPs on the tips of CdSe nanorods also affects the optical properties of the original particles, with a 30-fold decrease of the emission intensity and a shortening of the fluorescence lifetime, effects which are attributed to an electron transfer process from the semiconductor rod to the magnetic tip.[28]

The particles prepared by us present an excess of RhB that is not directly bound to the NPs surface. Nevertheless, this excess of RhB molecules in the crude solution forms aggregates around the particles, behaving like excimers in which the radiative decay transition is negligible. We could get rid of this excess by size exclusion chromatography but the pure solution obtained afterwards was not stable, most probably because these multilayers formed around the particles serve as spacers, avoiding flocculation of the colloidal suspension (a simplified sketch is presented in **Figure 4-25**).

The data obtained in the oxidized Co/RhB hybrids in both static and time-resolved spectroscopy show that the formation of the oxide shell around the particle decreases the binding affinity of the RhB, leading to a progressive flocculation and subsequent precipitation of the system. At the same time, the molecules that remain anchored at the surface during this process, present longer excited states (slower electron recombination) attributed to the formation of a CoO dielectric barrier.

6 Magnetic characterization

6.1 SQuID measurements

6.1.1 ZFC/FC curves and magnetization loops

Due to their small size, the Co/RhB nanohybrids are expected to present superparamagnetic behavior at room temperature. We studied the thermal variation of their magnetization applying a small magnetic field (10 mT) and recording classical ZFC/FC curves. The data show a blocking temperature of 38 K **(Figure 4-26a)**.

The broad morphology of the peak arises most probably from dipolar couplings between the particles and/or the effect of the size distribution of the sample. At the same time, when we plot the inverse of the magnetization as a function of temperature we observe that it can be extrapolated as a straight line above the blocking temperature, following the Curie-Weiss law **(Figure 4-26b)**. The fact that this straight line intercepts the x axis at –24 K instead of 0 K tells us that antiferromagnetic dipolar interactions exist between the particles.

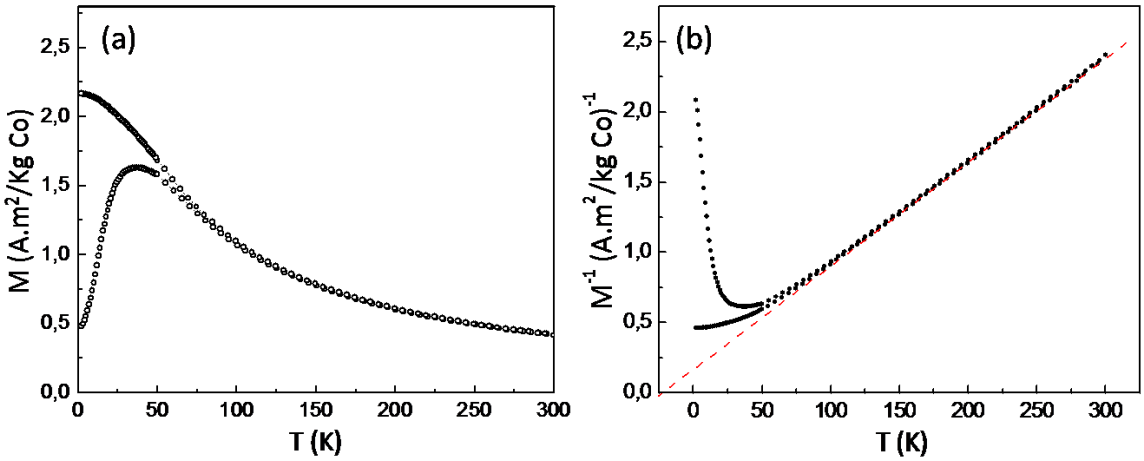

Figure 4-26. *(a) FC/ZFC curves for Sample 4-1 and (b) inverse of the magnetization as a function of the temperature.*

The magnetization curves recorded at 2 K show a magnetization of 152 $A{\cdot}m^2kg^{-1}$ **(Figure 4-27a)** at 5T, slightly below the bulk value (163 $A{\cdot}m^2kg^{-1}$).[viii] The small difference can be explained by a disordered surface spin structure (as suggested by the persistence of a differential susceptibility at 5 T) as a consequence of the coordination of carboxylate groups from RhB adsorbed at the surface of the NP or of the crystallographically disordered Co surface layer (see WAXS data). This magnetic behavior cannot be related with the presence of a Co^{2+} complex, since its presence has been ruled out by SEC. Surface oxidation can be dismissed too since no displacement of the hysteresis cycle is observed between the ZFC and FC magnetization curves **(Figure 4-27b)**.

[viii] The magnetization values reported here have been calculated taking into account the total Co content in the sample after determination by inductively coupled plasma mass spectrometry (ICP-MS).

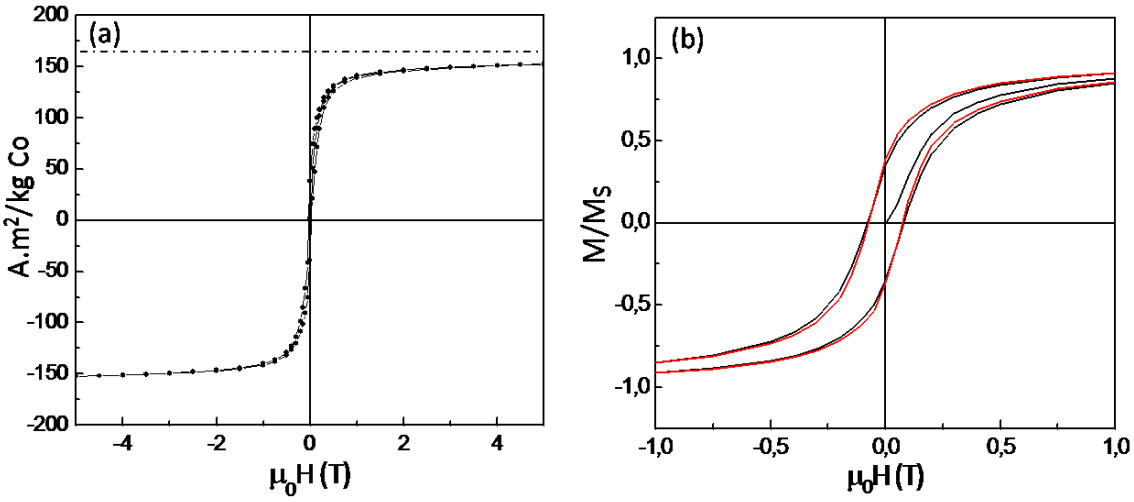

Figure 4-27. *(a) Magnetization curve recorded at 2 K for Sample 4-1 (the dotted line represents the magnetization value of bulk Co). (b) ZFC (black line) and FC (red line) curves recorded at 2 K for sample 4-1, in which no exchange-bias is observed.*

6.1.2 Magnetization measurements under irradiation

As we mentioned in the introductory section of this chapter, the previous papers published on the synthesis of fluorophore-stabilized magnetic NPs are mostly focused on the effect of the magnetic core over the optical properties of the fluorophore. Nevertheless, an interesting topic arises from the opposite process: how the fluorescent entity could affect the magnetic properties of the NP.

The Co/RhB hybrids presented in this chapter can serve as an original platform to investigate this question, since direct interaction between the organic fluorophore and the magnetic particle is strong enough to quench almost completely the optical properties of the dye. A photoinduced electron transfer process between the metal NP and the excited state of the molecule seems to be at the origin of the drastic decrease in fluorescence intensity, process that could have a net effect over the electron density at the Co surface and therefore over the magnetic properties of the whole particle. Magnetization measurements under light irradiation were performed to shed some light on this issue. The experimental set-up is the following:

1. Inside the glovebox, a small amount of the particles is introduced in a tiny quartz vessel (transparent to UV-visible light) and one drop of mineral oil is deposited on top of it in

order to avoid contact with air during the introduction of the sample inside the magnetometer.

2. The sample holder is introduced inside a tubular piece of quartz and connected to the rod that is introduced inside the magnetometer.
3. Light is driven inside the sample by an optical fiber connected to a lamp that emits white light. The original power of the lamp is 50 W but is reduced to 12 mW in the exit of the optical fiber. Irradiation periods of at least 10 minutes assure a photostationary population of the excited states of the molecules.

Once the sample is ready, it is cooled to 10 K (well below T_B = 38 K) and under a strong magnetic field (5 T) in order to avoid thermal fluctuations of the magnetization. Afterwards, the magnetization is measured before and after light irradiation. In all the experiments done under these conditions, a slight increase of the magnetization is always observed after the irradiation **(Figure 4-28)**. More precisely and depending on the experiment, the increase ranges between 0.3 % to 0.9% with respect to the magnetization value before irradiation. These variations between experiments are attributed to inhomogeneities in the powder at the microscopic level (only a few grains are introduced in the vessel) due to the presence of excess RhB. Still these values are similar to those obtained by Einaga and coworkers in their preliminary works on photoresponsive magnetic materials.[36] In these studies the authors intercalated Prussian blue (a ferromagnetic material at temperatures below 5.5 K) in vesicles containing azobenzene.[ix] An increase of approximately 1 % of the total magnetization of the sample was observed after photoisomerization of the azobenzene-loaded vesicles at low temperature (0.2 % when the sample was not purified, as in the present case), effect that remained for at least 2 hours after illumination.

Once the magnetization has been increased by light irradiation, the original value can be recovered by an increase of the temperature and subsequent cooling. Afterwards, the experiment can be reproduced successfully, proving the absence of photobleaching in our nanohybrids.

[ix] Azobenzene is a photoresponsive molecule that isomerizes from the *trans*- to the *cis*- conformation after UV irradiation. The opposite process is obtained with visible light (or heating).

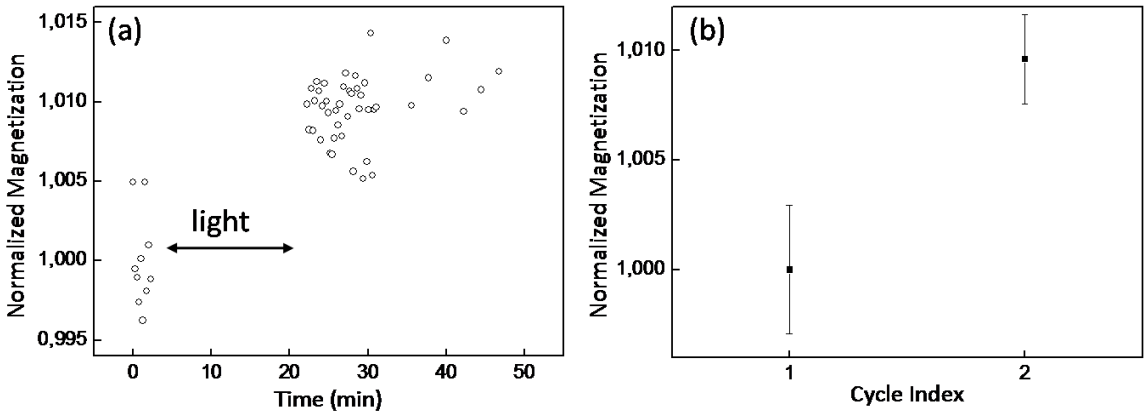

Figure 4-28. *Evolution of the magnetization of Sample 4-1 as a function of light-irradiation.*

Two control experiments have been carried out to ascertain the importance of the direct interaction between the dye and the metal surface on the photoinduced increase in magnetization. First, benzoic acid stabilized Co NPs with similar diameter (Sample 2-5) to that of the original hybrids reported here have been studied **(Figure 4-29a-b)**. In the second case, oleic acid stabilized Co NPs with a diameter of 3 nm and mixed with RhB (in the powder form) were submitted to the same experiment **(Sample 4-29c-d)**. Both control experiments show unambiguously a constant magnetization value (slight variations are within the experimental error), none of them comparable with that displayed by the Co/RhB hybrid and in agreement with the results obtained from photophysic studies.

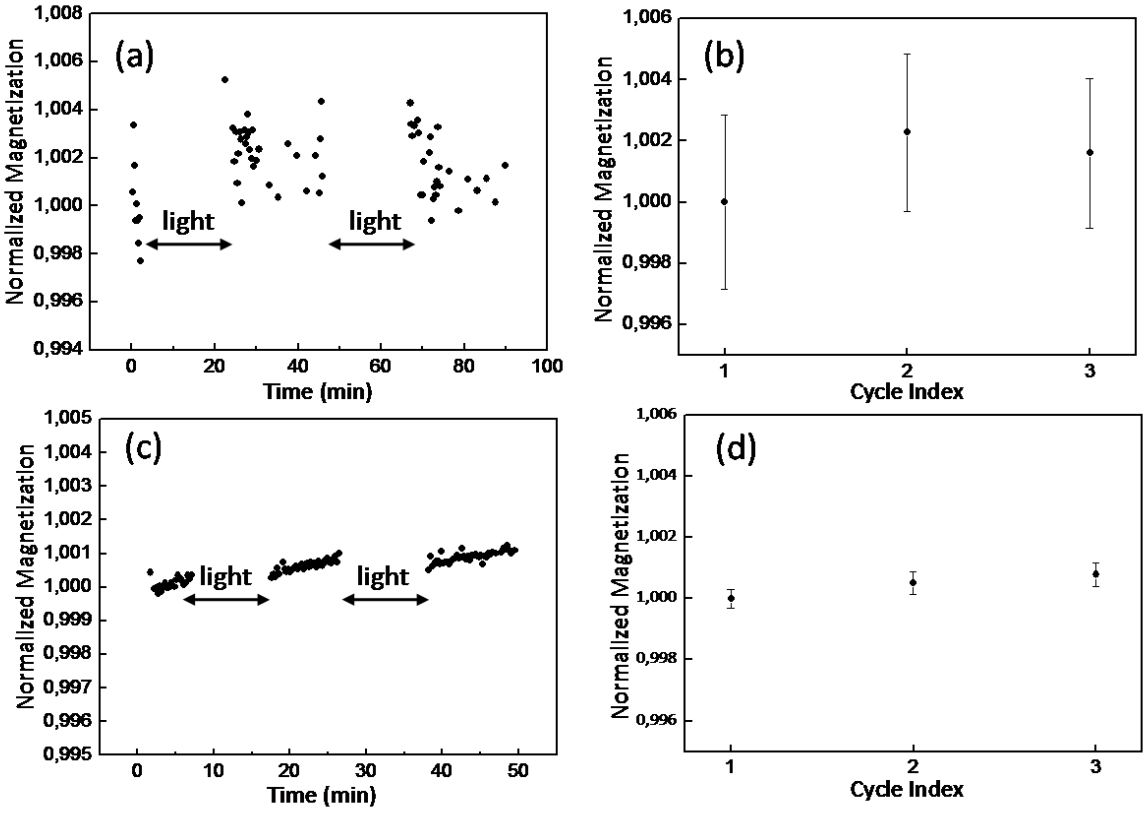

Figure 4-29. *Control experiments for the magnetization measurements under irradiation, (a-b) represent the experiment performed with Co NPs stabilized with benzoic acid and (c-d) those in which small Co NPs were mixed with RhB.*

6.2 Discussion

One important characteristic of the measurements done under irradiation is that they were always performed at an extremely low temperature (10 K). Under such conditions, and depending on the thermodynamics of the electron transfer which are yet unknown, three hypotheses can be made:

1. Temperature has no effect on the kinetics of the electron transfer.
2. At such a low temperature no electron transfer occurs.
3. Electron transfer between the particle and the excited state of the molecule is still effective but the return path is strongly slowed down or even completely suppressed.

If we assume that the first possibility is the correct one, no effect on magnetization should be observed given the relative time scales between light absorption (10^{-15} s), electron transfer (< 10^{-9} s) and the SQUID measurement (1-100 s): the whole photophysical process would take place before measurement of the magnetization be completed. The same conclusion holds for the second hypothesis. Indeed, in this case no quenching of the fluorescence should occur and RhB* would come back to its fundamental state with its characteristic time scale (3.2 ns) *i.e.* too fast for its effect to be detected by SQUID measurement. The third hypothesis implies a prolonged lifetime for the radical anion, modifying the local electric field surrounding the NP. Magnetoelectric effect has already been suggested by Einaga and coworkers to explain the increased magnetization observed in Fe_2O_3[37] and FePt[38] NPs after irradiation.

However here, the situation is more complicated as the formation of the radical anion supposes a decrease of the electron density of the NP, which is expected to have a negative effect on the magnetization of the NP. Compensation between these two effects may be the reason for the small increase in magnetization.

7 Conclusions

Within this chapter we have presented a new protocol for the synthesis of small Co NPs (diameter of 3.8 nm) with an organic fluorophore (Rhodamine B) as unique stabilizing agent which anchors at the surface via its carboxylic acid group. These particles present core crystallites (3 nm) with a ε crystalline structure, similar to that of β-Mn, and a disordered surface. As expected from their small size they are superparamagnetic at room temperature with a blocking temperature of 38 K. They display a high magnetization at 5 T (2 K) (93.2 % of bulk) and a differential susceptibility at high field probably related to their disordered surface.

As a result of the adsorption of the dye at the surface of the particle, a quenching of its intrinsic optical properties is observed. Such quenching is the direct consequence of an electron transfer from the metal surface to the excited state of the molecule. As a result of this, an excited complex is formed with separation of charges that subsequently recombine, with the decay of an electron from the LUMO of the RhB to the metal surface.

A small increase in the magnetization of the particles has been observed when measured at low temperatures and after light irradiation with white light. The origin of this phenomenon is yet unclear but may result from a modification of the polarity of the dye after excitation, variation that promotes a change on the local electric field experienced by the NP.

Time resolved magnetic measurements are now necessary to better understand and optimize the photomodulation of the magnetization, enabling better understanding of the different processes. Other dyes should be also tested (more strongly anchored to enable purification, or with LUMO and HOMO levels preventing electron transfer).

[1] S. A. Corr, Y. P. Rakovich, Y. K. Gun'ko, Nanoscale Res. Lett., 3 (2008), 87.
[2] J. R. Lackowicz, Principles of Fluorescence Spectroscopy, Springer, Ed. 2006.
[3] M. D. Lumb, Luminescence Spectroscopy, Academic Press, Ed. 1978.
[4] U. Resch-Genger, M. Grabolle, S. Cavaliere-Jaricot, R. Nitschke, T. Nann, Nature Methods, 5 (2008), 763.
[5] R. F. Kubin, A. N. Fletcher, J. Luminescence, 27 (1982), 455.
[6] V. O. Saik, A. A. Goun, M. D. Fayer, J. Chem. Phys., 120 (2004), 9601.
[7] P. Mulvaney, Langmuir, 12 (1996), 788.
[8] E. Dulkeith, M. Ringler, T. A. Klar, J. Feldmann, A. Muñoz Javier and W. J. Parak, Nano Lett., 5 (2005), 585.
[9] E. Dulkeith, A. C. Morteani, T. Niedereichholz, T. A. Klar, J. Feldmann, S. A. Levi, F. C. J.M. van Veggel, D. N. Reinhoudt, M. Möller, D. I. Gittins, Phys. Rev. Lett., 89 (2002), 203002.
[10] (a) C. S. Sun, A. Javier, T. Jennings, M. Fisher, S. Hira, S. Peterson, B. Hopkins, N. O. Reich, G. F. Strouse, J. Am. Chem. Soc. 127 (2005), 3115. (b) T. L. Jennings, M. P. Singh, G. F. Strouse, J. Am. Chem. Soc., 128 (2006), 5462.
[11] B. I. Ipe, K. G. Thomas, S. Barazzouk, S. Hotchandani, P. V. Kamat, J Phys. Chem. B, 106 (2002), 18.
[12] S. Barazzouk, P. V. Kamat, S. Hotchandani, J. Phys. Chem. B, 109 (2005), 716.
[13] J. R. Lakowicz, C. D. Geddes, I. Gryczynski, J. Malicka, Z. Gryczynski, K. Aslan, J. Lukomska, E. Matveeva, J. Zhang, R. Badugu, J. Huang, J. Fluoresc., 14 (2004), 425.
[14] Y. Chen, K. Munechika, D. S. Ginger, Nano Lett., 7 (2007), 690.
[15] F. Tam, G. P. Goodrich, B. R. Johnson, N. J. Halas, Nano Lett., 7 (2007), 496.
[16] G. Battistini, P. G. Cozzi, J.-P. Jalkanen, M. Montalti, L. Prodi, N. Zaccheroni, F. Zerbetto, ACS Nano, 2 (2008), 77.
[17] F. Bertorelle, C. Wilhelm, J. Roger, F. Gazeau, C. Ménager, V. Cabuil, Langmuir, 22 (2006), 5385.
[18] Q. Yang, J. Liang, H. Han, J. Phys. Chem. B, 113 (2009), 10454.
[19] A. C. Tedesco, D. M. Oliveira, Z. G. M. Lacava, R. B. Azevedo, E. C. D. Lima, P.C. Morais, J. Magn. Magn. Mater., 272–276 (2004), 2404.
[20] A. R. Simoni, M. P. Garcia, R. B. Azevedo, S. B. Chaves, Z. G. M. Lacava, E. C. D. Lima, P. C. Morais, A. C. Tedesco, J. Nanosc. Nanotech., 8 (2008), 5813.
[21] S. Chandra, S. Mehta, S. Nigam, D. Bahadur, New J. Chem., 34 (2010), 648.
[22] S. Otsuka, M. Rossi, J. Chem. Soc. A, 1968, 2630.
[23] J. Osuna, D. de Caro, C. Amiens, B. Chaudret, E. Snoeck, M. Respaud, J.-M. Broto, A. Fert, J. Phys. Chem., 1996, 100, 14571.
[24] D. P. Dinega, M. G. Bawendi, Angew. Chem. Int. Ed., 38 (1999), 1788.
[25] V. F. Puntes, K. M. Krishnan, P. Alivisatos, Appl. Phys. Lett., 78 (2001), 2187.
[26] D. L. Thorn, W. C. Wultz, J. Phys. Chem., 93 (1989), 1234.
[27] H. Kim, M. Achermann, L. P. Balet, J. A. Hollingsworth, V. I. Klimov, J. Am. Chem. Soc., 127 (2005), 544.
[28] J. Maynadié, A. Salant, A. Falqui, M. Respaud, E. Shaviv, U. Banin, K. Soulantica, B. Chaudret, Angew. Chem. Int. Ed., 48 (2009), 1814.
[29] A. Boulesbaa, A. Issac, D. Stockwell, Z. Huang, J. Huang, J. Guo, T. Lian, J. Am. Chem. Soc., 129 (2007), 15132.

[30] R. Berera, R. van Grondelle, J. T. M. Kennis, Photosynth. Res., 101 (2009), 105.
[31] P. C. Beaumont, D. G. Johnson, B. J. Parsons, J. Photochem. Photobiol. A, 107 (1997), 175.
[32] W. Gudat, O. Rader, O., 2.12.5 Co (Z = 27). A. Goldmann, (ed.), SpringerMaterials - The Landolt-Börnstein Database (http://www.springermaterials.com), DOI: 10.1007/10086040_11.
[33] K. Takaoka, S. Maeda, H. Miura, K. Endo, D. P. Chong, Bull. Soc. Chem. Jpn, 71 (1998), 807.
[34] A. Boulesbaa, Z. Huang, D. Wu, T. Lian, J. Phys. Chem. C, 114 (2010), 962.
[35] M. Zanella, A. Falqui, S. Kudera, L. Manna, M. F. Casula, W. J. Parak, J. Mater., Chem., 18 (2008), 4311.
[36] Y. Einaga, O. Sato, T. Iyoda, A. Fujishima, K. Hashimoto, J. Am. Chem. Soc., 121 (1999), 3745.
[37] R. Mikami, M. Taguchi, K. Yamada, K. Suzuki, O. Sato, Y. Einaga, Angew. Chem. Int. Ed., 43 (2004), 6135.
[38] (a) M. Suda, M. Nakagawa, T. Iyoda, Y. Einaga, J. Am. Chem. Soc., 129 (2007), 5538. (b) M. Suda, Y. Einaga, Angew. Chem. Int. Ed., 48 (2009), 1754.

General Conclusions

In this thesis we have tackled three main problems: the chemical control of the shape of magnetic oxide-free nanoparticles, the development of a suitable coating method for their protection against air oxidation and the design of new hybrid nanocomposites with luminescent and magnetic properties allowing photomodulation of their magnetization.

The decomposition of the organometallic complex $Co(\eta^3\text{-}C_8H_{13})(\eta^4\text{-}C_8H_{12})$ under dihydrogen and using Rhodamine B (an organic fluorophore of common use in biology) and hexadecylamine as capping agents leads to the formation of Co nanodisks. As observed by HRTEM, those objects present a hexagonal closed packed structure with the presence of twin planes along the [0001] direction. Control experiments suggest that the presence of defects is directly related with the anisotropic growth, since the presence of twin planes has been proved to be at the origin of the preferential 2D growth in similar structures. The bulkiness of Rhodamine B most probably prevents its interaction with the small nuclei formed in the first stages of the reaction, allowing the fast growth of their {0001} facets. These Co nanodisks present clean surfaces, bulk magnetization and blocked behavior at room temperature. Simulations show that these objects are single domains, holding an out of plane magnetization. All these characteristics make the Co nanodisks good candidates for magnetic recording applications. The next step would be the development of deposition methods onto the surface of *e.g.* silicon wafers.

As mentioned before, one of the main drawbacks for the use of fully-metallic magnetic NPs in real devices is their fast oxidation under ambient conditions and the loss of their magnetic properties over time. In the third chapter of this thesis we have demonstrated that it is possible to coat Co nanowires with a carbon shell by using the ligands adsorbed at their surfaces as carbon source. Such process, based on the annealing of the ligands, has to be performed under controlled conditions since a fast increase of the temperature leads to the decomposition of the anisotropic objects in a chain of spheres, as a consequence of the Rayleigh-Plateau instability. Under the conditions optimized to preserve the integrity of the nanowires, the carbon matrix is amorphous. Still, we have evidenced its efficiency in the protection of the magnetic NPs against air oxidation.

It is important to remark that this is the first example of the successful post-synthetic carbon coating of magnetic wires.

In the last part of this dissertation, we have reported on the design of new hydrid nanocomposites; Rhodamine B has been used to stabilize fully-metallic magnetic NPs of a few nanometers (3.8 nm in diameter). This nanohybrid presents a size and a surface state (no adventitious oxidation) well adapted to the study of surface effects. In addition, direct contact between the dye and the NP is ensured, offering the ideal conditions to study the interaction between both entities (magnetic core and luminescent dye). As expected, the fluorescence of the dye is completely quenched. We could demonstrate that this effect appears as consequence of an electron transfer from the particle to the HOMO of the excited molecule, leading to net charge separation. More importantly, we have observed that the magnetization of the Co NPs slightly increases when exposed to light, effect that might be controlled by the energetics of the electron transfer corresponding to the recombination process. This pioneering work could be a starting point for a series of experiments in which other fluorophores with different properties would be used to obtain magnetic hybrids with a high fluorescence intensity (avoiding charge separation) or with higher efficiency on photomodulation (controlling the recombination step). However, time resolved magnetic measurements will be necessary to better understand the fundamentals of the processes and select the suitable fluorophores.

Experimental section

Experimental section

1 Chemicals

1.1 Gases

The gases used have been supplied by Air Liquide-France **(Table 1)**. In the case of the glovebox, argon (Ar) is passed through a molecular sieve trap and Cu pellets in order to purify it prior to use (O_2 and H_2O < 1 ppm).

Table 1. *List of the gases used together with their degrees of purity.*

Gas	*Purity (%)*	*H_2O (ppm)*	*O_2 (ppm)*	*Hydrocarbons (ppm)*
Ar	99.995	3	2	0.5
Hydrogen	99.995	5	5	-

1.2 Solvents

Anisole (> 99 %) is purchased from Sigma-Aldrich. This solvent is purified following two different procedures, depending on the synthetic protocol for which it is used.

- NPs synthesized in chapters II and IV: anisole distilled over Na under Ar atmosphere.
- NPs synthesized in chapter III: anisole dried over Na and then filtered under Ar atmosphere.

Tetrahydrofuran (THF): obtained free of dioxygen and water from a Solvent Purification System (MBraun SPS800).

Toluene: obtained free of dioxygen and water from a Solvent Purification System (MBraun SPS800).

Pentane: obtained free of dioxygen and water from a Solvent Purification System (MBraun SPS800).

All the solvents are degassed by a freeze-thaw process prior to their use to avoid the presence of solubilized dioxygen.

1.3 Reactants

All the chemicals used in this work **(Table 2)** have been introduced inside the glovebox prior to their use in the synthesis of NPs.

Table 2. *List of chemicals used*

Reactant	***Company***	***Purity (%)***
$CoCl_2$ anhydrous	Alfa-Aesar	99,7
$Co(\eta^3\text{-}C_8H_{13})(\eta^4\text{-}C_8H_{12})$[1]	Nanomeps[i]	-
Hexadecylamine	Fluka	> 99
Oleylamine	Sigma-Aldrich	70
Oleic Acid	Fluka	>99
Stearic Acid	Fluka	> 99.5
Rhodamine B	Sigma-Aldrich	95
Benzoic Acid	Sigma-Aldrich	> 99.5
Biphenil-4-carboxylic acid	Sigma-Aldrich	95
Biphenil-2-carboxylic acid	Sigma-Aldrich	98
Pyronin Y	Sigma-Aldrich	≥ 45
Rhodamine 6G	Sigma-Aldrich	95
Rhodamine B base	Sigma-Aldrich	97

Rhodamine B, Rhodamine B base and Rhodamine 6G are dried overnight in presence of P_2O_5 prior to the introduction inside the glovebox. The rest of the chemicals are introduced without further purification.

1.4 Experimental requirements

All the synthetic protocols have been carried out using standard Schlenk techniques under Ar atmosphere to avoid contact with atmospheric conditions. The glass material is always kept at

[i] The product has been obtained following a procedure developed by Otsuka et al. that has been partially modified (Ref. 1).

least for one night inside an oven thermostated at 120°C and then warmed up under vacuum with a heating gun prior to use. Reactions under high pressures are performed in Fisher-Porter (FP) bottles, which resist pressures up to 8 bars. They are also kept in the oven and introduced inside the glovebox for their use. The system connecting the FP bottle and the H_2 bottle has to be purged by successive cycles of vacuum/H_2 (process repeated three times).

The preparation of the samples for analysis has been done inside the glovebox.

2 Synthesis of the samples

2.1 Sample 2-1

276 mg (1mmol) of Co(η^3-C_8H_{13})(η^4-C_8H_{12}), 479 mg (1mmol) of Rhodamine B and 241 mg (1mmol) of HDA are introduced inside a FP bottle. Afterwards, 20 mL of anisole are added and a suspension is formed. The bottle is pressurized with a dynamic current of 3 bars of H_2 for 15 minutes. After this period of time, it is introduced in a mineral oil bath previously thermostated at 150 °C. At this temperature the previously turbid mixture becomes a solution with very dark pink coloration. After 48 hours the F-P bottle is removed from the oil bath and cooled down to room T. At this point we observe a red solution and two solids: one black deposited on the stirring bar and other blue. The excess of H_2 is removed and the red solution and the blue precipitate can be evacuated with a canula. The black solid is washed 3 times with anisole to remove the excess of ligands and finally 40 mg of product are removed from the stirring bar with the help of a magnet and stored in the glovebox.

TEM: for the preparation of the sample a small amount of the product is solubilized with THF. Disk shaped NPs are observed in the TEM images.

Microanalysis: % Co = 97.

SQuID : M (5 T, 2 K) = 1.66 μ_B.

2.2 Sample 2-2

277 mg (1 mmol) of HDA-HCl are mixed with 64,9 mg (0.5 mmol) of $CoCl_2$ solubilized in 10 mL of anisole, forming the $CoCl_4(HDA)_2$ complex. At the same time, 138 mg (0.5 mmol) of Co(η^3-C_8H_{13})(η^4-C_8H_{12}) are solubilized in 10 mL of anisole inside a FP bottle. Subsequently, the blue solution composed by the $CoCl_4(HDA)_2$ complex is added over the solution of Co(η^3-

C_8H_{13})(η^4-C_8H_{12}) via of a canula. The bottle is pressurized with a dynamic pressure of 3 bars of H_2 for 15 minutes. After this, it is introduced in a mineral oil bath previously thermostated at 150 ^oC and the reaction takes place for 48 hours. After this period of time we observe the presence of a black precipitate on the magnetic bar. The excess of H_2 is evacuated and the blue solution removed via a canula. The black product (<10 mg) is collected with the help of a magnet and stored inside the glovebox.

TEM: for the preparation of the sample a small amount of the product is solubilized with THF. The sample is composed by nanocubes (edge length ≅ 80 nm) and big and polydisperse particles.

2.3 Sample 2-3

This reaction follows a procedure similar to that explained for Sample 2-1 but in this case without HDA. At the end of the reaction a pink solution and a black precipitate are obtained. The solution is evacuated with a canula and the product washed with anisole. Finally 20 mg of a black solid are recovered.

TEM: for the preparation of the sample a small amount of the product is solubilized with THF. Polydisperse and aggregated particles are observed.

2.4 Samples 2-4 to 2-9

The experimental conditions are those reported for Sample 2-1, the only difference is the use of substitutes for RhB (Table 3). In the particular case of Sample 2-7 bis and Sample 2-8 the reaction has been performed using only Pyronin Y or Rhodamine B base as ligands (without HDA), respectively.

2.4.1 Sample 2-4

TEM: the TEM sample is directly prepared with the crude solution. A population of small particles with a diameter of 2.24 nm is observed.

Microanalysis: % Co = 13.94.

SQuID: M(5 T, 2 K)= 1.74 μ_B.

2.4.2 Sample 2-9

TEM: for the preparation of the sample a small amount of the product is solubilized with THF. Disk shaped NPs with a high degree of aggregation are observed in the TEM images, together with big particles above the micrometer.

Microanalysis: % Co = 98.

SQuID: M(5 T, 2 K)= 1.65 μ_B.

Table 3. *RhB substitutes.*

Chemical	*MW (mg)*	*Sample*
Benzoic Acid	122.1	2-4
Biphenyl-4-carboxylic acid	198.2	2-5
Biphenyl-2-carboxylic acid	198.2	2-6
Pyronin Y	302.8	2-7
Rhodamine B base	442.6	2-8
Rhodamine 6G	479	2-9

2.5 Sample 3-1

284.5 mg (1 mmol) of stearic acid and 241 mg (1 mmol) of HDA are solubilized in 20 mL of filtered anisole. Then the solution is transferred with a canula to a FP bottle in which 276 mg (1 mmol) of Co(η^3-C_8H_{13})(η^4-C_8H_{12}) had been previously introduced. The brown solution is let under magnetic stirring for 15 minutes before hydrogenation for another 15 minutes. After this period of time, it is introduced in a mineral oil bath previously thermostated at 150^{o}C. After 48 hours the F-P bottle is removed from the oil bath and cooled down to room T. The brown solution (composed by spherical NPs with a diameter of 3 nm) is removed with a canula. A black solid is obtained (100 mg) that is stored inside the glovebox.

TEM: for the preparation of the sample a small amount of the product is solubilized with toluene. The sample is composed by Co nanorods with a length of 100 nm and a diameter of 4 nm. A population of spherical NPs with a diameter of 3 nm is also observed.

Microanalysis: % Co = 6.

SQuID: M(5 T, 2 K)= 1.52 μ_B.

2.6 Sample 3-2

In this case 2 mmol of oleic acid (633 μL) and 1 mmol of oleylamine (328 μL) are mixed in 20 mL of filtered anisole. The resultant solution is added over 276 mg (1 mmol) of Co(η^3-C_8H_{13})(η^4-C_8H_{12}) inside a FP bottle. A violet solution that is stirred for 15 minutes is formed. Then the hydrogenation with 3 bars of H_2 takes place for other 15 minutes and the FP bottle is introduced in an oil bath settled at 150°C for 48 hours. Like in Sample 3-1, a brown solution formed by spherical NPs is removed and the black solid deposited on the stirring bar (22 mg) is stored inside the glovebox for further characterization.

TEM: for the preparation of the sample a small amount of the product is solubilized with toluene. The sample is composed by Co nanowires with lengths above the micrometer and a diameter of 7 nm. A small population of spherical NPs with a diameter of 3 nm is also observed.

Microanalysis: % Co = 6.2.

SQuID (5 T, 2 K): 1.83 μ_B.

2.7 Sample 4-1

Inside the glovebox 95.8 mg of Rhodamine B (0.2 mmol) and 276 mg of Co(η^3-C_8H_{13})(η^4-C_8H_{12}) are mixed together in a FP bottle and solubilized with 20 mL of distilled anisole. The obtained reddish suspension is hydrogenated with 3 bars of H_2 and let to react at room temperature for 14 hours. After this period of time the excess of dihydrogen is evacuated and the solvent removed by evaporation with the schlenk line. The dark-pink solid obtained (130 mg) is kept inside the glovebox.

TEM: the TEM sample is directly prepared with the crude solution. A population of 3.8 nm NPs is observed. Even though the particles are in general well dispersed, in some areas big agglomerates of them can be observed.

Microanalysis: % Co = 33.9.

SQuID (5 T, 2 K): 1.60 μ_B.

2.8 Sample 4-2

We repeat the same conditions explained for Sample 4-1 but in this case the decomposition of the Co precursor is done without any stabilizer. Therefore, 276 mg (1mmol) of $Co(\eta^3\text{-}C_8H_{13})(\eta^4\text{-}C_8H_{12})$ are solubilized in 20 mL of distilled anisole and the reaction is left under 3 bars of H_2 with magnetic stirring for 14 hours. After this time a metallic deposition is observed in both the magnetic stirring bar and the glass of the FP bottle, together with a black solution.

TEM: the solid obtained here is solubilized in THF and observed in the microscope. It is composed by agglomerates and NPs of very polydisperse size. The solution only presents aggregates.

2.9 Sample 4-3

In Sample 4-3 95.8 mg (0.2 mmol) of Rhodamine 6G are mixed with 276 mg of $Co(\eta^3\text{-}C_8H_{13})(\eta^4\text{-}C_8H_{12})$ and solubilized with 20 mL of distilled anisole. 3 bars of H_2 are introduced and the orange-brown suspension reacts at room temperature for 14 hours. Like in Sample 4-1, the solvent is evaporated and the brown solid is collected (120 mg).

TEM: the TEM sample is directly prepared with the crude solution. Big aggregates of irregular Co NPs are observed.

Microanalysis: % Co = 36.2.

SQuID (5 T, 2 K): 1.67 μ_B.

2.10 Sample 4-4

The experimental conditions for Sample 4-4 are very similar to Sample 4-1 and 4-3. In this case the ligand added is Pyronin Y and in the same molar relation than the previous syntheses (0.2 mmol – 60.5 mg). In this case a black precipitate is obtained from the magnetic bar.

TEM: for the preparation of the sample a small amount of the product is solubilized with THF. Big aggregates are observed in the images.

3 Microanalysis

The quantification of the metallic composition in our samples has been determined by ICP-MS (Inductively Coupled Plasma–Mass Spectrometry). Such quantification has been done

by the personnel of Antellis (http://www.antellis.com), a scientific company settled in Toulouse (France) that provides results validated according to ISO specifications.

4 Electron microscopy

For the preparation of the samples one drop of the colloidal solution is cast on the C coated Cu grid in the case of TEM samples or in a SiO_2 substrate in the case of the SEM samples.

The TEM images have been obtained from different microscopes situated in the University of Toulouse (France) and the University of Duisburg-Essen (Germany). The full list is presented here:

4.1 University of Toulouse

JEOL JEM 1011 (100 kV).

JEOL JSM 6700F (0.5-30 kV).

JEOL JEM 2100F TEM-FEG (200 kV, field emission gun and a point resolution of 0.23 nm).

4.2 University of Duisburg

Philips FEI/TecnaiF20ST (200 kV, field emission gun, Super-Twin lens and a point resolution of 0.24 nm).

CM12/Philips (120 kV). For the in-situ heating experiments a Standard Philips single-tilt heating sample holder (PW 6592/00) was applied. The holder permits controlled heating of the sample in the range 20-1000 ^{o}C.

5 Wide angle X ray scattering (WAXS)

Structural characterization by WAXS was performed in the solid state by Pierre Lecante in the CEMES (Centre d'Elaboration des Matériaux et d'Etudes Structurales, CNRS) settled at Toulouse (France). The fine powder was introduced into a thin walled Lindemann capillary of 1 mm diameter subsequently sealed under argon. The samples were irradiated with graphite-monochromatised molybdenum K radiation (0.071069 nm). The scattered intensity was recorded by a dedicated two-axis diffractometer. Fluorescence from iron was removed at the measurement step by filtering. Time for data collection was typically 20 hours for a set of 457 measurements

collected at room temperature in the range $0 °< \theta < 65°$ for equidistant s values [$s = 4\pi(\sin\theta/\lambda)$]. Treatment of the data has been carried out according to a previous work by Dassenoy et al.[2] to allow the analysis of the radial distribution function (RDF) of the NPs.

6 Magnetic measurements

The measurements have been done by Alain Mari, in charge of the Magnetic Measurements Facility in the Laboratoire de Chimie de Coordination, with a Super Quantum Interference Device (MPMS Quantum Design 5.5), spectrometer that holds a precision of 10^{-8} emu. The temperature can be varied between 2 and 400 K and the magnetic field is created by a superconducting coil, reaching a maximum value of 5.5 T.

The samples are prepared inside the glovebox, introducing the powder inside a gelatin capsule. To avoid the physical movement of the particles during the measurement it is compressed with another capsule with a smaller diameter than the previous one and partially impregnated with silicon grease.

In the particular case of the magnetization measurements performed the experimental set-up is the following:

1. Inside the glovebox, a small amount of the particles is introduced in a tiny quartz vessel (transparent to UV-visible light) and one drop of mineral oil is deposited on top of it in order to avoid contact with air during the introduction of the sample inside the magnetometer.
2. The sample holder is introduced inside a tubular piece of quartz and connected to the rod that is introduced inside the magnetometer.
3. Light is driven inside the sample by an optical fiber connected to a lamp that emits white light. The original power of the lamp is 50 W but is reduced to 12 mW in the exit of the optical fiber. Irradiation periods of at least 10 minutes assure a photostationary population of the excited states of the molecules.

Once the sample is ready, it is cooled to 10 K and under a strong magnetic field (5 T) in order to avoid thermal fluctuations of the magnetization. Afterwards, the magnetization is measured before and after light irradiation.

7 Optical properties.

Solutions of Co/RhB NPs were prepared by dissolution of the powder in anisole (eventually further dilution steps were necessary) in the glovebox and transferred into air-tight cells for measurement. Electronic absorption spectra were recorded on a SPECORD 205 (Analytical Jena) spectrometer over the range 300-700 nm. Steady-state fluorescence emission spectra were recorded on a PTI model QM-4 spectrofluorimeter (Photon Technology International, USA) exciting at the maximum for the absorption spectra and scanning over the range 560-700 nm. Band pass was set at 1 nm both at the emission and excitation sides. All the solutions were freshly prepared inside the glovebox using air-tight fluorescence cells (Hellma).

Time-resolved spectroscopy measurements have been done by Pinar Batat, Gediminas Jonusauskas and Nathan D. McClenaghan in the Institut des Sciences Moléculaires & Centre de Physique Moléculaire Optique et Hertzienne located at Bordeaux (France).

Transient absorption/time-resolved fluorescence set-up was built as follows. A frequency tripled Nd:YAG amplified laser system (30 ps, 30 mJ @1064 nm, 20 Hz, Ekspla model PL 2143) output was used to pump an optical parametric generator (Ekspla model PG 401) producing tunable excitation pulses in the range 410 – 2300 nm. The residual of fundamental laser radiation was focused in a high pressure Xe filled breakdown cell where a white light pulse for sample probing was produced. All light signals were analyzed by spectrograph (Princeton Instruments Acton model SP2300) coupled with a high dynamic range streak camera (Hamamatsu C7700). Accumulated sequences (sample emission, probe without and with excitation) of pulses were recorded and treated by HPDTA (Hamamatsu) software to produce two dimensional maps (wavelength vs delay) of transient absorption intensity in the range 300 – 800 nm. Typical measurement error was better than 10^{-3} OD.

Oxidized samples were equally studied at the sub-picosecond timescale: A Ti:Sapphire laser system emitting pulses of 0.6 mJ and 30 fs at 800 nm and 1 kHz pulse repetition rate (Femtopower Compact Pro) with optical parametric generator (Light Conversion Topas C) and frequency mixers followed was used to excite samples at the maximum of the steady state absorption band. A white light continuum (360 nm – 1000 nm) pulses generated in a 5 mm D_2O cell were used as a probe. The variable delay time between excitation and probe pulses was obtained using a delay line with 0.1 µm resolution. The solutions were placed in 1 mm circulating

cell. White light signal and reference spectra were recorded using a two channel fibre spectrometer (Avantes Avaspec-2048-2). A home-written acquisition and experiment control program (in LabView) made possible to record transient spectra with an average error less than 10^{-3} of optical density for all wavelengths. The temporal resolution of the set-up was better than 50 fs. A temporal chirp of probe pulse was corrected by a computer program with respect to a Lawrencian fit of a Kerr signal generated in a 0.2 mm glass plate used in place of the sample.

8 X-Ray Diffraction

X-ray diffraction of Sample 2-Blue has been performed by Laure Vendier in charge of the X-Ray Diffraction Facility in the Laboratoire de Chimie de Coordination using a Bruker Kappa APEX II diffractometer.

Table 4. *Crystallographic data for Sample 2-Blue*

Empirical formula	2(C16 H36 N), Cl4 Co
Formula weight	685.65
Temperature	180(2) K
Wavelength	0.71073 A
Crystal system, space group	Monoclinic, P 21/c
Unit cell dimensions	a = 7.2680(8) A alpha = 90 deg. b = 10.1510(6) A beta = 91.278(4) deg. c = 52.6580(9) A gamma = 90 deg.
Volume	3884.0(5) A^3
Z, Calculated density	4, 1.173 Mg/m^3
Absorption coefficient	0.739 mm^-1
F(000)	1492
Crystal size	0.2 x 0.2 x 0.025 mm
Theta range for data collection	2.04 to 23.19 deg.
Limiting indices	-6<=h<=8, -11<=k<=11, -57<=l<=58
Reflections collected / unique	25676 / 5480 [R(int) = 0.0555]
Completeness to theta = 23.19	99.3 %
Absorption correction	Semi-empirical from equivalents

Max. and min. Transmission	0.979 and 0.883
Refinement method	Full-matrix least-squares on F^2
Data / restraints / parameters	5480 / 2 / 356
Goodness-of-fit on F^2	1.126
Final R indices [I>2sigma(I)]	R1 = 0.057, wR2 = 0.1116
R indices (all data)	R1 = 0.0846, wR2 = 0.1205
Largest diff. peak and hole	0.433 and -0.401 e.A^-3

Table 5. *Atomic coordinates (x 10^4) and equivalent isotropic displacement parameters (A^2 x 10^3) for Sample 2-Blue. U(eq) is defined as one third of the trace of the orthogonalized Uij tensor.*

	x	y	z	U(eq)
N(1)	2223(5)	3862(4)	5238(1)	31(1)
C(2)	3394(6)	3211(4)	5436(1)	30(1)
C(3)	2590(6)	3324(5)	5695(1)	32(1)
C(4)	3671(7)	2533(4)	5893(1)	33(1)
C(5)	3140(6)	2868(4)	6163(1)	33(1)
C(6)	4214(7)	2168(4)	6373(1)	32(1)
C(7)	3795(6)	2688(4)	6636(1)	32(1)
C(8)	4862(7)	2054(4)	6854(1)	32(1)
C(9)	4444(6)	2656(4)	7111(1)	32(1)
C(10)	5516(7)	2043(4)	7333(1)	31(1)
C(11)	5090(7)	2659(4)	7588(1)	32(1)
C(12)	6168(6)	2064(4)	7810(1)	32(1)
C(13)	5745(6)	2679(4)	8066(1)	32(1)
C(14)	6846(7)	2093(4)	8287(1)	32(1)
C(15)	6405(6)	2687(4)	8545(1)	31(1)
C(16)	7551(7)	2116(5)	8764(1)	41(1)
C(17)	7044(7)	2678(5)	9022(1)	49(1)
N(2)	2361(5)	10630(4)	4641(1)	35(1)
C(19)	2989(7)	10729(5)	4374(1)	34(1)
C(20)	1591(6)	10199(5)	4186(1)	32(1)
C(21)	2160(7)	10519(5)	3916(1)	32(1)
C(22)	927(6)	9923(4)	3709(1)	30(1)
C(23)	1410(7)	10421(4)	3446(1)	32(1)
C(24)	260(6)	9846(4)	3229(1)	29(1)
C(25)	712(6)	10420(4)	2972(1)	29(1)
C(26)	-400(6)	9849(4)	2751(1)	29(1)
C(27)	45(7)	10438(4)	2496(1)	29(1)
C(28)	-1061(6)	9866(4)	2274(1)	30(1)
C(29)	-591(6)	10464(4)	2018(1)	27(1)
C(30)	-1681(6)	9880(4)	1796(1)	29(1)
C(31)	-1206(6)	10457(4)	1540(1)	29(1)
C(32)	-2246(6)	9849(4)	1316(1)	28(1)
C(33)	-1710(7)	10406(5)	1062(1)	33(1)
C(34)	-2711(7)	9759(5)	839(1)	41(1)
Co(1)	2506(1)	7696(1)	5128(1)	27(1)
Cl(1)	5115(2)	6617(1)	5239(1)	33(1)
Cl(2)	1836(2)	7516(1)	4704(1)	31(1)
Cl(3)	150(2)	6697(1)	5329(1)	35(1)
Cl(4)	2665(2)	9837(1)	5241(1)	45(1)

Table 6. *Bond lengths [A] and angles [deg] for Sample 2-Blue.*

N(1)-C(2)	1.483(5)
N(1)-H(1A)	0.91
N(1)-H(1B)	0.91
N(1)-H(1C)	0.91
C(2)-C(3)	1.500(6)
C(2)-H(2A)	0.99
C(2)-H(2B)	0.99
C(3)-C(4)	1.524(6)
C(3)-H(3A)	0.99
C(3)-H(3B)	0.99
C(4)-C(5)	1.516(6)
C(4)-H(4A)	0.99
C(4)-H(4B)	0.99
C(5)-C(6)	1.519(6)
C(5)-H(5A)	0.99
C(5)-H(5B)	0.99
C(6)-C(7)	1.518(6)
C(6)-H(6A)	0.99
C(6)-H(6B)	0.99
C(7)-C(8)	1.515(6)
C(7)-H(7A)	0.99
C(7)-H(7B)	0.99
C(8)-C(9)	1.520(6)
C(8)-H(8A)	0.99
C(8)-H(8B)	0.99
C(9)-C(10)	1.523(6)
C(9)-H(9A)	0.99
C(9)-H(9B)	0.99
C(10)-C(11)	1.522(6)
C(10)-H(10A)	0.99
C(10)-H(10B)	0.99
C(11)-C(12)	1.518(6)
C(11)-H(11A)	0.99
C(11)-H(11B)	0.99
C(12)-C(13)	1.522(6)
C(12)-H(12A)	0.99
C(12)-H(12B)	0.99
C(13)-C(14)	1.520(6)
C(13)-H(13A)	0.99
C(13)-H(13B)	0.99
C(14)-C(15)	1.526(6)
C(14)-H(14A)	0.99
C(14)-H(14B)	0.99
C(15)-C(16)	1.521(6)
C(15)-H(15A)	0.99
C(15)-H(15B)	0.99
C(16)-C(17)	1.524(7)
C(16)-H(16A)	0.99
C(16)-H(16B)	0.99
C(17)-H(17A)	0.98
C(17)-H(17B)	0.98
C(17)-H(17C)	0.98
N(2)-C(19)	1.488(5)
N(2)-H(2C)	0.91
N(2)-H(2D)	0.91

N(2)-H(2E)	0.91
C(19)-C(20)	1.502(6)
C(19)-H(19A)	0.99
C(19)-H(19B)	0.99
C(20)-C(21)	1.524(6)
C(20)-H(20A)	0.99
C(20)-H(20B)	0.99
C(21)-C(22)	1.522(6)
C(21)-H(21A)	0.99
C(21)-H(21B)	0.99
C(22)-C(23)	1.519(6)
C(22)-H(22A)	0.99
C(22)-H(22B)	0.99
C(23)-C(24)	1.520(6)
C(23)-H(23A)	0.99
C(23)-H(23B)	0.99
C(24)-C(25)	1.518(6)
C(24)-H(24A)	0.99
C(24)-H(24B)	0.99
C(25)-C(26)	1.515(6)
C(25)-H(25A)	0.99
C(25)-H(25B)	0.99
C(26)-C(27)	1.513(6)
C(26)-H(26A)	0.99
C(26)-H(26B)	0.99
C(27)-C(28)	1.518(6)
C(27)-H(27A)	0.99
C(27)-H(27B)	0.99
C(28)-C(29)	1.523(6)
C(28)-H(28A)	0.99
C(28)-H(28B)	0.99
C(29)-C(30)	1.517(6)
C(29)-H(29A)	0.99
C(29)-H(29B)	0.99
C(30)-C(31)	1.520(6)
C(30)-H(30A)	0.99
C(30)-H(30B)	0.99
C(31)-C(32)	1.515(6)
C(31)-H(31A)	0.99
C(31)-H(31B)	0.99
C(32)-C(33)	1.513(6)
C(32)-H(32A)	0.99
C(32)-H(32B)	0.99
C(33)-C(34)	1.518(6)
C(33)-H(33A)	0.99
C(33)-H(33B)	0.99
C(34)-H(34A)	0.98
C(34)-H(34B)	0.98
C(34)-H(34C)	0.98
Co(1)-Cl(4)	2.2555(13)
Co(1)-Cl(1)	2.2566(13)
Co(1)-Cl(3)	2.2719(13)
Co(1)-Cl(2)	2.2804(13)

C(2)-N(1)-H(1A)	109.5
C(2)-N(1)-H(1B)	109.5
H(1A)-N(1)-H(1B)	109.5
C(2)-N(1)-H(1C)	109.5

H(1A)-N(1)-H(1C)	109.5
H(1B)-N(1)-H(1C)	109.5
N(1)-C(2)-C(3)	111.9(4)
N(1)-C(2)-H(2A)	109.2
C(3)-C(2)-H(2A)	109.2
N(1)-C(2)-H(2B)	109.2
C(3)-C(2)-H(2B)	109.2
H(2A)-C(2)-H(2B)	107.9
C(2)-C(3)-C(4)	112.3(4)
C(2)-C(3)-H(3A)	109.1
C(4)-C(3)-H(3A)	109.1
C(2)-C(3)-H(3B)	109.1
C(4)-C(3)-H(3B)	109.1
H(3A)-C(3)-H(3B)	107.9
C(5)-C(4)-C(3)	112.8(4)
C(5)-C(4)-H(4A)	109
C(3)-C(4)-H(4A)	109
C(5)-C(4)-H(4B)	109
C(3)-C(4)-H(4B)	109
H(4A)-C(4)-H(4B)	107.8
C(4)-C(5)-C(6)	116.2(4)
C(4)-C(5)-H(5A)	108.2
C(6)-C(5)-H(5A)	108.2
C(4)-C(5)-H(5B)	108.2
C(6)-C(5)-H(5B)	108.2
H(5A)-C(5)-H(5B)	107.4
C(7)-C(6)-C(5)	113.1(4)
C(7)-C(6)-H(6A)	109
C(5)-C(6)-H(6A)	109
C(7)-C(6)-H(6B)	109
C(5)-C(6)-H(6B)	109
H(6A)-C(6)-H(6B)	107.8
C(8)-C(7)-C(6)	115.7(4)
C(8)-C(7)-H(7A)	108.4
C(6)-C(7)-H(7A)	108.4
C(8)-C(7)-H(7B)	108.4
C(6)-C(7)-H(7B)	108.4
H(7A)-C(7)-H(7B)	107.4
C(7)-C(8)-C(9)	113.2(4)
C(7)-C(8)-H(8A)	108.9
C(9)-C(8)-H(8A)	108.9
C(7)-C(8)-H(8B)	108.9
C(9)-C(8)-H(8B)	108.9
H(8A)-C(8)-H(8B)	107.8
C(8)-C(9)-C(10)	114.1(4)
C(8)-C(9)-H(9A)	108.7
C(10)-C(9)-H(9A)	108.7
C(8)-C(9)-H(9B)	108.7
C(10)-C(9)-H(9B)	108.7
H(9A)-C(9)-H(9B)	107.6
C(11)-C(10)-C(9)	113.6(4)
C(11)-C(10)-H(10A)	108.8
C(9)-C(10)-H(10A)	108.8
C(11)-C(10)-H(10B)	108.8
C(9)-C(10)-H(10B)	108.8
H(10A)-C(10)-H(10B)	107.7
C(12)-C(11)-C(10)	114.0(4)
C(12)-C(11)-H(11A)	108.8

C(10)-C(11)-H(11A)	108.8
C(12)-C(11)-H(11B)	108.8
C(10)-C(11)-H(11B)	108.8
H(11A)-C(11)-H(11B)	107.7
C(11)-C(12)-C(13)	114.1(4)
C(11)-C(12)-H(12A)	108.7
C(13)-C(12)-H(12A)	108.7
C(11)-C(12)-H(12B)	108.7
C(13)-C(12)-H(12B)	108.7
H(12A)-C(12)-H(12B)	107.6
C(14)-C(13)-C(12)	113.9(4)
C(14)-C(13)-H(13A)	108.8
C(12)-C(13)-H(13A)	108.8
C(14)-C(13)-H(13B)	108.8
C(12)-C(13)-H(13B)	108.8
H(13A)-C(13)-H(13B)	107.7
C(13)-C(14)-C(15)	114.2(4)
C(13)-C(14)-H(14A)	108.7
C(15)-C(14)-H(14A)	108.7
C(13)-C(14)-H(14B)	108.7
C(15)-C(14)-H(14B)	108.7
H(14A)-C(14)-H(14B)	107.6
C(16)-C(15)-C(14)	113.6(4)
C(16)-C(15)-H(15A)	108.8
C(14)-C(15)-H(15A)	108.8
C(16)-C(15)-H(15B)	108.8
C(14)-C(15)-H(15B)	108.8
H(15A)-C(15)-H(15B)	107.7
C(15)-C(16)-C(17)	113.1(4)
C(15)-C(16)-H(16A)	109
C(17)-C(16)-H(16A)	109
C(15)-C(16)-H(16B)	109
C(17)-C(16)-H(16B)	109
H(16A)-C(16)-H(16B)	107.8
C(16)-C(17)-H(17A)	109.5
C(16)-C(17)-H(17B)	109.5
H(17A)-C(17)-H(17B)	109.5
C(16)-C(17)-H(17C)	109.5
H(17A)-C(17)-H(17C)	109.5
H(17B)-C(17)-H(17C)	109.5
C(19)-N(2)-H(2C)	109.5
C(19)-N(2)-H(2D)	109.5
H(2C)-N(2)-H(2D)	109.5
C(19)-N(2)-H(2E)	109.5
H(2C)-N(2)-H(2E)	109.5
H(2D)-N(2)-H(2E)	109.5
N(2)-C(19)-C(20)	112.3(4)
N(2)-C(19)-H(19A)	109.1
C(20)-C(19)-H(19A)	109.1
N(2)-C(19)-H(19B)	109.1
C(20)-C(19)-H(19B)	109.1
H(19A)-C(19)-H(19B)	107.9
C(19)-C(20)-C(21)	110.2(4)
C(19)-C(20)-H(20A)	109.6
C(21)-C(20)-H(20A)	109.6
C(19)-C(20)-H(20B)	109.6
C(21)-C(20)-H(20B)	109.6
H(20A)-C(20)-H(20B)	108.1

C(22)-C(21)-C(20)	114.7(4)
C(22)-C(21)-H(21A)	108.6
C(20)-C(21)-H(21A)	108.6
C(22)-C(21)-H(21B)	108.6
C(20)-C(21)-H(21B)	108.6
H(21A)-C(21)-H(21B)	107.6
C(23)-C(22)-C(21)	112.1(4)
C(23)-C(22)-H(22A)	109.2
C(21)-C(22)-H(22A)	109.2
C(23)-C(22)-H(22B)	109.2
C(21)-C(22)-H(22B)	109.2
H(22A)-C(22)-H(22B)	107.9
C(22)-C(23)-C(24)	115.1(4)
C(22)-C(23)-H(23A)	108.5
C(24)-C(23)-H(23A)	108.5
C(22)-C(23)-H(23B)	108.5
C(24)-C(23)-H(23B)	108.5
H(23A)-C(23)-H(23B)	107.5
C(25)-C(24)-C(23)	113.5(4)
C(25)-C(24)-H(24A)	108.9
C(23)-C(24)-H(24A)	108.9
C(25)-C(24)-H(24B)	108.9
C(23)-C(24)-H(24B)	108.9
H(24A)-C(24)-H(24B)	107.7
C(26)-C(25)-C(24)	114.5(4)
C(26)-C(25)-H(25A)	108.6
C(24)-C(25)-H(25A)	108.6
C(26)-C(25)-H(25B)	108.6
C(24)-C(25)-H(25B)	108.6
H(25A)-C(25)-H(25B)	107.6
C(27)-C(26)-C(25)	114.2(4)
C(27)-C(26)-H(26A)	108.7
C(25)-C(26)-H(26A)	108.7
C(27)-C(26)-H(26B)	108.7
C(25)-C(26)-H(26B)	108.7
H(26A)-C(26)-H(26B)	107.6
C(26)-C(27)-C(28)	114.4(4)
C(26)-C(27)-H(27A)	108.7
C(28)-C(27)-H(27A)	108.7
C(26)-C(27)-H(27B)	108.7
C(28)-C(27)-H(27B)	108.7
H(27A)-C(27)-H(27B)	107.6
C(27)-C(28)-C(29)	113.8(4)
C(27)-C(28)-H(28A)	108.8
C(29)-C(28)-H(28A)	108.8
C(27)-C(28)-H(28B)	108.8
C(29)-C(28)-H(28B)	108.8
H(28A)-C(28)-H(28B)	107.7
C(30)-C(29)-C(28)	113.7(4)
C(30)-C(29)-H(29A)	108.8
C(28)-C(29)-H(29A)	108.8
C(30)-C(29)-H(29B)	108.8
C(28)-C(29)-H(29B)	108.8
H(29A)-C(29)-H(29B)	107.7
C(29)-C(30)-C(31)	114.2(4)
C(29)-C(30)-H(30A)	108.7
C(31)-C(30)-H(30A)	108.7
C(29)-C(30)-H(30B)	108.7

C(31)-C(30)-H(30B)	108.7
H(30A)-C(30)-H(30B)	107.6
C(32)-C(31)-C(30)	114.5(4)
C(32)-C(31)-H(31A)	108.6
C(30)-C(31)-H(31A)	108.6
C(32)-C(31)-H(31B)	108.6
C(30)-C(31)-H(31B)	108.6
H(31A)-C(31)-H(31B)	107.6
C(33)-C(32)-C(31)	113.6(4)
C(33)-C(32)-H(32A)	108.8
C(31)-C(32)-H(32A)	108.8
C(33)-C(32)-H(32B)	108.8
C(31)-C(32)-H(32B)	108.8
H(32A)-C(32)-H(32B)	107.7
C(32)-C(33)-C(34)	113.3(4)
C(32)-C(33)-H(33A)	108.9
C(34)-C(33)-H(33A)	108.9
C(32)-C(33)-H(33B)	108.9
C(34)-C(33)-H(33B)	108.9
H(33A)-C(33)-H(33B)	107.7
C(33)-C(34)-H(34A)	109.5
C(33)-C(34)-H(34B)	109.5
H(34A)-C(34)-H(34B)	109.5
C(33)-C(34)-H(34C)	109.5
H(34A)-C(34)-H(34C)	109.5
H(34B)-C(34)-H(34C)	109.5
Cl(4)-Co(1)-Cl(1)	111.19(5)
Cl(4)-Co(1)-Cl(3)	110.01(5)
Cl(1)-Co(1)-Cl(3)	107.44(5)
Cl(4)-Co(1)-Cl(2)	110.09(5)
Cl(1)-Co(1)-Cl(2)	112.06(5)
Cl(3)-Co(1)-Cl(2)	105.88(5)

9 HRTEM Simulations

Dmitry Tyutyunnikov used “Generator”, special software in mathematical package MATLAB to generate atomic coordinates and therefore, create a model for a NP that can be subsequently used for the calculation of theoretical HRTEM images.[3]

The models were introduced in Quantitative Scanning Transmission Electron Microscopy (QSTEM), special software that uses the multislice approach for the simulation of the images. This approach consists in the division of the specimen in multiple slices that are normal to the incident beam and the phase and amplitude for the electrons is calculated for each of them.

In our case, a pure hcp Co model was created and twin planes were randomly introduced in the original model in order to obtain the crystalline particle with defects. More precisely, the

addition of twin planes on the pure hcp structure follows the pattern: ABABABCABACABCABCABCABACABACAB.

10 Micromagnetic simulations and calculation of K_{eff} and T_B of Co nanodisks

10.1 Micromagnetic simulations

The magnetic behavior of the nanodisks presented in Chapter II has been simulated by Sven Stienen using OOMMF (Object Oriented MicroMagnetic Framework) software.[4] The size and thickness of the nanodisks together with the interparticle distance have been obtained from TEM images (Figure 1).

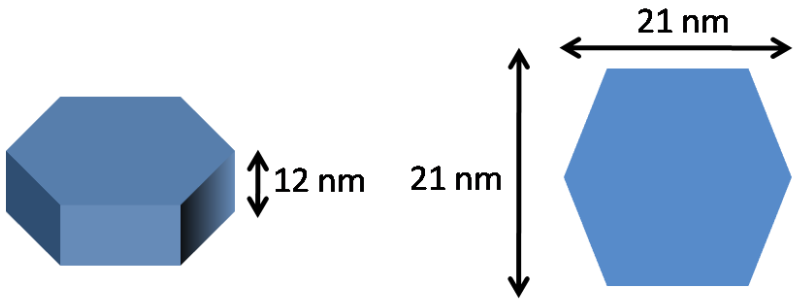

Figure 1. *Simple sketch representing the dimensions of the simulated Co nanodisks.*

The values of magnetocrystalline anisotropy, magnetization and exchange constant used are those of bulk hcp-Co. In the next tables we summarize the parameters included in the simulation:

Table 7. *Spatial coordinates of the NPs used for the simulation of one chain of 6 nanodisks (in m).*

	Coordinate x	***Coordinate y***	***Coordinate z***
Particle 1	$0 \cdot 10^{-9}$ to $21 \cdot 10^{-9}$	$0 \cdot 10^{-9}$ to $21 \cdot 10^{-9}$	$0 \cdot 10^{-9}$ to $12 \cdot 10^{-9}$
Particle 2	$0 \cdot 10^{-9}$ to $21 \cdot 10^{-9}$	$2 \cdot 10^{-9}$ to $23 \cdot 10^{-9}$	$14 \cdot 10^{-9}$ to $26 \cdot 10^{-9}$
Particle 3	$0 \cdot 10^{-9}$ to $21 \cdot 10^{-9}$	$1 \cdot 10^{-9}$ to $22 \cdot 10^{-9}$	$28 \cdot 10^{-9}$ to $40 \cdot 10^{-9}$
Particle 4	$0 \cdot 10^{-9}$ to $21 \cdot 10^{-9}$	$-1 \cdot 10^{-9}$ to $20 \cdot 10^{-9}$	$42 \cdot 10^{-9}$ to $54 \cdot 10^{-9}$
Particle 5	$1 \cdot 10^{-9}$ to $22 \cdot 10^{-9}$	$-1 \cdot 10^{-9}$ to $20 \cdot 10^{-9}$	$56 \cdot 10^{-9}$ to $68 \cdot 10^{-9}$
Particle 6	$0 \cdot 10^{-9}$ to $21 \cdot 10^{-9}$	$0 \cdot 10^{-9}$ to $21 \cdot 10^{-9}$	$70 \cdot 10^{-9}$ to $82 \cdot 10^{-9}$

Table 8. *Parameters fixed during simulations.*

Parameter	***Value***
Magnetization (M)	$1500 \cdot 10^3$ A/m
Uniaxial magnetocrystalline anisotropy (K_{uni})	$5 \cdot 10^5$ J/m^3
Exchange constant (A)	$30 \cdot 10^{-12}$ J/m

10.2 Calculation of K_{eff} and T_B

$$U = \left(\frac{\mu_0}{2}\right) N M_S^2$$

$$\mathrm{N} = \mathrm{N}_{\mathrm{out-of-plane}} - \mathrm{N}_{\mathrm{in-plane}} = (0.5272 - 0.2364) = 0.2908^{5}$$

$$U = 3.845 \cdot 10^6 \frac{erg}{cm^3}$$

$$K_{eff} = K_{mc} - K_{sh} = 5 \cdot 10^6 - 3.845 \cdot 10^6 = 1.1547 \cdot 10^6 \frac{erg}{cm^3}$$

$$Volume\ disk\ (aprox.\ hexahedral\ prism) = A_{base} \cdot h_{prism} = 6.2042 \cdot 10^{-18} cm^3$$

$$T_B = \frac{K_{eff} \cdot V}{25 k_b} = \frac{1.1547 \cdot 10^6 \frac{erg}{cm^3} \cdot 6.2042 \cdot 10^{-18} cm^3}{25 \cdot 1.38065 \cdot 10^{-16} \frac{erg}{K}} = 2075\ K$$

---

[1] S. Otsuka, M. Rossi, J. Chem. Soc. A. 1968, 2630.
[2] F. Dassenoy, K. Philippot, T. Ould-Ely, C. Amiens, P. Lecante, E. Snoeck, A. Mosset, M.-J. Casanove, B. Chaudret, New J. Chem., 22 (1998), 703.
[3] D. Tyutyunnikov, Diploma Thesis, Universität Duisburg-Essen (2010).
[4] www.math.nist.gov/oommf
[5] J. A. Osborn, Phys. Rev., 67 (1945), 351.

Resumé de thèse

Introduction Générale

Les nanoparticules (NPs) sont les briques de base des nanotechnologies, domaine scientifique actuellement en plein essor. A l'échelle du nanomètre, une nouvelle gamme de propriétés apparait, liées aux effets de taille et de surface comme par exemple, le superparamagnétisme dans les matériaux magnétiques, la présence des plasmons de surface pour les métaux nobles ou l'effet de confinement quantique dans les semiconducteurs. La possibilité de contrôler la synthèse des nanoparticules et donc ces propriétés nouvelles, permet d'envisager le développement de nouveaux dispositifs pour un vaste spectre d'applications. Dans le cas particulier du magnétisme, les perspectives les plus intéressantes se trouvent dans le domaine du stockage de l'information, et dans le diagnostique et le traitement du cancer (en permettant une meilleure localisation des tumeurs, un meilleur ciblage du médicament et la réduction des doses grâce au traitement localisé de la maladie).

Les NPs magnétiques métalliques ont une aimantation supérieure à celle des oxydes magnétiques, ce sont donc des supports très intéressants pour le stockage magnétique de l'information (une grande aimantation implique une lecture plus facile de l'information enregistrée) ou pour les applications biomédicales (par exemple, l'efficacité du transport in vivo du médicament assisté par des NPs magnétiques est proportionnel à l'aimantation). Pour ce type d'applications, les particules doivent être stables pendant longues périodes de temps. Or une des principales caractéristiques des métaux magnétiques de transition (fer, cobalt et nickel) est leur oxydation à l'air, oxydation d'autant plus facile que leur taille est réduite. En conséquence, l'enrobage de ce type d'objets par différents composés comme le carbone, la silice ou les métaux nobles (en fonction des applications) pour améliorer leur résistance face à l'oxydation a été testé, avec différents degrés de succès.

Pour atteindre une densité magnétique de stockage supérieure aux valeurs actuelles, la taille de la NP magnétique portant le bit d'information doit être réduite à quelques nanomètres. Cependant, à cette taille la barrière énergétique qui contrôle le retournement de l'aimantation devient très faible et l'énergie thermique devient suffisante pour provoquer la libre fluctuation des moments magnétiques, ce qui entraine la disparition de l'aimantation nette des particules à

température ambiante. En conséquence l'information enregistrée sous forme d'un bit magnétique disparait en l'absence d'un champ. Pour vaincre cette limitation physique, l'anisotropie intrinsèque du système doit être augmentée pour favoriser la formation de particules bloquées à la température ambiante (présentant une coercivité non nulle et donc une aimantation rémanente). Du point de vue chimique nous pouvons envisager deux solutions pour le contrôle de l'anisotropie: d'abord la modification de la composition chimique de la particule peut permettre la synthèse de systèmes avec une grande anisotropie (l'exemple le plus connu est l'alliage FePt). Cependant cette approche est limitée par la difficulté à contrôler la composition chimique d'une particule à l'autre dans un même lot de synthèse. La deuxième méthode consiste à développer des stratégies pour la synthèse de particules métalliques anisotropes. Dans ce cas, l'augmentation de l'anisotropie effective de la particule a comme conséquence directe le dépassement de la limite superparamagnétique et la stabilité thermique du moment magnétique. Toutefois un compromis entre anisotropie effective et coût énergétique doit être trouvé, car la synthèse d'objets très anisotropes avec des températures de blocage très hautes exige des champs magnétiques (ou températures) très élevées pour renverser les moments magnétiques, facteur rendant difficile l'écriture des domaines magnétiques. En conséquence, la forme des NPs ferromagnétiques doit être optimisée.

Dans un contexte différent, les matériaux magnétiques photocommutables ont attiré l'attention de la communauté scientifique depuis sa découverte en 1996, grâce au développement des nouveaux systèmes photocommutables ou de l'enregistrement optique de l'information. Jusqu'à présent, la plupart des travaux dans ce domaine ont été limités à l'étude à basse température des matériaux moléculaires et ce n'est que récemment que la photomodulation de l'aimantation d'une NP a été rapportée. Dans ce travail, les auteurs prennent avantage de l'enrobage de la particule magnétique dans une matrice photocommutable.

Cette thèse est centrée sur les trois points principaux que nous venons de présenter: protection contre l'oxydation, contrôle de forme et synthèse de systèmes multifonctionnels. Dans le chapitre d'introduction, nous présentons les résultats rapportés dans la littérature sur la synthèse et les propriétés générales des NPs magnétiques. Les chapitres II et III sont respectivement centrés sur la synthèse de nano-objets de Co avec une structure anisotrope et leur stabilisation par formation d'une couche protectrice de carbone. Ensuite, dans le chapitre IV

nous introduisons une nouvelle méthode de synthèse pour l'obtention de NPs de Co stabilisées par des fluorophores organiques ainsi que l'étude de leurs propriétés optiques et magnétiques. Des résultats préliminaires sur la photomodulation de leur aimantation sont aussi discutés.

1 Contexte théorique

1.1 Introduction au nanomagnétisme

La synthèse de nanoparticules est devenue un champ très important dans différents domaines scientifiques comme la chimie, la physique ou la science des matériaux, entre autres. Cet intérêt développé pendant les 20 dernières années est lié aux propriétés obtenues à l'échelle nanométrique dérivées de la grande importance des effets de surface, propriétés autrement introuvables dans l'état massif.

Dans le cas particulier du magnétisme, la réduction de la taille de la matière a comme conséquence première la configuration monodomaine du matériau: le maintien des parois de domaines magnétiques devient trop couteuse en énergie au dessous d'une taille critique, les moments magnétiques se comportent donc d'une façon coopérative. La réduction de taille dans des particules nanométriques a aussi une influence très importante sur les moments magnétiques de spin et orbital et donc, sur les propriétés globales de la particule.

La surface d'une nanoparticule (NP) devient un paramètre clé pour ses propriétés magnétiques car elle représente une proportion très importante des atomes de la particule. Conséquence de la perte de symétrie expérimentée par les atomes de surface, une contraction des bandes d et une polarisation de spin plus élevée sont prévues théoriquement et observées.

1.2 Synthèse colloïdale de NPs

La méthode la plus utilisée pour l'obtention de particules magnétiques est la synthèse colloïdale, dans laquelle un précurseur métallique (sel ou composé organométallique) est décomposé dans une solution en présence d'agents dispersants qui empêchent l'agrégation du matériau et assurent la stabilité de la solution colloïdale. Néanmoins, les mécanismes qui contrôlent cette procédure sont d'une grande complexité et restent encore mal compris par la communauté scientifique.

Les principaux points d'une synthèse colloïdale de NPs sont:

1. La formation de nuclei dans des solutions supersaturées dépend de la compétition entre énergie du massif et énergie de surface.
2. L'unicité temporelle de l'étape de nucléation est un paramètre clé pour l'obtention d'un échantillon monodisperse.
3. Un empilement hexagonal compact aléatoire est attendu pendant les premiers temps de la réaction, en conséquence de la faible différence énergétique entre les structures hexagonale et cubique.
4. Si la réaction reste sous contrôle thermodynamique, la particule expose les facettes cristallographiques avec les énergies surfaciques les plus faibles. Par contre, si la réaction se trouve sous contrôle cinétique la formation de clusters avec une grande tension de surface est favorisée.
5. La croissance anisotrope de particules colloïdales est contrôlée par trois paramètres: la structure du germe, l'adsorption spécifique des ligands sur certaines facettes du cristal ou la formation d'un template mesoporeux capable de diriger la croissance anisotrope de la particule.

1.3 Synthèse de NPs de Fe, Co, Ni et leurs alliages

Avant d'expliquer les résultats expérimentaux obtenus au cours de cette thèse les travaux développés précédemment dans la synthèse colloïdale de particules des trois métaux de transition présentant des propriétés ferromagnétiques (Fe, Co et Ni) seront rapportés.

Différentes méthodes sont généralement utilisées pour la synthèse colloïdale de NPs magnétiques de Fe, Co et Ni. Les méthodes les plus utilisées sont les suivantes :

– Décomposition thermique

Cette méthode est basée sur la décomposition d'un précurseur métallique à haute température. Normalement, une solution de ligands utilisés pour la stabilisation des particules est portée à reflux juste avant de l'introduction du précurseur métallique. Cette technique, connue comme « hot injection » technique, conduit à la synthèse de NPs très monodisperses (dispersions en taille de l'ordre de 5 %) car la nucléation est produite dans un intervalle de temps très petit.

– Décomposition par ultrasons

Dans ce type de synthèse, un précurseur est décomposé sur l'effet d'un son de grande intensité et haute fréquence. Des conditions extrêmes de pression et température sont produites dans lesquelles la décomposition d'un précurseur organométallique est possible. Par contre le contrôle sur la dispersité en taille est très faible et les particules formées sont généralement oxydées à la surface. En plus, ces conditions extrêmes peuvent endommager les agents stabilisants introduits pour contrôler la taille des particules et conduire à matrices carbonées englobant les particules.

- Réduction chimique

Des méthodes de synthèse très différentes (réduction dans des microémulsions, par polyols et décomposition à hautes ou basses températures) utilisent la réduction de sels métalliques pour l'obtention de particules magnétiques des métaux de transition. En général ces méthodes donnent des valeurs d'aimantation très acceptables mais par contre la présence d'oxydes à la surface ou même l'inclusion d'autres éléments dans le cœur de la particule (cas des microémulsions avec réduction par borohydrures) restent des inconvénients importants. Parmi ces différentes méthodes la voie polyol parait la plus intéressante:

Les polyols sont des molécules de formule générale $HOCH_2[CH(OH)]_nCH_2OH$ capables de dissoudre et réduire les sels de nombreux métaux grâce à la présence de multiples groupes hydroxyle dans leur structure. Un des points forts de cette synthèse est la possibilité d'utiliser ces espèces à la fois comme agents réducteurs et solvants. Le mécanisme général est résumé dans l'équation suivante en ce qui concerne les métaux 3d magnétiques:

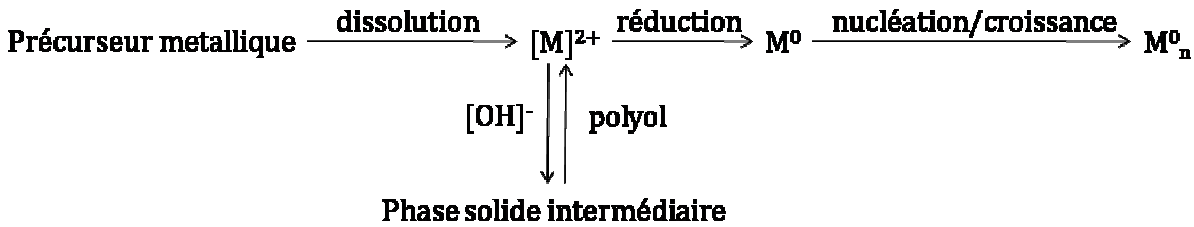

Dans cette réaction une phase intermédiaire, en équilibre avec les ions en solution permet de réguler la concentration de ces ions durant la quasi-totalité de la synthèse.

La qualité des NPs obtenues par cette méthode varie beaucoup en fonction du cas étudié. Par contre, la valeur de l'aimantation obtenue est toujours au dessous de celle du massif.

- Synthèse par voie hydrothermale

Dans cette méthode une solution aqueuse d'un précurseur métallique et agents stabilisants est introduite dans un autoclave et soumise à de hautes pressions et températures. Cette technique est peu utilisée pour la synthèse de métaux magnétiques. Les objets rapportés dans la littérature sont généralement de forme anisotrope, un important avantage pour certaines applications dans le domaine du stockage magnétique de l'information. Par contre, la valeur de leur aimantation n'a été pas signalée.

- Décomposition de précurseurs organométalliques sous atmosphère de dihydrogène

La décomposition sous atmosphère de dihydrogène de précurseurs organométalliques (oléfiniques ou de complexes amidure, par exemple) conduit dans des conditions douces de température et pression à la synthèse de particules de Fe, Co et Ni avec des caractéristiques optimales (monodispersité, cristallinité, surfaces propres et utilisation de ligands sans un effet important sur le magnétisme des NPs). Notamment, les propriétés magnétiques sont proches de celles rapportées pour des nanoparticules produites dans l'ultravide. Un des paramètres clés de cette méthode est la nature des précurseurs, facilement décomposés sous dihydrogène et donnant comme sous-produits des molécules sans aucune affinité pour les surfaces métalliques. Cette méthode permet également de contrôler la forme des objets produits. Ce résultat est lié aux conditions douces de réaction permettant l'adsorption spécifique de ligands acide/amine sur certaines facettes cristallographiques de la NP, et dirigeant ainsi la croissance dans une direction de l'espace.

Les principaux inconvénients résident dans la disponibilité et le coût élevé de ce type de précurseurs ainsi que dans le danger lié à l'utilisation de bouteilles de H_2 comprimé.

Les différentes méthodes de synthèse sont illustrées dans le tableau suivant, avec les caractéristiques les plus importantes des particules obtenues.

Table 1. *Comparaison pour les différentes méthodes de synthèse conduisant à l'obtention de NPs magnétiques des métaux de transition.*

Méthode	*Contrôle de taille*	*Cristallinité*	*Valeur maximale de M_S (% massif)*	*Surface*	*Références*
Décomposition thermique	Distribution très étroite	Bonne	95%	Oxydée	[1]
Décomposition par ultrasons	Distribution grande	Pauvre	50%	Oxydée	[2]
Réduction avec polyols	Distribution étroite (après procédure de sélection de taille)	Pauvre	80%	Oxydée	[3]
Décomposition sous atmosphère de dihydrogène	Distribution très étroite	Bonne	>100%	Propre	[4]

Nous pouvons constater la validité de la méthode de décomposition des précurseurs organométalliques sous atmosphère de dihydrogène pour la synthèse de NPs des métaux magnétiques de transition d'une très haute qualité. Dans cette thèse nous l'avons utilisée comme outil pour l'étude des effets de surface mentionnés précédemment. Ici, nous nous sommes focalisés sur le cas particulier du cobalt, un des trois métaux 3d du tableau périodique avec des propriétés ferromagnétiques. Plus concrètement, trois différentes thématiques ont été sélectionnées pour l'étude de surface des NPs de Co:

1. La synthèse de NPs de Co anisotropes.
2. L'enrobage des NPs de Co anisotropes par une matrice carbonée.
3. L'étude de l'interaction entre un cœur magnétique de Co et un fluorophore organique lié à sa surface.

2 Synthèse de nanodisques de Cobalt

2.1 Introduction

La synthèse de particules anisotropes de cobalt a été développée avec succès dans l'équipe de Bruno Chaudret au cours des dernières années.[5] La méthode choisie est basée sur la décomposition d'un précurseur de Co ($Co(\eta^3\text{-}C_8H_{13})(\eta^4\text{-}C_8H_{12})$ ou $Co(N(SiMe_3)_2)_2$) sous atmosphère de dihydrogène et en présence d'un mélange de ligands acide et amine. Cette méthode permet d'obtenir des nanobâtonnets ou des nanofils de Co avec un diamètre très fin (4-7 nm) et une longueur ajustable entre une vingtaine de nanomètres pour les bâtonnets les plus petits et plusieurs micromètres pour les nanofils en fonction du mélange de ligands utilisés.

Même si le mécanisme responsable de la croissance anisotrope de ces particules reste encore mal connu, plusieurs hypothèses ont été proposées:

- Adsorption spécifique d'un ou plusieurs ligands sur certaines faces du cristal.
- Auto-organisation des ligands ou d'un complexe intermédiaire en solution, capable de diriger la croissance de nanocristaux en son sein.

Même si les nanobâtonnets de Co possèdent des propriétés magnétiques remarquables pour leur implémentation dans le domaine du stockage magnétique de l'information, il faut prendre en compte trois inconvénients majeurs: la difficulté à les disposer perpendiculairement à un substrat, la nécessité d'un champ magnétique intense pour le retournement de leur aimantation et leur oxydabilité (ce troisième point sera abordé plus avant dans le Chapitre 3). En revanche, la synthèse de NPs magnétiques avec des formes intermédiaires, moins anisotropes, et plus facilement déposables sur un substrat peuvent être une bonne alternative. Dans ce contexte, la formation de nanodisques semble le choix idéal.

Dans notre étude nous avons profité du savoir-faire de l'équipe pour synthétiser des NPs de Co avec cette morphologie. Dans ce cas, nous avons utilisé un acide présentant un encombrement stérique très important (par opposition aux acides de longue chaîne aliphatique utilisés précédemment).

2.2 Résultats

Pour la synthèse des NPs anisotropes de Co nous avons choisi comme amine l'hexadecylamine (HDA) et comme acide la Rhodamine B (RhB), capable de stabiliser elle-même des petites NPs de Co (Chapitre 4). Les autres paramètres de la réaction (solvant, température, précurseur de Co, temps de réaction) sont ceux utilisés dans les synthèses de nano-bâtonnets et fils **(Figure 1)**.

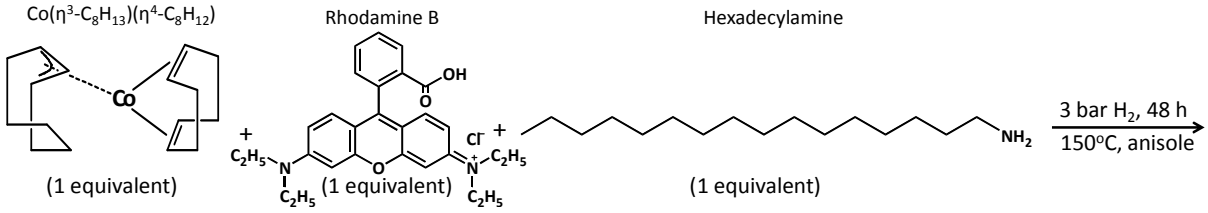

Figure 1. *Schéma général pour la synthèse de nanodisques de Co.*

À la fin de la réaction, deux précipités sont observés: un solide bleu correspondant à un complexe de Co ($Co(Cl)_4(HDAH)_2$) qui présente un arrangement spatial anisotrope **(Figure 2)** et un solide noire très magnétique.

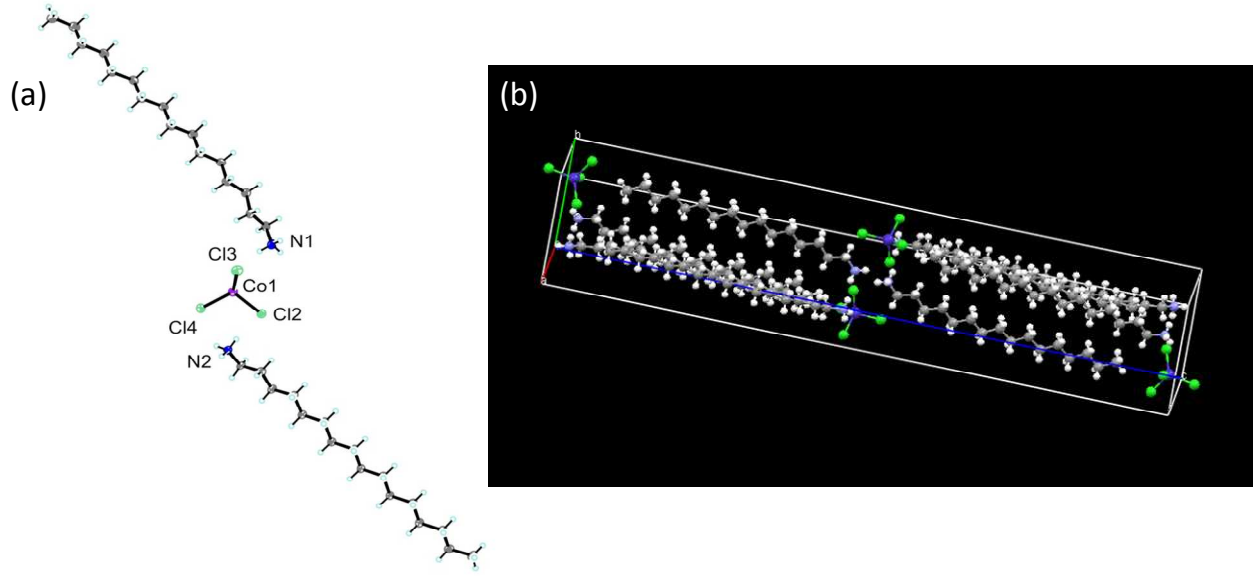

Figure 2. *Structure cristalline du solide bleu obtenu pendant la réaction (a) et sa distribution spatiale (b).*

Sur les images de microscopie du solide noir présentées dans la **Figure 3**, nous observons la présence de particules anisotropes de Co arrangées en longues chaînes.

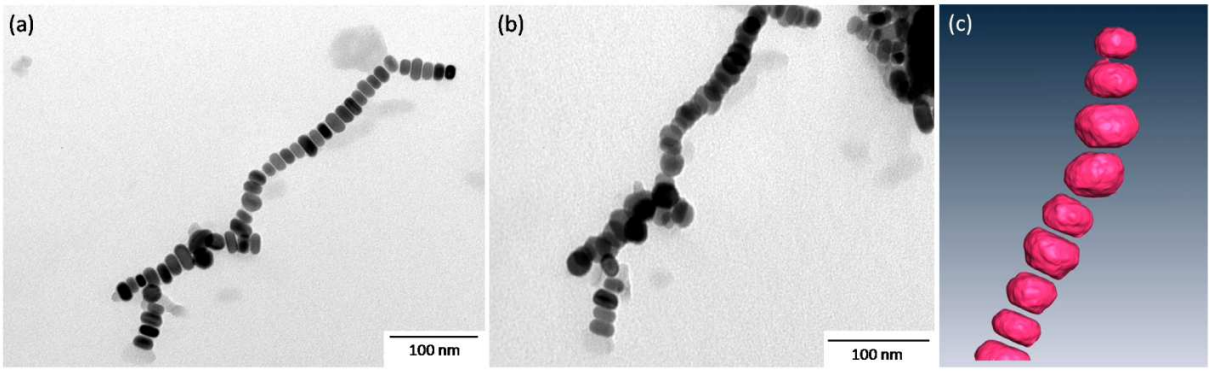

Figure 3. *(a) Image TEM des particules anisotropes obtenues et (b) les memes particules apres tourner le portaéchantillons 45°. En (c) une représentation 3D de ces particules.*

Même si la forme des particules est comparable à celle des nanobâtonnets obtenus précédemment, quand nous varions l'angle du porte-échantillons dans le microscope, nous observons des objets circulaires **(Figure 3)** et donc, nous pouvons parler de disques plutôt que de bâtonnets. La taille de ces objets est de 21,5 nm de diamètre et 12,5 nm d'épaisseur. Les images de haute résolution montrent la structure hexagonale compacte des NPs avec l'axe c formant un angle de 90° avec la base du disque. En opposition avec les bâtonnets, des fautes d'empilement sont observées dans la direction (0001).

À ce stade, trois mécanismes de croissance sont envisagés pour expliquer la formation des nanodisques:

1. Adsorption spécifique des ligands dans certaines facettes du cristal.
2. Formation d'un matériel mésoporeux capable de diriger la croissance anisotrope.
3. Présence de fautes d'empilement dans les germes dirigeant la croissance anisotrope en deux dimensions.[6]

Malheureusement, le dernier mécanisme est très difficile à mettre en évidence expérimentalement et donc, son rôle dans la formation des disques obtenus dans cette thèse doit être fait par l'élimination des autres deux alternatives.

Nous avons vérifié que le complexe $Co(Cl)_4(HDAH)_2$, même s'il est susceptible de former des organisations supramoléculaires dans le milieu n'est pas à l'origine de la croissance anisotrope du Co. Nous avons d'ailleurs montré que c'était un sous-produit de la réaction.

Parallèlement nous avons testé l'importance des deux ligands utilisés. Nous avons d'abord modifié la structure de l'acide. Plusieurs ligands qui partagent avec la RhB certains éléments structuraux ont été testés, mais aucun d'entre eux ne donne la même morphologie de particules. En fait seule la Rhodamine 6G et la Pyronin Y permettent d'obtenir des NPs de morphologie similaire. De son coté, l'hexadecylamine est aussi très importante car sa suppression du milieu réactionnel a comme conséquence la formation de particules sphériques.

Les résultats exposés dans les paragraphes précédents, rapprochés de la quantité de ligands présents à la surface des disques (< 5 %) suggèrent que les ligands n'ont pas un rôle très important pendant le processus de croissance des nuclei. Notamment, il est vraisemblable que la RhB ne s'adsorbe de façon significative que sur les faces étendues, c'est-à-dire qu'à partir d'un certain stade de croissance des particules. Dans ce contexte, la structure des germes n'est pas régulée par la présence d'un acide dans le milieu, ce qui peut expliquer la présence de nombreux défauts. En fait, dans le cas de bâtonnets l'adsorption spécifique des acides dans les faces {10-10} diminue leur énergie superficielle, favorisant leur croissance. Dans notre cas la rapide oxydation des faces {10-10} montre la faible population de ligands dans ses surfaces (plus probablement une faible quantité de Rhodamine B). Dans ce contexte, la croissance en deux dimensions est favorisée par la différence d'énergie de surface entre les faces {0001} et les faces {10-10}.[7] En conclusion, l'extension des faces, d'énergie la plus faible (ici faces {0001}), et donc la formation de disques est naturellement favorisée en l'absence de perturbation telles que l'adsorption de ligands, et renforcée par la présence éventuelle de défauts aux premiers stades de croissance.

Comme attendu compte tenu de leur morphologie et de leur taille, les nanodisques de Co présentent un comportement bloqué à température ambiante, avec une aimantation très proche de celle du massif et un champ coercitif plus faible que celui obtenu pour des particules plus anisotropes.[8] Des simulations micromagnétiques ont montré que ces disques comportent un domaine magnétique unique, et un axe de facile aimantation confondu avec l'axe c, *i.e.*

perpendiculaire au plan du disque. Ces particularités en font de bons candidats dans l'objectif d'application au stockage de l'information.

2.3 Conclusions

Nous avons montré dans ce chapitre la formation de particules de Co avec une nouvelle morphologie. Les disques obtenus sont probablement le résultat de la croissance de germes présentant des fautes d'empilement dans leur structure initiale, favorisant une élongation des particules en deux dimensions. Ces NPs forment des chaînes sur la grille de TEM attribuables aux fortes interactions dipolaires entre elles. Leur caractère monodomaine et le fait que ces particules restent bloquées à température ambiante est un résultat très encourageant pour une application dans des dispositifs de stockage magnétique de l'information.

3 Enrobage de nanoobjets magnétiques anisotropes par du carbone

3.1 Introduction

Même si l'intérêt industriel pour les particules anisotropes de cobalt est hors de doute, la haute réactivité de ses particules avec l'oxygène reste une limitation très importante qu'empêche leur application réelle dans le monde de la microélectronique. L'enrobage des particules des métaux de transition comme le Fe ou le Co a été testé dans les dernières années pour éviter leur oxydation. Dans ce contexte, des matériaux comme la silice, les métaux nobles ou le carbone ont donné des résultats avec différents degrés de succès. Parmi eux, l'utilisation de carbone est la méthode plus répandue car ce matériau est stable en solutions fortement acides ou basiques et aussi sous conditions de pression et température très drastiques.[9]

Dans ce chapitre nous présentons notre démarche visant l'enrobage de bâtonnets et de fils de Co par du carbone. Nous avons envisagé le recuit des particules de Co pré-synthétisées en utilisant les ligands situés à leur surface comme source de carbone. Pour ce faire, un traitement thermique avec une rampe contrôlée de température a été conçu. Par contre, le traitement de ce type de particules à hautes températures peut conduire à une instabilité de la morphologie originale. Ce type d'instabilité est décrit par le modèle de Rayleigh, développé à la fin du XIXème siècle.[10]

Dans ce modèle, les auteurs décrivent l'instabilité de fluides cylindriques comme conséquence d'une perturbation externe pouvant avoir des origines très différentes: une perturbation thermique, mécanique ou électrique, par exemple. En fait, si la surface de ce type de cylindres ondule avec une longueur d'onde caractéristique plus grande que la circonférence du cylindre lui-même, le cylindre va collapser en une ligne de sphères situées à une distance régulière les unes des autres. Ainsi, la tension superficielle du système diminue (à volume constant).

Quelques années plus tard, ce modèle a été étendu à des cylindres solides.[11] La perturbation externe est exprimée comme une fonction sinusoïdale:

$$r = R_0 + \delta \sin\left(\frac{2\pi}{\lambda} z\right)$$

où R_0 est le rayon du filament avant perturbation, δ et λ sont l'amplitude et la longueur d'onde de la perturbation et z est la coordonnée le long de l'axe du cylindre.

Lors d'une élévation de température, cette instabilité est une conséquence directe de l'excitation thermique des phonons (modes quantifiés de vibration dans les solides cristallins). La propagation de ces phonons avec une fréquence caractéristique le long d'un filament induit sa décomposition en une chaîne de sphères. La longueur d'onde spécifique pour une décomposition totale des cylindres s'exprime comme 8,89 R_0 (avec R_0 le rayon original du cylindre).

Un autre facteur important dans un cylindre solide est le processus de fusion. Dans ce contexte il faut prendre en compte deux étapes:

1. Les atomes de surface vont expérimenter le processus de fusion plus vite que les atomes de cœur parce que la perte de symétrie à la surface a comme conséquence la diminution de l'énergie de liaison.
2. Cette excitation est transmise depuis la surface jusqu'au centre de la particule.

3.2 Résultats

La synthèse des particules anisotropes de Co a été faite en suivant la méthode développée précédemment par Chaudret et al.[12]

Nous avons procédé au traitement thermique des filaments et bâtonnets de Co de deux façons différentes: dans un premier temps nous avons soumis les particules à hautes températures (jusqu'à 420^{o}C) directement dans un microscope électronique. Dans un second temps, nous avons chauffé l'échantillon à l'intérieur d'un four et sous atmosphère d'argon.

Pour la première expérience, nous avons observé la décomposition des fils et bâtonnets à très basses températures (pour les fils la procédure commence à 350 ^{o}C et pour les bâtonnets à

température ambiante). Par contre dans les deux cas la décomposition est très irrégulière et la formation d'une coquille protectrice de carbone n'est pas observée. Nous expliquons ce phénomène comme une conséquence de la désorption de ligands de la surface des particules et la sublimation directe des atomes de Co, en raison des basses pressions supportée par les particules dans le microscope (≈ 10^{-6} mbar). Entre bâtonnets et filaments, la différente de température à laquelle la décomposition commence est une conséquence du plus grand nombre d'atomes en surface pour le premier type de particules. De toute façon, la structure cristalline des fragments encore présents sur la grille de microscopie montrent la persistance de l'arrangement hexagonal compact initial.

Lorsque le recuit est effectué sous atmosphère d'argon une température maximale de 350 ^{o}C est choisie suite aux analyses thermogravimétriques sur les particules. Deux rampes de températures différentes, 5 et 10 ^{o}C par minute, ont été sélectionnées.

Dans le cas des filaments, quand l'échauffement le plus rapide est sélectionné nous pouvons observer la formation de particules sphériques dans une couche protectrice de carbone **(Figure 4, au centre)**.

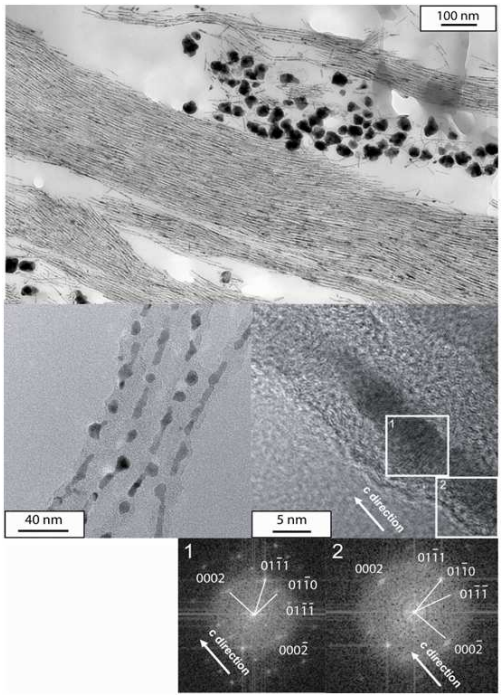

Figure 4. *Images MET (en haut) et MET de haute résolution (centre) pour les filaments recuits à 350 ^{o}C sous Ar avec une rampe de 10 ^{o}C/min.*

Par ailleurs, les fragments de Co trouvés gardent la structure hexagonale compacte initiale et donc la fragmentation n'est pas le résultat d'une transition de phase entre Co_{hcp} et Co_{fcc}, processus qui se produit à une température de 417 ^{o}C dans le massif. Quand le recuit est effectué avec une température maximale plus haute (500 ^{o}C) les sphères formées présentent un espacement entre elles régulier et très proche de la valeur théorique 8,89 R_0.

Même si les filaments présentent une décomposition très importante, le cycle d'hystérésis montre une coercivité, résultat de la présence de filaments ou de chaînes de particules sphériques en interaction. Le cycle d'hystérésis enregistré après un mois d'exposition à l'air montre de plus que le matériau est efficacement protégé de l'oxydation par la couche de carbone, la baisse d'aimantation est minime **(Figure 5)**.

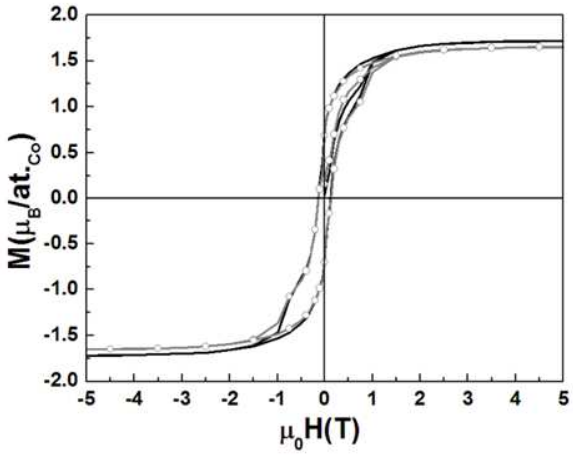

Figure 5. *Courbes d'aimantation enregistrées à 2 K pour les filaments de cobalt avant (noir) et après 1 mois d'oxydation à l'air.*

Les résultats obtenus quand la vitesse d'échauffement est réduite montrent par contre la présence de fils que gardent sa morphologie originale intacte **(Figure 6)** sans modification de sa structure cristalline hcp. Dans ce cas, la décomposition des ligands se produit avant la décomposition de la particule, résultant en la formation d'une structure magnétique anisotrope avec une couche protectrice de carbone.

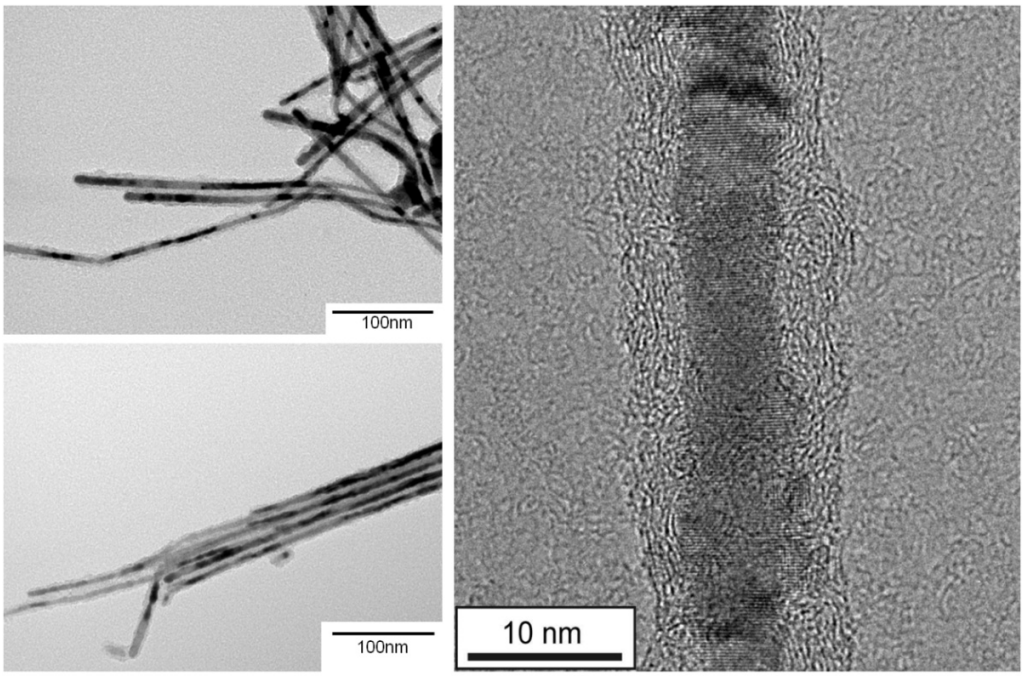

Figure 6. *Images MET de basse (gauche) et haute (droite) résolution pour les fils de Co recuits à 350 °C avec une rampe de 5 °C/min.*

Malheureusement, la même procédure appliquée aux nanobâtonnets de cobalt, entraîne leur décomposition totale. Seule une couche amorphe de carbone, empreinte de la forme originale de la particule, est observée en microscopie électronique.

3.3 Conclusions

Le recuit des particules anisotropes de cobalt sous atmosphère d'argon conduit bien à la formation d'une couche de carbone passivante vis-à-vis de l'oxydation. De plus, les conditions ont pu être optimisées de sorte que les nanofilaments de cobalt présentés dans ce chapitre gardent leur structure originale et leur morphologie durant le recuit.

4 Synthèse de nanohybrides de Co

4.1 Introduction

Le design de matériaux moléculaires photocommutables est un sujet scientifique de grande importance pour différentes applications comme l'optoélectronique, pour la création de mémoires optiques ou pour le contrôle optique de mémoires magnétiques. Les études sur ce thème sont nombreuses, notamment en ce qui concerne les complexes à transition de spin photocommutables. Par contre, très peu de travaux concernent l'étude de la photomodulation des propriétés de NPs magnétiques. En fait les études d'hybrides fluorophore/NP magnétique se focalisent généralement sur l'effet de la NP sur le fluorophore.

Généralement une interaction directe entre une espèce fluorescente et une NP (magnétique ou non magnétique) a comme conséquence la modification des propriétés photophysiques du fluorophore (changement des processus de desexcitation et variation des temps de vie des états excités). Ce type d'interaction a été étudié en détail dans le cas de particules de métaux nobles comme l'or et l'argent. Les principaux résultats publiés peuvent être résumés d'une façon succincte:

- La présence de la bande plasmonique des métaux nobles nanostructurés peut avoir des effets opposés sur les propriétés optiques du fluorophore: l'augmentation de l'intensité du champ électromagnétique peut augmenter la constante d'excitation du fluorophore[13] (fluorescence plus intense: *enhancement*) mais un transfert énergétique de l'état excité du fluorophore à la surface de la particule peut augmenter aussi la constante de desexcitation non radiative[14] (fluorescence plus faible: *quenching*). La compétition entre ces deux facteurs dépend de la distance entre fluorophore et particule et de leurs orientations relatives.
- Un transfert électronique entre l'état excité du fluorophore et la NP peut aussi avoir un effet de *quenching* sur l'intensité de fluorescence car il produit une diminution de la constante radiative de desexcitation.[15]

Dans le cas des hybrides magnétiques/fluorescents, l'effet du cœur magnétique sur les propriétés optiques d'un fluorophore situé à proximité a été déjà vérifié dans le cas des NP d'oxydes de fer, pour lesquels un *quenching* partiel de la fluorescence a été observé.[16]

Dans ce chapitre nous présentons la synthèse et la caractérisation magnétique et optique d'un système hybride composé d'une NP magnétique métallique et d'un fluorophore organique comme unique agent stabilisant et les premiers résultats de photomodulation de l'aimantation de ce type de nanohybride.

4.2 Résultats

Pour la synthèse des NPs nous avons choisi comme fluorophore la Rhodamine B (RhB) car cette molécule présente plusieurs groupes fonctionnels susceptibles de stabiliser des particules de Co. Le précurseur de Co choisi est le complexe $Co(\eta^3\text{-}C_8H_{13})(\eta^4\text{-}C_8H_{12})$. Il donne des particules avec surfaces propres et est facilement décomposé à basses températures,[17] assurant la conservation de la structure de la molécule fluorescente. L'intérêt de travailler à basse température est également de favoriser l'interaction entre la RhB et les NPs (interaction dont nous avons vu au Chapitre II qu'elle est faible malgré le nombre de site d'ancrage possibles) et donc de favoriser la stabilisation de particules de très petite taille (quelques nanomètres).

Les particules obtenues après hydrogénation pendant 14 heures à température ambiante ont une taille moyenne de 3,8 nm et une structure cristalline ε–Co. Le fluorophore semble être lié à la surface de la NP par son groupe acide carboxylique car une autre expérience réalisée comme référence avec la Rhodamine 6G (molécule dans laquelle la fonction acide carboxylique est masquée sous forme d'un ester) montre la présence de particules plus grandes et polydisperses.

Concernant les propriétés optiques de l'hybride, les spectres d'absorption et émission ont été enregistrés. Le spectre d'absorption montre le spectre typique de la RhB, illustrant la stabilité de la molécule dans les conditions de synthèse utilisées. Par contre, la fluorescence est presque totalement annulée en comparaison à celle de la molécule libre.

L'oxydation des hybrides montre une légère augmentation de la fluorescence, accompagnée d'une modification de la solution colloïdale, phénomène suivi par microscopie électronique **(Figure 7)**.

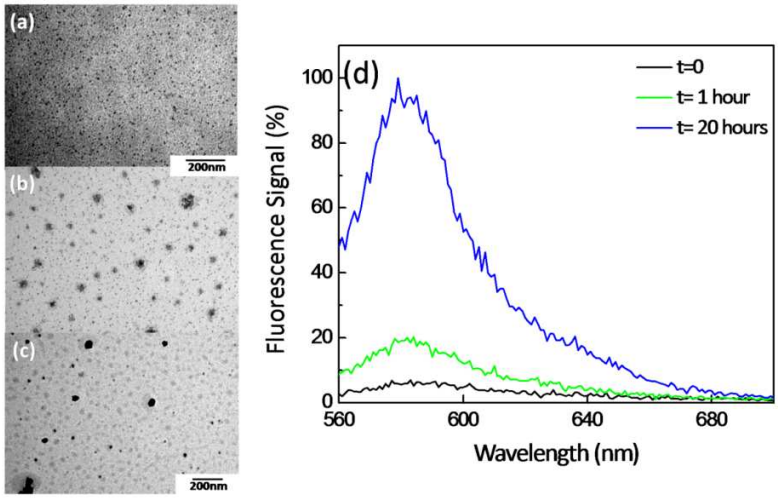

Figure 7. *(a-c) Images MET pour les NPs Co/RhB avant exposition à l'air (a), et après 2 jours (b) et une semaine (c) d'exposition. (d) Spectre de fluorescence pour le hybride en fonction du temps d'oxydation.*

En fait, une agrégation est observée, signe du décrochage des agents stabilisants présents initialement en surface des particules. La **Figure 8** montre aussi que cet effet de *quenching* est beaucoup plus important que celui obtenu quand une solution de RhB est mélangée avec particules de Co stabilisées avec un acide carboxylique simple (acide oléique par exemple). Cette différence est due à la présence d'un *quenching* statique entre la NP et les molécules liées à sa surface et non à une interaction entre la NP et des molécules libres en solution.

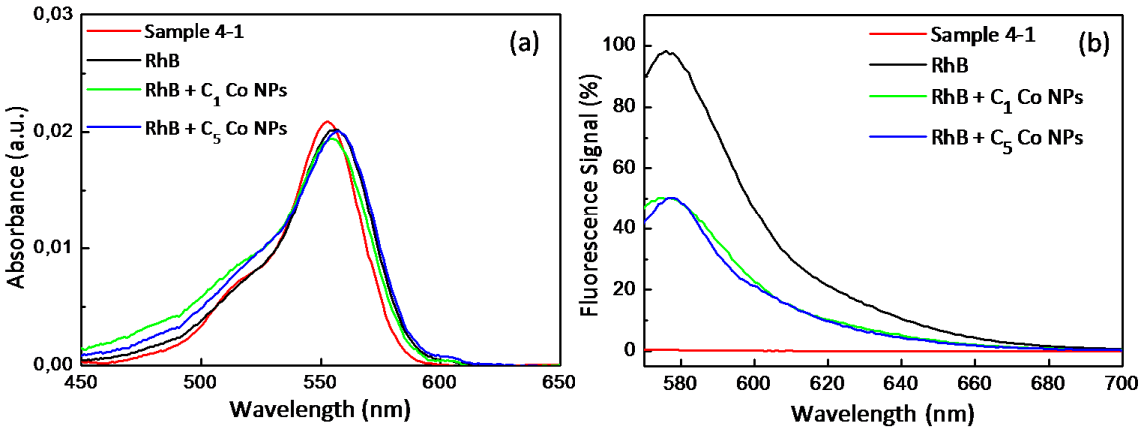

Figure 8. *Spectres d'absorption (a) et fluorescence (b) pour les NPs de Co/RhB et comparaison avec RhB libre et RhB avec deux différentes concentrations de NPs de Co stabilisées par l'acide oléique (C_5 représente une concentration 5 fois supérieure à celle de C_1).*

Pour mieux comprendre l'interaction entre la RhB et la particule de Co, nous avons mesuré la durée de vie de l'état excité. Nous observons deux composantes différentes dans notre hybride: une très rapide attribuée à la désexcitation de la molécule liée à la surface et une autre plus longue attribuée à l'excès de fluorophores présents dans la solution.

À ce stade nous avons deux possibilités pour expliquer l'interaction entre molécule et surface magnétique: un transfert énergétique ou un transfert électronique. Le premier est peu probable car les NPs de Co ne présentent pas de bande plasmon dans le visible. Nous avons donc cherché à mettre en évidence et comprendre le transfert électronique. Pour ce faire, nous avons étudié le spectre d'absorption spécifique de l'état excité des molécules de RhB liées à la surface de la particule par spectroscopie d'absorption transitoire « *Transient Absorption Spectroscopy* » (TRABS).

Le spectre obtenu par cette méthode correspond à celui d'un intermédiaire de réaction avec séparation de charges (la molécule sous la forme d'un radical anion et la particule avec une densité électronique partialement déficitaire) **(Figure 9)**.

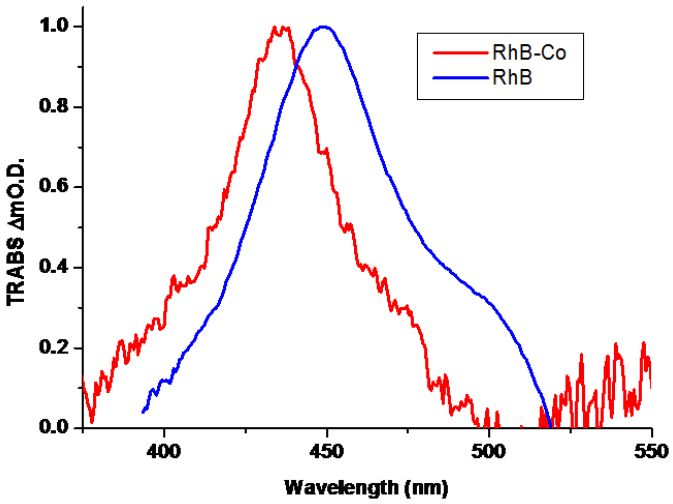

Figure 9. *Signature de l'absorption de l'état excité dans un spectre de TRABS pour l'hybride Co/RhB solubilisé dans l'anisole (rouge) et comparaison avec le signal typique de la RhB libre (bleu).*

Ceci nous permet de conclure que la perte de fluorescence que nous observons dans notre système est une cause directe d'un transfert électronique entre la surface métallique et l'HOMO de la molécule photoexcitée. Un état intermédiaire se forme avec une séparation de charges

(formation d'un radical anion de la RhB et surface métallique partialement déficitaire en électrons). De plus, les spectres montrent deux composantes pour le processus de recombinaison que nous pouvons expliquer de deux manières:

- La recombinaison électronique dans la particule se produit avec deux types d'atomes de Co différents : ceux de la surface et ceux du cœur de la NP.
- Le chemin de retour de l'électron peut se produire directement ou en passant par les différentes molécules de RhB voisines suivant un processus complexe de excitation/désexcitation, jusqu'à rejoindre la surface de la NP.

Les propriétés magnétiques des particules ont ensuite été mesurées sous irradiation. Compte tenu de leur petite taille (3,8 nm), ces nanoparticules présentent un comportement superparamagnétique, avec une température de blocage de 38 K.

Les mesures sous irradiation ont donc été faites dans le SQuID, en appliquant sur l'échantillon un faisceau de lumière blanche à une température au dessous de la température de blocage (10 K) et en présence d'un champ magnétique très fort (5 T) de façon à s'affranchir des fluctuations thermiques de l'aimantation. Une augmentation de l'aimantation de l'échantillon par rapport à sa valeur initiale (0.3 % - 0.9%) est observée **(Figure 10)**.

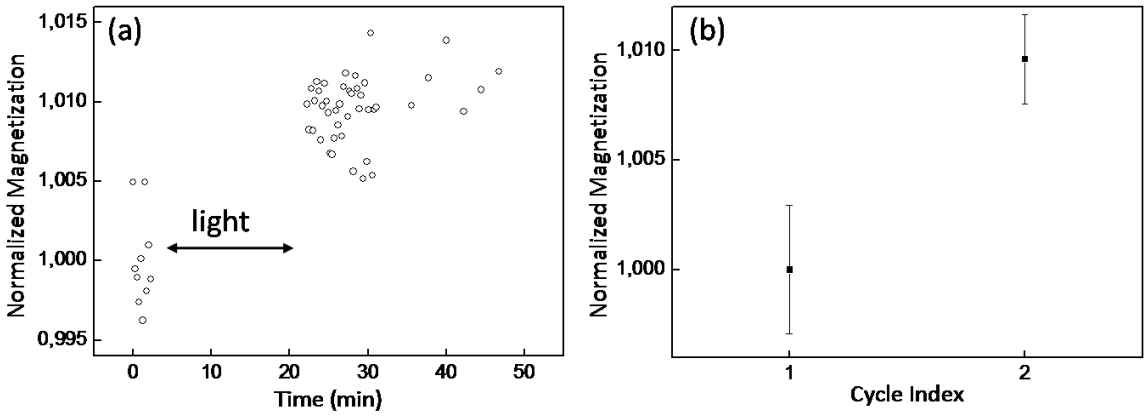

Figure 10. *Evolution de l'aimantation après irradiation.*

Même si l'effet trouvé est très faible il est reproductible et caractéristique de notre hybride. En effet, deux expériences de contrôle ont été effectuées : une avec des particules de Co

de taille similaire mais sans RhB, et une autre avec un mélange physique de particules de Co stabilisées par l'acide oléique, et de RhB sans qu'aucune modification de leur aimantation ne soit observée sous irradiation.

Une explication plausible pour cette variation photoinduite de l'aimantation considère que le transfert électronique entre la surface métallique et le fluorophore est encore effectif à la température à laquelle nous avons fait l'expérience (10 K) mais que le chemin de retour est par contre bloqué, ayant donc un effet net sur l'aimantation globale du système et sur l'environnement diélectrique du cœur magnétique (effet magnétoélectrique).[18] Des expériences complémentaires (fluorophores différents, mesures d'aimantation résolues en temps) doivent être conduites pour pouvoir mieux comprendre et donc maitriser le processus de transfert électronique.

4.3 Conclusions

Nous avons synthétisé avec succès un système hybride composé d'un cœur magnétique non oxydé de cobalt et de molécules de RhB, un agent fluorophore. Les particules formées montrent une taille de 3,8 nm avec une structure ε-Co. Les propriétés optiques du fluorophore sont fortement perturbées par la présence du cœur magnétique conséquence d'un transfert électronique entre la surface métallique et l'état excité de la molécule. D'un autre côté, les propriétés magnétiques de la particule sont aussi modifiées sous irradiation.

Conclusion Générale

Au cours de ce travail nous avons abordé trois points: le contrôle chimique de la synthèse des NPs de métaux magnétiques anisotropes (et sans trace d'oxydation), le développement d'une couche protectrice pour empêcher leur oxydation sous air et le design de nouveaux nanocomposites hybrides, associant propriétés magnétiques et de fluorescence, permettant la photomodulation de l'aimantation.

La décomposition du complexe organométallique $Co(\eta^3\text{-}C_8H_{13})(\eta^4\text{-}C_8H_{12})$ sous dihydrogène en présence de Rhodamine B et d'hexadecylamine comme agents stabilisants conduit à l'obtention de nanodisques de Co. La caractérisation par microscopie électronique à haute résolution permet d'observer la structure hexagonale compacte de ces NPs et la présence de fautes d'empilement dans la direction [0001]. Expériences et simulations suggèrent que la croissance anisotrope est une conséquence directe de la formation de ce type de défauts, comme déjà observé pour des systèmes de morphologie similaire. L'encombrement de la Rhodamine B limite très certainement son interaction avec les germes formés dans les premiers temps de la réaction, permettant la croissance des faces {0001}. Les disques de Co présentés ici ont une surface propre, l'aimantation du massif, et restent bloqués à température ambiante. Des simulations micromagnétiques montrent qu'ils sont monodomaines, et que leur moment magnétique est orienté selon l'axe c de la structure hcp, donc perpendiculairement à la direction de croissance du disque. Toutes ces caractéristiques font des nanodisques des objets bien adaptés au stockage magnétique de l'information. Le prochain objectif doit être le développement d'un processus de dépôt organisé sur des surfaces (*e.g.* sur wafer de silicium).

Cependant, un des inconvénients majeurs pour l'utilisation de NPs métalliques magnétiques dans des dispositifs réels est leur oxydation rapide sous conditions atmosphériques. Dans le troisième chapitre de cette thèse nous avons donc adapté aux objets anisotropes une méthode d'encapsulation par couche de carbone. Nous avons ainsi montré qu'il était possible d'enrober des nanofilaments de Co avec une coquille de carbone amorphe, en utilisant les ligands adsorbés à la surface comme source de carbone. Ce procédé, basé sur le recuit des ligands, doit être parfaitement contrôlé car une augmentation trop rapide de la température

conduit à la fragmentation des objets en une chaine de sphères comme conséquence de l'instabilité de Rayleigh-Plateau. Malgré son caractère amorphe, la couche de carbone permet de protéger de l'oxydation les NPs enrobées. Ce travail est le premier exemple d'une méthode post-synthétique pour l'enrobage de nanofils magnétiques avec du carbone.

Dans le dernier chapitre de ce manuscrit, nous présentons la conception et la synthèse d'un nouvel hybride nanostructuré. La Rhodamine B, un fluorophore organique d'utilisation fréquente en biologie, a été choisie pour stabiliser des NPs métalliques magnétiques de très petite taille (diamètre moyen de 3,8 nm). Ce nanohybride présente une taille et une chimie de surface (sans aucune trace d'oxydation) bien adaptées pour l'étude des phénomènes de surface. Par ailleurs, le contact direct entre le fluorophore et la particule donne les conditions optimales pour étudier l'interaction entre les deux espèces. Comme prévu, la fluorescence du fluorophore est complètement quenchée. Nous avons montré que cet effet est la conséquence d'un transfert électronique entre la particule et la HOMO de la molécule excitée, produisant une séparation de charges. De plus, nous avons observé que l'aimantation des particules est légèrement augmentée sous irradiation. En l'attente de mesures magnétiques résolues en temps, nous proposons que cet effet résulte de la différence entre les cinétiques de transfert d'électrons (de la NP vers la RhB et de recombinaison), conduisant à une modification de la densité électronique de la NP et de son environnement diélectrique. Ce travail pose les bases pour le développement de nouveaux nanohybrides avec une grande intensité de fluorescence ou avec une plus grande efficacité de photomodulation (*i.e.* un meilleur contrôle de l'étape de recombinaison).

---

[1] V. F. Puntes, K. M. Krishnan, P. Alivisatos, Appl. Phys. Lett., 78 (2001), 2187.
[2] K. S. Suslick, M. Fang, T. Hyeon, J. Am. Chem. Soc., 118 (1996), 11960.
[3] C. B. Murray, S. Sun, H. Doyle, T. Betley, MRS Bulletin, 26 (2001), 985.
[4] J. Osuna, D. de Caro, C. Amiens, B. Chaudret, E. Snoeck, M. Respaud, J.-M. Broto, A. Fert, J. Phys. Chem., 100 (1996), 14571.
[5] (a) F. Dumestre, B. Chaudret, C. Amiens, M.-C. Fromen, M.-J. Casanove, P. Renaud, P. Zurcher, Angew. Chem. Int. Ed., 2002, 41, 4286. (b) F. Dumestre, B. Chaudret, C. Amiens, M. Respaud, P. Fejes, P. Renaud, P. Zurcher, Angew. Chem. Int. Ed., 2003, 42, 5213. (c) F. Wetz, K. Soulantica, M. Respaud, A. Falqui, B. Chaudret, Mater. Sci. Eng. C, 27 (2007), 1162.
[6] C. Lofton, W. Sigmund, Adv. Funct. Mater., 15 (2005), 1197.
[7] Q. Jiang, H. M. Lu, Surf. Sci. Rep., 63 (2008), 427.
[8] K. Soulantica, F. Wetz, J. Maynadié, A. Falqui, R. P. Tan, T. Blon, B. Chaudret, Appl. Phys. Lett., 95, (2009), 152504.

[9] (a) R. N. Grass, E. K. Athanassiou, W. J. Stark, Angew. Chem. Int. Ed., 46 (2007), 4909. (b) S. Liu, J. Zhu, Y. Mastai, I. Felner, A. Gedanken; Chem. Mater., 12 (2000), 2205. (c) A.-H. Lu, W.-C. Li, N. Matoussevitch, B. Spliethoff, H. Bonnemann, F. Schuth, Chem. Commun., 1 (2005), 98. (d) C. Desvaux, C. Amiens, P. Fejes, P. Renaud, M. Respaud, P. Lecante, E. Snoeck, B. Chaudret, Nat. Mater. 4 (2005), 750.
[10] Lord Rayleigh, Proc. London Math. Soc., 10 (1878), 4.
[11] F. A. Nichols and W. W. Mullins, Trans. Metall. Soc. AIME, 233 (1965), 1840.
[12] F. Dumestre, B. Chaudret, C. Amiens, M.-C. Fromen, M.-J. Casanove, P. Renaud, P. Zurcher, Angew. Chem. Int. Ed., 41 (2002), 4286.
[13] J. R. Lakowicz, C. D. Geddes, I. Gryczynski, J. Malicka, Z. Gryczynski, K. Aslan, J. Lukomska, E. Matveeva, J. Zhang, R. Badugu, J. Huang, J. Fluoresc., 14 (2004), 425.
[14] (a) C. S. Sun, A. Javier, T. Jennings, M. Fisher, S. Hira, S. Peterson, B. Hopkins, N. O. Reich, G. F. Strouse, J. Am. Chem. Soc. 127 (2005), 3115. (b) T. L. Jennings, M. P. Singh, G. F. Strouse, J. Am. Chem. Soc., 128 (2006), 5462.
[15] B. I. Ipe, K. G. Thomas, S. Barazzouk, S. Hotchandani, P. V. Kamat, J Phys. Chem. B, 106 (2002), 18.
[16] F. Bertorelle, C. Wilhelm, J. Roger, F. Gazeau, C. Ménager, V. Cabuil, Langmuir, 22 (2006), 5385.
[17] J. Osuna, D. de Caro, C. Amiens, B. Chaudret, E. Snoeck, M. Respaud, J.-M. Broto, A. Fert, J. Phys. Chem., 1996, 100, 14571.
[18] M. Suda, M. Nakagawa, T. Iyoda, Y. Einaga, J. Am. Chem. Soc., 129 (2007), 5538. (b) M. Suda, Y. Einaga, Angew. Chem. Int. Ed., 48 (2009), 1754.